Laser diagnostics of an Ar atmospheric pressure plasma jet for biomedical applications

Sylvain Iséni

Sylvain Iséni. Laser diagnostics of an Ar atmospheric pressure plasma jet for biomedical applications. Reactive fluid environment. Ernst-Moritz-Arndt-Universität Greifswald, Germany, 2015. English. NNT : . tel-01241659

HAL Id: tel-01241659
https://theses.hal.science/tel-01241659
Submitted on 18 Jan 2016

Thèse de Doctorat présentée par Sylvain Iséni

Soutenue le 31 août 2015 à l'Université Ernst-Moritz-Arndt, Greifswald, Allemagne.

Diagnostic laser d'un jet plasma froid d'argon à la pression atmosphérique pour les applications biomédicales

Dissertation présentée pour l'obtention du titre de Docteur
de la Faculté de Mathématique et des Sciences de l'Université
Ernst-Moritz-Arndt, Greifswald.

Président du comité d'évaluation:

- Prof. Dr. Jürgen Meichsner

Rapporteurs

- Prof. Dr. Kaus-Dieter Weltmann[†]
- Prof. Dr. Jean-Michel Pouvesle[†]

Membres du jury:

- PD. Dr. Franz Bronold
- Prof. Dr. Andre Melzer
- Prof. Dr. Jürgen Röpcke
- Prof. Dr. Fritz Scholz
- Prof. Dr. Kaus-Dieter Weltmann

Directeur de thèse:

- Prof. Dr. Kaus-Dieter Weltmann

[†] membre co-fondateur de la Société Internationale Plasma-Médecine.

[⋆] cette page a été ajoutée afin de rendre le document conforme à la publication sur HAL.

Laser diagnostics of an Ar atmospheric pressure plasma jet for biomedical applications

INAUGURALDISSERTATION

zur
Erlangung des akademischen Grades
doctor rerum naturalium (Dr. rer. nat.)
an der Mathematisch-Naturwissenschaftlichen Fakultät
der
Ernst-Moritz-Arndt-Universität Greifswald

vorgelegt von
Sylvain Roger René Iséni
geboren am 17.10.1988
in Gien (Loiret), France

Greifswald, den 2. Februar 2015

Dekan:	Prof. Dr. Klaus Fesser
1. Gutachter:	Prof. Dr. Klaus-Dieter Weltmann
2. Gutachter:	Prof. Dr. Jean-Michel Pouvesle
Tag der Promotion:	31. August 2015

« Le bon sens est la chose du monde la mieux partagée : car chacun pense en être si bien pourvu, que ceux même qui sont les plus difficiles à contenter en toute autre chose, n'ont point coutume d'en désirer plus qu'ils en ont. En quoi il n'est pas vraisemblable que tous se trompent ; mais plutôt cela témoigne que la puissance de bien juger, et distinguer le vrai d'avec le faux, qui est proprement ce qu'on nomme le bon sens ou la raison, est naturellement égale en tous les hommes ; et ainsi que la diversité de nos opinions ne vient pas de ce que les uns sont plus raisonnables que les autres, mais seulement de ce que nous conduisons nos pensées par diverses voies, et ne considérons pas les mêmes choses. Car ce n'est pas assez d'avoir l'esprit bon, le principal est de l'appliquer bien. Les plus grandes âmes sont capables des plus grands vices, aussi bien que des plus grandes vertus ; et ceux qui ne marchent que fort lentement, peuvent avancer beaucoup davantage, s'ils suivent toujours le droit chemin, que ne font ceux qui courent, et qui s'en éloignent. »

René Descartes (1596-1650), *Discours de la méthode*, Première partie, 1637.

Contents

Glossary

2D-LIF	2-dimensional laser-induced fluorescence
APPJ	atmospheric pressure plasma jet
Ar	argon
Ar_2^*	argon excimer
DBD	dielectric barrier discharge
DCM	dichloromethane - CH_2Cl_2
DPBS	Dulbecco's phosphate-buffered saline solution
EET	electronic energy transfer
EHD	electrohydrodynamic
FTIR	Fourier transform infrared spectrometer
H_2O_2	hydrogen peroxide
He	helium
HWHM	half width at half maximum
ICCD	intensified charge-coupled device
IR	infrared
LIF	laser-induced fluorescence
MBMS	molecular beam mass spectrometer
Mid-IR	middle infrared
N_2	molecular nitrogen
Nd:YAG laser	neodymium-doped yttrium aluminium garnet, Nd:$Y_3Al_5O_{12}$
Ne	neon
NO	nitric oxide
NO_2	nitrogen dioxide
NO_2^-	nitrite
NO_3^-	nitrate

O_2	molecular oxygen
O_3	ozone
OES	optical emission spectroscopy
OH	hydroxyl
ppb	particles per billion
Q-MACS	quantum cascade laser measurement and control system
QCL	quantum cascade laser
QCLAS	quantum cascade laser absorption spectroscopy
RET	rotational energy transfer
RF	radio-frequency
RH	relative humidity
RNS	reactive nitrogen species
RONS	reactive oxygen-nitrogen species
ROS	reactive oxygen species
SPS	second-positive-system
T_{rot}	rotational temperature
TDLAS	tunable diode laser absorption spectroscopy
UV	ultraviolet
VET	vibrational energy transfer

1 Introduction

In the history of NATURAL SCIENCE, sense of observation has always dominated the attempts of the scientists to acquire more knowledge about the Universe and the secrets of Life. Hence, following this empirical approach, Sir William Crookes provides in 1879 a few phenomenological descriptions of light emission from artificially ionized gases, here called "radiant matter" [1]. A couple of decades later, one proposed the following to explain prior observations,

> *"Except near the electrodes, where there are* sheaths *containing very few electrons, the ionized gas contains ions and electrons in about equal numbers so that the resultant space charge is very small. We shall use the name* plasma *to describe this region containing balanced charges of ions and electrons."* [2].

By analogy with the blood plasma to name the fourth fundamental state of matter, *plasma* [3], in 1928 Irvin Langmuir was light years away from imagining that plasma will be applied in medicine.

Since this time, plasma physics has become a large object of research worldwide aiming at exploring intrinsic properties of the matter [4–6] but also towards a multitude of applications [7, 8]. Several categories of plasmas can be derived from the previous quote and are mainly related to the gas, ion and electron temperatures, T_g, T_i and T_e respectively. A general classification of plasmas is presented in table 1.1. As shown, fundamental differences lie between each type of plasmas, e.g. T_g. The latter is actually a key parameter regarding desire processes. From now and in the context of plasma in interaction with biological substances, one focuses exclusively on low-temperature, *non-thermal plasma* [9]. Essentially, partial ionized gases are not a stable state of matter and thus require an energy input to be sustained. Fortunately, divers technologies exist resorting to various electrical excitation waveforms to maintain sufficient electric field strength for the electrons to gain kinetic energy.

	low-temperature plasma		**high-temperature plasma**
	non-themal	thermal	
relative temp.	$T_\mathrm{g} \approx T_\mathrm{i}$	$T_\mathrm{g} \approx T_\mathrm{i} \approx T_\mathrm{e}$	$T_\mathrm{g} \approx T_\mathrm{i} \approx T_\mathrm{e}$
temp. / K	$T_\mathrm{g,i} \lesssim 500 \ll T_\mathrm{g} \leq 10^5$	$T_\mathrm{g,i,e} \lesssim 2 \times 10^4$	$T_\mathrm{g,i,e} \geq 10^7$
n_e / m^{-3}	$\approx 10^{20}$	$\geq 10^{20}$	$\geq 10^{20}$
characteristic	non-equilibrium	local-equilibrium	equilibrium
examples	DBD, corona, APPJ low pressure glow	arcs and torches at normal pressure	fusion, center of the sun

Table 1.1: General classification of plasmas [8, 9].

The non-equilibrium features of those plasmas operating at ambient atmosphere lead to the formation of reactive oxygen-nitrogen species (RONS) which often cannot be produced by conventional chemical kinetics at room temperature [10]. This exclusive advantage of low temperature plasma chemistry has already been demonstrated for surface modification of heat sensitive material [11–14]. For instance, etching of polymers [15], adhesion enhancement [16] and biological functionalization of surface [17, 18] are applications where atmospheric pressure plasma processes are continuously developing and represent a serious alternative to low pressure systems.

The introduction of new methods appealing to plasma in the medical field has followed a slow progression. The first attempt to use plasma in medicine dates back to the beginning of the XX$^{\text{th}}$ century with the commercialization of the Violet Ray devices [19–22]. Starting indeed from the 1970s and the use of Ar atmospheric pressure discharge as an efficient alternative to conventional electrocauterization [23–25], it is now commonly used to assist surgery. Later, in the 1990s, atmospheric pressure plasmas opened a new way for sterilization and bio-decontamination alternatives offering more flexibility to process microscopic cavities of medical materials and surgical instruments [26]. However, due to well established techniques, most of the plasma devices designed to support sterilization and bio-decontamination turn out to be more related to the general field of hygiene [27, 28]. Intuitively, this thematic quickly led to study anti-microbial effects and deactivation of bacteria by dielectric barrier discharge (DBD) [29–31] and atmospheric pressure plasma jet (APPJ) [32, 33] triggering a real potential of plasmas to induce biological actions.

Hence, over the past decade, the plasma physics community has seen budding a new field of ionized gas research and plasma health care application namely *plasma medicine* [34–41]. Indeed, the latter has been considered *"as an independent medical field emerging worldwide - comparable to the development of laser technology years ago."* [42]. Based on pioneer experiments aiming at investigating how Life could benefit from its –partial– interaction with plasma [43–45], consequent efforts have been spent the last couple of years worldwide to continue those researches and to develop new medical therapies, for instance wound healing in dermatology [46], cancer treatment [47], endoscopy [48] and dentistry [25].

However, the fact remains that as an interdisciplinary topic, *plasma medicine* is a real challenge which involves essentially physicist, chemist and life scientists from various domains (e.g. biologist, pharmacist, clinician). Progresses in this novel field are rising rapidly thanks to parallel studies in each discipline. As a general motivation –for the physicists– to develop and diagnose plasma sources, experimental investigation of plasma treated liquids and cell culture media have revealed intriguing findings concerning liquid activation [31, 49–51], cell responses [52–57], signaling pathways [58] and down to the DNA level [59–61]. Furthermore, *in vivo* studies have already unveiled promising antitumoral effects of plasma treated cancer [47, 62–65] as well as tissue oxygenation [66]. Last but not least, several clinical trials and/or case studies have been launched and report on efficient healing of chronic wounds compared to traditional prescriptions [67–72].

Nevertheless, the success of interactions plasma with biological material are not entirely understood yet, and further investigations of plasma properties are necessary in order to disentangle the role of plasma in cell activation. Often, plasma sources involved in plasma medicine are either DBD or APPJ due to the main advantage that they can operate at gas temperature close to room temperature. A large amount of those sources exists [73–75] and usually operate with noble gases e.g. He and Ar or dry air. Accordingly, the plasma composition differs from each geometry and electrical arrangement which determines the electric field, radiation (vacuum UV, visible), charge, ion, neutral and radical densities as well as the gas temperature. Hence, diagnostics are essential to characterize plasma sources in order to support interpretations of biologists regarding the responses of the cells. Experimental works also contribute to the validation of numerical simulations and plasma models. The latter are of crucial importance to get better insights on plasma chemistry mechanisms and then allowing optimization of the plasma source for the production of specific RONS being relevant in biology [76].

As a general claim, the major effect of plasma treatments to trigger cell activation e.g. apoptosis, cell signaling cascade, is attributed to redox mechanism induced by the plasma chemistry [77]. Indeed, room temperature atmospheric pressure plasmas are prone to form reactive oxygen species (ROS) [78]. These are defined as products created from reactions with O_2, such as ozone (O_3), O, superoxide anion (O_2^-), etc. Another type of reactive compounds so-called reactive nitrogen species (RNS) have been identified to be produced by APPJs [79]. Among them nitric oxide (NO) turns out to be extremely beneficial in the human body since it plays a central role in cell signaling. This findings was actually part of the research of Prof. Dr. Günter Blobel rewarded in 1999 with the Nobel Prize in Physiology or Medicine. Thus, investigation of NO produced by room temperature plasma is in the scope of this Ph.D. thesis.

In the present work, the main focuses is on the diagnostics of RONS resulting from the plasma chemistry of an Ar RF APPJ and its interaction with the ambient atmosphere. To conduct this study, a commercially available plasma device, so-called *kinpen* is used due to its technical development maturity and its accessibility on the market. Furthermore, extending the knowledge about the latter apparatus in the direction of health-care applications will support current and future clinical studies [80, 81] performed by a specific by-product fulfilling all technical requirements of a medical device, namely *kinpen MED* (neoplas tools GmbH Greifswald, Germany) [82].

Consequently, the aim of this thesis is to clarify unanswered questions regarding the plasma jet output chemistry relevant for biological activation and the transfer of chemical compound into the ambient atmosphere.

- What RONS are produced by the plasma jet and which are the key species of the main plasma chemistry kinetics while molecular admixture are introduced?
- How the absolute distribution profile of NO density looks like in the outer plasma volume?
- How the filamentary discharge develops into the ambient according to different neutral gas flow pattern?

As a method of choice, diagnostic techniques are based on optical spectroscopy known to be a reliable tool to investigate plasmas [83–86]. Unfortunately, OES –often used in plasma diagnostic for its relatively simple experimental part– will be substituted to other methods since the latter severely suffers from the non-equilibrium properties of our plasma [87, 88]. Hence, more effort have been invested to use more sophisticated experimental setups resorting to laser systems which allow absolute density measurements, high selectivity and excellent space resolution. The outcome of this thesis will bring new insights in the field of Ar APPJs chemistry and its interaction with the ambient atmosphere which can be valuable to support modeling and to consider for the application in plasma medicine.

2 Plasma jets and laser diagnostics

Mutual interactions between ionized gas and cells are complex, therefore specific attention is required to each side separately but must be considered together. Focusing on plasma jet non-equilibrium chemistry is a reasonable motivation towards plasma medicine since RONS have been pointed as a major key player of cell activations [77]. Moreover, in case of plasma jets, the active volume of the ionized gas is expanding into the ambient atmosphere, inducing additional chemical reactions, e.g. electron losses into ro-vibrational excitations of N_2 and O_2 which will affect the discharge, its development and its non-equilibrium chemistry [89].
This chapter is structured twofold: section 2.1 introduces basics about APPJs. The plasma jet used in this work is reviewed in detail. After announcing why one resorts to laser diagnostics to characterize the jet, the second section will present basics of laser-based techniques chosen to determine absolute RONS densities produced by the plasma. Last but not least, a novel approach to visualize flow structure and discharge propagation into the visible effluent – being actually the interaction region during treatments – will also be described.

2.1 Micro-discharge: atmospheric pressure plasma jets

In this first section, a general introduction about plasma jets –commonly used in research in biomedical applications– is presented. Next, a description of the investigated Ar plasma source is detailed.

2.1.1 Basic about atmospheric pressure plasma jets

APPJs are generally described as non-thermal plasmas operating at pressures around 1 bar (10^5 Pa). The plasma ignition is mostly possible in noble gases which flows through a tube open in the atmosphere. From the opening yields a visible effluent of a few millimeters up to several centimeters [73]. One can associate APPJs to a category of micro-plasma sources for their intrinsic feature of having a short gap between electrodes – in the millimeter scale – in order to keep the product pressure-gap, $p \cdot l$, reasonable for a breakdown to occur [4, 74]. Nevertheless, with this respect, different geometries, electrode arrangements and electric excitation exist. Most of them have been reviewed by Lu et al. [75].
Figure 2.1 shows the visible effluent of the an Ar RF APPJ (*kinpen*, neoplas tools GmbH, Germany) running with typical parameters in open-space. One notices the elongated and symmetric shape of the plume which is quite common for plasma jets [90]. The color of the plume is attributed to the spontaneous emission of Ar and the second-positive-system (SPS) of N_2 diffusing into the vicinity of the jet nozzle while the green emission –in the vicinity of the capillary– results from the "aurora green band" $O(^1S)N_2$ excimer at 557.7 nm [91]. In the case of this plasma jet, overview spectra published by Weltmann et al. [42] validate this interpretation. In addition, the authors observed the emission of OH(A-X) coming from the dissociation of water impurities [92]. Indeed, in case of plasma jet running in open space, one needs to take into account the interaction between the plasma, its resulting chemistry and the ambient, e.g.

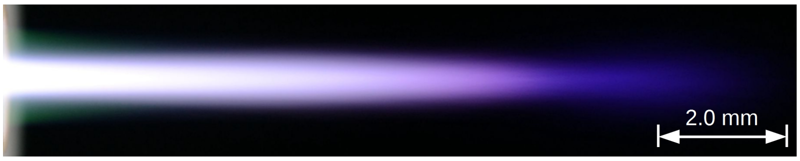

Figure 2.1: Photograph of the plasma jet visible effluent operating with 3.0 slm Ar. Exposure time of 0.25 s, $f \setminus 7.1$, 100 ISO.

involving ambient due to air diffusion into the plume. Later, Winter et al. [50] figured that even a small amount of humidity impurities mixed in the feed gas induces significant changes on the plasma chemistry and does effect the treated cell viability via the production of OH, precursor of H_2O_2 [93, 94]. Although this photograph illustrates well the active volume involved in the applications, the observation is time averaged and corresponds to multiple electrical excitations (about 2.5×10^5periods in the present case).

Looking at the visible effluent on a shorter time-scale of the RF period leads to a completely different insight as shown in figure 2.2 and in ARTICLE I. The latter depicts two distinct ionized streams corresponding to two non-consecutive excitations. At this time scale, spontaneous emission is preceded by breakdown and electron collisions inducing ionization, electronic, rotational and vibrational excitations as well as dissociation [96]. By superimposing two shots, the intention is to highlight the constricted and non-uniform morphology of the Ar discharge. Indeed, in general plasma jet does not generate a continuous plasma. The ignition mechanism of the discharge is driven by the propagation of an ionization wave which then forms a partly ionized gas channel of typically 100 µm diameter called streamer [97, 98]. Those streamers are usually bright due to the intense spontaneous emission of the excited gas. In case of APPJs, one can find in the literature a phenomenological description of the ionization wave propagation named *plasma bullet* by Teschke et al. [99], Lu and Laroussi [100]. Plasma jets formed by single voltage pulse up to frequencies of tens of kHz are typically known in the literature to be composed of bullet-like plasma volumes moving with high velocities, typically several $\mathrm{km \cdot s^{-1}}$. Reuter et al. [101] reported recently on the observation of bullets produced at higher frequencies, here the *kinpen* was investigated.

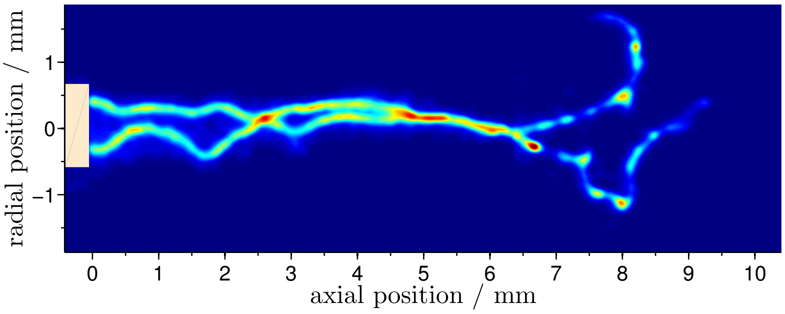

Figure 2.2: Overlay of two ICCD single shot images of the plasma jet visible effluent operating with 3.0 slm Ar. The beige rectangle depicts the nozzle [ARTICLE I]. Exposure time of 800 ns, spectral range from 250 nm to 800 nm.

The theory of streamer creation and transition from avalanche to self-propagation is well described by Meek: *A streamer will develop when the radial field about the positive space charge in an electron avalanche attains a value of the order of the external applied field* [102]. Photoionization, known to be the leading process of the streamer head is of crucial importance for the discharge to develop.
As the result of their simulation of a guided streamer in a jet, Boeuf et al. [103] remind the latter formulation of Meek by highlighting the direct link between direct ionization coefficient of the leading gas and the reduced electric field. However, the authors have considered a very simplified case which consists of a rectilinear He channel surrounded by air with sharp boundaries between the two gases interface excluding any diffusion process. This question will be discussed along this thesis and several answers regarding the case of an Ar APPJ will be unveiled.

2.1.2 Argon atmospheric pressure plasma jet, *kinpen*

In this thesis, the work is mainly focused on the investigation of the commercially available plasma device *kinpen* (neoplas Tools GmbH, Germany) [42]. This plasma source is the achievement of years of development based on research led at the INP Greifswald e.V. A solid scientific background about the application of this plasma jet for thin film deposition, polymer surface modification and decontamination exist inherited from several prototypes [12, 104–107]. The *kinpen* adopts, according to Schutze et al. [108], a coaxial geometry which consists of a concentric needle electrode located within an alumina capillary of 1.6 mm inner diameter as illustrated in figure 2.3. A ring electrode connected to the ground is crimped around the capillary and positioned a few millimeters away from the needle tip. The needle is powered by a miniaturized RF generator producing a sinusoidal voltage waveform ranges from 2 kV to 3 kV amplitude peak. The current flowing through does not exceed 60 mA peak and a power between 1.4 W to 2.3 W is transfered to the plasma. A continuous sinusoidal excitation of 1 MHz is intrinsically set.
The device is fed with an adjustable Ar gas flow rate ranging from 1.0 slm to 5.0 slm with a typical value of 3.0 slm. Admixtures of molecular gases, e.g. N_2 and O_2 are possible and can be used to tailor the output plasma chemistry and RONS as demonstrated in section 3.1. Moreover, Reuter et al. [109] developed a gas curtain cap which allows flowing an additional gas

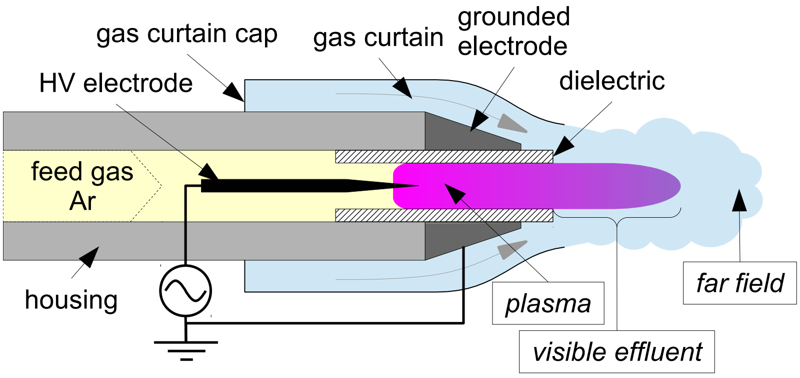

Figure 2.3: Schematic of a coaxial APPJ such as *kinpen* (neoplas GmbH, Germany) [104]

around the device nozzle e.g. dry air in order to control the surrounding atmosphere around the visible effluent.

As shown in figure 2.2, streamers does not propagate in a straight direction and does not originate from the same point. Further investigations are in the framework of this thesis and the results and interpretations have been published and can be found in section 5.3. The main key points and recent understanding about the streamer propagation and the neutral gas flow pattern will be summarized in section 3.3.

From this point, the present work is going to focus on two different aspects of the argon streamer generated by the *kinpen*. The streamer is a very energetic volume from where derives the non-equilibrium chemistry once impurities are involved. Therefore, admixtures of O_2 and N_2 will be admixed separately and simultaneously in order to trigger different chemical mechanisms. On the other hand, the streamer must interact with the atmosphere during its development. In this context, the gas flow pattern is an important parameter and must be investigated simultaneously with the discharge.

2.2 Laser diagnostics for plasma jet characterization

In essence, not a single diagnostic method is able to provide all the necessary information about the plasma. Hence the needfulness to resort to different complementary active optical spectroscopy techniques. The implementation of each method is different as well as the degree of complexity of each theory. For the sake of the reader, each technique is described with the same level of detail and may result in different text length.

This section describes threefold the methods and experimental setups all centered on laser systems. Firstly, absorption spectroscopy by QCL is used to determine absolute density of long living reactive species space averaged. Then, LIF has been performed to measure, space resolved, absolute NO density profile within the visible effluent. Finally, an adaptation of the previous technique to 2D-LIF combined with spectrally resolved stereoscopic imaging allowing flow field visualization and discharge propagation is applied to plasma for the first time and will be presented.

2.2.1 Mid-IR quantum cascade laser absorption spectroscopy - QCLAS

The absorption spectroscopy has an important role in plasma diagnostic all the more since it allows to measure absolute ground state concentration and is often simple to calibrate. It also has the undeniable advantage to be non-invasive provided that the inspected medium remains optically thin. With good control of the light source intensity, it does not influence plasma properties. An interesting property of heteronuclear molecules is the non-permanent nature of their transition dipole moment and thus enabling them to absorb IR and Mid-IR radiation. Mid-IR ranges from 3 µm to 20 µm in the electromagnetic spectrum which corresponds to energies in the magnitude of 0.1 eV. The large amount of vibrational bands subdivided in rotational transitions can be populated after absorbing photons of this order of energy down to 0.01 eV to yield very dense and complex absorption spectra. The uniqueness of those spectra are the fingerprint of each molecule and thus makes this diagnostic extremely selective.

Absorption spectroscopy

Absorption spectroscopy is based on the ability of atoms and molecules to interact with electromagnetic radiation. The result of this interaction is a change of the energy state of the molecule by exciting rotational and/or vibrational and/or electronic transitions. The latter depends on the frequency ν (s^{-1}), being proportional to the energy of a single photon, $E = h\nu$. The radiative energy transfer between a light beam going through a homogeneous absorbing volume of gas is now described. The change of intensity $dI(\nu)$ over an infinitesimal slice dl is described by the equation 2.1:

$$
\begin{aligned}
dI(\nu) &= [\eta(\nu) - \kappa(\nu) I_{in}(\nu)] dl && (2.1)\\
I(\nu) &= I_0(\nu) \cdot \exp\left(-\kappa(\nu) \cdot L\right) && (2.2)
\end{aligned}
$$

Emission coefficient $\eta(\nu)$ (cm^{-1}) is neglected in case of a neutral gas, $\kappa(\nu)$ (cm^{-1}) is the absorption coefficient and L the absorption length of the radiation beam. I_{in} is the light intensity going through the slab element dl. Integrating equation 2.1 leads to the known expression of the Beer-Lambert law, equation 2.2. $I_0(\nu)$ is the intensity of the beam entering the absorbing medium and $I(\nu)$ the intensity covered by the light along a distance L.
The determination of the ground state concentration n (cm^{-1}) is possible by using the line-strength, $S_{\nu_0}(\mathrm{T})$ ($\mathrm{cm} \cdot \mathrm{molecule}^{-1}$), specific for each absorption line at temperature (T),

$$
\kappa(\nu) = S_{\nu_0}(\mathrm{T})\ f(\nu - \nu_0) \cdot n \tag{2.3}
$$

with the natural line-shape being a normalized Lorentz-profile,

$$
f(\nu - \nu_0) = \int \frac{\nu_L}{\pi \cdot (\nu - \nu_0)^2 + \nu_L^2}\ d\nu = 1 \tag{2.4}
$$

where ν_0 is the resonance frequency of the transition and ν_L the HWHM derived from the Heisenberg uncertainty principle, $\nu_L = (2\pi \cdot \Delta E)/h$.
Practically, equation 2.2 can be rewritten as,

$$
I(\nu, T) = I_0(\nu) \cdot \exp\left[-S_{\nu_0}(\mathrm{T})\ f(\nu - \nu_0) \cdot n\right] \tag{2.5}
$$

to be directly applied for a single line. The line-strength constants have been tabulated for a multitude of compounds. In this work, the values are taken from the HITRAN database [110].

Q-MACS to diagnose the kinpen output chemistry

During the last two decades, tunable diode lasers have become a serious alternative to continuum broad band light sources in the Mid-IR. Indeed, in 2003 McManus et al. [111] promoted the advantage of using a compact system based on tunable lead-salt diode laser for very high resolution spectroscopy ($10^{-4}\,\mathrm{cm}^{-1}$). A couple of years later, Röpcke et al. [112] published a review about the tunable diode laser absorption spectroscopy (TDLAS) highlighting its advantages compared to the well established Fourier transform infrared spectrometer (FTIR). However, the method is mostly used at reduced pressure (200 mbar or lower), which is understandable to turn to good account the high spectral resolution and minimizing the pressure broadening. Finally, in 2008 Pipa et al. used a TDLAS system to measure the net production rate of NO generated by an APPJ under atmospheric conditions [113]. The plasma jet used in the referred work was a non-commercial version of the *kinpen* in a earlier phase development.

Nowadays, TDLAS is being replaced by QCLAS since the lead-salt laser diodes require cryogenic cooling and intensive effort to maintain sufficient stability [114].
The recent progress on QCLAS allows the measurement of trace gas down to $10^{-16}\,\mathrm{m}^{-3}$ in a low pressure chamber. Considering the importance of RONS when it comes in contact with cells, it is of high interest to resort to this technique. For that purpose, a commercially available quantum cascade laser measurement and control system (Q-MACS) apparatus was used to diagnose the *kinpen*. The main asset of the Q-MACS is taken from the quantum cascade laser (QCL) [115] and its narrow bandwidth and continuous tunable monochromatic radiation over the absorption profile to produce highly resolved spectra [116].
Another powerful aspect of the Q-MACS is the combination of simultaneous spectrum acquisition with numerical spectrum simulation analysis. Indeed, the system consists of a driver unit controlled by software allowing to tune the laser wavelength and to read-out the detector. Since this work was done with the first generation of QCL, the latter was pulsed and thus requires a precise temporal synchronization with the detector ensured by the driver unit. Once a spectrum recorded, the software applies fitting algorithms in order to match a simulated spectrum with the experimental data. The sampling rate is variable and strongly depends on the spectral range as well as the number of absorption lines to consider in the spectra simulation. In the present work, a concentration value was able to be determined every 2 s to 5 s. Initially developed by the company neoplas control GmbH, Germany, the fitting routines included in the simulation algorithm have been optimized during this study to handle spectra at atmospheric

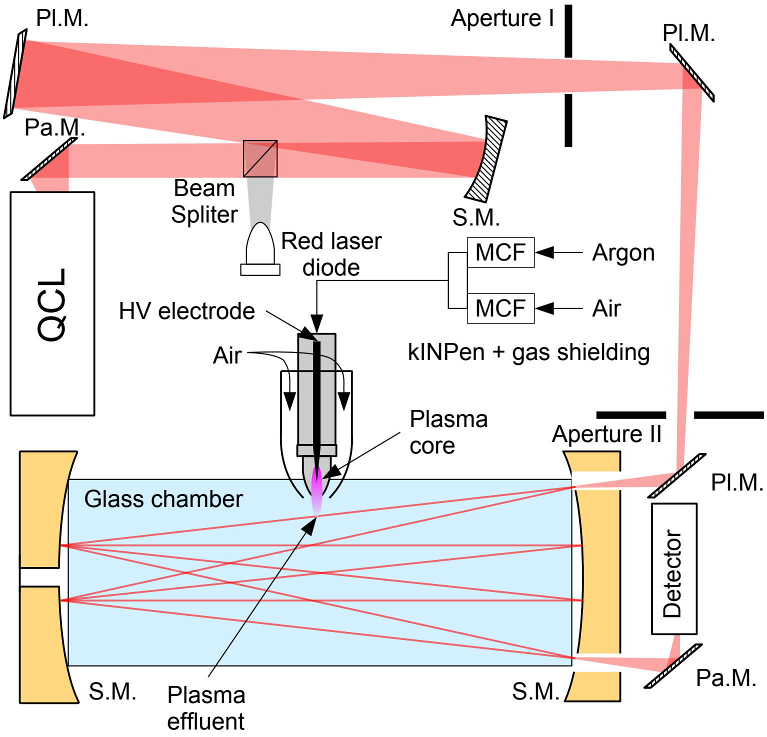

Figure 2.4: Schematic of the Q-MACS apparatus adapted to diagnose APPJs.
Pl.M.: plano-mirror, Pa.M.: parabolic mirror, SM: spherical mirror, MCF: mass-flow controller. Figure from ARTICLE II, reprinted in color.

pressure which suffer from a strong broadening. More details concerning this optimization of the simulation are reported in ARTICLE II. This approach enhances drastically the reliability of the diagnostic due to the absorption recognition pattern spectrally resolved which does not rely only on the integrated intensity as it is often performed, for example in the case of O_3 in the UV. Hence the very high selectivity of this technique regarding the detection and concentration determination of RONS.
Notwithstanding, the Q-MACS was initially designed to operate at reduced or low pressure which requires adaptation of the system for the diagnostic of the *kinpen*. Figure 2.4 depicts the experimental configuration to probe the output chemistry produced by the jet. As seen, the *kinpen* is connected in the middle of a cylindrical glass chamber and blows into it. Additional air is added via the gas curtain in order to reproduce conditions of the jet running in open atmosphere and thus avoid the saturation of the chamber with Ar. Moreover, concentric injection of air around the visible effluent (see figure 2.3) allows to keep the chemistry resulting from the ambient air diffusion into the visible effluent unchanged. A tunable multipass cell (White type [118]) is used in order to adjust the path length of the Mid-IR beam through the cell. For more details about the adaptation of the plasma jet to the Q-MACS as well as the laser energy calibration, the reader is referred to ARTICLE II. The latter was preceded by an earlier publication where the authors aimed to validate the approach of using QCLAS for the diagnostic of APPJs [101]. In this work, O_3 was used as a ROS produced by the *kinpen* and presents the advantage to be detected in the UV and Mid-IR ranges. The results of both methods are in excellent agreement and are considered as a proof of principle. Additionally, the comparison shows the advantage of the high accuracy of the Q-MACS to determined absolute

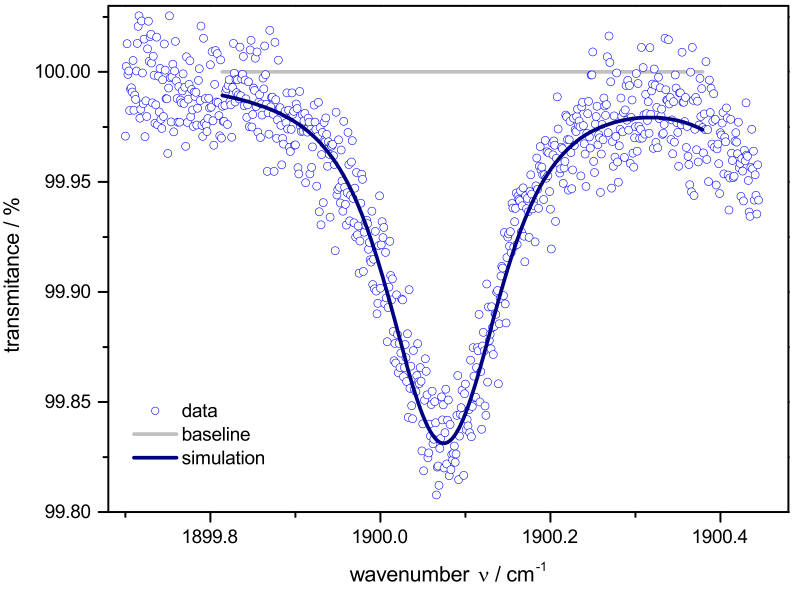

Figure 2.5: NO absorption profile measured with the Q-MACS and the fit immediately performed after acquisition. The corresponding NO concentration measured in the chamber is $1.1 \times 10^{18}\,\mathrm{m}^{-3}$.
Experiment realized at 296 K, 1.0 bar, 24.0 m absorption length with a spectral resolution of $0.04\,\mathrm{cm}^{-1}$.

concentration of RONS produced by the *kinpen*.
In the framework of plasma medicine, other reactive species than O_3 have a higher potential to activate cells. Therefore NO molecules produced by the plasma jet is aimed to be diagnosed with the Q-MACS. Figure 2.5 shows an absorption profile of NO recorded for the calibration of the system. The simulation of the absorption spectrum and plotted on the graph is the best match with the experimental data. It was determined that the detection limit of the setup reaches a concentration of $6.0 \times 10^{17}\,\mathrm{m}^{-3}$. Unfortunately, no detection of NO molecules in the far field of the *kinpen* was observed. Indeed, NO is known as a very reactive molecule leading to the formation of more complex oxygen and nitrogen compounds (N_xO_y). Consequently, the Q-MACS has been reconfigured to performed measurements of NO_2. This molecule is less reactive than its precursor, NO and thus is considered here as an indirect detection of NO in the chemistry of the plasma jet. However, ARTICLE II contains the complete work related to the diagnostic of NO_2 produced by the *kinpen*. The latter reports on the first detection and measurement of NO_2 at atmospheric pressure with QCLAS technology down to the ppb scale. To put it in a nutshell, table 2.1 summarized all the RONS investigated for the first time in this study with the QCLAS operating at atmospheric pressure for the investigation of the *kinpen*. The very high selectivity and sensitivity allow us to resolve the plasma chemistry dynamics by means of admixture of N_2 and O_2. The experimental results compared to plasma chemistry modeling are reported in ARTICLE VI and reviewed in section 3.1.

	O_3	NO	NO_2
spectral range / cm^{-1}	1026.7 - 1027.2	1611.3 - 1611.9	1899.8 - 1900.3
detection limit / m^{-3}	4.8×10^{18}	6.0×10^{17}	4.8×10^{17}
stat. error / m^{-3}	5.9×10^{18}	5.3×10^{17}	4.2×10^{17}

Table 2.1: Measured RONS concentration achieved by QCLAS at atmospheric pressure.

Concerning the outstanding study of NO being of crucial interest for the motivated applications, another diagnostic technique must be considered while the successful measurements of NO_2 hint the production of NO. All evidences point out that NO is formed in the vicinity of the jet nozzle therefore, resorting to a space-resolved diagnostic to probe the visible effluent is necessary, e.g. LIF.

2.2.2 Laser-induced fluorescence

As a step further towards applying absorption spectroscopy, LIF is a more advanced technique based on absorption and emission (fluorescence) of photons [120]. The general concept of LIF is to probe particles in a non-radiative state to an excited state and then collecting its fluorescence in order to determine the particle concentration being in the initial energy state. Extensively, ground state molecular concentration is measured. LIF has been applied by the combustion community to characterize important chemical reactions [121]. Thanks to pioneer studies of flames, a multitude of reaction rates has been measured [122, 123]. One of the first application of LIF in plasma has been reported by Burgess and Skinner [124] but it is only in 1995 that it was used for the first time at atmospheric pressure [125].
Yet, it has become the preferred technique to diagnose chemical radicals produced in plasma chemistry due to its high selectivity of species and high sensitivity (down to ppb range depending on experimental conditions). Although LIF is used to localize molecules with a µm space

resolution, it is possible to determine absolute concentration of ground state molecules with a high temporal resolution (in the tens of ns time scale). Nevertheless, this achievement requires to calibrate the signal and is often a challenging step for the experimentalist.

Basics

To have a better understanding of this powerful method, theoretical basics are briefly presented highlighting the most important key points. Let's consider a two-level energy model constituted of level 1 and level 2 with their relative energy distributed as $E_1 < E_2$ and belonging to two different electronic states. Consequently, an electronic transition (1-2) exists. The total number of molecules n_{tot} is known as $n_{\mathrm{tot}} = n_1 + n_2$. Populations of energy levels are in thermodynamical equilibrium which means that all molecules are at level 1, $n_{\mathrm{tot}} = n_1$. Tuning the laser wavelength to generate photons with an energy $h\nu = E_2 - E_1$ will excite some molecules from level 1 to level 2. This transient mechanism resulting from the laser pulse is described by the following rate equation,

$$\frac{\mathrm{d}n_2(t)}{\mathrm{d}t} = B_{12} I(t) n_1(t) - \left[B_{21} I(t) + A_2 + Q\right] n_2(t). \tag{2.6}$$

$I(t)$ $(\mathrm{J \cdot m^{-2}})$ is the laser intensity, B_{12} $(\mathrm{m^2 \cdot J^{-1} \cdot s^{-1}})$ and B_{21} $(\mathrm{m^2 \cdot J^{-1} \cdot s^{-1}})$ are the absorption and stimulated emission coefficients respectively of the transition (1-2). A_2 $(\mathrm{s^{-1}})$ the spontaneous emission coefficient being the sum over all transitions to level state 1 originating from level state 2. Finally, the total rate of all collisional processes that depopulate the fluorescence of level 2 is the quenching, Q $(\mathrm{s^{-1}})$. It includes electronic energy transfer (EET), vibrational energy transfer (VET) and strongly depends on the gas composition,

$$Q = \sum_i q_i n_i, \tag{2.7}$$

with q_i $(\mathrm{m^3 \cdot s^{-1}})$ the quenching coefficient and n_i $(\mathrm{m^{-3}})$ the density of a specie i, e.g. O_2, N_2,...
To allow for a simplified model of LIF, some assumptions have to be made and are often justified [96].

(i) the LIF signal is linearly proportional to the laser intensity used to excite the transition $1 \rightarrow 2$. This means that the quantity of laser energy is as low as possible to excite only a small faction of level 1 to consider its population density constant. Thus, stimulated emission, B_{21}, is aptly neglected.

(ii) the vibrational and rotational populations of the interested molecular state (usually the ground state of the molecule, but it can be a metastable, e.g. N_2(A)) must be in equilibrium with the translational temperature. In this case, one can determine from the density of the pumped level (level 1), the total density of the interested molecular state using the Boltzmann factor, f_{B}. The latter is assumed to depend only on the gas temperature.

(iii) VET belonging to the excited state must be insignificant to be neglected.

(iv) the lifetime of the excited state (including quenching) is independent of the pumped rotational state. This assumption is correct if rotational energy transfer (RET) is much faster than the laser pulse duration. Thus, the effective lifetime of the vibrational band is used.

(v) to ensure any loss of signal in case of strong RET, a broadband detection covering the whole vibrational band is necessary.

(vi) fluorescence losses due to chemical reaction of the excited state with other compounds is often negligible (this does not consider quenching).

According to assumption (i), equation 2.6 becomes,

$$\frac{\mathrm{d}n_2(t)}{\mathrm{d}t} = B_{12} n_1 I(t) - [A_2 + Q]\, n_2(t). \tag{2.8}$$

A solution to this differential equation is known to be a convolution product between the laser intensity and an exponential decay [126] and formulated as,

$$n_2(t) = B_{12} n_1 \int_0^t I(t) \exp\left[(-A_2 + Q)\,(t - \tilde{\tau})\,\mathrm{d}\tilde{\tau}\right]. \tag{2.9}$$

The expression of the time-dependent LIF signal, $S_{\mathrm{lif}}(t)$, measured by the detector is taken from [127] and adapted considering (iii), (iv) and (v),

$$S_{\mathrm{lif}}(t) = \int_{V_{\mathrm{c}}} \epsilon \frac{\Omega_{\mathrm{c}}}{4\pi} A_{\mathrm{rec}} n_2(t)\ \mathrm{d}V_{\mathrm{c}}, \tag{2.10}$$

with ϵ a factor accounting for the optical efficiency of the detection chain and Ω_{c} (sr) the solid angle of fluorescence collection. The integral is over the focal volume, V_{c} (m^{-3}), defined by the intersection of the laser beam and the collection optics. A_{rec} (s^{-1}) is the emission coefficient of the excited state decay of the fluorescence and recorded by the detector. The integration of equation 2.10 over the time involving n_1 makes it more pragmatic,

$$S_{\mathrm{lif}} = \epsilon \frac{\Omega_{\mathrm{c}}}{4\pi} V \cdot \frac{E_{\mathrm{l}} \Gamma}{\varnothing_{\mathrm{l}}} \cdot \frac{A_{\mathrm{rec}}}{A_2 + Q} n_1 B_{12}. \tag{2.11}$$

The integration of $I(t)$ results in the quantity ($E_{\mathrm{l}}\Gamma/\varnothing_{\mathrm{l}}$) where E_{l} (J) is the laser energy, Γ (s) the overlap integral and $\varnothing_{\mathrm{l}}$ (m^2) the laser beam cross-section area. A definition of the overlap integral as well as its implication in LIF can be found in [128, 129].
Having S_{lif} proportional to n_1 is of great interest if the latter is the ground state of the investigated molecule, n_{gnd}. However, it may happen that it is not the case thus one relies on the assumption (ii) which gives,

$$n_{\mathrm{gnd}} = f_{\mathrm{B}}(J, T_{\mathrm{rot}}) \cdot n_1 \tag{2.12}$$

$$f_{\mathrm{B}}(J, T_{\mathrm{rot}}) = \frac{(2J+1) \exp\left[\frac{-E_J}{k_{\mathrm{B}} T_{\mathrm{rot}}}\right]}{\sum_J (2J+1) \exp\left[\frac{-E_J}{k_{\mathrm{B}} T_{\mathrm{rot}}}\right]}. \tag{2.13}$$

The Boltzmann factor $f_{\mathrm{B}}(J, T_{\mathrm{rot}})$ [130] is expressed according to the rotational quantum number J and rotational temperature, $\mathrm{T}_{\mathrm{rot}}$ (K). According to the experimental conditions, the investigated compound and the aims, one may have to face different scenario which requires to apply the described theory more or less rigorously. Often, difficulties occur at the absolute calibration step although various methods may be used as it will be discuss later on with the diagnostic of NO and OH.

LIF applied for NO and OH measurements in the kinpen

In this work, LIF was used to measure density profiles of NO ground state within the visible effluent of the *kinpen*. Tuning the laser wavelength around 226.2 nm allows to excite the rotational transition NO(A-X)(0-0). The fluorescence of the whole rotational band NO(A-X)(0-2) is observed with a spectrally resolved detector centered at 247.0 nm with 12.0 nm bandwidth. The experimental setup which involves many optical components is described in ARTICLE IV. The latter also describes accurately the application of LIF to diagnose NO in cold APPJs and the validity of the assumptions to allow the method to carry out absolute density measurements. Besides thermalization of NO A $^2\Sigma^+(v{=}0)$ rotational states for a gas temperature being up to 600 K occurs during the laser pulse [132]. Advantageously, it allows to perform a calibration of the LIF signal with a known density of NO from a reference source at room temperature. Details can be found in ARTICLE IV and [133].

An example of a typical LIF signal resulting from a laser pulse tuned at the transition energy is shown in figure 2.6. The fact that the data fit well with an exponential decay model is consistent with the basics presented previously. Moreover, one can calculate the importance of the quenching Q since $\tau = A_{\mathrm{det}}^{-1}$ which can be inserted in equation 2.11. In the case of the main quenchers are identified and their quenching rate with the excited state of NO A $^2\Sigma^+(v{=}0)$ known, one can determine the total density of quenchers but this is not often the case. Nevertheless, in ARTICLE IV air density profiles are calculated from the quenching of NO fluorescence and in excellent agreement with other techniques applied to the *kinpen* [134, 135]. In the same article, a comparison of NO absolute density measured by LIF and MBMS is reported. Back to the pioneer study of Stoffels et al. [79, 136] who reported first the production of NO produced by APPJs and used MBMS, the result of this comparison concludes that LIF is more sensitive and very selective method regarding chemical compounds, especially in case of APPJs.

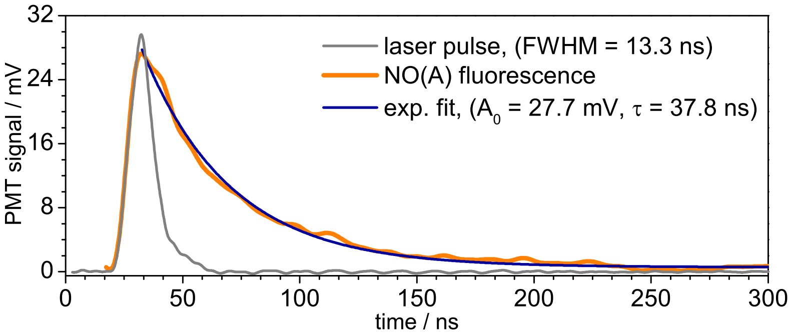

Figure 2.6: Typical recorded NO fluorescence resulting from a laser pulse excitation. The signal fits with a simple exponential decay model and gives information about the amplitude and the decay time of the fluorescence.

By scanning the laser wavelength over the NO(A-X)(0-0) energy range and recording the resulting fluorescence, one can produce a rotational excitation spectrum such as depicted in figure 2.7. The intensity of each line depends on the rotational temperature which is involved in the Boltzmann energy distribution. Advantageously, if the translational temperature is equal to the rotational temperature, one can use this non-invasive approach to estimate the gas temperature [88]. Unfortunately, those atmospheric pressure plasmas are far from local-thermal equilibrium and often, simple OES leads to an overestimation of the rotational temperature.

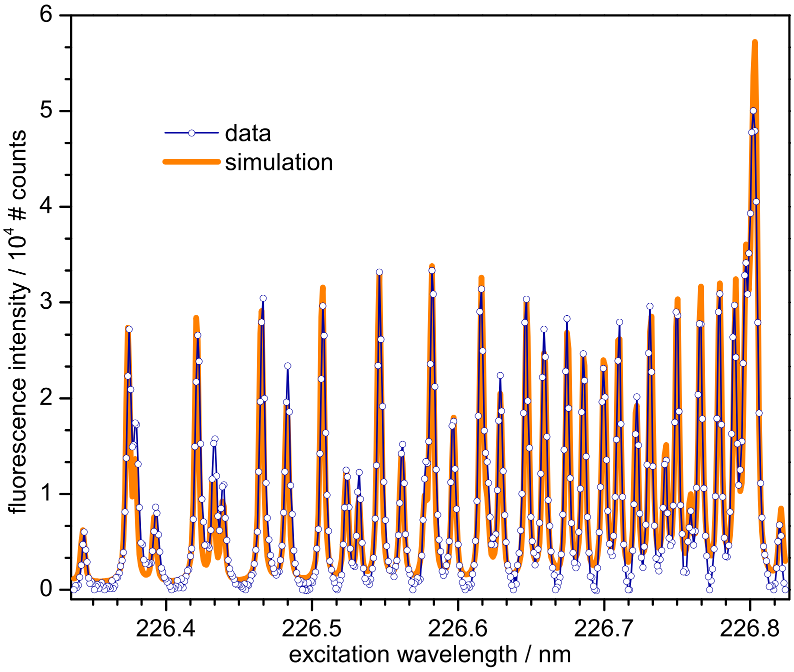

Figure 2.7: Experimental LIF excitation spectrum of NO(A-X)(0-0) collected from the plasma effluent at 3.0 mm from the nozzle. The rotational temperature determined by the fit algorithm is 399(22) K.
The feed gas flow rate was set at 3.0 slm and the gas curtain flow rate set at 5.0 slm [137].

For instance, it was experimentally shown in [138] that there are significant discrepancies between T_{rot} of NO(A) measured by recording OES spectra and T_{rot} of NO(X) appraised from the LIF excitation. The authors attribute the non-Boltzmann energy distribution of NO(A) to high efficient energy transfer between N_2(A) and NO(X) producing NO(A). Hence the main asset of LIF to evaluate T_{rot}. In addition, an accurate approach to determine T_{rot} involving advanced fitting spectra algorithms has been carried out in [137]. An example is given in figure 2.7 and the results are reported in ARTICLE IV.
In this work, LIF was not only applied to the diagnostic of NO but also to OH radical. Indeed, in the framework of a complete interdisciplinary study dealing with plasma generated H_2O_2 and its impacts on cell viability [139], a better insight about OH production –known to be the precursor of H_2O_2– is required. The latter will be discussed in section 3.1 reporting the main production pathways of OH and H_2O_2. The complete interdisciplinary study including OH measurements presently mentioned can be found in ARTICLE V. OH radical is a highly oxidative agent with a typical lifetime of a few milliseconds in atmospheric conditions [140, 141] and thus having an important role in atmospheric pressure plasma chemistry [10, 77, 89]. Although OH has been under investigation for decades in combustion, the fact remains that the measurement of absolute density is still a real challenge as soon as its fraction reaches 10^{-4}. Often, LIF approach offers the highest degree of flexibility. If none of the postulates (i)-(vi) are respected, the diagnostic becomes trivial and is limited to the detection of OH ground state space-resolved (in the tens of micrometer scale). In this case, LIF is used to locate OH molecules in space.

However, applying LIF in a way that at least assumption (i) becomes correct is a denoting fact which means that the LIF signal is proportional to the laser intensity,

$$S_{\text{lif}} \propto \frac{n_{\text{OH}}}{\sum\limits_i q_i n_i} I. \tag{2.14}$$

Here, no calibration is required however the signal is rigorously corrected for quenching of OH(A) since the fluorescence decay strongly depends on water content [129]. This approach has been successfully applied and gives an additional value to this work since it allows to get a better insight of the dynamic of the (relative) OH density with water admixture in the *kinpen*. To yield absolute density measurement of OH, one needs to calibrate the LIF signal. This challenging procedure often requires experimental skills and can be achieved through several approaches: empirical and pragmatic way of estimating each optical loss, collection solid angle, etc. [142], with chemical models [143], via laser scattering (Rayleigh [144] or Raman [145]) [129, 146] or with direct UV absorption when this is possible [147]. Moreover, OH molecule is prone to slow thermalization when water molecules are involved [148] as well as significant influence of VET increasing fluorescence losses. The necessity to resort to an extensive chemical model including many energy levels to describe the LIF scheme is of higher interest in order to obtain an accuracy limited to one order of magnitude [147, 149]. More generally, a complete experimental study of OH formed in APPJ chemistry requires several years focused on this topic as evidenced by the publication over the last three years of many Ph.D. works dedicated to the diagnostics of OH by LIF [150–152].

Consequently and as a matter of choice, this work has –for the first time– contributed to determine relative OH density for low admixture of humidity in the Ar feed gas bringing solid evidence that OH is the precursor of chemical reaction pathways leading to cell oxidative stress which could be at some point lethal for the cells [ARTICLE V].

2.2.3 Single shot, 2D laser-induced fluorescence

Using 2D-LIF to visualize flow field is well reported in fluid-mechanics literature [153, 154] and agreeably reviewed in the monograph of Muraoka and Maeda [155]. It is performed by adding a tiny amount of tracer (usually organic compounds) into the investigated gas phase and provide very high quality images of the flow pattern e.g. shock-wave or supersonic fluid expansion [155]. Notwithstanding, this flow visualization technique has been implemented on plasmas for the first time in this work. It is in all likelihood because essentially plasma state tends to dissociate complex chemical compounds usually prone to absorb and fluoresce in the UV and visible light spectrum. Moreover, visualization of flows by fluorescence of Ar, He, N_2 or O_2 requires very short wavelength which cannot be reached easily by powerful tunable lasers. Unfortunately, admixing a tracer in the plasma would change its properties and most probably alter the tracer inhibiting any chance of fluorescence.

As mentioned earlier, OH fluorescence can be used to reveal its spatial distribution while spontaneous emission will just indicates where the area are located with enough energy to excite OH. In addition, it has been shown that ambient air humidity diffusing into the visible effluent of APPJs is an efficient transport mechanism of water vapor leading to OH production distributed in the boundary region between visible effluent and ambient air [156]. The authors discussed a second source of water coming directly from the residual humidity in the feed gas pipe resulting in an homogeneous mixture. This fact had earlier been investigated in our laboratory and is entirely supported [50].

As a result, together with 2D-LIF, OH radicals are suitable for APPJs flow field visualization enabling to study the interaction between the visible effluent and ambient air. The investigation of such interaction is highly relevant to get a better insight about plasma chemistry and its fundamental mechanism.

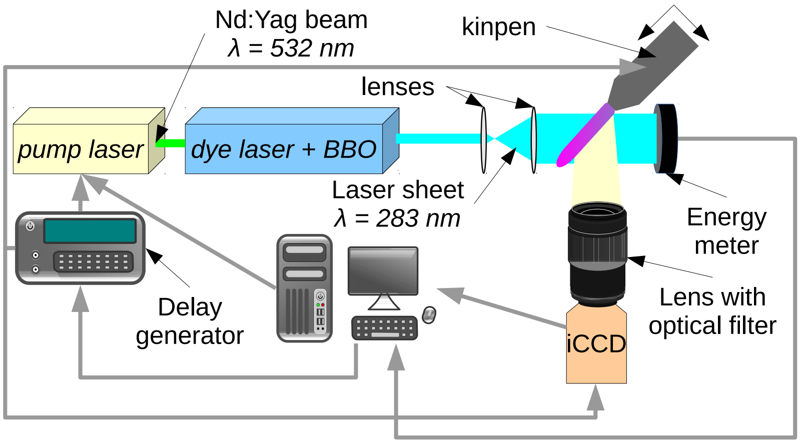

Figure 2.8: Diagram depicting the 2D-LIF experimental setup for the diagnostic of APPJs. This system was used to conduct the experiment published in ARTICLE III where detailed descriptions are given.

Recently, other approaches have been used to characterize neutral gas flow pattern of APPJs. Frequently, Schlieren imaging [158] is the preferred diagnostic for its simple experimental setup and low-cost compared to 2D-LIF. The information obtained with Schlieren is an integration over a volumetric sample, whereas 2D-LIF images the fluorescent molecules distribution along the entire path of the laser beam going across the visible effluent. By means of simple optics, the laser beam can be shaped as a sheet in order to slice thin section of the flow. Note that the validity of this interpretation requires assumption (i) from section 2.2.2 to be correct. As an advantage with regard to Schlieren imaging, 2D-LIF allows clear distinction of tracer mixed gas phase revealing its boundaries with another gas phase free from tracer.

This method has been applied to the *kinpen* to investigate the flow regimes –laminar and turbulent– and part of the results will be discussed in section 3.3. The reader is referred to ARTICLE III to access the complete study. In the latter publication is detailed the experimental protocol step-by-step and each relevant component is carefully reviewed. The experimental setup is illustrated in figure 2.8 since no drawing could be placed to support the technical description in the Fast Track Communications [ARTICLE III].

A step further from imaging the flow pattern of the *kinpen* is to obtain simultaneously and with the same precision the position of the discharge (see figure 2.2). For this purpose, the 2D-LIF system has been upgraded with spectrally resolved stereoscopic imaging. This novelty has been carried out for the first time in this research for the diagnostic of plasmas. Technically, a stereoscopic imaging optical system is mounted in front of the ICCD lens allowing the splitting of the detector in to two area as shown in figure 2.9. As reported in ARTICLE III, bandpass optical filters are mounted on each of the two inputs to isolate on one side the OH fluorescence

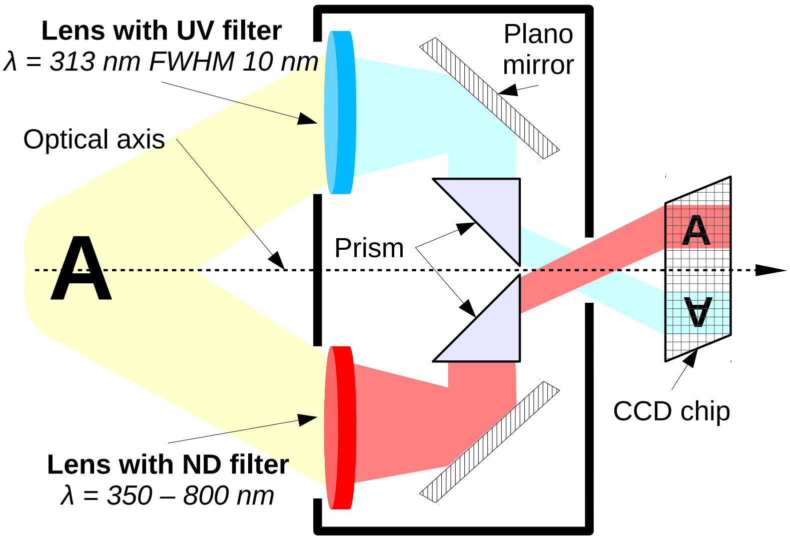

Figure 2.9: Flow diagram of spectrally resolved stereoscopic imaging system used in combination with 2D-LIF for flow and discharge distribution visualization. This apparatus has been used for the study published in ARTICLE III.

and on the other side visible light emission mostly resulting from Ar emission. This innovative approach allows to observe flow pattern and discharge propagation simultaneously.

This experiment has been designed to answer questions regarding flow profiles with different feed gas flow rates with and without plasma and gas curtain. The results dealing with this diagnostic are mostly reported in ARTICLE III and section 3.3 concerning the physical findings. In the context of applications of the *kinpen* with the gas curtain to biology, flow field imaging has been a reliable tool to setup specific plasma treated cell experiments as presented in ARTICLE VIII.

3 Results: plasma jet properties

This chapter summarizes the main outcomes of this Ph.D. thesis. Starting from a general investigation on the plasma chemistry in section 3.1, one focuses more on the plasma plume and the distribution of NO within this small volume (see section 3.2). Having a closer look into the discharge itself, section 3.3 reports on observations of the interaction with the neutral gas flow involved in the plasma chemistry. Finally, investigation results lead to the definition of a parameter set which enables a better control of the discharge, the neutral gas flow and thus the chemistry. Section 3.4 reports on the successful application of such defined parameter set for the *kinpen* on direct treatment of cell suspension.

3.1 Plasma chemistry

In this section, the *kinpen* throughout chemistry depending on admixtures is reported, highlighting the main production mechanisms of RONS with molecular admixture. Essentially, the plasma chemistry results from a multitude of parameters related to the plasma device, namely voltage/electrical power, feed gas (including admixture), gas flow, geometry, materials and ambient atmosphere [96].
Apropos of the *kinpen*, geometrical and material features are defined by the manufacturer. Concerning the power, the feed gas and the flow rate, these parameters are limited in narrow ranges as described in section 2.1 but allows the user to perform slight tuning windows influencing the chemistry. However, one notices that a factor two increase of the input power and/or a reduction of the gas flow rate will induce a significant temperature change [42, 105, 160] which could inhibit the plasma jet to be used for thermal limitation. The feed gas with a known fraction of admixture is thus considered as the parameter allowing the largest amplitude to tailor the plasma chemistry output. Moreover, it is known that low molecular admixture in noble gas discharges significantly affect the plasma properties and as follows plasma chemistry [10].
The plasma chemistry is studied twofold: first, dry admixtures of N_2 and O_2 are used as input parameters to change the plasma chemistry composition. Dry air is applied as a gas curtain. Indeed, it is important to prevent humidity trapped in the gas pipes to have a major role in the plasma chemistry [50, 161]. The reason for that is a water molecule will massively contribute to OH production [89, 129]. The latter is highly reactive and will completely change reaction pathways since OH reacts with nearly any species. Therefore, a drying procedure is performed and applies for the studies reported in ARTICLE II and ARTICLE VI. The case where water will be considered as an exclusive admixture will be summarized in a second part regarding its main chemical species output. As discussed in ARTICLE V and ARTICLE VII, the main effect of water admixture upon plasma chemistry and cell treatment will be highlighted.

3.1.1 Plasma chemistry dynamics regarding O_2 and/or N_2 admixtures

In this study, admixtures of N_2 and O_2 are used as input parameters to change the plasma chemistry composition. The fraction of admixture ranges from 0.0 % to 1.0 %. Three mixtures are used:

- pure N_2,
- pure O_2,
- artificial ratio of O_2/(O_2+N_2).

These two molecular gases are chosen for two reasons: they are relatively abundant in the nature and thus cheap, which is taken into account in case of industrial processes. The second advantage is the intrinsic properties of oxygen being prone to produce more negative ions compared to nitrogen. Hence, the plasma chemistry dynamic is expected to change significantly according to the type of admixture.

As mentioned earlier in section 2.2.1, absolute densities of O_3 and NO_2 are measured with the Q-MACS within a glass chamber mounted in a multipass cell. For the sake of comparison with earlier studies [113, 162] and literature data, the net production rate of NO_2 and O_3, $R_{\mathrm{NO_2}}$ and $R_{\mathrm{O_3}}$ ($\mathrm{m^{-3} \cdot s^{-1}}$) respectively, is calculated as follows,

$$R_{\mathrm{X}} = n_{\mathrm{X}} \cdot \left(\Phi_{\text{feed gas}} + \Phi_{\text{gas curtain}}\right). \tag{3.1}$$

n_{X} ($\mathrm{m^{-3}}$) is the specie density measured in the multipass cell and Φ ($\mathrm{m^3 \cdot s^{-1}}$) denotes the gas flux applied to operate the feed gas and the gas curtain. Aspects of the diagnostic has been introduced in section 2.2.1. More specifically, NO_2 and O_3 investigations with the Q-MACS are subjected to ARTICLE II and [101][1] respectively.

Experimental results obtained during the measurement campaign have been brought together in ARTICLE VI. The latter publication synthesizes the results of the collaborative work with the PLASMANT[2] simulation group of Prof. dr. Annemie Bogaerts from the University of Antwerp. Indeed, in order to resolve the main mechanisms inducing the dynamics of O_3 and NO_2 formation with N_2 and O_2 admixtures, a global plasma kinetic model is necessary. The chemical processes are described by a 0-D semi-empirical chemical kinetic model originally based on the GlobalKin code developed by Dorai and Kushner [163]. A complete $Ar/O_2/O_2/H_2O$ reaction set of 85 species has been implemented considering more than 300 electron impact reactions and nearly 1700 heavy particle reactions. Details about the model are obviously out of the scope of this work and the reader is referred to [76, 89].

As explained in ARTICLE VI, some characteristics of the *kinpen* and the operating conditions must be set as input parameters for the model namely, the power, averaged gas temperature, ambient air fraction and flow velocity profile (see figure 2, ARTICLE VI). As a result of the computation, the average specie densities are carried out for three different positions along the jet axis.

(1) A primary volume element located in the vicinity of the electrodes and restricted within the capillary is isolated from the ambient air diffusion,

(2) Downstream, a second volume describing the visible effluent zone (see figure 2.1) and interacting with the atmosphere,

---

[1] Part of this work was done while S. Iséni was not Ph.D. candidate yet. Therefore, the journal article [101] is not explicitly included in Chapter 5, although the experimental part involving the Q-MACS and the dedicated paragraphs of [101] are the work of S. Iséni.

[2] Plasma, Laser Ablation and Surface Modelling - Antwerp (PLASMANT).

(3) Finally, the third volume is considered as the far plasma jet effluent where are formed the long living species ($\gtrsim 5\,\mathrm{s}$).

The outcome of the comparison between experimental data and kinetic model prediction are in very good qualitative and quantitative agreement with a maximum discrepancy of a factor 3 for the worth scenario. Furthermore, the trend of the experimental data are well reproduced by the model which is interpreted as a token of reliability towards the model output. Figure 3.1 depicts R_{NO_2} regarding $O_2/(O_2+N_2)$ admixture ratio and reveals a complex dynamic of the plasma chemistry. A complete interpretation is detailed in ARTICLE VI. Presently, only the main chemical pathways are going to be summarized. Note that the single point of discrepancy –while no O_2 and only N_2 is admixed– is conscientiously discussed in ARTICLE VI.

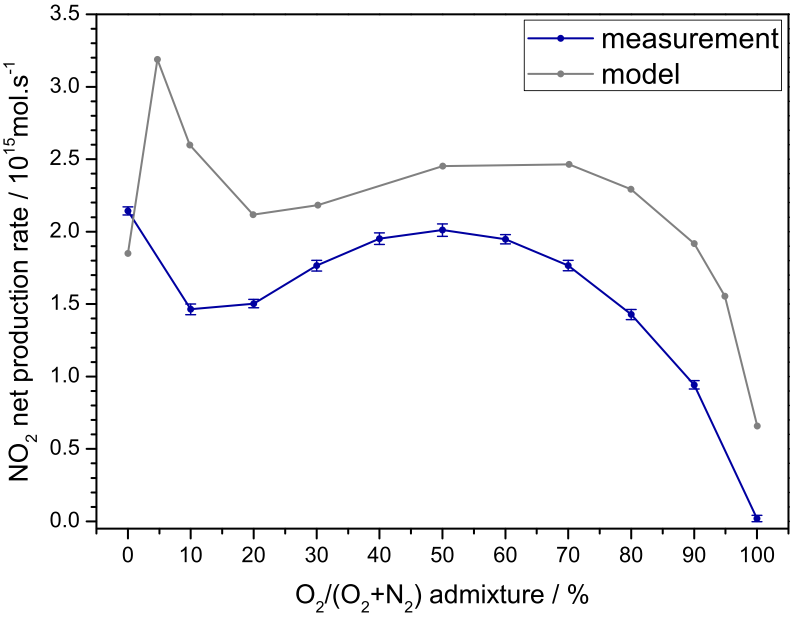

Figure 3.1: Example of the comparison between experimental data and computed net production rate of NO_2. The data result from the measurement campaign with the Q-MACS [ARTICLE II]. The figure is reprinted from ARTICLE VI.

As expected, NO_2 formation derives far more than 85 % from reactions involving NO molecules. The main reaction leading to NO_2 production is,

$$O + NO + M \;\rightarrow\; NO_2 + M \tag{3.2}$$

involving atomic oxygen. Interestingly, the creation of NO differs from the Zeldovich mechanism, known to be an efficient reaction set to produce NO [10, 164]. The latter requires an important dissociation of N_2 clearly irrelevant by electron impact when typical electron temperature of APPJs is a few eV [165]. Energies to dissociate N_2 are usually reached in case of efficient translational energy transfer into vibrational excitation which induces gas temperature of several thousands of K. The production of NO is, according to the chemical kinetic model, resulting from nitrogen metastable, $N_2(A)$, and atomic oxygen again,

$$N_2(A) + O \;\rightarrow\; NO + N(^2D). \tag{3.3}$$

A very important remark about reaction (3.3) need to be addressed: this reaction plays a major role in NO production in pure N_2 and in pure O_2 admixture. In the first scenario, $N_2(A)$ is predominantly formed by electron impact excitation,

$$e^- + N_2 \rightarrow e^- + N_2(A) \tag{3.4}$$

inside the device and in the visible effluent (zone (1) and (2)), whereas in the far field argon excimer ($Ar_2{}^*$) and argon metastables ($Ar(^4P)$) excites efficiently N_2,

$$Ar_2^* + N_2 \rightarrow N_2(A) + 2\ Ar \tag{3.5}$$

$$Ar(^4P) + N_2 \rightarrow N_2(A) + Ar. \tag{3.6}$$

However, in case of pure O_2 admixture, $N_2(A)$ is produced in the far field (zone (3)) mostly by reaction (3.4) due to the change of the electron temperature and the energy distribution ARTICLE VI. Nevertheless, $N_2(A)$ density is expected to drop by 4 orders of magnitude compared to admixture of pure N_2 because of the lack of N_2 molecules in the vicinity of the needle electrode –limited to the Ar and O_2 bottle impurities and considered in the simulation– where most of the energy is dissipated.
The other specie being of crucial importance is atomic oxygen.

$$N_2(A) + O_2 \rightarrow 2\ O + N_2 \tag{3.7}$$

$$e^- + O_2 \rightarrow 2\ O + e^- \tag{3.8}$$

$$Ar_2^* + O_2 \rightarrow 2\ O + 2\ Ar \tag{3.9}$$

Here again, $N_2(A)$ metastable and its energy of 6.0 eV is prone to dissociate O_2 (6.2 eV) and is significantly involved in case of pure N_2 and $O_2/(O_2+N_2)$ mixtures. With an admixture of pure O_2, reactions (3.8) and (3.9) are dominating within the plasma device and the visible effluent whereas reaction (3.7) takes over a few millimeters from the nozzle. This is explained by the diffusion of ambient air, increasing the N_2 fraction within the Ar effluent where the streamer develops (discussed in details in ARTICLE III, section 3.2 and 3.3).
Concerning the production of O_3, it is strongly dependent on atomic oxygen,

$$O + O_2 + M \rightarrow O_3 + M. \tag{3.10}$$

To summarize, NO_2 and O_3 production derive from two common species: atomic oxygen and $N_2(A)$ metastable. This does not exclude contributions of $Ar_2{}^*$, Ar metastables, and atomic nitrogen to the plasma chemistry.
To summarize the outcome of this study, one must know that, qualitatively, the combination of both techniques –Q-MACS and kinetic modeling– has been demonstrated to access the main plasma chemistry dynamics in the three regions of the *kinpen*. Quantitatively, molecular admixture of N_2 and/or O_2 allows variation of R_{NO_2} and R_{O_3} by one order of magnitude keeping other parameters constant, e.g. flow rate, input power. Moreover, the NO density calculated in the model at 0.2 % O_2 with 0.8 % N_2 (see ARTICLE VI) are in excellent agreement with the value measured by LIF and MBMS reported in ARTICLE IV.

3.1.2 Water admixture in the kinpen

Water is an abundant molecule on the Earth existing in its three different states and present in varying quantities in the atmosphere. Due to its abundance in air, water vapor succeeds in penetrating into most of materials sometimes leading to oxidative reactions. In atmospheric pressure plasmas containing water vapor, generation of OH is inevitable and results from various chemical processes [166]. According to [76, 89], in Ar APPJs containing water admixture, the production of OH is predominantly due to charge exchange with Ar dimer ions (reaction (3.11)), followed by dissociation by Ar metastables and excimers (reaction (3.12) and (3.13)).

$$\begin{aligned} \mathrm{Ar}_2^+ + \mathrm{H_2O} &\rightarrow \mathrm{OH} + \mathrm{Ar} + \mathrm{ArH}^+ && (3.11)\\ \mathrm{Ar}(^4\mathrm{S}) + \mathrm{H_2O} &\rightarrow \mathrm{OH} + \mathrm{Ar} + \mathrm{H} && (3.12)\\ \mathrm{Ar}_2^* + \mathrm{H_2O} &\rightarrow \mathrm{OH} + 2\ \mathrm{Ar} + \mathrm{H} && (3.13) \end{aligned}$$

These processes take place in the plasma volume located inside the capillary and having no interaction with the ambient. The diffusion of humid air into the visible effluent of the plasma jet enhances the complexity of the OH generation and the reader is referred to [76]. As a radical, OH is endowed with a high oxidative potential. In a gas mixture mostly constituted of Ar and Ar related species, effective recombination of OH with itself leads to the formation of H_2O_2,

$$\mathrm{OH} + \mathrm{OH} + \mathrm{M} \rightarrow \mathrm{H_2O_2} + \mathrm{M}. \qquad (3.14)$$

H_2O_2 is known to be a stable molecule [ARTICLE V] and biologically active inducing oxidative processes at low concentrations [77].

As motivated in section 2.2.2, relative OH density has been determined by LIF for low fraction of water admixture in the feed gas. The results are shown in figure 3.2 together with absolute concentration of H_2O_2 produced in the gas phase [ARTICLE V]. In contrast with the plasma dynamic of NO_2 resulting from admixtures of N_2 and O_2, OH and H_2O_2 densities increase linearly while raising the water content. The linear evolution of OH with reduced humid feed gas variation has also been reported for the *kinpen* in [129] where a saturation is observed for humidity fraction higher than 2200 ppm ((9.5 %RH at 293 K)).

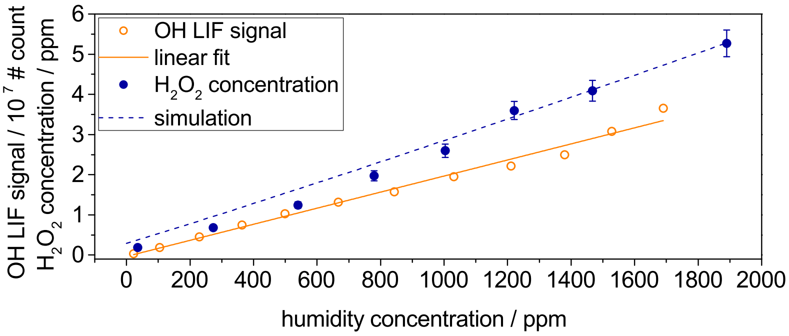

Figure 3.2: Relative OH LIF signal measured in the visible effluent and H_2O_2 concentration in the gas phase versus feed gas humidity. OH data are fitted with a linear function and H_2O_2 measurement are compared to the kinetic simulation from [167]. Reprinted from ARTICLE V.

Obviously, the reported linear correlation between OH and H_2O_2 -within the given range of water admixture- is of high interest and rather convenient for applications which require fine tuning of the output chemistry. Remarkably, direct effects on H_2O_2 concentration in plasma treated liquid have been clearly identify and discussed in ARTICLE V. The latter aims at tracking the chain of H_2O_2 generation induced by feed gas humidity from the plasma/gas phase into the liquid phase and its consequence on skill cells viability. For the sake of plasma medicine, this application-oriented study has revealed that in case of plasma treating cells, humidity as an input parameter for the plasma will induce inevitably formation of H_2O_2 which may induce cell death in case of reaching lethal dosage.

Considering the effects of plasma containing water in biological treatment, it is of high interest to evaluate the impact of ambient moisture diffusing from the atmosphere into the visible effluent and to determine the relevant consequences upon H_2O_2 formation and the viability cell response. ARTICLE VII answers this question and concludes that variation of ambient humidity does not have a significant effect on the production of H_2O_2 and on the cell viability. Furthermore, concentrations of O_3 –known to be an oxidative molecule and biologically active [77]– have been measured with the Q-MACS regarding the influence of humidity as a feed gas admixture and in the ambient.

The results, also part of ARTICLE VII, show that 2000 ppm (8.6 %RH at 293 K) water fraction admixture reduces the production of O_3 by one order of magnitude whereas 2.5 % absolute humidity in the ambient air results in a factor 2 reduction in O_3 formation. This is explained by efficient quenching of atomic oxygen by OH molecules [168]. For the record, atomic oxygen is pointing up in the conclusion of section 3.1.1 to have a central role for O_3 and NO formation. As a conclusion regarding water admixed in the feed gas, studies published in ARTICLE V – previously initiated in [50]– and in ARTICLE VII have identified H_2O_2 as the main agent directly affecting the viability of the plasma treated cells. Moreover, the production of other relevant biologically active species, especially NO, is inhibited in the gas phase since atomic oxygen density is severely reduced while involving more than 100 ppm of water (0.43 %RH at 293 K), as also demonstrated in the modeling of an Ar APPJ [168].

3.2 2D NO distribution in the visible effluent

In the early stage of plasma attempting activation or deactivation of biological elements successfully leading to plasma-medicine, NO was one of the first investigated species produced by plasma jets [79, 113, 136]. Both studies are dealing with RF APPJs but were investigated by different diagnostic techniques. Although both approaches do not provide density space resolved, efforts were spent regarding the NO selectivity.

In the pioneer studies [79, 136], MBMS was used to determined specie densities based on molecular weight carrying out interesting results. However, in the present work, diagnostics of NO by MBMS have been re-investigated and published in ARTICLE IV. A comparison with LIF measurements reveals an overestimation of NO densities while other N_xO_y must contribute significantly to the NO mass after going though the ionization stage of the MBMS apparatus. Hence, for the sake of this study, the advantage is given to laser diagnostic techniques [ARTICLE IV].

Previously in [113] and then in [162, 169], TDLAS and FTIR are used allowing high molecular selectivity and yielding an absolute net production rate. However, as mentioned in section 2.2.1, a similar approach was attempted in the present work in vain, simply because NO is expected to be produced within the plasma device and several millimeters away from the nozzle.

To overcome this difficulty, LIF was introduced in section 2.2.2 as a successful alternative. Production of NO in RF Ar APPJ has recently been the subject of [133] with dry air admixture. The authors report a maximum NO production for 2 % air admixture at constant power. Remembering that the input power of the *kinpen* is limited to a narrow range (see section 2.1) by the manufacturer, admixture of 1.0 % dry air is applied in ARTICLE IV in order to not vary the deposited power. Moreover, the focus is rather on the distribution of NO molecules within the visible effluent since the glow length is actually often a reference for distance treatment with plasma jets. Last but not least, no investigation has been reported about the spatial distribution of NO and its transport within the visible plasma effluent.

Consequently, ARTICLE IV aims at answering these questions through an application-oriented study using the *kinpen*. According to other findings published in ARTICLE III and relayed to section 3.3, the nature of the flow pattern appears to be an important feature of the visible effluent. Indeed, commensurate with the feed gas flow rate, the *kinpen* throughout flow is either laminar or turbulent. Although the kinetic model used in ARTICLE VI predicts NO concentration in good agreement with the absolute densities reported in ARTICLE IV for the turbulent case, an implementation of numerical methods accounting for the turbulence in a plasma kinetic model is out of reach yet. Therefore, NO distribution profile is experimentally examined in ARTICLE IV assuming two flow rates set as input parameter e.i. 1.0 slm and 3.0 slm for the laminar and turbulent case respectively.

From the NO 2D maps shown in ARTICLE IV, one concludes that NO maximum density is reached for the laminar case by a factor 1.5 higher than in turbulent condition. A NO density of 2.5×10^{20} molecule $\cdot$ cm^{-3} is determined at the nozzle tip with a feed gas flow rate. Several reasons explain this observation: first, in laminar regime the temperature of the plasma jet is higher by about 100 K than in turbulent mode (see table 1 [ARTICLE IV]). Indeed, a larger feed gas flow rate tends to cool down the plasma effluent but also reduces the resident time of the molecules where the power is deposited, resulting in a lower production of NO.

The influence of the gas curtain has also been investigated. Interestingly, it is shown that the gas curtain will affect the distribution of NO, reducing its density along the on-axis. This is explained twofold: firstly, the gas curtain induces an additional cooling of the effluent [ARTICLE IV] which is in favor of increasing the O_3 prone to oxidized NO. Furthermore, the absolute air density maps deduced from the decay time of NO fluorescence (see section 2.2.2 and ARTICLE IV for more details) attest that the gas curtain enhances the diffusion of air into the visible effluent by turbulent mixing. As a result, NO density is reduced due to chemical losses mainly to form NO_2.

Intriguingly, it seems that in both regimes –without use of the gas curtain– the air density maps have a similar pattern and absolute values within the first 7.5 mm. Besides for 3.0 slm flow rate, the air entrainment into the visible effluent intuitively results from the turbulence whereas in laminar condition, thermal diffusion dominates the mass transfer simply due to the higher temperature gradient with the ambient. Time averaged, the same goes for NO transport in the radial direction since the temperature gradient is more important than along the jet axis.

Contrary to all expectations, NO is not exclusively produced inside the plasma device and then blown away as if its transport would be dominated by the flow field. This statement was already argued in ARTICLE IV according to the production and destruction rates being faster than the particle flux. Lately, single shot 2D-LIF on NO molecules have been carried out with the experimental setup introduced in section 2.2.3 and used in ARTICLE III. Technically, the laser wavelength was set to 226.2 nm resulting from the sum frequency mixing of the Nd:YAG laser third harmonic (355 nm) with radiation from a tunable dye laser operating with DCM (623 nm). The results are shown in figure 3.3 presenting a comparison between single shot imaging and averaged. The operating conditions of the *kinpen* are identical with to ARTICLE IV. As an important result, figures 3.3 C) and D) resembling the 2D NO distributions look like the maps

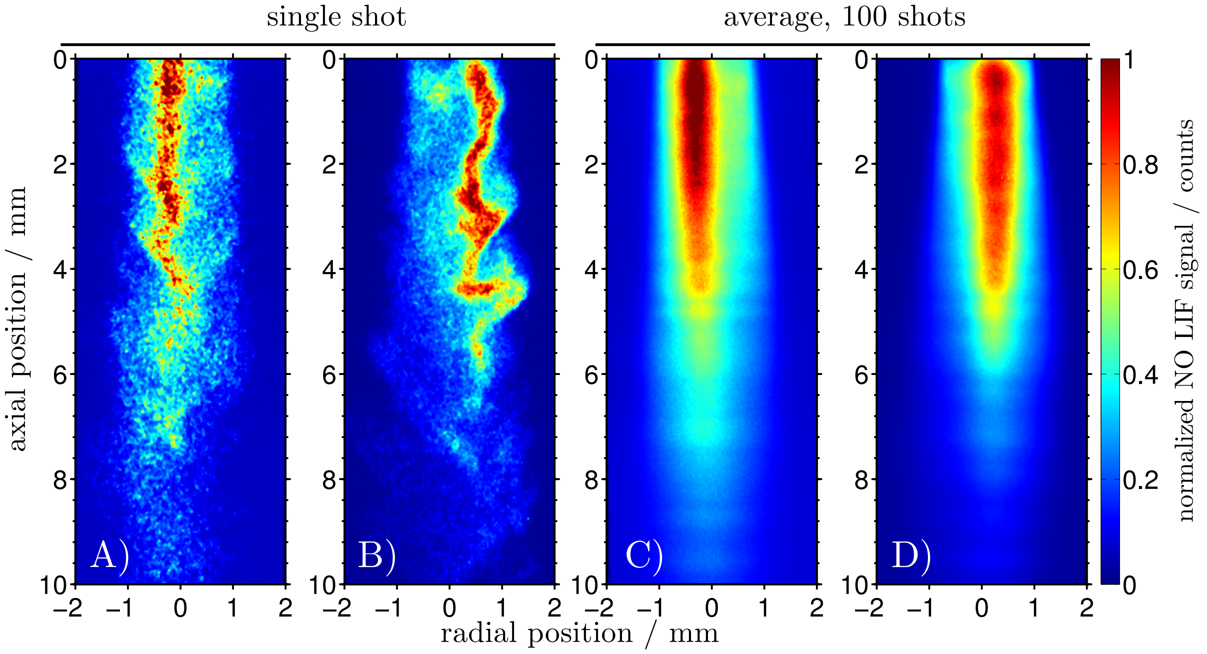

Figure 3.3: NO 2D-LIF of the *kinpen* visible effluent operating with 1.0 % dry air admixture. The measurements are performed with the system described in section 2.2.3. A) and B) are single shot acquisitions while C) and D) are averaged. A) and C) correspond to a flow rate of 1.0 slm whereas C) and D) are at 3.0 slm.
The signal is proportional to the laser energy but not corrected regarding quenching. Estimation of the density may be possible by comparing the images with the respective case in ARTICLE IV figure 6 a) and b).
Laser excitation wavelength at 226.2 nm, exposure time of 100 ns, optical filter central wavelength at 248 nm with 5 nm HWHM, laser pulse duration of 6 ns, laser fluence of 3.3 kJ $\cdot$ m^{-2}.

produced by point-to-point LIF (see ARTICLE IV, figure 6 a) and b)). Conclusively, both approaches show that in average –and on a millisecond time scale or longer– the mean density profile of NO have been resolved for the first time in this kind of plasma source.
Furthermore, the latter paper discussed a lateral shift of the maximum concentration attributed to the location of the plasma filament. This statement has been confirmed by figures 3.3 A) and B). In both cases, NO is located along a thin path of about 200 µm diameter elongated in the direction of the flow. Obviously, the mass transfer of NO is not the origin of this distribution but rather the discharge itself since images A) and B) reminds the streamer shape pictured in figure 2.2. The red rectilinear trajectory described in figure 3.3 A) in contrast with the stochastic-like features visible in figure 3.3 B) is consistent with the turbulent guided streamer presented in ARTICLE I and ARTICLE III. These aspects are the subject of section 3.3 developed further in.
Considering the previous findings regarding the instantaneous distribution of NO, a comment must be addressed about the gas temperature reported in ARTICLE IV derived from NO excitation spectra (see figure 2.7). At first sight, these temperature values seemed overestimated compared to the gas temperature. However, this resembles the gas temperature on a time scale

of hundreds of nanoseconds to a few microseconds while heat transfer (typically hundreds of milliseconds to seconds) has not occurred yet as described in [96]. Practically, treated surfaces –including biological matter– do not react to heating in a short time scale therefore only average temperature, when heat transfer is established, is relevant regarding applications involving heat sensitive materials.

Furthermore, the domination of thermal diffusion in case of laminar regime is clearly visible comparing the radial gradient of NO profiles in figures 3.3 A) and B). Image A) shows smoother transition edges with the background indicating an homogeneous diffusion process driven by heat whereas image B) depicts strong contrast with the background revealing a lower radial diffusion.

This work has resulted in an expansion of fundamental knowledge in the understanding of the visible effluent chemistry –focused on NO– as well as regarding applications to plasma medicine. Indeed, transfer of RONS from the plasma device to the cells involves gas phase chemistry, liquid interface and bulk where each has their dominant processes. Here, NO density profiles were shown to be similar in laminar and turbulent regimes mainly affecting the maximum density. However, the fundamental mechanism involving plasma and flow pattern are underlying as shown here with single shot observations. Investigation of those interactions between plasma and neutral gas flow are in the scope of the next section of this thesis.

3.3 Effluent neutral gas flow pattern and discharge propagation

Essentially, plasma jets consist of a construction –usually a dielectric tube– channeling a gas flux exiting through a clear orifice in open-space. This geometrical feature combined with the feed gas flow rate results in different flow regimes, namely laminar and turbulent. While laminar flows are steady-state and fully controlled transition phases are observed and lead to turbulence which is a well known example of chaotic system being the subject of extensive studies.

As a general comment, it is intriguing to notice that before 2011, no preliminary study had been published in the literature about APPJs and neutral gas flow pattern [170, 171]. This is a surprising fact especially since atmospheric pressure plasmas –mostly DBD– had been used for a while in airflow control by non-thermal plasma actuators [172]. Moreover, as already discussed previously in section 3.1 and reported in ARTICLE IV, the amount of air fraction introduced into the visible plasma effluent is crucial for the throughput products of the plasma chemistry [167]. Among the variety of APPJs designed worldwide, one may speculate that the feed gas flow rate is often set to achieve satisfying gas temperature cooling effect of the neutral gas flow to be safely applied to heat sensitive materials e.g. living tissue. Hence, basic investigations of neutral gas flow dynamic have slipped through the net and left aside.

Since 2011 and the publications [170, 171] –which unfortunately might go unnoticed– no any further study about this topic have been reported in the literature. It is only in the early 2014 that a couple of laboratories working with APPJs –and plasma medicine as a motivation– have published many tremendous and exciting results [173, 174][ARTICLE III]. The recent findings reported in these articles will be partly discussed throughout this section.

As an outstanding part of this thesis, ARTICLE III deals with simultaneous observation of neutral flow pattern and discharge propagation[3]. According to previous statement, the feed gas flow rate is used as a variable parameter in order to drive the flow regime. The visualization

---

[3] ARTICLE III has been chosen to be part of the **IOPselect** collection for its novelty, significance and potential impact on future research.

of the neutral gas flow was carried out by 2D-LIF (see section 2.2.3) whereas all other studies resort to Schlieren imaging technique [170, 171, 173, 174]. As detailed in section 2.2.3 and ARTICLE III, 2D-LIF offers some advantages compared to Schlieren diagnostic particularly the possibility of combining spectrally filtered stereoscopic observation and performing single-shot imaging acquisition of the flow field and the discharge propagation.

In the context of treating microorganisms, cells and tissues with plasma jets, one can consider the gas gap between the plasma device and the target as a vector to transport RONS resulting from the plasma and gas chemistry. Therefore, an initial consideration regarding the delivery of chemical products, a study of the neutral gas effluent flow pattern has been performed with and without plasma for different gas flow rates.

Visualization of the flow field without plasma ignition was realized by admixing small amount of organic tracer ($\lesssim 400$ ppm of acetone) and applying 2D-LIF [ARTICLE III]. The results published in the first part of ARTICLE III show that at 0.5 slm and 1.0 slm Ar flow rates, the flow is completely laminar over more than 25 mm whereas strong turbulence is observed for a rate of 3.0 slm. The transition between laminar and turbulent regime is observed around 2 slm.

The experiments are reproduced while the plasma jet is turned on yielding a long visible effluent like in figure 2.1. Obviously, acetone could not be used as a flow tracer at the risk of affecting plasma properties and even altering the device. However, as motivated in ARTICLE III, OH was found to have all the necessary properties to be used as a fluorescent flow tracer. Beneficing from the residual moisture in the gas pipe as well as the ambient [156], OH radical is observed to be homogeneously distributed in the Ar flow. This is not the case with NO as it can be demonstrated by comparison of figure 3.3 A) and B) with OH single shot images published in ARTICLE III.

Surprisingly, the outcome of the experiment while the plasma is ignited reveals some instabilities in the Ar flow at a flow rate of 1.0 slm [ARTICLE III]. Remembering that laminar regime was initially observed without plasma hints that plasma ignition and flow fluctuation are correlated. Lately, similar findings have been reported for He APPJs [173, 174]. Although He is lighter than Ar, the authors of [173] have also led their investigations with Ne and confirm diagnosis of the same effect of the plasma on the flow field. The latter study also addresses a very important fact while using He APPJs for a control test with neutral gas in biological treatments [173]. Indeed, when operating the jet in the direction of the gravitational field, plasma is able to compensate the He buoyancy and brings the neutral gas onto a target located several millimeters in front of the jet nozzle. Following the same line of thought a more pragmatic study aiming at visualizing a He APPJ inducing turbulence and being in contact with various surfaces is published in [174]. Fortunately, such a buoyancy issue does not occur in the case of the *kinpen* since Ar is heavier than air.

At present, the modification of the neutral gas flow pattern induced by the plasma is not understood and is unanimously stated in each publication [170, 171, 173, 174]. The fact remains that hypotheses are arising whereas certain physical parameters are already no longer regarded as viable. For instance, thermal effect motivated in [174] are not likely as discussed in ARTICLE III and [173]. Nevertheless, recently in [175, 176] comparison of Schlieren imaging and hydrodynamic modeling of an He and Ar APPJ bring consistent results which tend to explain the interaction plasma/neutral gas flow. Electrohydrodynamic (EHD) force was implemented based on a previous calculation applied to surface DBD [177]. As the results of their comparative studies, EHD is claimed to play the major role in the activation of the neutral gas in He and Ar. Although no clear evidence exists to demonstrate that EHD force is responsible of the neutral gas flow modification in Ar APPJ, this hypothesis is merely supported in ARTICLE III.

The second part of ARTICLE III aims at investigating the propagation of the ionization wave through the neutral gas flow for both regimes. Practically, this experiment has been performed using the diagnostic method described in section 2.2.3. As one of the key stone of ARTICLE III, figure 3.4 depicts the discharge/neutral flow pattern for the three gas flow rates mentioned earlier.

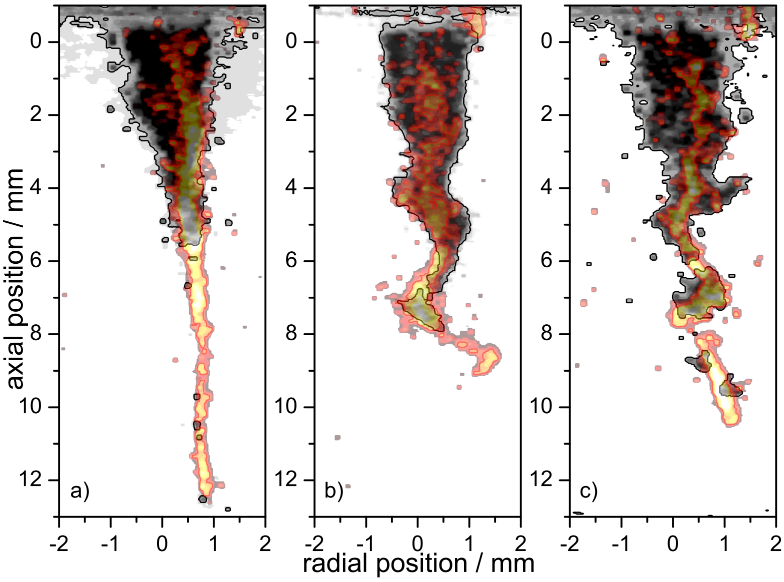

Figure 3.4: Overlay of the spatial OH fluorescence (gray color map) revealing the Ar/air boundaries and of the spatial Ar plasma emission (fire color map) for different Ar gas flow rates of a) 0.5 slm, b) 1.0 slm and c) 3.0 slm. Both signals were obtained simultaneously on the same detector. Reprint from ARTICLE III.
Laser excitation wavelength at 283.5 nm, exposure time of 200 ns, optical filter central wavelength at 313 nm with 5 nm HWHM and at a band-bass filter from 350 nm to 800 nm for OH fluorescence and Ar emission respectively, laser pulse duration of 6 ns, laser fluence of 3.5 kJ · m^{-2}.

Thanks to much higher quenching rate of OH fluorescence by air [178] than by Ar [149], it is possible to clearly visualize the Ar field with the highest purity meanwhile the ambient is diffusing into the visible effluent. This is well demonstrated with 0.5 slm flow rate (figure 3.4 a)) where the gas temperature will be the highest enhancing thermal diffusion of ambient air into the visible effluent [ARTICLE IV]. The conic shape of OH fluorescence results from the diffusion of air into the laminar flow and unveils the Ar/air boundaries. Laminar flow can allow analytical calculation to determine the air density threshold for this Ar/air boundary. In ARTICLE III, *non-dispersive path mapping* approximation is used and estimates an air concentration ranged from 0.1 % to 1 % at the boundaries [179]. This value corresponds roughly to the maximum fraction of admixture tolerated by the *kinpen* to ignite the plasma with a visible effluent exiting the device nozzle.

Looking at the plasma spontaneous emission, figure 3.4 shows that the discharge and the Ar field are both following the same path independently of the flow pattern. This phenomenon has already been simulated for laminar He APPJs and introduced the denomination of *guided-*

streamer [103]. However, the He flow used for the simulation was simplified at the maximum, neglecting the diffusion of ambient air into the He channel reducing the concept of the He flow to a virtual He tube.

The present study asserts the first experimental evidence that a guided-streamer from an APPJ is able to propagate either in laminar and in turbulent neutral gas flow pattern. Although these results may raise questions and open a new field of investigation, several hypotheses about the propagation mechanisms have already been discussed in ARTICLE IV. Considering the excitation frequency of the *kinpen* (1 MHz), and the time scale of the turbulent eddies in the oder of milliseconds, pre-ionization of the Ar channel and metastables remaining from the previous excitations must play an important role in the propagation of the guided-streamer [180].

This argumentation has been strengthened with the observation of the guided-streamer over non-consecutive excitation cycles [ARTICLE IV]. The results show that for perfect laminar conditions (0.5 slm), the spatial distribution of the discharge along the radial direction does not deviate more than the diameter of the streamer itself. In contrast with the laminar situation, the radial distribution of the guided-streamer is much broader in case of turbulence. Moreover, it has been shown in ARTICLE I that in case of turbulent flow, the guided-streamer may turn back to the direction of the device nozzle.

Intuitively, the plasma chemistry must depend on the nature of the flow regime, although the changes will be difficult to quantify. An important point concerns the impurities fraction contained within the thine Ar channel where the guided-streamer develops. Indeed, the latter will propagate where the Ar content is the purest since the fast ionization rate of Ar is higher than O_2 and N_2 in this type of plasma device.

Regarding the applications, it is difficult to evaluate how big are the consequences of the present findings on processes. However, in the context of plasma treated cells, it is possible to hypothesize that biological effects generated at the impact point of the guided-streamer may differ with indirect treatment where the area is exposed to the gas flow containing RONS. A convincing example is illustrated by figure 3.3 A) or B) considering the knowledge of this section: the delivery of NO depends not only on the average distribution driven by the neutral flow field, but also on strong density gradient located along the guided-streamer path which may trigger cell signaling cascades simply by threshold effect. Lately, results of simulations shows that NO diffusion into water is sensitive to the repetition rate of the guided-streamer impinging on the liquid surface and the distribution of the impact on the surface [181, 182]. Both conditions determine whether the formation of new reactive species will overlap with prior excitations inducing an effect of accumulation on and in the liquid interface. In case of a too spread streamer distribution e.g. turbulent regime, the latter acts as a buffer preventing NO to accumulate and then diffuse into the bulk with the cells. Operating the plasma jet device in laminar regime will allow a better control of the discharge position, of the ambient diffusion processes and thus on the plasma chemistry.

3.4 Application to biological treatments

Interaction of non-thermal room-temperature atmospheric pressure plasmas with biological elements can be described as plasma processing. Depending on the goal, processes are more of less complex to optimize. In case of cell activation to support wound healing, cells must stay alive and need to be surrounded by aqueous solutions e.g. biological serum. Liquid media activation by plasma treatment has been observed for different type of plasma sources (APPJ [51, 183], DBD [184], surface DBD [31]) and is of high importance to trigger cell responses [185]. Although liquid chemistry is a crucial interface between plasma gas phase and cells, it is a vast topic which cannot match the scope of this thesis but is mentioned here to give a broader picture. In parallel with this thesis work, aqueous chemistry studies have been performed by fellow members and lead to many interesting results which can be related to the present thesis outcome [186]. For instance, co-workers have investigated nitrite (NO_2^-) and nitrate (NO_3^-) generation in plasma treated medium as shown in figure 3.5. Comparing the latter figure with figure 3.1 –which depicts the NO_2 production rate in the gas phase– illustrates that plasma and gas phase chemistry "activate" the liquid chemistry. Indeed, both figures have the same trend and the maximum is found to be at the same gas composition. The latter comparison reveals a clear correlation with the plasma chemistry detailed in ARTICLE VI. However, due to the complexity of aqueous solution chemistry, this topic is deliberately put aside of the present thesis and the reader is referred to more proper literature [49, 77, 93, 94, 187] and references therein.

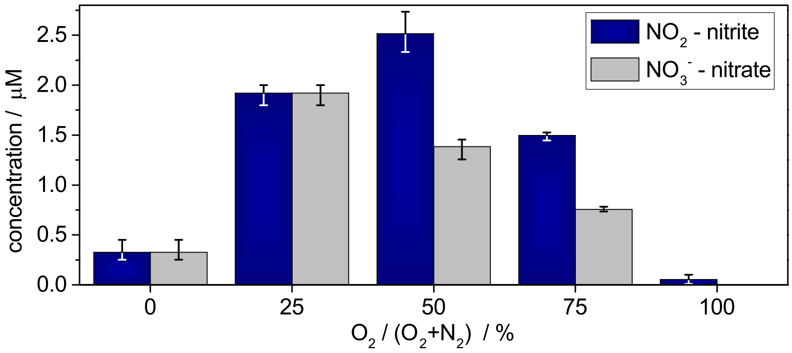

Figure 3.5: NO_2^- and NO_3^- concentration in DPBS after 3.0 min treatment with the *kinpen* operating in pure Ar and different ratio of the gas curtain composition (same as in section 3.1.1).
By courtesy of Helena (Tresp) Jablonowski. Reprint from [186].

In ARTICLE VIII, one aims at directly plasma treat cell suspension in liquid medium, taking into account most of the findings presented in this dissertation. Therefore adjustments of the standard *kinpen* operating parameter set were necessary. First the gas flow rate is set such as the neutral gas flow resembles a laminar pattern. Secondly, as demonstrated earlier (see section 3.1), plasma/gas chemistry and liquid chemistry are trickily tangled. One needs to lighten the chemistry while keeping the advantage of the non-equilibrium chemistry (plasma chemistry). A counter example would be to admix water which leads to massive production of H_2O_2 already available by other alternative.

According to the outputs of section 3.1 and ARTICLE VI, atomic oxygen and $N_2(A)$ metastable are both identified as *intermediate* species –with a lifetime of a couple of second for $N_2(A)$ [188, 189]– which are worth to investigate regarding their indirect biological effects. As a matter of choice –and because atomic oxygen is prone to form ozone in our conditions– the *kinpen* was intensionally set to enhance its production of $N_2(A)$. Accordingly, a laminar gas curtain of pure N_2 is implemented and acts as a real shielding. Experimental visualization of the effectiveness of the shielding gas pattern was carried out by 2D-LIF and printed in ARTICLE VIII. Additionally, 1.0 % admixture of N_2 is added to Ar.

By preventing molecular oxygen and humidity in the plasma jet and its visible effluent vicinity, one argues with consistence in ARTICLE VIII that the chemical throughput is exempt of ROS. Indeed, the conditions are in favor of RNS production such as atomic nitrogen, N_2(A) and nitrogen ions ($N_2{}^+$). High energetic particles like argon excimer ($Ar_2{}^*$) and metastables are not expected to reach the water surface in large amount.

Lately, *in situ* detection of N_2(A) metastable in the visible effluent of an APPJ has been successful by LIF. The diagnostic of N_2(A) metastable in atmospheric condition still remains a challenge even though several approaches exist [190, 192–196]. Presently, figure 3.6 shows the fluorescence of $N_2(B\,{}^3\Pi_g, v = 2)$ resulting from the pumping of $N_2(A\,{}^3\Sigma_u^+), v = 0)$ to $N_2(B\,{}^3\Pi_g, v = 3)$ by laser excitation at 687.44 nm. The latter result confirms the existence of N_2(A) metastable in the plasma plume as suggested in ARTICLE VIII although no density value has been carried out from the measurement which aimed to evaluate the feasibility of applied LIF for N_2(A) measurement in a APPJ. However, clear hints of such metastables transfered onto the liquid surface is now established.

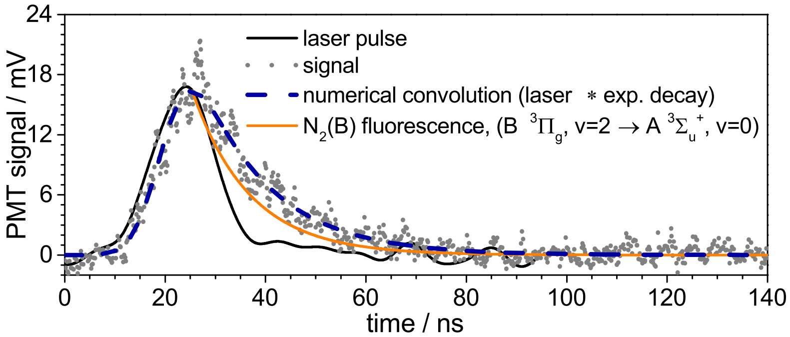

Figure 3.6: Detection of the N_2(A) LIF signal within the visible effluent of the *kinpen* operating in the same conditions as in ARTICLE VIII. The decay time of the fluorescence is calculated by numerical deconvolution to be 11.4 ns. The laser spot is located at 4.5 mm from the nozzle exit. The LIF is performed according to [190, 191] Data averaged over 1×10^4 shots, laser energy of 7.5 mJ, laser spot unfocused $\varnothing$ =2.0 mm at 687.440 nm with a laser linewidth of about 9 pm, detection bandwidth of 5.0 nm centered at 762.0 nm.

Consequently biological cell viability tests have been published in ARTICLE VIII and reveal surprising outcome. While in the present conditions the plasma plume is about 400 K (see section 3.2 and ARTICLE IV), the cell viability after 1 min plasma treatment is enhanced by a factor 4 compared with the standard parameters (3.0 slm pure Ar without gas curtain).

This demonstrate that higher gas temperature is not necessarily lethal when heat transfer is well regulated mostly via the gas shielding [ARTICLE IV]. Furthermore, the present experimental conditions which tend to drastically reduce the variety of species and chemical reactions is a real advantage to track chemical pathways between gas phase and liquid phase. Moreover, the low cytotoxic degree of this parameter set reciprocally allows biologists to investigate cell activation by plasma and a better identification of the possible involved mechanisms due to the lack of ROS diffusing from the gas phase into the liquid.

4 Summary and Outlook

Summary

About a decade after the emergence of *plasma-medicine* in the scientific community, a vast amount of interdisciplinary studies have been led worldwide. Until now, most of the findings have been reported in many international conferences and scientific journals where many of them have lately launched new sessions/sections with the scope of biological applications of non-thermal plasmas. Nevertheless, the publication of recent studies brings permanently new questions which are often left open because of the novelty of the field and the vast amount of unique plasma device being used.

The present work focuses on the diagnostic of a commercially available plasma source, so-called *kinpen*, wisely chosen for its potential to be involved in many biological experiments and clinical trials. Accordingly, the investigation of this Ar RF APPJ is reported in this thesis threefold:

- characterization of the plasma chemistry dynamic regarding the production of biologically active RONS is studied with singular and simultaneous admixture of N_2 and O_2 fractions,
- the absolute 2D profile of NO density within the visible effluent according to the gas flow rate and the presence of an external gas shroud has been investigated,
- investigating the neutral gas flow regime –being either laminar or turbulent– together with the discharge propagation and its influence on the plasma chemistry.

As a method of choice to achieve these tasks, three complementary optical laser diagnostics have been successfully applied to the plasma jet itself or its effluent. Each technique has been able to carry out reliable and consistent results with each other.

After an optimization phase of the QCLAS system –Q-MACS– initially designed for low pressure diagnostics, the latter has shown remarkable abilities to diagnose, for the first time, plasma jets at atmospheric pressure. Practically, space averaged absolute densities of O_3, NO and NO_2 can be measured with a detection limit down to $4.8 \times 10^{17}\,\mathrm{m}^{-3}$ which represents a significant technical achievement.

The O_3 and NO_2 chemistry dynamics of the *kinpen* have been characterized and the net production rates are able to be tuned over one order of magnitude at similar input power. Maximum are measured to be $4.9 \times 10^{17}\,\mathrm{s}^{-1}$ and $2.4 \times 10^{15}\,\mathrm{s}^{-1}$ for O_3 and NO_2 respectively. Numerical analysis have been carried out in collaboration with PLASMANT (University of Antwerp) via kinetic simulations of the entire plasma chemistry. Expectingly, atomic oxygen and NO turn out to be precursors of O_3 and NO_2. However, it was intriguing to unveil that atomic oxygen and $N_2(A)$ metastables play together a key part –as *intermediate* species– in the generation of more stable RONS, e.g. NO. Those findings have contributed to comprehend throughout room-temperature Ar plasma chemistry at atmospheric pressure with molecular admixture fractions and tailor the throughout product for biomedical applications e.g cell growth enhancement, signaling cascade triggering.

On the contrary, water impurities have been correlated to the production of H_2O_2 in the first order via generation of OH radicals. The latter dependency on water content has been determined by LIF and linearly related to H_2O_2. As a results towards biological treatments, humidity admixed to the feed gas will induce systematically production of H_2O_2 in the gas and liquid phase which causes cell death if the lethal threshold dosage is reached. Thus, specific care must be addressed to the residual moisture in the gas carrier.

In the framework of plasma aiming at cell activation, NO molecules are known to be prone to trigger cell signaling cascades. Practically, the visible effluent is often used as a reference length to describe relatively the distance nozzle-sample during treatments. Moreover, the visible plume is actually the volume where most of the transient chemical species are progressing (*e.i.* e^-, O, N, ${Ar_2}^*$, Ar metastable, $N_2(A)$...) forming more stable and long living compounds (*e.i.* NO, NO_2, H_2O_2, O_3...).

As a complementary approach to the Q-MACS, LIF offers the best alternative to probe this tiny volume and to carry out absolute quantitative space-resolved densities. The LIF was absolutely calibrated and characterized to allow fiddling corrections of vignetting effects. Although optimization of NO generation with dry air admixture has been previously published for a similar device [133], special attention is payed, here, to the 2D spatial distribution of NO and the gas flow rate. The consequences of the latter on the neutral flow pattern have been investigated for the first time in this work by 2D-LIF with either organic compound or OH radical as a flow tracer. Hence, as a novel insight, neutral gas flow regimes –laminar and turbulent– have been determined experimentally for the *kinpen* geometry.

The time average NO density is found to be maximum in the laminar situation ($2.5 \times 10^{20}\,\mathrm{m^{-3}}$) while in turbulent regime the concentration is lowered by a factor 1.5. The latter NO concentration is found to be in good agreement with the prediction of the kinetic model. The production of NO is observed to be on the discharge path from which NO molecules diffuse. Although the flow does not dominate transport mechanism, in case of laminar regime, thermal diffusion caused by a temperature increased –in the order of 100 K– contributes to the diffusion in the radial direction while in turbulent situation, mixing occurs. Interestingly, applying a gas shroud around the plume will enhance the heat transfer and cooling down the effluent which is an important point regarding treatment of heat sensitive materials. Additionally, absolute densities of air diffusing into the visible effluent (around 2 % at 7.5 mm from the nozzle) as been deduced by quenching of the NO fluorescence and is in agreement with prior studies and the literature data.

Although most of the chemical reactions occur in a shorter time scale than the development of the flow, the present work has unveiled important novelty regarding neutral gas flow field and the discharge propagation. Indeed, by means of a unique combination of single shot 2D-LIF for the visualization of the flow pattern, optically filtered stereoscopic imaging technique is used simultaneously to track the ionization wave trajectory. Two outstanding results are carried out from this study.

First, it is observed that the laminar to turbulent transition regime is different with and without plasma. Indeed, one reports in this work that instabilities occur in the neutral gas flow field with plasma and the transition between both regimes shifts to a lower flow rate than conditions without plasma. At present, only a couple of studies [170, 171, 173, 174] dealing with neutral flow structure for APPJs have been published including this work [157]. Although each article unanimously states that the changes in the hydrodynamics properties are not clearly understood, EHD force is consistently hinted to be involved [175], for He APPJs at least.

The second outcome concerns the discharge propagation through a turbulent flow and reveals the existence of an Ar channel. The latter is marked out by the significant quenching rate of flow tracer fluorescence (OH) which draws the Ar/air boundaries. Consequently, the so-called *guided-streamer* always develops where the Ar fraction is the highest. Intuitively, the guided-streamer propagates in the direction of the flow velocity field but may turn back and continue –partly– its progression towards the jet nozzle resembling a hook-like shape. Inevitably, a strong link with the plasma chemistry is anticipated and one may question about the gas composition and the real air fraction within the volume where the guided-streamer deposits its energy.

Fortunately, the control of the guided-streamer is possible and demonstrates the advantage of resorting to a laminar neutral gas flow. Although in this condition the gas temperature rises up by about 100 K, the position of the guided-streamer is fully controlled allowing reliable and realistic numerical simulation of the plasma and its chemistry. Moreover, recent outstanding modeling results demonstrate the necessity of guided-streamer stability in space in order to benefit from RONS accumulation to lead to efficient dissolution through the liquid layer and reach the bulk containing cells [181].

In the framework of this Ph.D. study, such operating conditions have been successfully applied to direct treatment of cell suspension in liquid medium. The experimental parameters were chosen in order to produce a laminar flow and to minimize the contribution of oxygen in the plasma chemistry leading to a domination of RNS. Cytotoxicity is reported to be lower by a factor 4 compare with the standard *kinpen* operating conditions which open further hopes for looking into biological plasma activation effects.

Outlook

The knowledge related to *plasma-medicine* is in permanent increase in the different fields involved namely, biology, chemistry, physics and modeling. Obviously, many directions of future work exist and only a few of them are suggested here.

According to the plasma chemistry composition carried out from the global kinetic model, it is of high interest to pay attention to metastable states, particularly $N_2(A)$ for its long lifetime and high energy state. As mentioned earlier, its diagnostic still remains a challenge. Nevertheless, in this work, one reports on the successful feasibility to apply LIF for its detection in APPJs. Thorough studies must be conducted in this direction following [126] which will bring new insights about the energy transport leading to potential unique chemistry while interacting with liquids.

Regarding the study of RONS, efforts must be spent to consolidate the actual knowledge but also to move further on . For instance, the transfer of biologically active compounds from the gas phase to the liquid still remains unclear. Those investigations could benefit from space resolved measurement techniques since the neutral gas flow must be involved in the transfer mechanism.

About plasma diagnostics, the advantages of single-shot diagnostic technique have been well illustrated in this work. Nonetheless, absolute calibration procedure needs to be extended.

Regarding applications, the knowledge about APPJs reaches a level which now requires to take into consideration different targets and investigate how the plasma interact with it. Such studies have already been initiated [173, 197] but are still limited.

Last but not least, recent works dealing with APPJs and neutral gas flow pattern have raised new questions towards biological treatments [173], but also to support numerical simulations of APPJs often used to validate experimental works.

5 Original publications

This thesis is based on the following peer-reviewed articles published in international scientific journals:

Article I:
S. Iseni, S. Reuter, A. Schmidt-Bleker, and K. D. Weltmann. Flow and discharge development in an argon atmospheric pressure plasma jet observed by ICCD and PLIF imaging. *IEEE Transactions on Plasma Science*, 42(10):2458–2459, 2014
SI has designed and realized the experiment. ASB helped for the analysis of the results. SI and SR wrote the manuscript. It was edited by all the co-authors.

Article II:
S. Iseni, S. Reuter, and K. D. Weltmann. NO_2 dynamics of an Ar/Air plasma jet investigated by in situ quantum cascade laser spectroscopy at atmospheric pressure. *Journal of Physics D: Applied Physics*, 47(7):075203, 2014
SI has upgraded the experimental setup to operate from low to atmospheric pressure. Then he has realized the experiments. SI wrote the manuscript. It was edited by all the co-authors.

Article III:
S. Iseni, A. Schmidt-Bleker, J. Winter, K. D. Weltmann, and S. Reuter. Atmospheric pressure streamer follows the turbulent argon air boundary in a MHz argon plasma jet investigated by OH-tracer PLIF spectroscopy. *Journal of Physics D: Applied Physics*, 47(15):152001, 2014
SI developed the experiment and conducted the measurement campaign. ASB has developed the analytical diffusion model. SI wrote the manuscript with the contribution of ASB and SR. It was edited by all the co-authors.

Article IV:
S. Iseni, S. Zhang, A. F. H. van Gessel, S. Hofmann, B van Ham, S. Reuter, K. D. Weltmann, and P. Bruggeman. Nitric Oxide density distributions in the effluent of an RF argon APPJ: effect of gas flow rate and substrate. *New Journal of Physics*, 16(12):123011, 2015
SI and SZ used the LIF setup previously designed by AFHvG to perform the measurement campaign. SH and BvH assisted SI to performed MBMS diagnostic. SI and PB wrote the manuscript. It was edited by all the co-authors.

Article V:
J. Winter, H. Tresp, M. U. Hammer, S. Iseni, S. Kupsch, A. Schmidt-Bleker, K. Wende, M. Dünnbier, K. Masur, K. D. Weltmann, and S. Reuter. Tracking plasma generated H_2O_2 from gas into liquid phase and revealing its dominant impact on human skin cells. *Journal of Physics D: Applied Physics*, 47(28):285401, 2014
JW coordinated the work and conducted the FTIR measurements. HT measured OH radicals in the liquid. Together with MUH and SK dealt with H_2O_2 and the liquid chemistry. SI per-

formed the OH relative measurement in the gas phase by LIF. ASB developed the kinetic model and KW conducted the biological experiments. The manuscript was written by JW and edited by all the co-authors.

Article VI:
W. Van Gaens, S. Iseni, A. Schmidt-Bleker, K. D. Weltmann, S. Reuter, and A. Bogaerts. Numerical analysis of the effect of nitrogen and oxygen admixtures on the chemistry of an argon plasma jet operating at atmospheric pressure. *New Journal of Physics*, 17(3):033003, 2015
WVG developed the kinetic model. SI conducted the QCLAS measurement compaign with the Q-MACS and the power measurements. ASB ran the CFD simulation. WVG wrote the manuscript with SI and ASB. It was edited by all the co-authors.

Article VII:
S. Reuter, J. Winter, S. Iseni, A. Schmidt-Bleker, M. Dünnbier, K. Masur, K. Wende, and K. D. Weltmann. The influence of feed gas humidity versus ambient humidity on atmospheric pressure plasma jet-effluent chemistry and skin cell viability. *IEEE Transactions on Plasma Science*, 99, 2015
SR coordinated the study and wrote the manuscript. JW and MD performed the FTIR measurements of H_2O_2. SI conducted the QCLAS investigations with Q-MACS. ASB was in charge of the CFD and kinetic simulations. KM and KW dealt with the cell cultures and the biological experiments. The manuscript was edited by all the co-authors.

Article VIII:
S. Bekeschus, S. Iseni, S. Reuter, K. Masur, and K.-D. Weltmann. Nitrogen shielding of an argon plasma jet and its effects on human immune cells. *IEEE Transactions on Plasma Science*, 43(3):776–781, 2015
SB performed the biological experiments and analyses. SI suggested the operating parameter set for the plasma jet and performed the spectroscopic experiments. The article was written by SB and SI then edited by all the co-authors.

Read and approved,

Sylvain R. R. Iséni	Date
Prof. Dr. Klaus-Dieter Weltmann	Date

5.1 Article I

Flow and Discharge Development in an Argon Atmospheric Pressure Plasma Jet Observed by ICCD and PLIF Imaging[a]

doi:10.1109/tps.2014.2321226

---

[a] © 2014 IEEE. Reprinted, with permission, from [Iseni, Reuter, Schmidt-Bleker, and Weltmann, Flow and Discharge Development in an Argon Atmospheric Pressure Plasma Jet Observed by ICCD and PLIF, IEEE TRANSACTIONS ON PLASMA SCIENCE, August 2014]

Flow and Discharge Development in an Argon Atmospheric Pressure Plasma Jet Observed by ICCD and PLIF Imaging

Sylvain Iseni, Stephan Reuter, Ansgar Schmidt-Bleker, and Klaus-Dieter Weltmann

***Abstract*— In this paper, a megahertz atmospheric pressure plasma jet is investigated regarding its discharge pattern in correlation with the flow. Single-shot imaging shows plasma streamer development in a flow pattern determined by turbulent interaction with the atmosphere. Planar laser-induced fluorescence imaging on hydroxyl shows the flow pattern. The discharge pattern is streamerlike. Here, it can be observed that the streamer exhibits a hook-like structure at the end, which might also be attributed to the gas flow pattern.**

***Index Terms*— Atmospheric-pressure plasmas, measurement by laser beam, optical imaging, plasma diagnostics.**

IN NATURAL sciences, observations of phenomena have always been the motivation to understand the physical environment. For instance, in the history of ionized gases, Sir William Crookes reported for the first time the observation of light emitted by a discharge in noble gases [1]. Similarly observational, in this paper, a radio-frequency (RF) atmospheric pressure argon plasma jet (kinpen, neoplas GmbH, Germany) has been investigated by means of imaging techniques. Jet plasma sources have proven to be suitable for biomedical application and eukaryotic cell activation-induced wound healing [2], [3]. The plasma jet investigated in this paper is fed with 3-slm argon, and is operated with roughly 1-MHz excitation frequency. The jet nozzle is circular, and has a diameter of 1.6 mm. The jet generates reactive oxygen and nitrogen species when interacting with the surrounding atmosphere [4], [5]. In this paper, the spatial distribution of hydroxyl used to resemble the flow pattern of the plasma effluent is investigated with planar laser-induced fluorescence (PLIF) spectroscopy. The OH molecule produced within the plasma jet originates from water impurities in the discharge. The results presented here are related to the spatial distribution of reactive species, such as the OH molecule [Fig. 1 (right)]. Furthermore, the spatial distribution of the discharge during one excitation period [Fig. 1 (left)] is presented.

Fig. 1 (left) shows a single-shot discharge emission (250–800 nm) recorded with a charge-coupled device camera Imager Pro X (LaVision GmbH, Germany) combined with an external gated image intensifier (Intensified Relay Optics). The intriguing character of this picture is the hook-like shape at the end of the discharge. It has been shown recently that turbulent flow is strongly considered to be the origin of this discharge propagation character [6]. Fig. 1 (right) shows a spatial distribution of the OH fluorescence observed by single-shot PLIF, which interestingly occurs to have a similar pattern as the hook-shaped discharge propagation. The images in the present case are taken in different RF cycles, and consequently, only a qualitative observation of the similarity in shape can be made. The hook features, however, appear in both emission and fluorescence at different distances to the nozzle so that it can be safely assumed that the occurrence of both features within one cycle is linked. Due to the nozzle geometry, the gas flow is turbulent and from distances of about 4 mm, significant mixing with ambient is occurring. It is here, where branching and hook structures can be observed.

These observations on plasma jets are necessary to control the discharge regarding applications, for instance, surface modification or plasma medicine. In addition, the stochastic nature of density fields must be considered when evaluating experimental data and computer simulations on turbulent atmospheric pressure plasma jets obtained on time scales not significantly shorter than the Kolmogorov time scale, which describes the shortest time scale relevant for mixing in a turbulent flow [7].

To summarize, in this paper, PLIF measurements on OH show the flow pattern, which exhibits turbulent properties. A single-shot image of the discharge pattern shows a streamer-like property, which seems to be coinciding with the OH flow pattern. The study will help to understand fundamental mechanisms of discharge propagation and development.

Manuscript received November 2, 2013; revised January 17, 2014; accepted February 21, 2014. This work was supported by the Federal German Ministry of Education and Research under Grant 03Z2DN12 through the Plasmatis EZE Group.

S. Iseni, S. Reuter, and A. Schmidt-Bleker are with the Centre for Innovation Competence Plasmatis, Greifswald 17489, Germany (e-mail: sylvain.iseni@inp-greifswald.de; stephan.reuter@inp-greifswald.de; ansgar.schmidt-bleker@inp-greifswald.de).

K.-D. Weltmann is with the Leibniz Institute for Plasma Science and Technology, INP Greifswald e.V., Greifswald 17489, Germany (e-mail: weltmann@inp-greifswald.de).

Color versions of one or more of the figures in this paper are available online at http://ieeexplore.ieee.org.

Digital Object Identifier 10.1109/TPS.2014.2321226

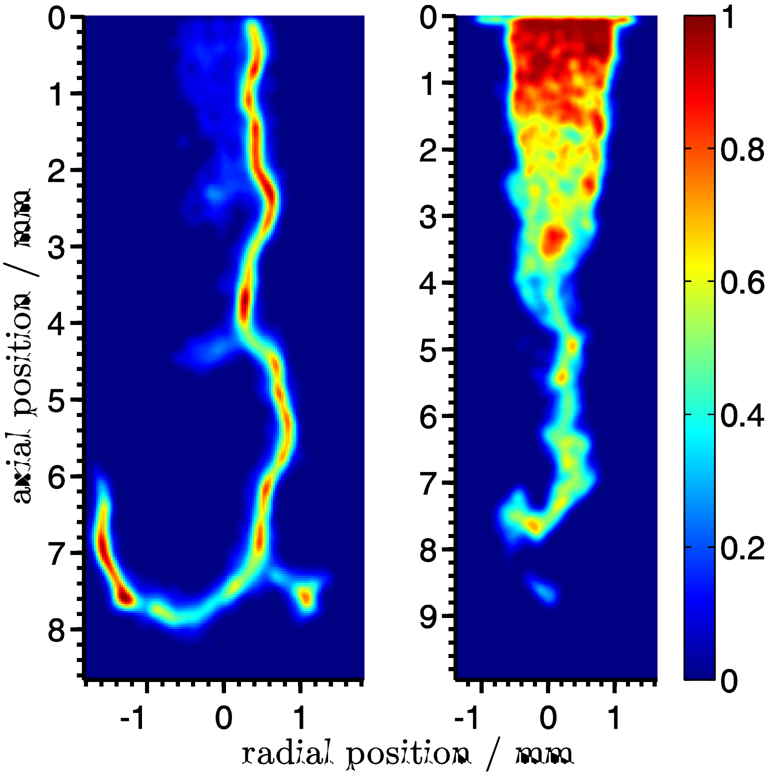

Fig. 1. ICCD pictures over one excitation period of an RF atmospheric pressure plasma jet fed with 3-slm argon. The jet nozzle is located at an axial distance of zero. Left: spontaneous radiative emissions (250–800 nm) depict the streamer propagation and 1.0-μs exposure time single-shot. Right: single-shot space resolved PLIF signal of OH molecules generated by the plasma due to dissociation of water impurities in the feed gas.

REFERENCES

[1] W. Crookes, "The Bakerian lecture: On the illumination of lines of molecular pressure, and the trajectory of molecules," *Philosoph. Trans. Roy. Soc. London*, vol. 170, pp. 135–164, Jan. 1879.

[2] K.-D. Weltmann *et al.*, "Atmospheric pressure plasma jet for medical therapy: Plasma parameters and risk estimation," *Contrib. Plasma Phys.*, vol. 49, no. 9, pp. 631–640, Oct. 2009.

[3] L. Bundscherer *et al.*, "Impact of non-thermal plasma treatment on MAPK signaling pathways of human immune cell lines," *Immunobiology*, vol. 218, no. 10, pp. 1248–1255, Oct. 2013.

[4] S. Reuter *et al.*, "Detection of ozone in a MHz argon plasma bullet jet," *Plasma Sources Sci. Technol.*, vol. 21, no. 3, p. 034015, 2012.

[5] S. Reuter *et al.*, "From RONS to ROS: Tailoring plasma jet treatment of skin cells," *IEEE Trans. Plasma Sci.*, vol. 40, no. 11, pp. 2986–2993, Nov. 2012.

[6] S. Iseni *et al.*, "Atmospheric pressure streamer follows the turbulent argon air boundary in a MHz argon plasma jet investigated by OH-tracer PLIF spectroscopy," *J. Phys. D, Appl. Phys.*, vol. 47, no. 15, p. 152001, 2014.

[7] S. B. Pope, *Turbulent Flows*. Cambridge, U.K.: Cambridge Univ. Press, 2000.

5.2 Article II

NO_2 dynamics of an Ar/Air plasma jet investigated by *in situ* quantum cascade laser spectroscopy at atmospheric pressure

doi:10.1088/0022-3727/47/7/075203

IOP Publishing | Journal of Physics D: Applied Physics

J. Phys. D: Appl. Phys. **47** (2014) 075203 (7pp) | doi:10.1088/0022-3727/47/7/075203

NO_2 dynamics of an Ar/Air plasma jet investigated by *in situ* quantum cascade laser spectroscopy at atmospheric pressure

Sylvain Iséni[1,2], **Stephan Reuter**[1,2] **and Klaus-Dieter Weltmann**[2]

[1] Centre for Innovation Competence Plasmatis, Felix-Hausdorff-Str. 2, 17489 Greifswald, Germany
[2] Leibniz Institute for Plasma Science and Technology INP Greifswald e.V., Felix-Hausdorff-Str. 2, 17489 Greifswald, Germany

E-mail: sylvain.iseni@inp-greifswald.de

Received 10 October 2013, revised 10 December 2013
Accepted for publication 16 December 2013
Published 29 January 2014

Abstract

In this work, quantum cascade laser (QCL) absorption spectroscopy was used to investigate the nitric dioxide (NO_2) production dynamics at ambient conditions. For the first time, QCL detection of NO_2 and NO was used at ambient conditions in order to remain close to the conditions that are present in the application of plasma jets in open atmosphere. For the investigations, the plasma jet was placed inside an open multi-pass cell. The detection limit of the setup was 20 ppb for NO_2 and similar for nitric oxide (NO). Since the effective production of NO was below the detection limit, further investigations of the NO density were performed with optical emission spectroscopy.

Keywords: quantum cascade laser absorption spectroscopy (QCLAS), atmospheric pressure argon plasma jet, reactive oxygen nitrogen species, atmospheric pressure diagnostic

(Some figures may appear in colour only in the online journal)

1. Introduction

The scientific and technological interest in quantum cascade lasers (QCLs) for plasma diagnostic has increased over the last few years [1–5]. These types of lasers emit monochromatic mid-infrared (mid-IR) radiation with appropriate power for absorption spectroscopy.

Laser absorption spectroscopy in the mid-IR spectral region of 3–20 μm has proven useful for diagnostics of infrared active molecules. Applications have included environmental monitoring [6], process monitoring [7] and plasma chemistry diagnostics [3]. The technology is based on using a frequency tunable diode laser and determining a molecular fingerprint of the absorption spectrum based on Beer–Lambert's law [8]. Early on, lead salt lasers were used to generate the laser radiation [4]. The intricate use of the technology, especially the requirement for cryogenic cooling, made the search for new techniques a key issue. QCLs provide a new technology with the use of several tunnel barriers of varying thickness, resulting in quantum wells with different population probabilities and a resulting population inversion, from which lasing can be induced [9]. Compared with lead salt lasers distributed feedback (DFB) QCLs provide (i) continuous mode-hop free (MHF) wavelength tuning, (ii) increasingly high output powers, (iii) near room temperature operation, and in the case of cw-DFBQCL (iv) narrow linewidth radiation [1]. QCLs require a higher power input which, when pulsed, will increase the QCL diode's temperature considerably during one pulse. This will change the material's refractive index and thus result in an inherent frequency-down chirp [5]. This is applied to acquire entire absorption spectra during one laser pulse. The technology is known as intra pulse mode [10].

In this paper, QCL mid-IR absorption spectroscopy is used for the first time to investigate NO_x species produced by a radio frequency (RF) argon driven plasma jet operating at atmospheric conditions. This jet is suitable for biomedical applications [11, 12]. It is known that plasma treatment can induce biological responses [13] and anti-microbiological effects have been reported in recent literature [14, 15]. One type of plasma component responsible for these effects is reactive oxygen and nitrogen species (RONS) by inducing oxidative stress to micro-organisms leading to microbial inactivation [14]. Previous studies have already reported the excellent anti-microbiological effects of argon plasma, which are mostly attributed to RONS [16]. A study of the production of NO_x species by plasma sources will help to disentangle fundamental processes in plasma medicine. By using mid-IR QCL absorption spectroscopy under atmospheric conditions, the NO_2 absorption profile and absolute NO_2 concentration in the ppb range were determined.

2. Experimental setup

2.1. Apparatus

The plasma source used for the investigations was an atmospheric pressure argon plasma jet (kinpen 09, neoplas GmbH, Germany) [17] This plasma jet is a 1 MHz RF driven concentric needle electrode within a dielectric ceramic capillary of 1.6 mm inner diameter. A grounded ring electrode surrounds the outer side of the capillary. This type of plasma jet configuration is referred to in the literature as a DBD-like jet and more general information can be found in [18]. The electrical potential of the needle can be from 2 to 6 kV and the dissipated power within the plasma is known to be in the range 1.6–2.2 W. The kinpen generates an argon discharge with a spatial afterglow—also called effluent in this work—of about 10 mm outside of the ceramic capillary. The working gas (argon 99.999% purity) is fed through the discharge zone with a gas flow rate of 3 standard litres per minute (slm). To protect the plasma jet effluent from the surrounding atmosphere, a shielding gas curtain device, described and investigated in previous papers [19, 20], was used. As shielding gas pressurized air was employed.

The diagnostic of this plasma device has been performed by mid-IR QCL absorption spectroscopy. This spectroscopic technology has already been used on ozone, as presented by Reuter *et al* [20] and also recently reviewed by Röpcke *et al* [1, 4]. Figure 1 illustrates the complete diagnostic setup with the implementation of the kinpen and the gas shielding device which was used in this work to generate controlled and reproducible conditions [17]. The measurement system is mainly based on the Q-MACS platform developed by Neoplas Control GmbH and adapted and optimized here in order to lead *in situ* diagnostics at atmospheric conditions. The mid-IR source is a nanosecond pulsed QCL from Alpes lasers SA which emits in the spectral range from 1607.72 to 1619.43 cm^{-1}. The laser is driven in the so-called intra-pulsed mode. The wavelength is tuned by temperature via a Peltier element which is directly in contact with the laser chip. A water cooling system is installed in order to increase the Peltier element efficiency and increase temperature stability. According to the manual, the laser operates in single mode emission. The wavelength fine tuning is realized by a current ramp which varies the temperature and allows for a sweeping of 0.8 cm^{-1} range within 1100 laser pulses. The laser beam, which comes directly from the chip, is not symmetric and the strong divergence is corrected by an off-axis parabolic gold coated mirror (PaM). It is then focused by a 1 m spherical mirror (SM) and directed through a 0.60 m length ‘White’ type multi-pass spectroscopic absorption cell. The number of passes within the multi-pass cell can be adjusted according to the requirements of the absorber densities. In the applied working conditions, 32 passes are achieved resulting in an optical path of 19.2 m within the multi-pass cell. The laser beam is then focused on a very fast mercury cadmium telluride detector via a PaM. Since mid-IR radiation is not directly visible, a red laser diode is installed and its beam pathway is overlapped with the mid-IR beam for easier optical adjustment through the multi-pass cell. Data acquisition is performed via a PC and processed by Q-MACSoft Monitor software [21]. Additionally, an optical fibre is inserted within the chamber and connected to a spectrometer (Avantes, AvaSpec, 25 μm slit, 0.7 nm resolution) in order to record optical emission spectroscopic information. The fibre is aligned with the plasma jet front side. A spectral range from 200 to 960 nm is observed.

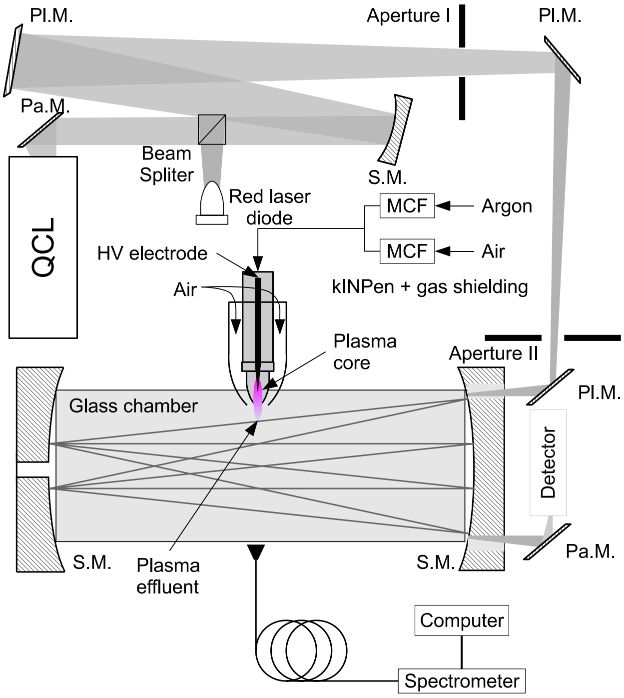

Figure 1. Schematics of the spectroscopic experimental setup based on a QCL absorption diagnostic system with the implementation of the plasma jet. The system contains various reflective components such as planar mirror (PlM), off axis parabolic mirror (PaM), spherical mirror (SM), and a red laser diode as optical alignment for the IR beam. The plasma jet is inserted through the glass chamber wall in such a way that the plasma effluent of a few millimetres is blown into the chamber. The so-called far field is defined as post-effluent, where short living plasma species are not relevant and here considered as the volume of the chamber (3.6 L).

Implementation and measurement of NO_2 produced by the plasma jet are possible under the following conditions. First, the plasma jet has to operate and be diagnosed as close to the operating conditions as possible, meaning that it has to be surrounded by air at atmospheric pressure. Therefore, a cylindrical glass chamber (3.6 L volume), 9 cm inner diameter and 57.5 cm length, which is positioned between the multi-pass cell’s mirrors, was used. The two glass chamber exits are partially closed with glass but each side has a rectangular opening which the mid-IR reflection of the beam can go through without disturbance such as interferences. As shown in figure 1, the plasma jet is situated in the middle of the long side of the multi-pass cell. The plasma jet can qualitatively be separated in three distinguished regions: the core plasma region is within the dielectric tubing and is dominated by plasma processes. The effluent is the spatial afterglow of the plasma and exits the nozzle for a few millimetres; here plasma species are still present. The far field has no dominating plasma species and is the volume of the multi-pass cell in the present case. However, it is important to note that this type of multi-pass cell does not allow the absorption beam to go through the effluent. Indeed, the laser optical path is located within a sagittal plane to the plasma jet axis along the radial direction of the chamber. The 10 to 12 mm long plasma effluent is too short to be on the optical path. Moreover, this would induce steep density gradients and induce a non-homogeneous absorption medium. The plasma jet is fed with 3 standard litres per minute (slm) of argon (99.999%) and blows directly into the glass chamber. In order to avoid saturation of the inner atmosphere, a gas curtain all around the plasma jet body was used, which provides an additional 5 slm air flux within the chamber. More information about the purpose of the gas curtain can be found in [17, 23]. The reactive species are generated either within the plasma core or in the effluent and then blown directly into the chamber. Our working conditions allow us to presume a homogenous distribution of the species within the chamber. This assumption was partially checked by rotating the input or the plasma source by 90° which changes its position regarding the two side outlets of the chamber.

2.2. Calibration procedure

In order to identify the spectral position of the laser radiation, a calibration process is required. For this, two gas reference cells of 15 cm long, filled with different gases, where used. Because of the complexity of the NO_2 absorption spectra, the spectral position cannot be easily identified. Therefore the second NH_3 filled reference cell is used because of its capability of absorbing mid-IR radiation in the close vicinity of NO_2. With the absorption spectrum measured from the NH_3-cell, the wavelength position can accurately be defined. The one with NO_2 is filled at 4.5 mbar and the other one with NH_3 at 10 mbar. Figure 2 shows the recorded absorption spectra of NO_2 and NH_3 from 1611.2 to 1612.4 cm^{-1}. The recorded spectra are compared to a simulation performed by Q-MACSoft–HT [22] software based on the HITRAN database [23]. From the graph it can be concluded that simulated and recorded spectra are in good agreement despite some mismatches. These mismatches can be explained by the fact that the reference cells are closed with MgF_2 windows which—despite optical path optimization—are causing interferences, which appear in the spectra. However, by superposition of the simulated and the measured spectrum, excellent frequency correlation is observed. The calibration of the wavenumber scale is realized with a germanium (Ge) Fabry–Pérot cavity which generates a known interference signal with peaks of defined spectral distance. The absorption method is based on the Beer–Lambert law described by equation (1) for a simple ro-vibrational energy transition

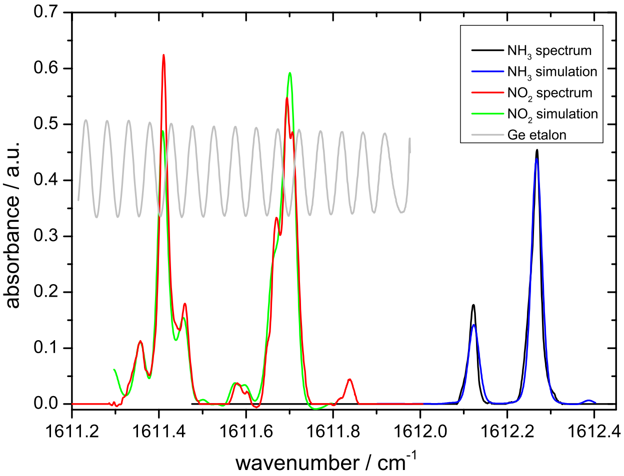

Figure 2. Absorption spectrum of NO_2 produced by the jet at atmospheric pressure plotted with the result from the real-time fit.

$$T_n = \frac{I_{T_n}}{I_0} = e^{-S_n(T_k)NLf_{p_n}}. \tag{1}$$

With T_n the transmittance, I_{T_n} the transmitted intensity, I_0 the intensity of the source, $S_n(T_k)$ the line strength in $cm^{-1}/(molecule\ cm^{-2})$, N the density of absorbing molecules, L the absorption length in m and f_{p_n} the line shape of the n ro-vibrational transition including the broadening. The experimental conditions allow assuming pressure broadening as the major broadening effect of many orders of magnitude higher than Doppler and Stark broadening. Pressure broadening can be well described by a Lorentzian function. Therefore the Voigt function of the whole broadening can be simplified as a Lorentzian function $L_n(\nu, \gamma_n)$,

$$L_n(\upsilon, \gamma) = \frac{\gamma_n}{\pi[(\upsilon - \upsilon_0)^2 + \gamma_n^2]} \tag{2}$$

with

$$\gamma_n = p_{\text{atm}}\left[\eta_x\left(\gamma_{n_{\text{self}}} - \gamma_{\text{air}}\right) + \gamma_{n_{\text{air}}}\right] \tag{3}$$

where $\gamma_{n_{\text{self}}}$ and $\gamma_{n_{\text{air}}}$ are the broadening coefficients of an n ro-vibrational transition, ν_0 is the centred spectral position of the transition n and η_x is the density ratio between the selected molecule x and the total density. Then f_{p_n} is the results of a convolution between the natural line shape $f(\nu - \nu_0)$ and $L_n(\nu, \gamma_n)$ with $\int f(\nu - \nu_0)d\nu = 1$:

$$f_{p_n}(\nu - \nu_0) = f_n(\nu - \nu_0) \otimes L_n(\nu, \gamma_n). \tag{4}$$

The absorption spectrum is then calculated by the sum of all the absorption lines,

$$T(\nu) = \sum_n T_n(\nu). \tag{5}$$

It is also necessary to include the instrumental profile $h(\nu)$ in the simulation spectrum T_s:

$$T_s(\nu) = T(\nu) \otimes h(\nu). \tag{6}$$

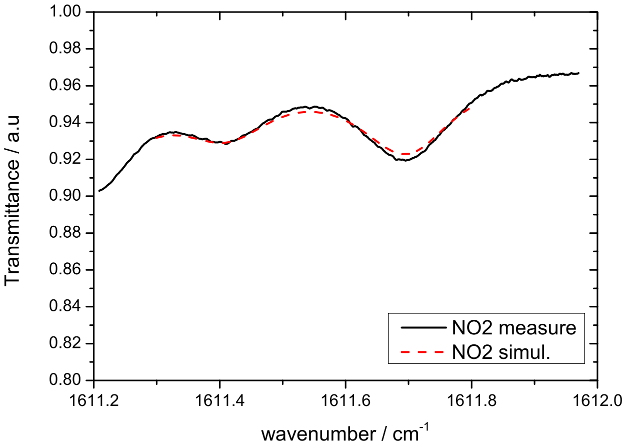

Figure 3. Transmittance spectrum of NO_2 produced by the jet at atmospheric pressure plotted with the result from the real-time fit.

3. Absolute densities determination

To determine the selected species density, the measured spectrum T_m is first compared to T_s in real time with Q-MACSoft Monitor software [21]. As temperature, pressure, absorption length and instrumental profile of the experiment are usually known one can run a fit routine with the concentration as a free parameter. Figure 3 depicts a recorded transmittance spectrum of NO_2 at atmospheric pressure generated by the plasma jet and the result of the fit from the simulation. Very good agreement is shown between both. Due to the very high spectral resolution, the measurement selectivity for the respective specie is considerably enhanced compared to other methods such as Fourier transform infrared spectroscopy (FTIR) or UV absorption. In the case of absorption overlap with other molecules, a significant difference will occur between the simulation and the measurement. As a consequence, this approach ensures a perfect and reliable detection of specific species. The recorded spectrum in figure 3 shows that the absorption process is occurring over the whole scan range, resulting from a global absorption. In other words, the inherent laser intensity I_0 cannot be measured in the presence of NO_2. This is due to the pressure broadening which is dominating the broadening processes of the absorption lines. It is assumed that constant laser source intensity is not reasonable and must lead to significant measure uncertainty. The first investigations by Reuter *et al* were performed by normalizing the recorded spectrum to I_0 and fitting the baseline by a polynomial function. This polynomial was set as a baseline to initialize the fit routine. This approach, however, allows only short measurement times of a few tens of minutes until the light source intensity changes significantly. The signal-to-noise ratio was low and the typical detection limit was found to be around 300 ppb for the detection of O_3. Additional issues have been found and linked to the non-uniform linearity of the detector which induces a shift of the signal intensity. This performance was not sufficient for the investigation of NO_2. Therefore, a new method of measurements was developed as follows: First, a template baseline spectrum B_{temp} at the intensity I_0 is recorded. Then, a transmission spectrum T_m is acquired as shown in figure 3. The fit routine is executed to match the simulation spectrum T_s and the measurement T_m with B_{temp} as an initial baseline parameter. The quality of the signal T_m strongly affects the output result of the fit routine to match the simulation and associated spectrum. Once the optimum value of the concentration is reached, the position of the baseline is determined by the optimization of a first-order polynomial function as described by

$$B = a \times B_{temp} + b. \tag{7}$$

With a and b as two scalars adjusting the slope and the translation of the template baseline around the initial position. This approach has been validated by artificially reducing the intensity I_0 by 35% during experiment, where no change of the concentration was observed. This is due to the fact that the shape of the transmittance spectrum is the key to optimize b. It is observed that the parameter b of the polynomial has the strongest influence on the results and corresponds directly to a variation of the light source intensity. By this method, the typical noise deviation is measured to be around 15 ppb centred and a detection limit of 20 ppb is determined from the signal-to-noise ratio. Similar results have also been obtained for the detection of NO.

Working at atmospheric conditions is also intricate due to the abundance of water and carbon dioxide molecules within the chamber. These species efficiently absorb mid-IR radiation. Therefore, they may disturb the diagnostic of other species significantly. NO_2 and water absorption spectra overlap in many spectral ranges. The very narrow spectral radiation of the QCL has the advantage of selecting a range where the overlapping is negligible or well contained.

4. Results and discussion

Since water can strongly affect the $NO_{(x)}$ production (see e.g. Pipa *et al* [24]), before each measurement, the gas flow is kept running for at least 2 h in order to reduce the residual humidity within the pipe. Recently, Winter *et al* also showed that humidity does influence the chemistry produced by this plasma jet [25]. The same procedure is applied for the gas shielding: pressured air is flowing for 12 h at least in order to dry the chamber. The plasma jet is switched on for 1 h before the first measurement in order to ensure stable conditions. While this is an overcautious procedure, it ensures that the results are independent of strong impurity influences. For each step of the varied parameter, the background spectrum is recorded for 5 min before and after the measurement and the measurement itself is performed for 5–6 min. One data sample is derived by recording and fitting an average spectrum every 5 s. The final density value is obtained from an average over the complete data set. The errors are stated as a standard deviation of the density. In addition the deviation of the baseline determined from the fit routine is also included in the final error estimation. However, in this study, the discharge fluctuations result on an error estimation which is in the order of 80 ppb.

Figure 4 presents the net production rate of NO_2 in the far field of the argon plasma jet as a function of air admixture to

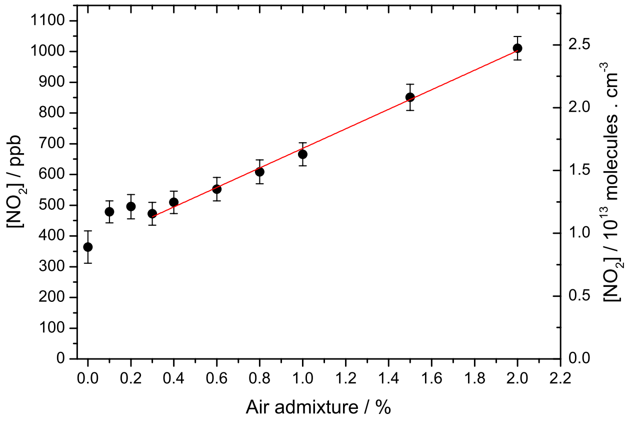

Figure 4. Absolute concentration of NO_2 produced by the kinpen for different dry air admixtures.

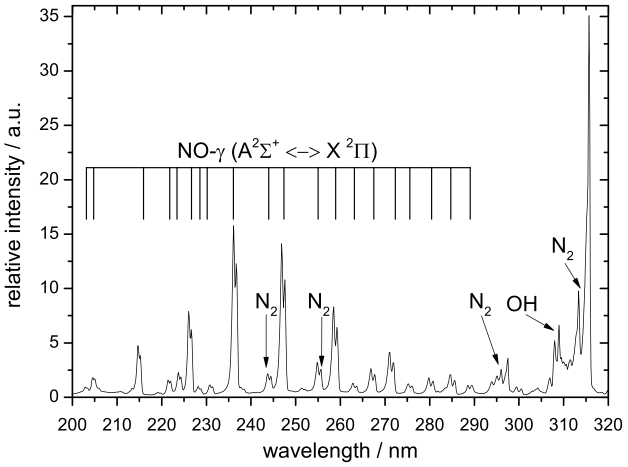

Figure 5. Emission spectrum, side on, from the argon plasma jet running with 3.0 slm and 0.3% admixture.

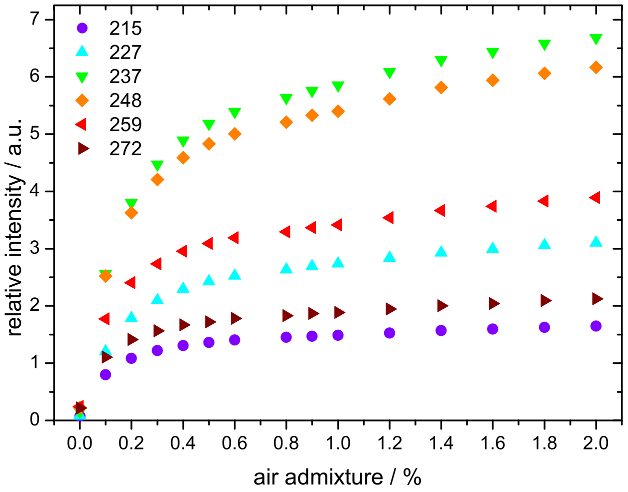

Figure 6. Normalized integrated NO(A–X) bands emission for different dry air admixtures.

the feed gas. The NO_2 generation is strictly monotonically increasing and does not seem to reach a local maximum until 2.0% admixture of air. It was not possible to keep the plasma running at higher admixture, which is why the expected decrease due to a drop of the plasma efficiency cannot be observed. However, the points measured for 0.1% and 0.2% are quite interesting and can be ascertained only due to the sensitivity of the measurement technique. It can be clearly observed that admixing air to the argon feed gas induces a linear process of NO_2 production (at higher admixtures). The slight but observed deviation for 0.1% and 0.2% admixture can be explained by an effective dissociation process of molecular oxygen and nitrogen. An emission spectrum is presented on figure 5 and shows the emission bands of NO (A–X), the so-called γ system from 215 to 272 nm. It is also possible to observe the OH emission and some N_2 lines. As described in the experimental setup section, OES spectra are collected side on which has the advantage of obtaining information about the excitation on NO molecules within the plasma core, close to the needle electrode. During the experiment, NO (A–X) emission intensity appears to be dependent on the air admixture. Figure 6 shows the relative intensity of different NO (A–X) bands for several ratios of air admixture. As a result, we observe that the excitation process of NO (A–X) increases monotonically. In cases of low air admixture, a very drastic excitation of NO molecules is observed, especially at 0.1% and 0.2%. Moreover, Pipa *et al* [24] were able to measure NO by absorption from a similar plasma jet at higher power for this type of discharge. The NO (A–X) emission dynamics depending on air admixture has an excellent agreement with the absolute density of NO. This is especially true for dry air admixtures. Nevertheless, the authors report that ozone was not detected, which should be attributed to the higher power input inducing a higher gas temperature in the reported case. According to their study, here it is assumed that the NO production dynamic follows in good approximation the excited NO species emission—however, a detailed study needs to follow. The QCL system was also set up to measure absolute NO molecule densities in the far field. The detection limit for NO was determined to be 20 ppb. However, no NO has been detected from this low power plasma jet. One reliable and evident reason is the high density of ozone, which is about two or three orders of magnitude higher than NO_2. The main chemical loss of NO in the presence of O_3 is well known and the high reactivity of NO is also important to consider [26]. It is very likely that the following equation is responsible for the transformation of NO into NO_2:

$$O_3 + NO \rightarrow NO_2 + O_2. \tag{8}$$

5. Conclusion

In this work, for the first time, quantum cascade laser absorption was performed to determine NO_2 species production rate on a plasma jet operating in ambient conditions and pressure. The investigated rf argon plasma jet kinpen was placed in a multi-pass cell with open gas flux. For the measurements, an algorithm was developed to perform a fit of the background radiation. Due to pressure broadening, the observed transitions—in this case

NO_2 (1611.3–1611.8 cm^{-1})—are broadened so much that the values of zero absorption cannot be observed directly with the laser system. By performing a background measurement and by including a fitted polynomial of this background into the fit of the absorption signal with data taken from a spectra database, the absolute densities of NO_2 could be obtained. The quality of the gained evaluation was tested successfully. The accuracy of the measurements was determined to be down to 20 pbb for both NO and NO_2 molecules. However, tiny fluctuations of the plasma discharge increase the error estimations.

This technique was used to investigate the far-field NO_2 production dynamics as a function of dry air admixture to the plasma jets feed gas. As described here, non-linear increase is observed at small admixtures whereas a linear increase takes place up to 0.3% admixed air.

From emission spectroscopic measurements, the NO dynamics were also investigated. As shown in [24], the NO density correlates with the NO emission for low admixtures of dry air. These measurements were performed because, with the quantum cascade laser absorption, NO could not be detected within the multi-pass cell for the investigated plasma jet, which mainly produces oxygen derived species. The NO emission dynamic at air admixtures below 0.2% exhibits a non-linear increase, while at admixtures of greater than 0.4% this becomes an increasingly linear increase, which adds to the interpretation that dissociation of N_2 and O_2 at low admixtures dominate the NO and NO_2 dynamic.

The presented study yields a new way to investigate a plasma jet regarding its NO_2 production mechanisms at atmospheric conditions almost identical to those in applications such as plasma medicine.

Far-field measurements such as the ones shown in this study can be used to investigate the reactive species production processes at varying parameters and will help us to understand and control the reactive species component composition to tailor, e.g., biological responses to plasma treatment in plasma medicine.

Acknowledgments

The authors thank Dr Andrei V Pipa for the discussions about IR spectroscopy and Dipl. Ing. Henrik Zimmermann (neoplas control GmbH) and Dipl. Ing. Sven Glitsch for the technical support and their expertise about QCL. Very deep acknowledgements are addressed to Professor Dr Röpcke for his knowledge and previous works on QCL absorption spectroscopy. Dr Jan Schäfer and Dr Rüdiger Foest are also acknowledged for their contribution to the experimental settings. The authors gratefully acknowledge the funding by the Federal German Ministry of Education and Research (BMBF, grant number 03Z2DN12).

References

[1] Röpcke J, Davies P B, Lang N, Rousseau A and Welzel S 2012 Applications of quantum cascade lasers in plasma diagnostics: a review *J. Phys. D: Appl. Phys.* **45** 423001

[2] Guaitella O, Hubner M, Marinov D, Guerra V, Pintassilgo C D, Welzel S, Ropcke J and Rousseau A 2011 Oxidation of NO into NO_2 by surface adsorbed O atoms *Contrib. Plasma Phys.* **51** 176–81

[3] Marinov D, Lopatik D, Guaitella O, Hübner M, Ionikh Y, Röpcke J and Rousseau A 2012 Surface vibrational relaxation of N_2 studied by CO_2 titration with time-resolved quantum cascade laser absorption spectroscopy *J. Phys. D: Appl. Phys.* **45** 175201

[4] Röpcke J, Lombardi G, Rousseau A and Davies P B 2006 Application of mid-infrared tuneable diode laser absorption spectroscopy to plasma diagnostics: a review *Plasma Sources Sci. Technol.* **15** S148–68

[5] Welzel S, Hempel F, Hubner M, Lang N, Davies P B and Ropcke J 2010 Quantum cascade laser absorption spectroscopy as a plasma diagnostic tool: an overview *Sensors (Basel)* **10** 6861–900

[6] Tuzson B, Zeyer K, Steinbacher M, McManus J B, Nelson D D, Zahniser M S and Emmenegger L 2012 Selective measurements of NO, NO_2 and NO_y in the free troposphere using quantum cascade laser spectroscopy *Atmos. Meas. Tech. Discuss.* **5** 8969–93

[7] Hübner M, Marinov D, Guaitella O, Rousseau A and Röpcke J 2012 On time resolved gas temperature measurements in a pulsed dc plasma using quantum cascade laser absorption spectroscopy *Meas. Sci. Technol.* **23** 115602

[8] Winter J, Dunnbier M, Schmidt-Bleker A, Meshchanov A, Reuter S and Weltmann K D 2012 Aspects of UV-absorption spectroscopy on ozone in effluents of plasma jets operated in air *J. Phys. D: Appl. Phys.* **45** 385201

[9] Faist J, Capasso F, Sivco D L, Hutchinson A L, Sirtori C and Cho A Y 1995 Quantum cascade laser: a new optical source in the mid-infrared *Infrared Phys. Technol.* **36** 99–103

[10] Normand E, McCulloch M, Duxbury G and Langford N 2003 Fast, real-time spectrometer based on a pulsed quantum-cascade laser *Opt. Lett.* **28** 16–8

[11] Ehlbeck J, Schnabel U, Polak M, Winter J, von Woedtke T, Brandenburg R, von dem Hagen T and Weltmann K D 2011 Low temperature atmospheric pressure plasma sources for microbial decontamination *J. Phys. D: Appl. Phys.* **44** 013002

[12] Weltmann K D, Brandenburg R, von Woedtke T, Ehlbeck J, Foest R, Stieber M and Kindel E 2008 Antimicrobial treatment of heat sensitive products by miniaturized atmospheric pressure plasma jets (APPJs) *J. Phys. D: Appl. Phys.* **41** 194008

[13] Bundscherer L, Wende K, Ottmuller K, Barton A, Schmidt A, Bekeschus S, Hasse S, Weltmann K D, Masur K and Lindequist U 2013 Impact of non-thermal plasma treatment on MAPK signaling pathways of human immune cell lines *Immunobiology* **218** 1248–55

[14] Matthes R, Bekeschus S, Bender C, Koban I, Hubner N O and Kramer A 2012 Pilot-study on the influence of carrier gas and plasma application (open resp. delimited) modifications on physical plasma and its antimicrobial effect against Pseudomonas aeruginosa and Staphylococcus aureus *GMS Krankenhhyg Interdiszip* **7** Doc02

[15] Lademann J, Richter H, Schanzer S, Patzelt A, Thiede G, Kramer A, Weltmann K D, Hartmann B and Lange-Asschenfeldt B 2012 Comparison of the antiseptic efficacy of tissue-tolerable plasma and an octenidine hydrochloride-based wound antiseptic on human skin *Skin Pharmacol. Physiol.* **25** 100–6

[16] Nosenko T, Shimizu T and Morfill G E 2009 Designing plasmas for chronic wound disinfection *New J. Phys.* **11** 115013

[17] Reuter S, Winter J, Schmidt-Bleker A, Tresp H, Hammer M U and Weltmann K D 2012 Controlling the ambient air affected reactive species composition in the

effluent of an argon plasma jet *IEEE Trans. Plasma Sci.* **40** 2788–94

[18] Lu X, Laroussi M and Puech V 2012 On atmospheric-pressure non-equilibrium plasma jets and plasma bullets *Plasma Sources Sci. Technol.* **21** 034005

[19] Reuter S, Tresp H, Wende K, Hammer M U, Winter J, Masur K, Schmidt-Bleker A and Weltmann K D 2012 From RONS to ROS: tailoring plasma jet treatment of skin cells *IEEE Trans. Plasma Sci.* **40** 2986–93

[20] Reuter S, Winter J, Iséni S, Peters S, Schmidt-Bleker A, Dunnbier M, Schafer J, Foest R and Weltmann K D 2012 Detection of ozone in a MHz argon plasma bullet jet *Plasma Sources Sci. Technol.* **21** 034015

[21] neoplas control GmbH, Q-MACSoft Monitor, 1.2.8.929, 2011, www.neoplas-control.de

[22] neoplas control GmbH, Q-MACSoft HT, 1.2.8, 2011, www.neoplas-control.de

[23] Rothman L S, Gordon I E, Barbe A, Benner D C, Bernath P F, Birk M, Boudon V, Brown L R, Campargue A, Champion J-P, Chance K, Coudert L H, Dana V, Devi V M, Fally S, Flaud J-M, Gamache R R, Goldman A, Jacquemart D, Kleiner I, Lacome N, Lafferty W J, Mandin J-Y, Massie S T, Mikhailenko S N, Miller C E, Moazzen-Ahmadi N, Naumenko O V, Nikitin A V, Orphal J, Perevalov V I, Perrin A, Predoi-Cross A, Rinsland C P, Rotger M, Šimečková M, Smith M A H, Sung K, Tashkun S A, Tennyson J, Toth R A, Vandaele A C, and Vander Auwera J 2009 The HITRAN 2008 molecular spectroscopic database *J. Quant. Spectrosc. Radiat. Transfer* **110** 533–72

[24] Pipa A V, Reuter S, Foest R and Weltmann K D 2012 Controlling the NO production of an atmospheric pressure plasma jet *J. Phys. D: Appl. Phys.* **45**

[25] Winter J, Wende K, Masur K, Iseni S, Dünnbier M, Hammer M U, Tresp H, Weltmann K D and Reuter S 2013 Feed gas humidity: a vital parameter affecting a cold atmospheric-pressure plasma jet and plasma-treated human skin cells *J. Phys. D: Appl. Phys.* **46** 295401

[26] van Gessel A F H, Hrycak B, Jasinski M, Mizeraczyk J, van der Mullen J J A M and Bruggeman P J 2013 Temperature and NO density measurements by LIF and OES on an atmospheric pressure plasma jet *J. Phys. D: Appl. Phys.* **46** 095201

5.3 Article III

Atmospheric pressure streamer follows the turbulent argon air boundary in a MHz argon plasma jet investigated by OH-tracer PLIF spectroscopy
doi:10.1088/0022-3727/47/15/152001

IOP Publishing
Fast Track Communications
Journal of Physics D: Applied Physics
J. Phys. D: Appl. Phys. **47** (2014) 152001 (6pp)
doi:10.1088/0022-3727/47/15/152001

Fast Track Communication

Atmospheric pressure streamer follows the turbulent argon air boundary in a MHz argon plasma jet investigated by OH-tracer PLIF spectroscopy

S Iseni[1,2], **A Schmidt-Bleker**[1,2], **J Winter**[1,2], **K-D Weltmann**[2] **and S Reuter**[1,2]

[1] Centre for Innovation Competence plasmatis, Felix-Hausdorff-Str. 2, 17489 Greifswald, Germany
[2] Leibniz Institute for Plasma Science and Technology INP Greifswald e.V., Felix-Hausdorff-Str. 2, 17489 Greifswald, Germany

E-mail: sylvain.iseni@inp-greifswald.de

Received 17 November 2013, revised 13 February 2014
Accepted for publication 17 February 2014
Published 27 March 2014

Abstract

An open question in the research of the dynamics of non-equilibrium cold atmospheric pressure plasma jets is the influence of ambient species on streamer propagation pathways. In the present work, by means of planar laser-induced fluorescence (PLIF), an atmospheric pressure argon plasma jet is investigated in a laminar and turbulent gas flow regime. The flow pattern is investigated with plasma on and plasma off. It is shown that in turbulent mode, the streamer path changes according to the flow pattern changes and the resulting changes in air abundance. From a comparison of an analytical diffusion calculation and LIF measurements, the air impurity boundary is determined. Most importantly, the origin of the streamer pathway is investigated in detail, by recording the flow pattern from OH-PLIF measurements and simultaneously measuring the streamer path by an overlay technique through emission measurements. It is shown that the streamer path is correlated to the turbulent flow pattern.

Keywords: atmospheric pressure plasma jet, planar laser-induced fluorescence, discharge propagation, plasma medicine, plasma jet effluent regime

(Some figures may appear in colour only in the online journal)

1. Introduction

Only a few years ago, so-called plasma bullet [1, 2] and guided-streamer [3] jets came to be known. Recently, researchers have identified the fundamental processes behind these dynamics (see e.g. [4, 5]). However, their propagation in air has continued to raise questions. In this work, the connection of gas flux regime, ambient species and streamer head propagation in a MHz atmospheric pressure argon plasma jet is investigated by laser spectroscopic methods. The diagnostic technique is based on planar laser-induced fluorescence (PLIF) on hydroxide molecules (OH) generated by the plasma jet itself due to water impurities. With stereoscopic imaging, both flow structure and streamer propagation are investigated simultaneously for a single discharge event. The study reveals that the flux field with plasma differs strongly from the flux field without plasma. Furthermore, it is most prominently and for the first time shown that the streamer propagates in the noble gas channel of a turbulent plasma jet effluent itself and follows the boundaries of ambient species impurities. Especially revealing are the differences observed for the laminar and turbulent case.

2. Experimental setup

In this work, the flux and streamer propagation of a MHz atmospheric pressure plasma jet (kINPen, neoplas tools GmbH, Germany) [6, 7] have been investigated. The feed gas is argon (Ar purity 99.999%), which may contain water impurities of up to 20 ppm originating from the gas pipe as reported in [8]. The OH PLIF measurements are performed with a frequency doubled dye laser (Cobra Stretch, Sirah Laser und Plasmatechnik GmbH, Germany) pumped with a 10 Hz pulsed Nd : Yag laser (Spectra-Physics, Inc.). The pulse duration is measured to be 8.1 ns after frequency doubling at 283 nm. The laser linewidth has been recently measured on a similar dye laser from the same company to be 1.4 pm [9]. Although this parameter remains crucial for the determination of absolute density [10], it does not influence qualitative measurements. The P1(4) transition of the OH(A, X)(1,0) at 283.5 nm is chosen as the energy transition due to its good absorption efficiency. Additionally, it is well separated from other lines. The linearity of the OH fluorescence signal versus the laser energy has been checked. The laser beam is expanded to a sheet via a cylindrical quartz lens and guided through the plasma jet effluent. The laser energy integrated along the 12 mm high sheet is measured to be 13 mJ. An aperture is mounted in front of the jet in order to illuminate only the area of interest. A CCD camera Imager Pro X (LaVision GmbH, Germany), combined with an external gated image intensifier and a 100 mm f/2.8 UV lens, is used as detection system. The fluorescence emission is observed at a 90° angle to the p-polarized laser beam in order to reduce unwanted signals due to Rayleigh scattering. Additionally, a stereoscopic optical imaging system is coupled to the lens in order to record two images with each laser shot. By installing different filters for the two images respectively, different information can be gathered simultaneously. Here, on the first optical input, a BK7 neutral density filter is mounted, which allows observation from 350 to 1100 nm, where most of the plasma emission is found due to argon lines [8, 11]. On the second optical input, a 10 nm FWHM band-pass filter centered at 313 nm is used to collect the fluorescence only of OH. Both signals are recorded on a vertical split CCD chip, so that the exposure time is identical for both signals.

The plasma jet frequency is phase locked with the laser pulse as well as the detection system, which allows phase-resolved optical emission spectroscopy (PR-OES). The exposure time is set to 200 ns, which is sufficient to obtain enough intensity for single shot acquisition. The optical aberrations such as distortion produced by the stereoscopic imaging system are corrected by Davis software [12] after the calibration procedure described in the manual [13]. The inhomogeneity of the laser sheet is measured by Rayleigh scattering and corrected by intensity normalization.

The observation of the flow pattern with plasma off is performed by PLIF using acetone as a tracer. As described in [14], acetone fluorescence is a suitable tracer to image turbulent flows. During the measurements, the feed gas is bubbled through acetone into the plasma device. The acetone molecules are excited by the laser beam at 283.5 nm, and the fluorescence from 350 to 800 nm is collected by an intensified CCD camera and recorded. Observing the flow pattern with plasma-on requires the use of a different tracer, since acetone would be destroyed by the reactive species in the plasma. In the past, hydroxyl fluorescence was already used in combustion with good success on turbulence studies [15]. Moreover, one report stated that the hydroxyl molecule lifetime is 1 ms to a few milliseconds at atmospheric conditions [16, 17]. The hydroxyl radical is produced by the plasma itself from water impurities within the feed gas [8], meaning that the plasma generates the tracer itself and no external species need to be admixed for the flow measurements. Recently, hydroxyl molecule densities on-axis were measured by UV absorption on the same discharge [18]. The results show that the density remains constant up to a 7 mm distance from the nozzle. It can thus be assumed that the hydroxyl density does not decay significantly along the first 10 mm from the nozzle [18]. For these reasons, the hydroxyl radical, for the present studies, can be used as a fluorescent tracer.

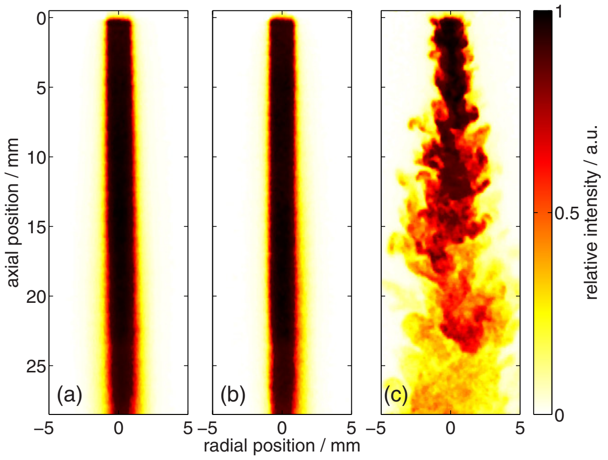

Figure 1. Space resolved single shot fluorescence signal of acetone for different argon gas flow rates of (a) 0.5 slm/Re= 465, (b)1.0 slm/Re= 930 and (c) 3.0 slm/Re= 2790. The jet nozzle is located at an axial distance of zero. The plasma was switched off.

3. LIF on acetone—plasma off measurements

Figure 1 shows the fluorescence of acetone for three different feed gas flow rates. As can be seen, at both 0.5 and 1 standard liter per minute (slm) the flow is laminar, while at 3 slm the flow is turbulent. The indicated Reynolds numbers $Re = 2r_0 v_{\mathrm{av}}/\nu$ are defined via the capillary radius r_0 and the kinematic viscosity ν. The critical Reynolds number (Re) for the transition from the laminar to turbulent regime in pipe flows is $Re_{\mathrm{C}} = 2300$, which is consistent with the observed flow regimes.

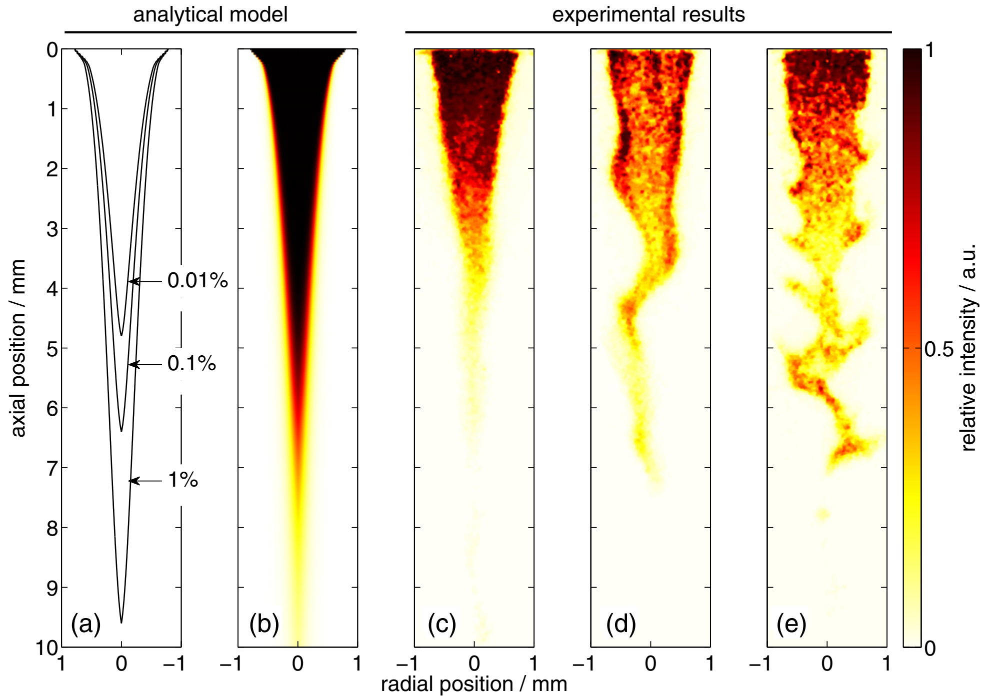

Figure 2. Analytical estimation of the ambient species density (*a*) and the resulting analytical OH emission pattern (*b*). Space resolved fluorescence signal of hydroxyl for different argon gas flow rates of (*c*) 0.5 slm, (*d*) 1.0 slm and (*e*) 3.0 slm. The jet nozzle is located at an axial distance of zero. The plasma was switched on. Single shot acquisition.

4. OH fluorescence and quenching by ambient air—plasma on measurements

The radiative lifetime of the OH(A, X)(1,0) is known to be around $\tau = A^{-1} = 748$ ns, where A is the Einstein coefficient for spontaneous emission. The emission is strongly quenched by atmospheric species [18]: the combined quenching rate (Q) and vibrational energy transfer (VET) coefficient of OH(A, X)(1,0) by argon ($0.27 \times 10^{-11}\,\mathrm{cm^3\,s^{-1}}$ [19]) is two orders of magnitude lower than for nitrogen ($k_Q^{\mathrm{N_2}} = 23.3 \times 10^{-11}\,\mathrm{cm^3\,s^{-1}}$ [20]), oxygen ($k_Q^{\mathrm{O_2}} = 20.6 \times 10^{-11}\,\mathrm{cm^3\,s^{-1}}$ [20]) and water ($k_Q^{\mathrm{H_2O}} = 66 \times 10^{-11}\,\mathrm{cm^3\,s^{-1}}$ [20]). Despite that, the quenching rate of OH fluorescence by water is in the same order of magnitude as dry air, and ambient humidity has a negligible effect on the OH fluorescence quenching due to a much lower density compared to air. In consequence, OH(A, X)(1,0) has a longer lifetime when it is mixed with argon than in presence of air. The OH originates dominantly from the dissociation of water impurities in the feed gas. Even at what is considered to be dry feed gas conditions, the quantity of water molecules lies in the order of some 10 ppm. When the gas leaves the jet, the OH concentration is distributed relatively homogeneously along the diameter of the nozzle (see figure 2(*c*)). Similar observations have been reported earlier. Here the main hydroxyl production is localized near the powered electrode in case of water impurities in the feed gas [21]. Additionally, the hydroxyl density remains presumably constant until several mm distance [18]. The spatial distribution can be expected to resemble the acetone distribution as shown above (see figure 1). From these as well as the quencher considerations, it can be safely assumed that the LIF signal reveals rather the influence of the quenching by the ambient species than the ground state OH molecule distribution. The measured data therefore reflects the argon flow pattern and the argon air boundary shape, as will be described in the following.

The diffusion of ambient species into the effluent of the plasma jet can be estimated by solving the convection diffusion equation

$$v(r)\partial_z n_A + D\Delta_r n_A = 0$$

with the boundary condition $n_A = \theta(r - r0)n_A^0$ for the ambient species density, where $\theta(x)$ is the Heaviside step function $\theta(x) = 0$ for $x < 0$, $\theta(x) = 1$ for $x \geqslant 0$. Here, D is the diffusion coefficient and $v(r)$ a velocity field with a radial dependence and Δ_r the radial part of the Laplace operator. The solution in the case of a constant velocity profile is given in [22] and can be evaluated using an infinite series. For a laminar jet flow, the velocity field in the near field of the jet can be approximated by a Poiseuille flow profile$v(r) = 2v_{\mathrm{av}}(1 - r^2/r_0^2)$. In order to account for this flow profile, non-dispersive path mapping [23] can be applied, mapping the constant velocity solution according to the flow field. The contour lines of the resulting ambient air density n_A/n_A^0 for an average velocity of $v_{\mathrm{av}} = 4.1\,\mathrm{m\,s^{-1}}$ and diffusion coefficient $D = 0.2\,\mathrm{cm^2\,s^{-1}}$ are shown in figure 2(*a*). Assuming a constant OH-density in the jet's effluent, the fluorescence intensity of OH(A, X)(1,0) can be estimated to be proportional to

$$I_{\mathrm{LIF}} \sim A/(A + n_{\mathrm{O_2}}k_Q^{\mathrm{O_2}} + n_{\mathrm{N_2}}k_Q^{\mathrm{N_2}} + n_{\mathrm{H_2O}}k_Q^{\mathrm{H_2O}})$$

as depicted in figure 2(*b*). In figures 2(*c*)–(*e*), the single shot LIF signal at flow rates of 0.5, 1 and 1.5 slm are displayed. The signal is a pure LIF signal, as spontaneous emission from excited hydroxyl OH(A, X)(1,0) is negligible. The analytically obtained triangular emission pattern (figure 2(*b*)) agrees very well with the experimentally observed OH emission at a gas flux of 0.5 slm (figure 2(*c*)). A sharp edge in the emission pattern occurs at an ambient air density of approximately 0.01–1%. This shows that due to the strong hydroxyl fluorescence quenching by air, the contour of the argon–air boundary can be determined and reflects the relative space-resolved argon density. The plasma does not change the flow regime at this flow rate.

For a flow rate of 1 slm, the occurrence of Kelvin–Helmholtz (KH) instabilities is observed, leading to a breaking of the laminar jet downstream. KH instabilities are likely to appear at the mixing layer of two fluids with different densities and/or in a shear flow [24]. Both mechanisms may be triggered when heating of the gas by the plasma occurs: its density is decreased, while its expansion leads to an increased shear.

Electro hydrodynamic forces can also trigger flow regime transitions. In [25] it is observed that the flow regime of a helium jet is significantly affected by the plasma while the temperature remains at around room temperature. It is noted that helium jets may be affected more strongly by equal electro hydrodynamic forces, as their momentum is ten times less compared to argon jets at identical flow conditions. It was recently observed that the air mixing in an argon plasma jet similar to the one used in the present study is significantly increased when the plasma is turned on, which agrees with our findings [26]. Their gas temperature is around 480 K. They also attribute this effect to the occurrence of KH instabilities and/or electro hydrodynamic forces.

At 3 slm, the flux seems to remain fully turbulent as in the plasma-off case.

5. Turbulent flow and streamer propagation

The observation of the turbulent behavior of the effluent flow is possible only if the acquisition time is much faster than the turbulence time scale. At 200 ns exposure time, the flow dynamics is static, but the discharge propagation is fast enough to grow and develop itself. Therefore looking at the effluent turbulence pattern as well as the streamer path within the same single time shot leads to fundamental information about the discharge propagation. Figure 3 shows a superimposed image of the streamer and the hydroxyl fluorescence. The hydroxyl fluorescence resembles the argon flow pattern. Both are following the same path and—especially at greater distances to the nozzle, where the argon abundance has the same dimension as the streamer thickness—the patterns are identical. On figure 3(*b*) and (*c*), which corresponds to 1 slm and 3 slm flow rates respectively, the flow patterns are not laminar and result in density gradients of argon which form a non-rectilinear argon channel. Also the streamer propagation does not follow a straight path. For the 3 slm case, it is clear that the turbulent flow has an impact on the streamer morphology (see figure 1(*c*)). This argon channel is about 2 mm in size at the nozzle and thins down as it propagates along the jet-axis. The experimental results show that the streamer propagates into the argon channel from the wider side and ends its propagation within the very thin argon channel surrounded by air impurities from diffusion, at the space where the argon density remains the highest. This means that the streamer is always bound by argon abundance, as shown in figure 3. In the case of 0.5 slm (figure 3(*a*)), the argon flow is laminar, inducing a rectilinear argon channel where the streamer propagates linearly. The argon flow is only clearly visible along the first 5 mm because of the induced fluorescence, which is quenched by the diffusion of ambient species as described previously. Moreover, we observe that the streamer position is well aligned on the axis of a right circular cone resulting from the gradient of the air diffusion into the argon channel. It is especially true towards greater distances from the nozzle. These observations are in perfect agreement with the fact that the streamer propagation follows the highest argon density which obviously is located on the axis of the channel. However, those measurements have been made over a 200 ns gate which means that the flow dynamics remains static with respect to the streamer head propagation. In order to confirm the results observed from single shot acquisitions, successive acquisitions of streamer propagations are recorded with the same gating time with an interval of 100 ms between two shots. At this acquisition frequency, the flow dynamics has time to develop from one shot to the other. Thus, it is ensured that between two consecutive acquisitions, the flow pattern must differ from one to the other in the case of turbulence or non-stationary flow.

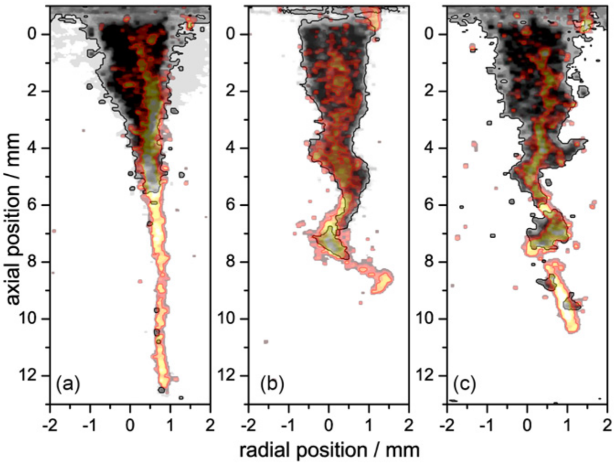

Figure 3. Overlay of the spatial OH fluorescence signal and of the spatial plasma emission (visible and near-infrared) for different argon gas flow rates of (*a*) 0.5 slm, (*b*) 1.0 slm and (*c*) 3.0 slm. Both signals were obtained simultaneously on the same detector.

Accumulation of 50 streamers is recorded for 0.5 slm and 3 slm flow rates, which correspond to a laminar and a turbulent flow, respectively. The results are presented in figure 4. In the turbulent case at 3 slm, the streamers' spatial distribution is spread over a wider area compared to the laminar case at 0.5 slm. This observation is even more pronounced after a 6 mm distance from the nozzle, where the structure

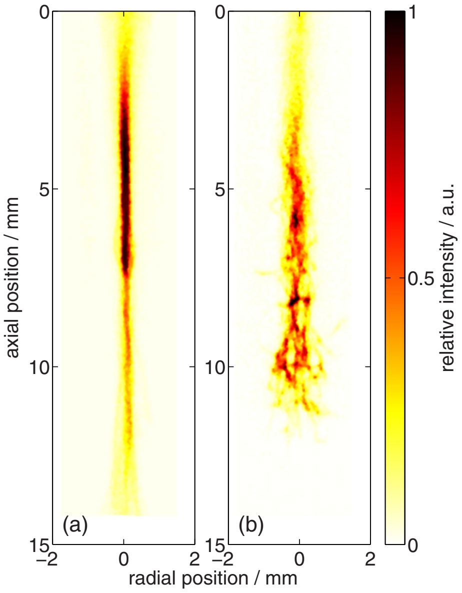

Figure 4. Spatial streamer distribution in the jet effluent for an argon gas flow rate of (*a*) 0.5 slm and (*b*) 3.0 slm. The number of accumulations was 50. (The slight vertical tilt is due to the alignment of the plasma jet.)

of the turbulence is developing, as shown in figure 2(*c*). For the laminar case, (figure 4(*a*)), the position of the streamers remains constant. This is in agreement with the laminar flow pattern measured for the same conditions and presented in figure 2(*a*) . It thus becomes evident that the atmospheric streamers are bound by argon and propagate through this argon channel. A previous study on streamer propagation in argon flow surrounded by air has been published [27]. The authors report that the reason for the propagation of a guided streamer in argon in the ambient air is due to the interface between these two gases. They observe the brightest emission on the edge on the plasma effluent and identify it as an emission from the second positive system of nitrogen, $N_2(C)$, mainly resulting from the efficient energy transfer of the near-resonant transition between the argon metastables of the $(^3P_{0,2})$ states and $N_2(X)$ to produce $N_2(C)$ [28]. In this work, N2(C) emission position differs from the referred study and is located in the center of the effluent. Moreover, the highest emission intensity was detected in the range from 4 mm up to 7 mm from the nozzle. This is in excellent agreement with figure 2(*c*)), where one sees that OH quenching by ambient molecules reaches the on-axis. Therefore it can be assumed that metastables of argon are, in the present case, located within the argon channel where the streamer develops. One reliable reason for the difference observed to [27] is attributed to the presence of a grounded ring electrode in the plasma source which must induce a different electric field and thus different ionization mechanisms. Due to the high frequency in the present case, streamer events will benefit from previous ionization and excitation phenomena. The memory effect of metastables and ions contributes largely to the development of the discharge within the argon dominating channel. This is also valid for the turbulent cases as the vortexes remain constant on the time scale of streamers. A simulation of discharge development in the case of a pure helium laminar flow surrounded by air *without diffusion* explains that so-called streamer bullet propagation is more favourable within the helium tube than in air because of the ionization coefficient differences of each gas [29].

The similarity in streamer path and gas flow path was also found by [30] in pulsed atmospheric pressure plasma streams operated in helium and neon. Interestingly, they found clear evidence that under their experimental conditions, the plasma determines the gas channel behavior and not, as commonly thought, vice versa [25, 30, 31]. Since the mass density of argon is ten times higher than for helium, this plasma-induced gas channel forming is not directly transferable to the argon plasma jet investigated in this work. Hence, for the laminar-to-turbulent transition in the 1.0 slm case when the plasma is switched on, it is not clear whether the streamers are responsible for inducing the turbulence of the argon flow or whether the argon flow becomes turbulent itself by pure fluid dynamics. Experiments with the focus on this effect need to be performed in future. The studies presented in the present work clearly show that the path of highest argon density, lowest air impurity density and streamer propagation are identical.

6. Conclusion

In this study, it was shown by means of PLIF on an atmospheric pressure argon plasma jet that in turbulent mode, the streamer path changes according to the flow pattern changes and the resulting changes in air abundance. Furthermore, with known OH quenching coefficients from a comparison of analytical diffusion calculation and LIF measurements, the air impurity boundary can be determined. Comparing the plasma-on and plasma-off case, it was shown that in the laminar case, the development of KH instabilities is promoted, while in the turbulent flow, the flow patterns remain comparable. Most importantly, it was shown that the streamer pathway is defined by the ambient air diffusing into the effluent. From a convection diffusion model, a steep increase of ambient air particle density in radial direction was revealed. This gradient forms a boundary which leads to the observed streamer enclosure within the argon channel.

Acknowledgments

Discussions with Dr E Robert and Professor J-M Pouvesle in the frame of collaborative project between Leibniz Institute for Plasma Science and Technology INP Greifswald e.V. and Groupe de Recherches sur l'Energétique des Milieux Ionisés (GREMI) are gratefully acknowledged. The authors gratefully acknowledge the funding by the Federal German Ministry of Education and Research (BMBF, grant number 03Z2DN12).

References

[1] Laroussi M, Hynes W, Akan T, Xinpei L and Tendero C 2008 The plasma pencil: a source of hypersonic cold plasma bullets for biomedical applications *IEEE Trans. Plasma Sci.* **36** 1298–9

[2] Teschke M, Kedzierski J, Finantu-Dinu E G, Korzec D and Engemann J 2005 High-speed photographs of a dielectric barrier atmospheric pressure plasma jet *IEEE Trans. Plasma Sci.* **33** 310–1

[3] Robert E, Sarron V, Ries D, Dozias S, Vandamme M and Pouvesle J M 2012 Characterization of pulsed atmospheric-pressure plasma streams (PAPS) generated by a plasma gun *Plasma Sources Sci. Technol.* **21** 034017

[4] Xiong Z M and Kushner M J 2012 Atmospheric pressure ionization waves propagating through a flexible high aspect ratio capillary channel and impinging upon a target *Plasma Sources Sci. Technol.* **21** 034001

[5] Niemeyer L 2001 *Wiley Encyclopedia of Electrical and Electronics Engineering* (New York: Wiley)

[6] Weltmann K D, Kindel E, Brandenburg R, Meyer C, Bussiahn R, Wilke C and von Woedtke T 2009 Atmospheric pressure plasma jet for medical therapy: plasma parameters and risk estimation *Contrib. Plasma Phys.* **49** 631–40

[7] Reuter S, Winter J, Iseni S, Peters S, Schmidt-Bleker A, Dünnbier M, Schäfer J, Foest R and Weltmann K-D 2012 Detection of ozone in a MHz argon plasma bullet jet *Plasma Sources Sci. Technol.* **21** 034015

[8] Winter J, Wende K, Masur K, Iseni S, Dünnbier M, Hammer M, Tresp H, Weltmann K-D and Reuter S 2013 Feed gas humidity: a vital parameter affecting a cold atmospheric-pressure plasma jet and plasma-treated human skin cells *J. Phys. D: Appl. Phys.* **46** 295401

[9] Verreycken T, van der Horst R M, Sadeghi N and Bruggeman P J 2013 Absolute calibration of OH density in a nanosecond pulsed plasma filament in atmospheric pressure He–H_2O: comparison of independent calibration methods *J. Phys. D: Appl. Phys.* **46** 464004

[10] Verreycken T, Mensink R, van der Horst R, Sadeghi N and Bruggeman P J 2013 Absolute OH density measurements in the effluent of a cold atmospheric-pressure Ar–H_2O RF plasma jet in air *Plasma Sources Sci. Technol.* **22** 055014

[11] Reuter S, Tresp H, Wende K, Hammer M U, Winter J, Masur K, Schmidt-Bleker A and Weltmann K D 2012 From RONS to ROS: tailoring plasma jet treatment of skin cells *IEEE Trans. Plasma Sci.* **40** 2986–93

[12] LaVision GmbH, DaVis, 8.1.1, 2012, www.lavision.de

[13] LaVision GmbH 2011 *1004067 Image Doubler D80* (Göttingen: LaVision GmbH) p 46

[14] Lozano A, Yip B and Hanson R K 1992 Acetone: a tracer for concentration measurements in gaseous flows by planar laser-induced fluorescence *Exp. Fluids* **13** 369–76

[15] Tanahashi M, Murakami S, Choi G-M, Fukuchi Y and Miyauchi T 2005 Simultaneous CH–OH PLIF and stereoscopic PIV measurements of turbulent premixed flames *Proc. Combust. Inst.* **30** 1665–72

[16] Kanazawa S, Tanaka H, Kajiwara A, Ohkubo T, Nomoto Y, Kocik M, Mizeraczyk J and Chang J S 2007 LIF imaging of OH radicals in DC positive streamer coronas *Thin Solid Films* **515** 4266–71

[17] Pei X, Lu Y, Wu S, Xiong Q and Lu X 2013 A study on the temporally and spatially resolved OH radical distribution of a room-temperature atmospheric-pressure plasma jet by laser-induced fluorescence imaging *Plasma Sources Sci. Technol.* **22** 025023

[18] Verreycken T, Mensink R, Horst R v d, Sadeghi N and Bruggeman P J 2013 Absolute OH density measurements in the effluent of a cold atmospheric-pressure Ar–H2O RF plasma jet in air *Plasma Sources Sci. Technol.* **22** 055014

[19] Dilecce G and De Benedictis S 2011 Laser diagnostics of high-pressure discharges: laser induced fluorescence detection of OH in He/Ar–H_2O dielectric barrier discharges *Plasma Phys. Control. Fusion* **53** 124006

[20] Williams L R and Crosley D R 1996 Collisional vibrational energy transfer of OH ($A\,^2\Sigma^+$, $v' = 1$) *J. Chem. Phys.* **104** 6507

[21] Yonemori S, Nakagawa Y, Ono R and Oda T 2012 Measurement of OH density and air–helium mixture ratio in an atmospheric-pressure helium plasma jet *J. Phys. D: Appl. Phys.* **45** 225202

[22] Saìnchez A L, Vera M and Liñán A 2006 Exact solutions for transient mixing of two gases of different densities *Phys. Fluids* **18** 078102

[23] Schmidt-Bleker A, Reuter S and Weltmann K-D 2013 Non-dispersive path mapping approximation for the analysis of ambient species diffusion in the near-field, near-axis region of laminar jets in preparation, for details see www.plasmatis.de/NDPM.html

[24] Kull H J 1991 Theory of the Rayleigh–Taylor instability *Phys. Rep.* **206** 197–325

[25] Sarron V, Robert E, Fontane J, Darny T, Riès D, Dozias S, Joly L and Pouvesle J M 2013 Plasma plume length characterization *21st Int. Symp. on Plasma Chemistry (ISPC 21) (Cairns Convention Centre, Australia)*

[26] van Gessel B, Brandenburg R and Bruggeman P 2013 Electron properties and air mixing in radio frequency driven argon plasma jets at atmospheric pressure *Appl. Phys. Lett.* **103** 064103

[27] Hofmann S, Sobota A and Bruggeman P 2012 Transitions between and control of guided and branching streamers in dc nanosecond pulsed excited plasma jets *IEEE Trans. Plasma Sci.* **40** 2888–99

[28] Nguyen T D and Sadeghi N 1983 Rotational and vibrational distributions of $N_2(C\ 3\Pi u)$ excited by state-selected Ar(3P2) and Ar(3P0) metastable atoms *Chem. Phys.* **79** 41–55

[29] Boeuf J P, Yang L L and Pitchford L C 2013 Dynamics of a guided streamer (‘plasma bullet’) in a helium jet in air at atmospheric pressure *J. Phys. D: Appl. Phys.* **46** 015201

[30] Robert E, Sarron V, Darny T, Riès D, Dozias S, Fontane J, Joly L and Pouvesle J M 2013 Rare gas flow structuration in plasma jet experiments *Plasma Sources Sci. Technol.* submitted

[31] Pouvesle J-M, Sarron V, Robert E, Fontane J, Darny T, Ries D, Dozias S and Joly L 2013 Plasma jets for biomedical applications: PAPS control of the rare gas jets *66th Gaseous Electronics Conf. (Princeton, NJ)* vol 58 (American Physical Society) http://meetings.aps.org/link/BAPS.2013.GEC.MR1.61

5.4 Article IV

Nitric Oxide density distributions in the effluent of an RF argon APPJ: effect of gas flow rate and substrate

doi:10.1088/1367-2630/16/12/123011

New Journal of Physics
The open access journal at the forefront of physics

Deutsche Physikalische Gesellschaft DPG | IOP Institute of Physics

Nitric oxide density distributions in the effluent of an RF argon APPJ: effect of gas flow rate and substrate

S Iseni[1,2], S Zhang[3], A F H van Gessel[3], S Hofmann[3], B T J van Ham[3], S Reuter[1,2], K-D Weltmann[2] and P J Bruggeman[3,4]

[1] Center for Innovation Competence plasmatis, 17489 Greifswald, Germany
[2] Leibniz Institute for Plasma Science and Technology (INP), 17489 Greifswald, Germany
[3] Eindhoven University of Technology, Department of Applied Physics, PO Box 513, 5600 MB, Eindhoven, The Netherlands
[4] Department of Mechanical Engineering, University of Minnesota, 111 Church Street SE, Minneapolis, MN 55455, USA
E-mail: pbruggem@umn.edu

Received 27 July 2014, revised 4 October 2014
Accepted for publication 30 October 2014
Published 2 December 2014

New Journal of Physics **16** (2014) 123011
doi:10.1088/1367-2630/16/12/123011

Abstract

The effluent of an RF argon atmospheric pressure plasma jet, the so-called kinpen, is investigated with focus on the nitric-oxide (NO) distribution for laminar and turbulent flow regimes. An additional dry air gas curtain is applied around the plasma effluent to prevent interaction with the ambient humid air. By means of laser-induced fluorescence (LIF) the absolute spatially resolved NO density is measured as well as the rotational temperature and the air concentration. While in the laminar case, the transport of NO is attributed to thermal diffusion; in the turbulent case, turbulent mixing is responsible for air diffusion. Additionally, measurements with a molecular beam mass-spectrometer (MBMS) absolutely calibrated for NO are performed and compared with the LIF measurements. Discrepancies are explained by the contribution of the NO_2 and N_2O to the MBMS NO signal. Finally, the effect of a conductive substrate in front of the plasma jet on the spatial distribution of NO and air diffusion is also investigated.

1367-2630/14/123011+22$33.00

Keywords: atmospheric pressure plasma jets, nitric oxide, laser induced fluorescence, molecular beam mass spectrometry, spectroscopy, plasma medicine

1. Introduction

Due to the various advantages of atmospheric pressure plasmas compared to low pressure plasmas, a strong interest in these discharges is growing which opens up new fields in plasma technology [1, 2]. One of these fields is known as plasma medicine which is aiming to combine room temperature atmospheric pressure plasmas with living matter and clinical medicine [3, 4]. Different applications are currently under investigation since plasma appears to be a promising tool for decontamination and an alternative to the usual chemical approaches to the inactivation of pathogens [5–7]. Additionally, it has been observed that plasma treatments may lead to improved wound healing e.g. in chronic wound treatments [8–10]. Various plasma agents, such as (V)UV radiation, electric field, charges and reactive oxygen and nitrogen species (RONS), can influence cells and tissues. Especially reactive species such as hydrogen peroxide (H_2O_2) or nitric-oxide (NO) are known to induce effects on cells and tissues [11–14]. While NO is toxic at higher concentration ($2.5 \times 10^{13}\,\mathrm{cm}^{-3}$) it triggers cell signaling and biological mechanisms at low concentrations as reported in the monograph of Lancaster and references therein [15]. The generation of NO by atmospheric pressure plasmas and its diagnostics have been investigated for different kinds of plasma devices, operating with helium and argon with an admixture of air [16–21].

In this work, the spatial distribution of NO from a radio-frequency (RF) argon atmospheric pressure plasma jet is investigated. The present work builds on the previous research of van Gessel *et al* [16] and aims to study the influence on the NO density profiles within the effluent and near field of the plasma jet with different flow patterns. Recently, it has been shown by Iseni *et al* [22] and Robert *et al* [23] that in such plasma jet devices, discharge propagation and gas flow pattern are strongly correlated. Consequently, an effect of the reactive species generation is anticipated. In this work, both laminar and turbulent flow regimes are investigated. Moreover, the plasma jet is equipped with an additional cap allowing for the supply of an external gas as a curtain around the plasma jet effluent [24]. The influence of this gas curtain on the distribution of NO is presented. The gas temperature of the plasma effluent is measured by LIF [17] to interpret the results. The influence of a metal substrate on the NO density distribution which also has an effect on the flow pattern in the effluent will be presented for varying conditions. The use of a substrate close to the region of interest requires us to take into consideration technical issues such as optical vignetting. Additionally, the influence of the flow regime and the air entrainment into the effluent is deduced from the decay time of the fluorescence which is determined by the collisional quenching of the NO(A) state by Ar and air.

Two different techniques used in the present work, laser-induced fluorescence (LIF) and molecular beam mass spectrometer (MBMS), have been used in previous publications for the determination of absolute NO densities [25]. Nevertheless, the comparison of both diagnostics was performed at different orientation of the plasma jet which led to uncertainties on the origin of the discrepancies found between the two methods. The present work re-investigates the NO densities at comparable conditions and additional observations and conclusions are presented. The previous work of Iseni *et al* [26] dealing with the absolute density of nitric dioxide (NO_2)

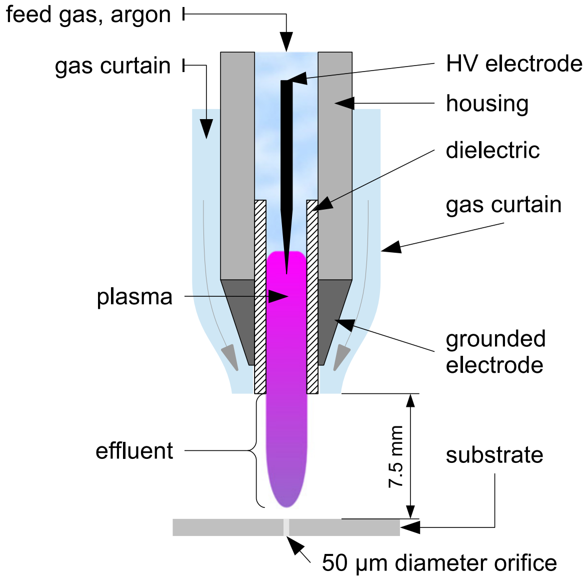

Figure 1. Schematic of the plasma jet (kinpen) and the implementation of the gas curtain around the effluent [3, 24]. A metal substrate resembling the MBMS sampling plate with a 50 μm diameter orifice is positioned at a distance of 7.5 mm from the jet nozzle.

as well as literature data are used to discuss the proposed non-selectivity of the mass spectrometer measurement in more detail.

2. Experimental setup

2.1. Plasma source

The cold non-equilibrium atmospheric-pressure argon discharge investigated in this work is the commercially available device kinpen (neoplas GmbH, Germany) [3]. It is driven with a 1 MHz radio frequency (RF) electric excitation. Figure 1 illustrates the basic geometrical and electrical configuration which consists of a high-voltage (HV) needle electrode centered within a 1.6 mm dielectric capillary. An RF continuous voltage with an amplitude between 2–6 kV is applied to the needle. The jet is driven at an RF power between 0.9–2.2 W and operates with a flow rate between 0.5–3.0 slm dry argon. The typical argon luminous effluent length is between 10–15 mm and depends on the input power and impurities such as air or water but is independent of the flow rate. Admixtures of molecular oxygen and nitrogen within the feed gas are possible up to 2.0%. However, the molecular admixtures significantly reduce the effluent length from about 15 mm to a few millimeters. In this work, 1.0% of dry air is admixed to the argon in order to prevent any fluctuation with the nitric oxide production due to potentially varying air impurities of the argon feed gas.

In order to control the interaction of the effluent with the surrounding atmosphere, an external gas flow is applied through a concentric cylindrical channel of the jet nozzle. More information can be found e.g. in [24]. This gas shroud can be fed with different gases and prevents the diffusion of ambient humid air into the effluent for particular flow conditions [27]. Consequently, the gas curtain can enhance the reproducibility and the stability of the treating

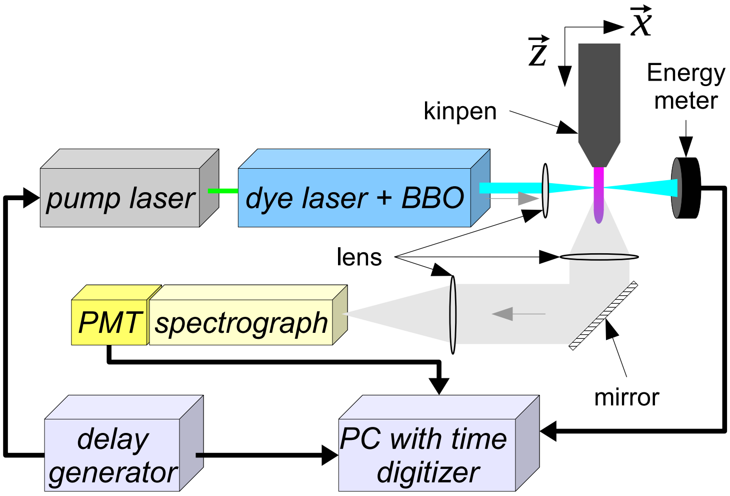

Figure 2. Experimental setup of the LIF diagnostic applied to the kinpen.

conditions by excluding any variation of surrounding humid air which can vary from lab to lab around the world. Furthermore, a choice of gas used for the curtain allows influencing of the effluent chemistry and may be an additional tunable parameter to adjust plasma treatments [24]. During all the experiments, the plasma device is operated vertically, with the gas flow in the direction of the gravitational field.

2.2. Laser-induced fluorescence of NO

LIF of NO is a standard technique in the combustion community [28]. LIF has been applied to investigate plasma discharges such as the process mechanism used to remove pollutants with positive streamers [29]. Thanks to fundamental studies on the NO energy structure (initiated in the combustion community) the spectroscopic constants are well known [30]. The experimental setup used in this work (see figure 2) is identical to the one introduced by van Gessel *et al* [17]. The most important aspects of the system are described and the reader is referred for more details to the latter reference. The excitation of the rotational transition NO(A-X)(0–0) is obtained by using a frequency doubled tunable dye laser system (Cobra, Sirah Laser und Plasmatechnik GmbH, Germany) around 226.2 nm with Coumarin 2 as a dye. The latter is pumped at 355 nm by a high repetition rate Nd:YAG laser operating at 1.0 kHz (IS6III-E, EdgeWave GmbH, Germany). The typical pulse energy is measured to range between 2.5–3.5 μJ with pulse-to-pulse fluctuations of about 1.0 μJ and a pulse duration of 6 ns FWHM. The energy variation is corrected for in post-processing with regards to the synchronized data from the detector and the laser energy meter. The laser beam is focused with a lens to a 200 μm diameter spot aligned with the radial center of the jet nozzle. Focusing the beam maintains sufficient spatial resolution compared to the 1.6 mm diameter of the capillary. The fluorescence intensity was checked to be proportional to the laser pulse energy and confirms that no saturation of the transition occurs [17]. The fluorescence is collected and imaged on the entrance slit of a 0.2 m monochromator (model 234/302, McPherson Inc., USA) by two 200 mm quartz lenses. A spectral resolution of 0.2 nm FWHM is reached with a 1200 groove mm^{-1}grating. With a nominal dispersion of $4.0\,\text{nm}\cdot\text{mm}^{-1}$, the bandwidth is set at 12.0 nm centered at 247.0 nm which allows a recording of the full rotational band NO(A-X)(0–2). The signal at the output of the monochromator is detected by a photomultiplier (model R8486, Hamamatsu, Japan) operating in photon-counting mode and read out via a 1.0 GHz sampling rate digitizer card connected to a computer.

The laser linewidth allows us to resolve a single rotational transition, thus the total NO(X) density needs to be obtained by the knowledge of the Boltzmann factor (f_B) [17]. Hence, correcting for the temperature is important and different approaches are suitable, such as e.g. resorting to Rayleigh scattering [16]. However, here the approach of van Gessel *et al* is followed to excite a small band of transitions of which the total fluorescence is quasi-independent of the temperature [16] in the investigated temperature range. Indeed, for temperatures included within the range from 300–600 K, which is the case in this work, integrating the fluorescence signal resulting from the excitation wavelength scan from 226.23–226.28 nm ($P_1(4)$, $P_1(5)$, $P_1(12)$, $Q_2(16)$, $Q_{12}(16)$andR$_2(11)$[5]) provides a temperature dependence of the fluorescence intensity below 3% . Hence, for each measurement, an excitation wavelength scan is performed from 226.225–226.280 nm with a scan speed of 0.42 pm $\cdot$ s^{-1}and the LIF signal results as the sum of the fluorescence intensity of the stated transitions.

Collisional quenching with other particles, such as argon and air, reduces significantly the fluorescence intensity; however, these fluorescence losses are taken into consideration according to the relation $\tau_{\mathrm{det}} = (A_{\mathrm{tot}} + Q)^{-1}$, with τ_{det} being the recorded decay time of the fluorescence, A_{tot} being the spontaneous emission coefficient of the whole vibrational band and Q the collisional quenching rate in the unit of s^{-1}.

To determine the ground state NO(X) density, a simplified two-level energy scheme of NO is considered and leads to the following rate equation,

$$\frac{\mathrm{d}n_{\mathrm{u}}}{\mathrm{d}t} = B_{\mathrm{lu}} I(t) n_{\mathrm{l}} - \left(A_{\mathrm{tot}} + Q\right) n_{\mathrm{u}}, \tag{1}$$

where the subscript u and l refer to the upper and lower energy levels of the molecule respectively, n_x (m^{-3}) is the population density of an energy level x, B_{lu} (m$^{-2}\cdot$J$^{-1}\cdot$s^{-1}) is the absorption coefficient from the lower to the upper state, $A_{\mathrm{tot}} = \sum_l A_{\mathrm{ul}} = \frac{1}{\tau_0}$ (s^{-1}) is the sum over all the transitions from the upper to the lower state. Stimulated emission from the upper to the lower state is neglected since the laser fluence is small and only a minor fraction of NO(X) state is excited. $I(t)$ (J $\cdot$ m^{-2}) is the laser intensity defined as,

$$I(t) = \frac{E_{\mathrm{I}} \Gamma}{a} i(t) \tag{2}$$

with E_{I} (J) being the energy of the pulse, Γ (s) being the overlap integral and a (m^2) the laser spot area. More information about the definition and the characterization of the overlap integral Γ can be found in [31] and references therein. $i(t)$ (s^{-1}) is the temporal shape of the laser pulse normalized to the area as $\int_{-\infty}^{+\infty} i(t)\mathrm{d}t = 1$. The relation between the integrated LIF signal S and the NO(X) density n_{gnd} can be deduced from equation (1):

$$S = n_{\mathrm{gnd}} C \frac{V}{a} E_{\mathrm{I}} \cdot \frac{A_{\mathrm{det}}}{A_{\mathrm{u}} + Q} \cdot B_{\mathrm{lu}} f_{\mathrm{B}} \tag{3}$$

where V (m^{-3}) is the sampled volume, C is a dimensionless factor characterizing the optical efficiency of the collection optics including the quantum efficiency of the detector, A_{det} (s^{-1}) is a sum of the Einstein coefficients over all allowed rotational transitions and f_{B} refers to the

---

[5] The transitions are denominated here with the Hund's case b.

Boltzmann factor. More details can be found in [17]. The absolute calibration of the laser induced fluorescence measurement is described in section 3.2.

2.3. Molecular beam mass spectrometer (MBMS)

The study of the NO production and distribution in the jet effluent by LIF is complemented with mass spectrometry. Here, a molecular beam mass spectrometer (EPIC/IDP Series 1000, Hiden Analytical Ltd, Warrington, UK) is used as previously introduced in [6, 25]. It consists of a quadrupole mass spectrometer (QMS) coupled to a home-made three stage pressure reduction system. The sampling orifice has a diameter of 50 μm. The reader is referred to [25] for a sketch of the sampling stage and all details. A cylinder of 80 mm diameter, 43 mm hight is mounted on the sampling plate and centered with the orifice. An exhaust ring is implemented in the bottom of this cup-like cylinder in order to prevent accumulation of argon and advantageously influence the partial pressure of air to not saturate the cup with argon, thus preventing artificial change of the plasma chemistry. The exhaust system is powered by a pump and a rotameter to adjust the exhaust rate (typically 30 slm). The three stage pressure reduction system is operated at 10^{-3} mbar, 10^{-6} mbar and 10^{-8} mbar respectively. A Bessel box is installed within the third chamber in front of the QMS to prevent UV and V-UV radiation from the plasma reaching the detector. In this work, the ionization source is tuned to generate electrons with a maximum energy peak at 70 eV. This is necessary to have a signal which is significantly larger compared to the detection limit. The high ionization energy causes higher energetic electron inducing dissociative ionization processes which will require additional efforts to analyze the data. Consequently, heavier molecules will be partially dissociated into lighter ones and thus reduce the number count at their original mass. These so-called cracking patterns are described and tabulated in the literature and are used to analyze data and correct for the species density [32]. For instance, molecules like N_xO_y will contribute significantly to the NO mass count with a known ratio. Unfortunately, threshold ionization potential measurement did not yield a signal above the detection limit for NO under the present experimental condition. During the calibration procedure [25] as well as the measurements, the plasma jet is positioned vertically, the flow oriented parallel to the gravitational force. With 1.0% of air admixed, the effluent length is shorter than with pure argon. The capillary tip is set accurately 7.5 mm away from the orifice in order to avoid attachment of the plasma with the metallic surface of the MBMS. The latter case will strongly influence the plasma which tends to a filamentary discharge which could interact with the orifice [33]. In the frame of this work, NO and O_3 densities are investigated for different radial positions of the plasma jet.

3. Measurement and calibration procedures

3.1. Rotational temperature of NO(X)

The determination of the gas temperature of atmospheric plasma discharges can pose a challenge since those plasmas are far from thermodynamic equilibrium. However, several interpretations and experimental approaches have led to accurate gas temperature estimations [34]. It is reported that the NO(A) rotational temperature leads to an overestimation of the gas temperature at elevated gas temperatures, $T_g > 1000$ K [35]. Similar issues are presented for N_2(C) in an argon mixture due to the near resonant excitation of N_2(C) by Ar metastable atoms

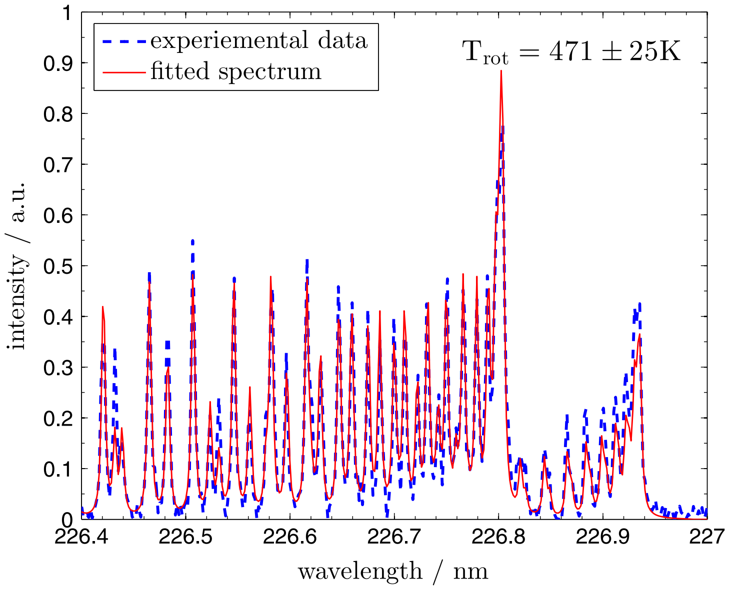

Figure 3. Experimental NO(A-X)(0–0) LIF excitation spectrum collected from the plasma effluent at 3.0 mm from the nozzle operating under laminar flow conditions (1.0 slm). The rotational temperature resulting from the fit is 471 ± 25 K.

Table 1. Comparison of different parameters for three fixed positions in the effluent and far field area for laminar and turbulent conditions. No gas curtain is used except for †.

	laminar *Re* = 930			turbulent *Re* = 2790		
ax. pos./mm	0	3	7	0	3	7
gas temp./K	521 ± 32	471 ± 25	447 ± 23	432 ± 28	418 ± 20	424 ± 37
gas temp.†/K	476 ± 24	448 ± 22	433 ± 31	—	—	—
Q / $10^7\,s^{-1}$	1.64	1.89	6.80	1.80	2.30	7.69
[NO]/$10^{19}\,m^{-3}$	30	20	7	19	5.9	1.9
[air]/$10^{23}\,m^{-3}$	6.1	7.2	27	6.4	8.0	56

[36]. To this end NO(X) rotational temperature by LIF is used to measure the gas temperature in the jet. Figure 3 illustrates an example of a rotational spectrum resulting from a wavelength scan from 226.4–227.0 nm. The fitting algorithm introduced by van Gessel *et al* [37] is used to fit the ro-vibrational spectrum. In practice, a high spectral resolution from the laser (typically 2.0 pm) is essential in order to decrease the uncertainties induced by the fit routine. Due to the time consuming nature of the measurement, measurements have only been performed o*n*-axis. The results are presented in the table 1 in section 4.1.2.

3.2. Absolute NO(X) density from LIF and vignetting correction

The absolute calibration of the NO fluorescence is performed as described by van Gessel *et al* [16]. Briefly, a mixture of argon and 10.0 ppm NO ($n_{calib.} = 2.45 \times 10^{20}\,m^{-3}$) flows through the 1.6 mm inner diameter capillary at a flow rate of 1.0 slm. The fluorescence is induced from the laser spot position located at the tip of the jet nozzle (axial position at 0.5 mm) and the central radial position where the density of NO is assumed to remain constant. At this position with a non-turbulent flow, dilution of the mixture due to surrounding air is negligible [22]. The

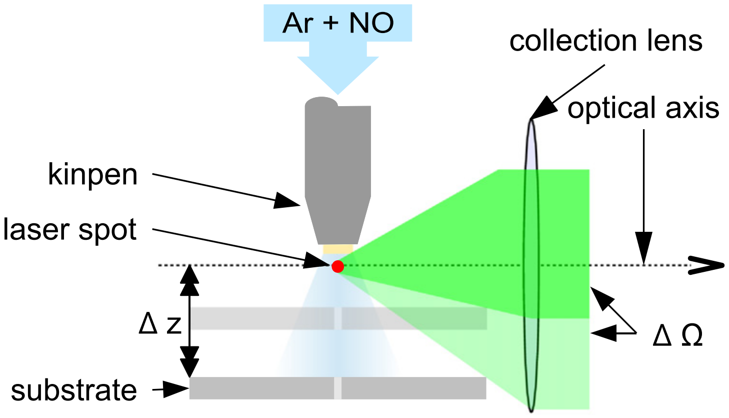

Figure 4. Scheme of the experimental method used to perform the absolute NO density calibration and the correction of the vignetting. The vertical position of the substrate, z, is set as a parameter for the vignetting correction.

absolute density of NO(X) can be expressed as follows,

$$n_{\mathrm{NO(X)}} = \frac{S}{E\tau} \cdot \left[\frac{n_{\mathrm{calib}}.E_{\mathrm{calib}}.\tau_{\mathrm{calib}}.}{S_{\mathrm{calib}}.} \right] \qquad (4)$$

where n_{x} is the density of the particle x (m^{-3}), S ($\mathrm{J} \cdot \mathrm{m}^{-2}$) refers to the time integrated LIF signal, E (J) is the laser pulse energy and τ (s) is the decay time of the fluorescence. However, the presence of a large substrate (compared to the effluent size) in our experiment induces additional complexity. The main one is *vignetting* and results in a variation of the collection solid angle close to the substrate. The latter masks a fraction of the photon flux coming from the sampled volume, which reaches the monochromator slit. As a consequence, the vignetting directly depends on the vertical position of the substrate. The substrate has a much larger diameter compared to the horizontal variation of the measurement thus the vignetting only depends on the axial portion in this case. Consequently, the translation ΔZ of the substrate compared to the jet nozzle induces a variation of the varying solid angle $\Delta\Omega$ (as illustrated in figure 4) which has to be characterized for each vertical position. By adding a known concentration of NO to the argon feed gas, it is possible to quantify the amount of fluorescence due to vignetting by the substrate. Figure 4 illustrates how the absolute calibration of the NO signal is performed including the vignetting artifact. The plasma jet is set vertically, with the tip of the capillary nozzle aligned 0.5 mm above the optical axis which is defined as the vertical origin. The laser beam is pointed to cross the optical axis perpendicularly and adjusted to the center of the capillary where the NO density remains constant. The substrate, mounted on a post with a vertical micrometer translation adjustment screw, is positioned in front of the jet nozzle. The fluorescence is then collected for different vertical positions of the substrate from 0.5–7.5 mm on the optical axis with an increment of 0.5 mm. Consequently, a relation between ΔZ and S (involving $\Delta\Omega$ and the geometry of the substrate) is, thus, experimentally determined and yields a correction factor of the vignetting plotted in figure 5. Equation (3) can be re-writen as,

$$n_{\mathrm{gnd}} = \zeta \cdot \frac{S \cdot a}{CVE_{\mathrm{I}}} \cdot \frac{A_{\mathrm{u}} + Q}{A_{\mathrm{det}}} \qquad (5)$$

with ζ the vignetting correction factor. From figure 5, it can be seen that the characterization of the vignetting corrects up to a factor 2 in the photon counts which would lead to a significant

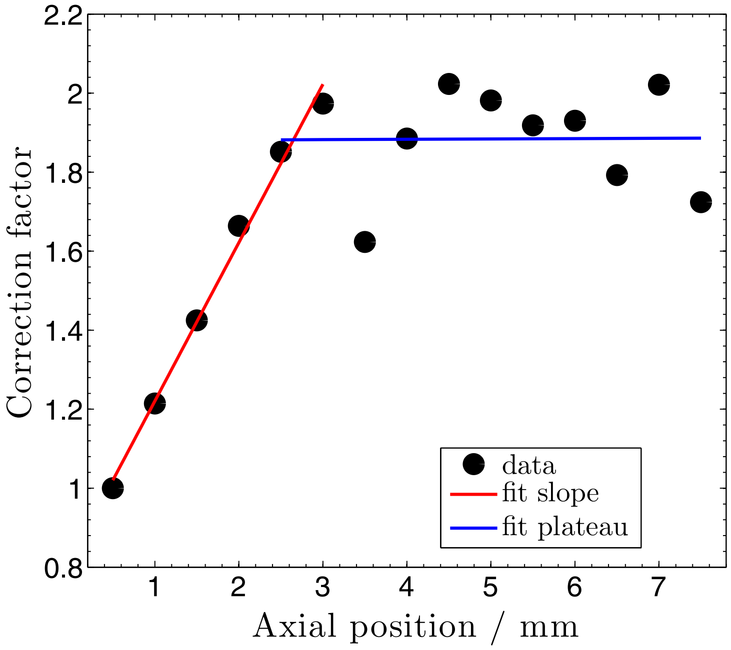

Figure 5. Map of the vignetting correction factor ζ for the investigated domain. The origin of the graph corresponds to the nozzle tip of the capillary and the position of the plate is 7.5 mm.

underestimation of the NO(X) density. The variation in the correction factor suggests an accuracy of about 25%. The reproducibility of the measurement has been determined to be 20%. Thus the total error on the vignetting measurements are estimated to be 45%.

3.3. Determination of air density in the effluent

Due to the dependence of the effective lifetime τ of NO(A) on the gas mixture due to quenching, it is possible to determine absolutely the air concentration diffusing into the effluent. From section 2.2, the detected decay time of the fluorescence signal can be defined as $\tau_{\mathrm{det}} = (A_{\mathrm{tot}} + Q)^{-1}$ with $Q = \sum_i k_{\mathrm{x}_i} n_{\mathrm{x}_i}$, n_{x} (m^{-3}) being the density of argon or air and k_{x} ($\mathrm{m}^3 \cdot \mathrm{s}^{-1}$) the rate coefficient of a reaction between NO(A) with a quencher x. Raiche *et al* report that the dependence of the NO(A) quenching rate coefficients of N_2 and O_2 are independent of the gas temperature between 300–750 K [38]. Moreover, Drake *et al* have published that Ar and NO quenching rate coefficients do not depend on the gas temperature in a range from 300–1750 K [39]. Additionally, the gas curtain may contain residual water vapor impurities. Consequently, the detected decay time, τ_{det}, can be expressed as,

$$\tau_{\mathrm{det}} = \frac{1}{A_{\mathrm{tot}} + \sum_i k_{\mathrm{x}_i} n_{\mathrm{x}_i}} = \frac{1}{A_{\mathrm{tot}} + k_{\mathrm{ar}} n_{\mathrm{ar}} + k_{\mathrm{air}} n_{\mathrm{air}} + k_{\mathrm{water}} n_{\mathrm{water}}}. \tag{6}$$

The calibration gas as described in section 3.2 allows us to determine the quenching rate of argon at room temperature. Indeed, $\tau_{\mathrm{calib}}^{-1} = A_{\mathrm{tot}} + k_{\mathrm{ar}} n_{\mathrm{ar}}$, hence the determination of $k_{\mathrm{ar}} = 3.5 \cdot 10^{-19}\ \mathrm{m}^3 \cdot \mathrm{s}^{-1}$at 300 K and atmospheric pressure which is in good agreement with the literature ($3.9 \times 10^{-19}\ \mathrm{m}^3 \cdot \mathrm{s}^{-1}$ [40], $2 \times 10^{-19}\ \mathrm{m}^3 \cdot \mathrm{s}$ [41]). Furthermore, it is found from previous studies that water has a quenching rate coefficient three times higher than air ($k_{\mathrm{air}} = 2.96 \cdot 10^{-16}\ \mathrm{m}^3 \cdot \mathrm{s}^{-1}$ [17], $k_{\mathrm{water}} = 8.97 \cdot 10^{-16}\ \mathrm{m}^3 \cdot \mathrm{s}^{-1}$ [41]) but as the water concentration will never exceed 2% of the air concentration, in a good approximation the quenching by water can be neglected. The air density can be calculated with the following equation,

$$n_{\mathrm{air}} = \frac{\tau_{\mathrm{calib}} - \tau_{\mathrm{det}}}{\tau_{\mathrm{calib}}\tau_{\mathrm{det}}k_{\mathrm{air}}}. \tag{7}$$

The dissociation degree of O_2 in the effluent should be considered for high dissociation degrees. Fricke *et al* reported on an absolute atomic oxygen density of $2.5 \times 10^{20}\,\mathrm{m}^{-3}$ for an admixture of 0.2% O_2 at 5 mm and 7 mm which corresponds to a dissociation degree of 0.25 % [42]. In order for O to be an important quencher, its quenching rate with NO(A) must be by a factor of a thousand higher than for air, which is highly unlikely. Therefore, the dissociation in the effluent has not taken influence into account for the fluorescence decay of NO(A).

3.4. MBMS calibration for nitric oxide and ozone

MBMS measurements also require an accurate calibration in order to reach absolute density determination. The absolute calibration of NO and O_3 is performed as presented in detail in [25]. Briefly, a known density of NO is applied at the entrance orifice of the MBMS similar to the conditions described for the LIF calibration. An identical procedure is realized for O_3 for which the molecules are generated via an ozone generator and the O_3 density is simultaneously measured by classical UV absorption. Concerning the accuracies, they have been determined to be in the order of 25 % including the reproducibility of the measurements. These are in agreement with the literature, e.g. Ellerweg *et al* reported an error of factor two on the data produced by their MBMS [43].

4. Results and discussions

The NO density profiles are presented as two dimensional color maps. The data is recorded with a sample step size of 250 μm and 500 μm in the radial (horizontal) and axial (vertical) direction respectively. The effect of the flow field, curtain flow, gas composition and the presence of a substrate are presented. In addition, MBMS data is compared with the LIF results.

4.1. Turbulent versus laminar flow

4.1.1. Spatial density distribution of NO. By increasing the feed gas flow rate a transition from a laminar to a turbulent flow regime in the effluent is induced. Earlier, Iseni *et al* reported that for this plasma jet geometry, the Reynolds number (*Re*) is 930 and 2790 for a feed gas flow rate of 1.0 slm and 3.0 slm respectively. The NO density distribution determined for the two different feed gas flow rates are mentioned above, with and without the presence of a gas curtain. The results are shown in figure 6. The corresponding gas temperatures are shown in table 1. The highest NO density is located at the tip of the nozzle. This is expected since most of the input energy is dissipated inside the dielectric capillary and it is thus anticipated that much of the NO is produced inside or close to the nozzle of the jet capillary. It could be that most of the NO is produced in a restricted area compared to the nozzle diameter (about 200 μm FWHM) and then diffuses into the effluent. The maximum NO density is not located on the axis of symmetry but is slightly shifted to one side by about 300 μm. This is not due to a misalignment of the visible plume to the laser beam, as the position of the maximum of NO density is found to

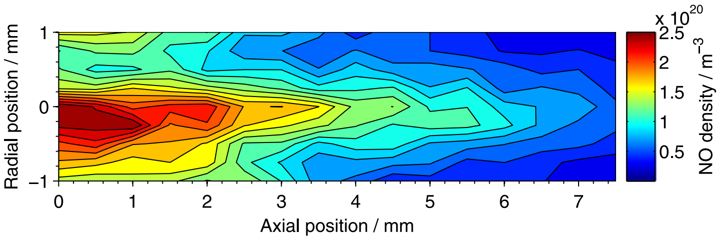

(a) Laminar flow, 1.0 slm argon + 1 % air, with gas curtain 1.6 slm

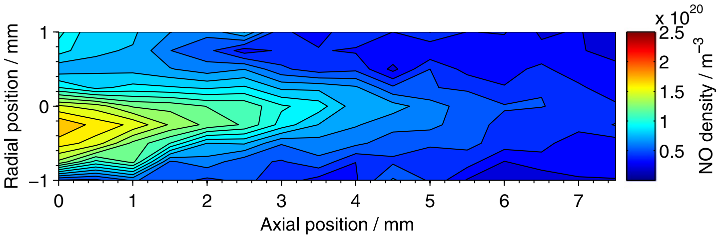

(b) Turbulent flow, 3.0 slm argon + 1 % air, no gas curtain.

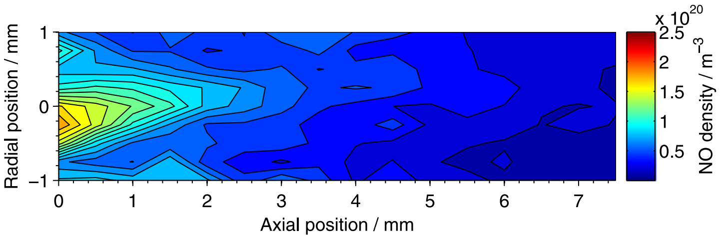

(c) Turbulent flow, the plasma jet fed with 3.0 slm argon + 1 % air and the gas curtain supplied with 5.0 slm dry air.

Figure 6. Absolute NO density profiles in the jet effluent. The laminar flow case with gas curtain (a) and the turbulent case without (b). (c) depicts the NO density profile for the turbulent case *with gas curtain*. The jet is free in air, without substrate and the plasma generator setup is kept constant.

be well correlated with the position of the plasma filament located within the capillary. Indeed, it was noticed during the experiment that the visible plasma effluent is not entirely homogeneous but a brighter filamentary area is observed. Note that in the laminar case the plasma filament is stable and often attached to the dielectric surface of the tube thus explaining the asymmetric NO production. As expected, the feed gas flow rate has an influence on the global NO density distribution. The NO density is larger for lower flow rates. This is explained, on one side, by a higher gas temperature (see table 1) due to a weaker heat dissipation. This is highly favorable to the NO production. Van Gaens *et al* have shown for similar conditions that the NO density is mainly determined by a local balance between production and destruction reactions in the early afterglow. In reference [44] the difference between the production and destruction rate is 10% at the position of maximum production rate. A moderate change in flow rate will have a limited effect on the NO density in the early afterglow. Moreover, an increase of the gas temperature strongly reduces the ozone production which is one of the key players in the destruction of NO [45]. On the other side, the residence time of N_2 and O_2 is larger for a lower flow rate which could enhance dissociation and chemical conversion in the discharge. In spite of a maximum NO density which is higher by a factor of about 1.5 in the laminar case than in the turbulent case, the density profiles are similar. Nonetheless, the NO density decays faster in the turbulent case. It is important to note that the length and the width of the plasma emission remain almost identical in both cases as shown in figure 7. Consequently, the volume of the

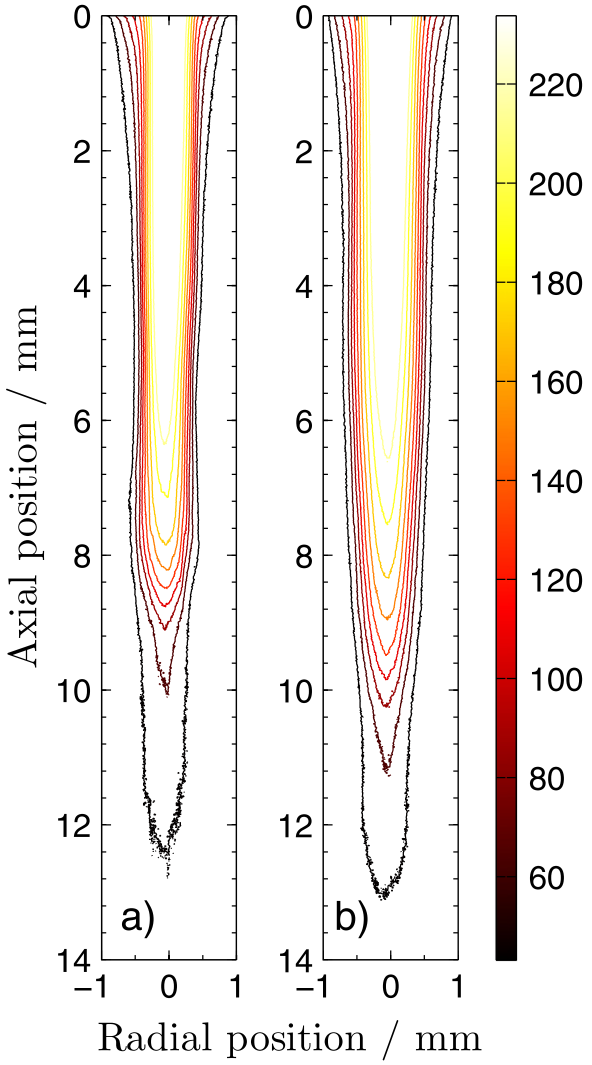

Figure 7. Comparison of the visible length of the effluent for 1.0 slm (a) and 3.0 slm (b) feed gas flow rate with 1.6 slm and 5.0 slm curtain gas flow rate respectively. The original data are grey-scaled photographs. Contour plots are chosen for a better readability and comparison.

afterglow is invariant and the spreading of NO is most likely due to a high mixing induced by the turbulence.

Recently, van Gaens *et al* reported from a computational simulation of a similar argon plasma source the main reactions responsible for the NO formation and destruction [44].

$$O + N_2(A) \rightarrow NO + N(^2D) \tag{8}$$

$$O + NO_2 \rightarrow NO + O_2 \tag{9}$$

Reactions (8) and (9) are identified to largely contribute to the NO production. NO molecules are mainly produced from atomic oxygen and the first metastable state of nitrogen rather than through Zeldovich mechanism [45]. The first reaction requires a high density of O and $N_2(A)$ which is inside the active plasma region and explains the higher NO density near the nozzle. In addition, a recycle reaction from NO_2 with O is important. Reaction (9) is dominant in the

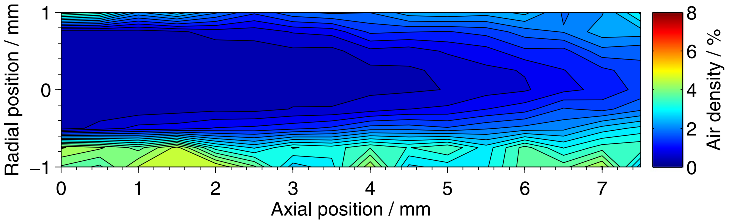

(a) Laminar flow, 1.0 slm argon + 1 % air with gas curtain 1.6 slm.

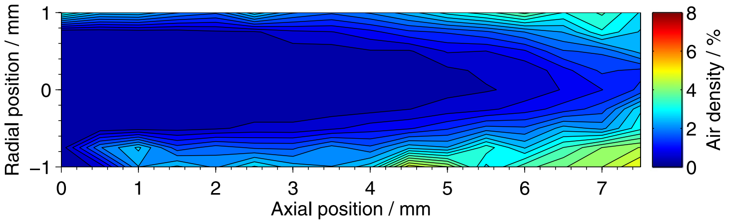

(b) Turbulent flow, 3.0 slm argon, no gas curtain.

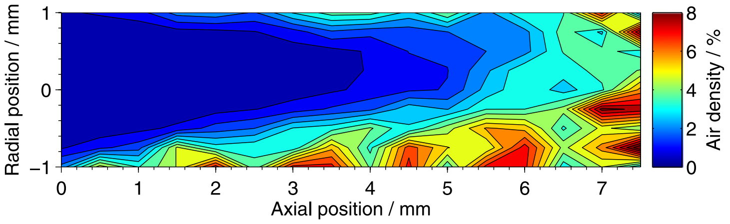

(c) Turbulent flow, 3.0 slm argon + 1 % air with gas curtain 5.0 slm.

Figure 8. Spatially-resolved air density distribution over the effluent and far field regions for 1.0 slm and 3.0 slm flow rate.

afterglow [44].

$$O + NO + M \rightarrow NO_2 + M \tag{10}$$

$$N + NO \rightarrow N_2 + O \tag{11}$$

Reactions (10) and (11) have been identified by van Gaens to play a significant role together in the NO loss. The rate of reaction (10) producing NO_2 increases with a decreasing gas temperature which could explain the differences observed in figure 6 between turbulent and laminar flow (see also table 1).

4.1.2. Effects of the gas curtain. A gas curtain fed by 5.0 slm dry air is added to the turbulent flow case of 3.0 slm argon + 1.0% air. Figure 6(c) depicts the NO density distribution which is compared to the case without gas curtain in figure 6(b). The gas curtain has a significant impact on the spatial distribution of the NO density. The presence of a strong decay of the NO density is observed along the axial direction. This is due to the additional gas flow from the curtain which enhances the mixing in the effluent and the far field region and reduces the gas temperature in the effluent, (table 1). The gas temperature is actually mostly affected by the curtain and will reduce thermal diffusion of NO in the laminar case. Interestingly, on the axis of symmetry, close to the nozzle, one can observe the same density. This observation corroborates the previous conclusion that NO is, in fact, mainly produced in the first millimeters in the vicinity of the nozzle. A decrease in T_{gas} leads to an enhancement of reaction (10) and the destruction of NO.

4.2. Surrounding air mixed in the effluent

Figure 8 depicts the air density derived from the fluorescence decay time constant of NO present within the effluent and far field for the conditions corresponding to figure 6. The three maps are corrected for the gas temperature variations, when the latter is known, which are dependent on the flow rate (see table 1). Starting with the laminar case with gas curtain on (figure 8(a)), one observes a smooth positive gradient along the axial direction and a very steep density gradient in the radial direction. In this case, where the flow is laminar, the diffusion process of air into the plasma effluent is enhanced by a higher temperature gradient between the effluent and the gas curtain. This has been experimentally shown in a similar jet by van Gessel *et al* [46] and by Reuter *et al* [47]. In addition, Iseni *et al* have also reported in a previous work the presence of Kelvin–Helmholtz instabilities and proposed those results from the temperature gradient [22]. The core of the effluent contains about 1% air which directly results from the fraction of air admixed to the feed gas. At 7.5 mm, the air density hardly reaches 2% and is in excellent agreement with the value measured by Raman scattering in a similar jet as reported by van Gessel *et al* [48].

Figure 8(b) shows the air density for a flow rate of 3.0 slm without gas curtain. Remarkably, the density map looks similar to the laminar case with shielding (figure 8(a)), except on one side where the gas curtain seems to force the air onto the border of the effluent. Despite the turbulent flow, which has been shown in [22], the diffusion of air in the first 5 mm is negligible o*n*-axis. This is not the case radially as shown by van Gessel *et al* [46]. It is also clear that the thermal diffusion is significantly reduced since the gas temperature is 90–30 K lower than the laminar case along the axial direction (see table 1 and figure 8(a)). The absolute value of the air distribution in a similar jet has been carried out by Dünnbier *et al* who investigated on the same plasma source the o*n*-axis diffusion of ambient species by means of MBMS complemented with fluid dynamic simulations [49]. The air concentration at 7.5 mm is measured to be 1.8% and is in excellent agreement with the present work. The results suggest that thermal diffusion in the laminar flow regime compensates for the turbulent mixing in the turbulent flow regime.

It was shown previously that switching on the gas curtain around the plasma effluent has an impact on the spatial distribution of NO (see figure 6(c)). The visualization of the enhanced mixing of the effluent with the gas curtain is presented in figure 8(c). The area containing an air density up to 1% is now reduced from 5.5–3.8 mm and is narrower than in the case with the gas curtain (figures 8(a) and (b)). The gas curtain enhances the air diffusion into the effluent which leads to an additional cooling of the gas. This result corroborates very well with the steeper NO density gradient (see figure 6(c)). Interestingly, the air density is asymmetric compared to the two other cases and can be attributed to the curtain gas device which may not have been perfectly aligned.

4.3. Influence of the substrate on the NO density distribution

In this section, the impact of a fixed substrate on the NO density distribution is studied. While previously the plasma jet and its effluent ran free into an open atmosphere, for most applications a substrate is present. A stainless-steel plate, grounded to avoid any charge accumulation on the surface, is fixed at a distance of 7.5 mm from the nozzle. LIF is performed as previously described and the recorded signal is corrected for vignetting during post-processing. For both

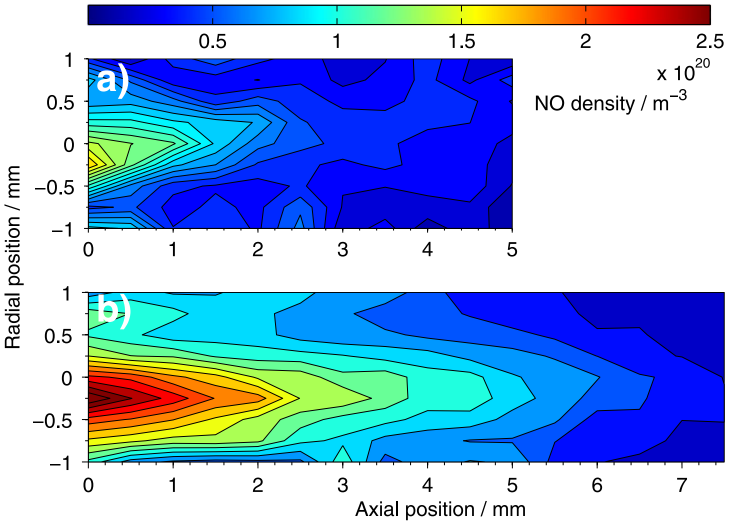

Figure 9. Absolute NO densities, measured without gas curtain in a turbulent (a) and with gas curtain in laminar (b) flow rate regime. A substrate is placed at a distance of 7.5 mm from the nozzle. The input power is supposed to be constant and identical as the previous measurements. The two maps have different lengths because it was not possible to obtain a significant signal-to-noise ratio in the turbulent case in the vicinity of the substrate. This issue is enhanced by the vignetting and higher density of quenchers (air) near the substrate surface.

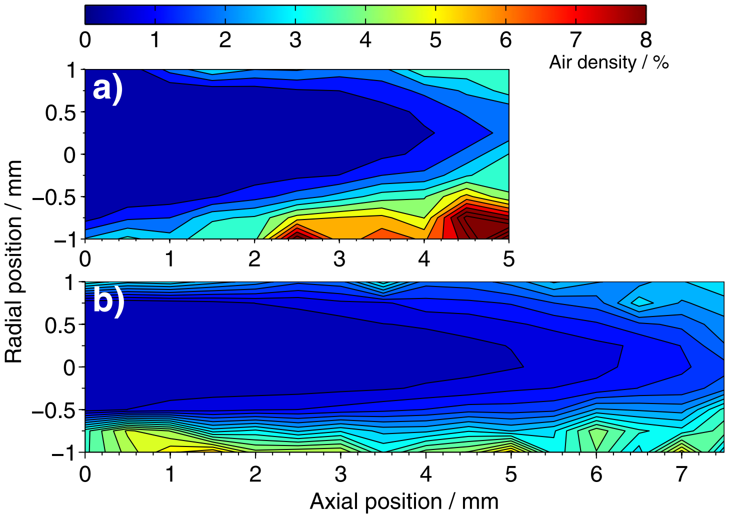

Figure 10. Air density distribution determined from the temporal evolution of the NO fluorescence. The corresponding NO densities are shown in figure 9. (a) and (b) depict the air density distribution for the turbulent case and for the laminar case respectively.

regimes (laminar and turbulent) 1.0 slm and 3.0 slm argon with 1.0% air admixed are applied with a gas curtain of 1.7 slm and 5.0 slm respectively. The results are depicted in figure 9. Significant differences in NO density profiles between the laminar and the turbulent case are observed. In the laminar case, the symmetry of the NO density profile is well conserved from the nozzle to the substrate whereas the pattern in the turbulent case appears to be asymmetric. The more distorted NO density profile shown in figure 9(a) beyond doubt is due to the

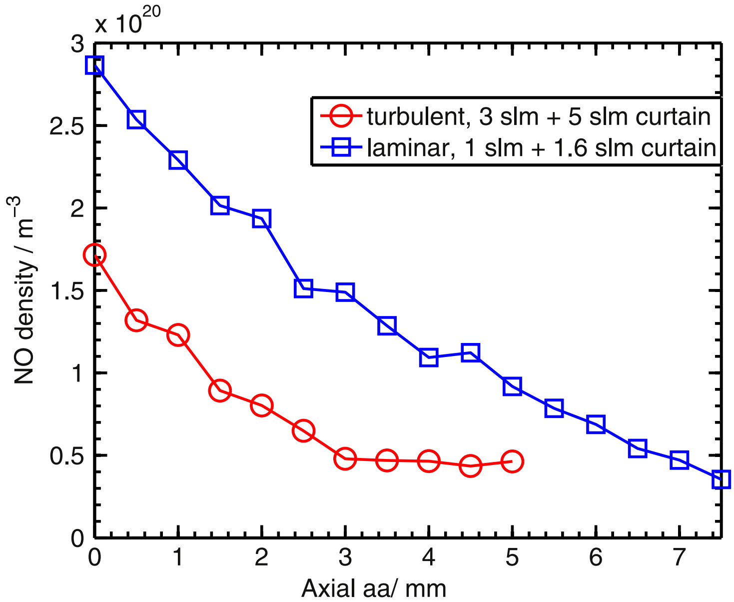

Figure 11. Absolute NO density along the axial position. The substrate is positioned at 7.5 mm from the nozzle.

turbulence which is enhanced by a natural back reflection of the flow on the substrate. figure 10 presents the air density distribution when the plate is present. As expected, figure 10(a), which corresponds to the turbulent flow case, shows a higher air density on one corner of the probed domain. This confirms the recycling pattern induced by the plate and enhances the mixing of the effluent with the ambient air. The argon flux keeps a quasi-symmetrical structure as without the plate and does not seem to drag more air into the effluent up to 4.0 mm. The axial dependence of the NO density is not easily readable on the color-map in figure 9. To this end, an additional plot of the maxima along the axial direction is shown in figure 11. In both cases, the NO density decreases linearly with the same slope from 0–3.0 mm from the nozzle. The density decay results from the diffusion either thermal or turbulent dominating but produces the same reduction of the NO density over the first 3 mm. Interestingly, from 3.0–5.0 mm with turbulent flow, the density remains constant. It is stressed that the detection limit (about $2 \times 10^{19}\ \mathrm{m}^{-3}$) was not reached in these measurements.

4.4. MBMS measurement of NO and O_3 densities: comparison with the LIF

Absolute densities of NO and O_3 have been measured by MBMS. The NO density will be compared to the densities determined by LIF in this section. The experimental conditions are identical to the ones used during the LIF measurement for the turbulent regime, 3 slm feed gas flow rate, 5 slm dry air as a gas curtain. It is emphasized that the plasma was not coupled or corrected to the MBMS plate containing the sampling orifice, which resulted in a significant increase of the current and luminous intensity easily noticeable with the naked eye.

4.4.1. NO and O_3 densities. Figure 12 depicts the results of the MBMS measurement for NO and O_3 densities at 7.5 mm from the jet nozzle. Quantitatively, densities measured by MBMS as well as LIF are in the same order of magnitude in spite of a factor 5 difference between both techniques. A discussion dealing with this discrepancy is developed in section 4.4.2.

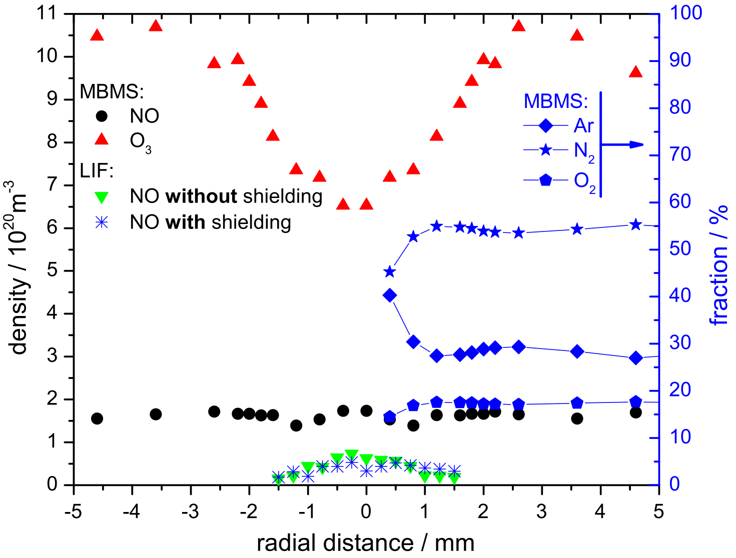

Figure 12. Radial absolute density profiles of the NO and O_3 measured by MBMS and LIF (left axis) and the absolute Ar, N_2 and O_2 fraction (right axis) from MBMS. The sampling orifice of the MBMS is 7.5 mm way from the jet nozzle. The plasma jet is fed with argon plus 1.0% air admixture and the deposited power into the plasma is similar for each measurement set with maximum 15% variation.

Interestingly, the density of NO measured on the axis of symmetry by MBMS (figure 12) is identical to the maximum of the NO density map measured by LIF in figure 9. The density is found to be $1.8 \times 10^{20}\,m^{-3}$.

Moreover, the MBMS recorded signal at mass 30 u (atomic mass unit) corresponds to a nearly constant NO density along the radial position which is not likely to be the case. In comparison with the LIF data, the trend in the radial direction from 0.0 mm to 1.0 mm are identical: the maximum density is at the axis of symmetry. A spatial resolution difference of the MBMS compared to the LIF might explain the slight shift of the position of the maximum. To be sure that the resolution limit was not reached, the response of the signal at 30 u has been checked by adding 0.2% air admixture instead of 1.0% initially. The result is a drop of the counts by 40%. According to the work of van Gessel *et al* [16] on a similar plasma source, the production of NO with regard to the air admixture is strongly affected and the experimental results confirm the same trend. Consequently, the signal at mass 30 is clearly reflecting the N_xO_y production from the plasma jet. A scan at mass 46, which corresponds to the NO_2 mass, is systematically performed and no variation is observed compared to the recorded background.

The interaction of the flow and the wall of the cup-like structure (in which the sampling orifice is located at the bottom) can act as a reservoir and influence the samples. Figure 12 shows on the right axis the fraction of Ar, N_2 and O_2 along the radial distance at 7.5 mm axial distance from the nozzle. A direct comparison with the air density profile in figure 10(a) can be partially made since the latter presents the first 5.0 mm of the effluent. However, a strong increase of N_2 and O_2 is expected due to the turbulent diffusion also known as eddy diffusion. Moreover, as mentioned in section 4.2, the air densities determined by LIF are in agreement with the value found in the literature. The MBMS density measurements of O_2 are in the order of 17% at 7.5 mm (figure 12) and are in excellent agreement with the Raman scattering

Table 2. Quantification of the maximum N_xO_y densities in the effluent at 7.5 mm from the nozzle of the kinpen. The data are either from this work (NO) or estimated from the literature [26, 51].

molecule	NO	NO_2	HNO_2	HNO_3	N_2O	N_2O_5
max. density / 10^{19} molecule m^{-3}	5.3	2.0	≈0.9	≈0.6	≈4	$\lesssim$0.1

measurements published in [48] at the same distance from the nozzle. Although an exhaust system has been implemented to keep the partial air pressure close to the free-field situation, an accumulation of air and argon occurs and leads to a recycling pattern as described by van Ham *et al* [25] which is partially visible in figure 10. This recycling pattern increases the residence time of N_xO_y species, enhances the oxidation of NO and contributes to the signal at 30 u as discussed further. In addition, it was observed during the measurement that by positioning the plasma jet 10.0 mm off-axis from the sampling orifice, the signal at 30 u reaches the level of the background recording.

The shape of the ozone density profile may be mainly by the larger residence time due to the above mentioned recycling pattern. The formation of ozone is known to result merely from a three body reaction involving molecular and atomic oxygen up to a temperature slightly above room temperature [45]. The dip in the center could be enhanced by a higher atomic oxygen density which quenches ozone efficiently [50].

4.4.2. Discussion. The fact that the NO density determined by the MBMS is significantly higher than the one obtained with LIF has already been reported in [25]. The authors would argue that the high electron energy of the MBMS ion source (maximum peak distribution at 70 eV) will dissociate any NO containing molecules (N_xO_y). For the kinpen, several experimental investigations have been reported on the net production rates of N_xO_y although in different flow conditions [26], HNO_3 [51], N_2O_5 [52]. In addition, Pipa and Röpcke, who have reported the measurements of the latter species, have also measured net production rates of N_2O and HNO_2 [18]. However, they used a different source and as the authors do not report any detection of ozone, it hints that the plasma source has a significantly higher gas temperature than the kinpen [19]. At present, the absolute net production rate of R_{NO_2} (expressed in molecules per second, molecule $\cdot$ s^{-1}) has been published for identical conditions (3 slm Ar with 1.0% air admixture and 5 slm curtain gas) and yields a net production rate of R_{NO_2}= 2.2×10^{15} molecule $\cdot$ s^{-1} [26]. Note that Verreycken measured OH radicals in the visible effluent by LIF and UV absorption and reported a concentration of 1.5×10^{21} m^{-3} 1.0 mm distance from the nozzle but for a gas flow rate of 4.0 slm with 1.3% water admixture [53]. Winter *et al* could determine the ozone concentration spatially resolved (starting from 4.0 mm from the nozzle tip) of 1.5×10^{22} m^{-3} at 4.0 mm axial distance with a argon flow rate of 3.0 slm and 1.0% oxygen admixture [54]. The formation of NO_2 already occurs within the effluent resulting from the oxidation of NO by atomic oxygen. In the case when the maximum gas temperature does not exceed significantly the room temperature, ozone formation will occur and lead to the efficient oxidation of NO within the effluent. The results of the kinetic model of van Gaens *et al* report on the formation of N_2O molecules which occurs in parallel to the NO generation. Recently, this N_2O has been detected in the far field beyond the visible plume of the kinpen [55]. In other words, N_2O is already produced in the vicinity of the electrodes. Interestingly, the production of

N_2O seems to reach a steady-state at the tip of the nozzle and yields a density slightly below the NO density. Table 2 shows the estimation of maximum densities of N_xO_y at 7.5 mm from the nozzle of the plasma jet susceptible to dissociation within the MBMS chamber by the ionization source. In spite of the data being all from the same plasma source (kinpen) the experimental conditions may differ. In the work reported in [26, 51], the plasma jet operates with a different surrounding atmosphere and blows into a multipass cell which is pumped down or at atmospheric pressure. These conditions are dissimilar from the experimental environment of the cup-like structure of the MBMS. Although the cracking patterns of some of the molecules given in table 2 remain unclear, N_2O and NO_2 have been identified to contribute by 25% and 60% respectively to 30 u [32]. As a consequence, both molecules are the most dominant secondary species which contribute to the NO signal at mass 30 u together with NO. This could lead to an overestimation of the NO density by about 50% in the present work when assuming the densities in table 2.

5. Conclusion

In this work, LIF was used to measured the absolute and spatially resolved NO density in the effluent of an argon RF cold plasma jet operating under atmospheric conditions in laminar and turbulent flow regimes. The LIF signal is absolutely calibrated with a known reference density of NO. Furthermore, a characterization of the vignetting induced by a substrate is performed. It is reported that NO is dominantly produced within the first part of the effluent and reaches a maximum of 2.5×10^{20} molecule. cm^{-3} and 1.7×10^{20} molecule. cm^{-3} at the jet nozzle for the laminar and turbulent flow case respectively. The gas temperature measured by LIF is higher in the laminar case than in the turbulent case by about 100 K at the nozzle. The temperature difference is argued to be the main cause of the different NO density. The absolute air density spatially resolved in the effluent was determined from the quenching of the NO fluorescence. The diffusion of air in the Ar effluent is mostly thermally driven in the laminar case whereas turbulent diffusion is responsible for the mixing with the ambient in a turbulent regime. Remarkably, both conditions lead to a similar spatial distribution of air within the jet effluent. Moreover, the gas curtain applied around the effluent appears not to affect the NO density close to the nozzle but enhances the diffusion of air into the effluent without affecting the visible emission length of the effluent. The air concentrations are in excellent agreement with the data obtained by other techniques reported in the literature [46, 47]. The maximum air density reaches about 4–7% and 2% at 7.5 mm from the nozzle respectively with and without gas curtain in the turbulent case. The NO lifetime decays faster due to an enhancement of the oxidation induced by atomic oxygen and ozone from the plasma which leads to the production of NO_2. The latter is assumed to play a role in a chemical recycling reaction in the effluent zone to form NO again. This reaction is gas temperature dependent.

Furthermore, measurements have been performed with an absolutely calibrated MBMS. The comparison of both techniques (LIF and MBMS) are in the same order of magnitude around 5×10^{19}–15×10^{19} molecule. cm^{-3}on the axial symmetry at 7.5 mm. The non-selectivity of the MBMS induces measurements which overestimate the NO density resulting from a significant contribution to the NO_2 and N_2O molecules generated in the effluent. An additional effect of the flow cannot be excluded and could contribute to the discrepancies.

Acknowledgments

This work was supported by the MPNS COST-Action MP1101 and the data was obtained during a Short-Term Scientific Mission (STSM) of SI at the TU/e Eindhoven University of Technology. PB would like to acknowledge the support of the Dutch Technology Foundation (STW), the University of Minnesota and the DOE Plasma Science Center. SH acknowledges the support of the Foundation for Fundamental Research on Matter (FOM). SI thanks Ansgar Schmidt-Bleker for the fruitful conversations. SI and SR thank the BMBF for supporting the ZIK plasmatis and the Leibniz Institute for Plasma Science and Technology (INP Greifswald e. V.) grant number 03Z2DN12.

References

[1] Lu X, Laroussi M and Puech V 2012 On atmospheric-pressure non-equilibrium plasma jets and plasma bullets *Plasma Sources Sci. Technol.* **21** 034005

[2] Samukawa S *et al* 2012 The 2012 plasma roadmap *J. Phys. D: Appl. Phys.* **45** 253001

[3] von Woedtke T, Reuter S, Masur K and Weltmann K D 2013 Plasmas for medicine *Phys. Rep.* **530** 291–320

[4] Kong M G, Kroesen G, Morfill G, Nosenko T, Shimizu T, van Dijk J and Zimmermann J L 2009 Plasma medicine: an introductory review *New J. Phys.* **11** 115012

[5] Ehlbeck J, Schnabel U, Polak M, Winter J, von Woedtke T, Brandenburg R, von dem Hagen T and Weltmann K D 2011 Low temperature atmospheric pressure plasma sources for microbial decontamination *J. Phys. D: Appl. Phys.* **44** 013002

[6] van Gils C A J, Hofmann S, Boekema B K H L, Brandenburg R and Bruggeman P J 2013 Mechanisms of bacterial inactivation in the liquid phase induced by a remote rf cold atmospheric pressure plasma jet *J. Phys. D: Appl. Phys.* **46** 175203

[7] Laroussi M, Karakas E and Hynes W 2011 Influence of cell type, initial concentration, and medium on the inactivation efficiency of low-temperature plasma *IEEE Trans. Plasma Sci.* **39** 2960–1

[8] Lademann J, Richter H, Schanzer S, Patzelt A, Thiede G, Kramer A, Weltmann K D, Hartmann B and Lange-Asschenfeldt B 2012 Comparison of the antiseptic efficacy of tissue-tolerable plasma and an octenidine hydrochloride-based wound antiseptic on human skin *Skin Pharmacol. Physiol.* **25** 100–6

[9] Matthes R, Bekeschus S, Bender C, Koban I, Hubner N O and Kramer A 2012 Pilot-study on the influence of carrier gas and plasma application (open resp. delimited) modifications on physical plasma and its antimicrobial effect against pseudomonas aeruginosa and staphylococcus aureus *GMS Krankenhhyg. Interdiszip.* **7** Doc02

[10] Nosenko T, Shimizu T and Morfill G E 2009 Designing plasmas for chronic wound disinfection *New J. Phys.* **11** 115013

[11] Graves D B 2012 The emerging role of reactive oxygen and nitrogen species in redox biology and some implications for plasma applications to medicine and biology *J. Phys. D: Appl. Phys.* **45** 263001

[12] Bekeschus S, Kolata J, Winterbourn C, Kramer A, Turner R, Weltmann K D, Bröker B and Masur K 2014 Hydrogen peroxide: a central player in physical plasma-induced oxidative stress in human blood cells *Free Radic. Res.* **48** 542–9

[13] Bundscherer L, Wende K, Ottmuller K, Barton A, Schmidt A, Bekeschus S, Hasse S, Weltmann K D, Masur K and Lindequist U 2013 Impact of non-thermal plasma treatment on MAPK signaling pathways of human immune cell lines *Immunobiology* **218** 1248–55

[14] Barekzi N and Laroussi M 2013 Effects of low temperature plasmas on cancer cells *Plasma Process. Polym.* **10** 1039–50

[15] Lancaster J 1996 *Nitric Oxide: Principles and Actions* (New York: Academic)

[16] van Gessel A F H, Alards K M J and Bruggeman P J 2013 NO production in an RF plasma jet at atmospheric pressure *J. Phys. D: Appl. Phys.* **46** 265202

[17] van Gessel A F H, Hrycak B, Jasiński M, Mizeraczyk J, van der Mullen J J A M and Bruggeman P J 2013 Temperature and NO density measurements by LIF and OES on an atmospheric pressure plasma jet *J. Phys. D: Appl. Phys.* **46** 095201

[18] Pipa A V and Ropcke J 2009 Analysis of the mid-infrared spectrum of the exhaust gas from an atmospheric pressure plasma jet (APPJ) working with an argon air mixture *IEEE Trans. Plasma Sci.* **37** 1000–3

[19] Pipa A V, Reuter S, Foest R and Weltmann K D 2012 Controlling the NO production of an atmospheric pressure plasma jet *J. Phys. D: Appl. Phys* **45** 085201

[20] Stoffels E, Gonzalvo Y A, Whitmore T D, Seymour D L and Rees J A 2006 A plasma needle generates nitric oxide *Plasma Sources Sci. Technol.* **15** 501–6

[21] Stoffels E, Aranda Gonzalvo Y, Whitmore T D, Seymour D L and Rees J A 2007 Mass spectrometric detection of short-living radicals produced by a plasma needle *Plasma Sources Sci. Technol.* **16** 549–56

[22] Iseni S, Schmidt-Bleker A, Winter J, Weltmann K D and Reuter S 2014 Atmospheric pressure streamer follows the turbulent argon air boundary in a MHz argon plasma jet investigated by OH-tracer plif spectroscopy *J. Phys. D: Appl. Phys.* **47** 152001

[23] Robert E, Sarron V, Darny T, Riès D, Dozias S, Fontane J, Joly L and Pouvesle J M 2014 Rare gas flow structuration in plasma jet experiments *Plasma Sources Sci. Technol.* **23** 012003

[24] Reuter S, Winter J, Schmidt-Bleker A, Tresp H, Hammer M U and Weltmann K D 2012 Controlling the ambient air affected reactive species composition in the effluent of an argon plasma jet *IEEE Trans. Plasma Sci.* **40** 2788–94

[25] van Ham B, Hofmann S, Brandenburg R and Bruggeman P J 2014 *In situ* absolute air, O_3 and NO densities in the effluent of a cold RF argon atmospheric pressure plasma jet obtained by molecular beam mass spectrometry *J. Phys. D: Appl. Phys.* **47** 224013

[26] Iseni S, Reuter S and Weltmann K D 2014 NO_2 dynamics of an ar air plasma jet investigated by *in situ* quantum cascade laser spectroscopy at atmospheric pressure *J. Phys. D: Appl. Phys.* **47** 075203

[27] Winter J, Wende K, Masur K, Iseni S, Dnnbier M, Hammer M U, Tresp H, Weltmann K-D and Reuter S 2013 Feed gas humidity: a vital parameter affecting a cold atmospheric-pressure plasma jet and plasma-treated human skin cells *J. Phys. D: Appl. Phys.* **46** 295401

[28] Tamura M, Berg P A, Harrington J E, Luque J, Jeffries J B, Smith G P and Crosley D R 1998 Collisional quenching of CH(A), OH(A), and NO(A) in low pressure hydrocarbon flames *Combust. Flame* **114** 502–14

[29] Hazama H, Fujiwara M and Tanimoto M 2000 Removal processes of nitric oxide along positive streamers observed by laser-induced fluorescence imaging spectroscopy *Chem. Phys. Lett.* **323** 542–8

[30] Heard D E, Jeffries J B and Crosley D R 1991 Collisional quenching of $A^2\Sigma^+$NO and $A^2\Delta$CH in low pressure flames *Chem. Phys. Lett.* **178** 533–7

[31] Verreycken T, van der Horst R M, Sadeghi N and Bruggeman P J 2013 Absolute calibration of oh density in a nanosecond pulsed plasma filament in atmospheric pressure $He-H_2O$: comparison of independent calibration methods *J. Phys. D: Appl. Phys.* **46** 464004

[32] Stein S E 2014 Mass Spec Data Center *NIST Chemistry WebBook* (*NIST Standard Reference Database No* 69) ed P J Linstrom and W G Mallard (Gaithersburg, MD: National Institute of Standards and Technology)

[33] Hofmann S, van Gils K, van der Linden S, Iseni S and Bruggeman P 2014 Time and spatial resolved optical and electrical characteristics of continuous and time modulated rf plasmas in contact with conductive and dielectric substrates *Eur. Phys. J.* D **68** 56

[34] Bruggeman P J, Sadeghi N, Schram D C and Linss V 2014 Gas temperature determination from rotational lines in non-equilibrium plasmas: a review *Plasma Sources Sci. Technol.* **23** 023001

[35] van Gessel A F H and Bruggeman P J 2013 Thermalization of rotational states of NOA$(2)\Sigma^+(v = 0)$ in an atmospheric pressure plasma *J. Chem. Phys.* **138** 204306

[36] Nguyen T D and Sadeghi N 1983 Rotational and vibrational distributions of N2$(C^3\Pi_u)$ excited by state-selected Ar$(^3P_2)$ and Ar$(^3P_0)$ metastable atoms *Chem. Phys.* **79** 41–55

[37] van Gessel A F H, Hrycak B, Jasinski M, Mizeraczyk J, van der Mullen J J A M and Bruggeman P J 2012 Temperature fitting of partially resolved rotational spectra *J. Instrum.* **7** C02054

[38] Raiche G A and Crosley D R 1990 Temperature dependent quenching of the $A^2\Sigma^+$ and $B^2\Pi$ states of NO *J. Chem. Phys.* **92** 5211

[39] Drake M C and Ratcliffe J W 1993 High-temperature quenching cross-sections for nitric-oxide laser-induced fluorescence measurements *J. Chem. Phys.* **98** 3850–65

[40] Stuart McDermid I and Laudenslager J B 1982 Radiative lifetimes and electronic quenching rate constants for single-photon-excited rotational levels of NO$(A^2\Sigma^+, v' = 0)$ *J. Quant. Spectrosc. Radiat. Transfer* **27** 483–92

[41] Paul P H, Gray J A, Durant J L and Thoman J W 1996 Collisional electronic quenching rates for NOA$(2)\Sigma^+(v' = 0)$ *Chem. Phys. Lett.* **259** 508–14

[42] Fricke K, Reuter S, Schroder D, Schulz-von der Gathen V, Weltmann K D and von Woedtke T 2012 Investigation of surface etching of poly (ether ether ketone) by atmospheric-pressure plasmas *IEEE Trans. Plasma Sci.* **40** 2900–11

[43] Ellerweg D, Benedikt J, von Keudell A, Knake N and Schulz-von der Gathen V 2010 Characterization of the effluent of a He/O_2 microscale atmospheric pressure plasma jet by quantitative molecular beam mass spectrometry *New J. Phys.* **12** 013021

[44] van Gaens W, Bruggeman P J and Bogaerts A 2014 Numerical analysis of the NO and O generation mechanism in a needle-type plasma jet *New J. Phys.* **16** 063054

[45] Fridman A 2008 *Plasma Chemistry* (Cambridge: Cambridge University Press)

[46] van Gessel B, Brandenburg R and Bruggeman P 2013 Electron properties and air mixing in radio frequency driven argon plasma jets at atmospheric pressure *Appl. Phys. Lett.* **103** 064103

[47] Reuter S, Winter J, Schmidt-Bleker A, Schroeder D, Lange H, Knake N, Schulz-von der Gathen V and Weltmann K D 2012 Atomic oxygen in a cold argon plasma jet: talif spectroscopy in ambient air with modelling and measurements of ambient species diffusion *Plasma Sources Sci. Techno.* **21** 024005

[48] van Gessel A F H, van Grootel S C and Bruggeman P J 2013 Atomic oxygen talif measurements in an atmospheric-pressure microwave plasma jet within situxenon calibration *Plasma Sources Sci. Technol.* **22** 055010

[49] Dünnbier M, Schmidt-Bleker A, Winter J, Wolfram M, Hippler R, Weltmann K D and Reuter S 2013 Ambient air particle transport into the effluent of a cold atmospheric-pressure argon plasma jet investigated by molecular beam mass spectrometry *J. Phys. D: Appl. Phys.* **46** 435203

[50] Zhang S, van Gessel A F H, van Grootel S C and Bruggeman P J 2014 The effect of collisional quenching of the O $3p^3P_J$ state on the determination of the spatial distribution of the atomic oxygen density in an APPJ operating in ambient air by TALIF *Plasma Sources Sci. Technol.* **23** 025012

[51] Schmidt-Bleker A, Winter J, Iseni S, Dünnbier M, Weltmann K D and Reuter S 2014 Reactive species output of a plasma jet with a shielding gas devicecombination of FTIR absorption spectroscopy and gas phase modelling *J. Phys. D: Appl. Phys.* **47** 145201

[52] Reuter S, Winter J, Iseni S, Schmidt-Bleker A, Dünnbier M, Masur K, Wende K and Weltmann K 2014 The influence of feed gas humidity versus ambient humidity on atmospheric pressure plasma jet-effluent chemistry and skin cell viability *IEEE Trans. Plasma Sci.* doi:10.1109/TPS.2014.2361921

[53] Verreycken T, Mensink R, van der Horst R, Sadeghi N and Bruggeman P J 2013 Absolute OH density measurements in the effluent of a cold atmospheric-pressure Ar-H_2O RF plasma jet in air *Plasma Sources Sci. Technol.* **22** 055014

[54] Winter J, Dünnbier M, Schmidt-Bleker A, Meshchanov A, Reuter S and Weltmann K D 2012 Aspects of UV-absorption spectroscopy on ozone in effluents of plasma jets operated in air *J. Phys. D: Appl. Phys.* **45** 385201

[55] Schmidt-Bleker A 2014 private communication

5.5 Article V

Tracking plasma generated H_2O_2 from gas into liquid phase and revealing its dominant impact on human skin cells
doi:10.1088/0022-3727/47/28/285401

IOP Publishing
Journal of Physics D: Applied Physics
J. Phys. D: Appl. Phys. **47** (2014) 285401 (12pp)
doi:10.1088/0022-3727/47/28/285401

Tracking plasma generated H_2O_2 from gas into liquid phase and revealing its dominant impact on human skin cells

J Winter[1,2], **H Tresp**[1,2], **M U Hammer**[1,2], **S Iseni**[1,2], **S Kupsch**[1,2],
A Schmidt-Bleker[1,2], **K Wende**[1,2], **M Dünnbier**[1,2], **K Masur**[1,2],
K-D Weltmann[2] **and S Reuter**[1,2]

[1] Centre for Innovation Competence plasmatis, Felix-Hausdorff-Str. 2, 17489 Greifswald, Germany
[2] Leibniz Institute for Plasma Science and Technology INP Greifswald e.V., Felix-Hausdorff-Str. 2, 17489 Greifswald, Germany

E-mail: winter@inp-greifswald.de

Received 2 March 2014, revised 14 May 2014
Accepted for publication 16 May 2014
Published 19 June 2014

Abstract

The pathway of the biologically active molecule hydrogen peroxide (H_2O_2) from the plasma generation in the gas phase by an atmospheric pressure argon plasma jet, to its transition into the liquid phase and finally to its inhibiting effect on human skin cells is investigated for different feed gas humidity settings. Gas phase diagnostics like Fourier transformed infrared spectroscopy and laser induced fluorescence spectroscopy on hydroxyl radicals ($^{\cdot}OH$) are combined with liquid analytics such as chemical assays and electron paramagnetic resonance spectroscopy. Furthermore, the viability of human skin cells is measured by Alamar Blue® assay. By comparing the gas phase results with chemical simulations in the far field, H_2O_2 generation and destruction processes are clearly identified. The net production rate of H_2O_2 in the gas phase is almost identical to the H_2O_2 net production rate in the liquid phase. Moreover, by mimicking the H_2O_2 generation of the plasma jet with the help of an H_2O_2 bubbler it is concluded that the solubility of gas phase H_2O_2 plays a major role in generating hydrogen peroxide in the liquid. Furthermore, it is shown that H_2O_2 concentration correlates remarkably well with the cell viability. Other species in the liquid like $^{\cdot}OH$ or superoxide anion radical ($O_2^{\cdot -}$) do not vary significantly with feed gas humidity.

Keywords: hydrogen peroxide, human skin cells, gas phase, plasma jet, humidity, liquid phase

(Some figures may appear in colour only in the online journal)

1. Introduction

Applications in plasma medicine require not only an understanding of the plasma sources and the generated plasma but also demand information on the active agent transition from the gas into the liquid phase and finally their interaction with the cells. However, this is a complex task since an interdisciplinary approach as well as extended experimental and theoretical research is necessary. Large efforts have been made in the diagnostics and control of atmospheric pressure plasmas intended for biomedical applications [1–4]. Also, by the support of sophisticated theoretical models first insights into the complex nature of plasma cell and plasma liquid interactions were obtained [5–8]. The aim of those investigations is to uncover work mechanisms of the plasma. This goes along with the identification of dominant species which are generated by the plasma in the gas and/or liquid phase and have a significant influence on the biological sample [9]. For prokaryotic cells Pavlovich *et al* and Shimizu *et al* found a correlation between the ozone concentration produced by a dielectric barrier discharge (DBD) operated in air and the inactivation efficacy of *Escherichia coli* [10, 11]. The impact of ozone on bacteria is well known and many water disinfection facilities are based on DBDs [12, 13]. However, that does not automatically mean that ozone is the dominant species in plasma medicine, where usually eukaryotic cells are plasma treated. Kalghatgi *et al* showed that DBD treatment of mammalian breast epithelial cells differ completely from pure ozone treatment, although ozone is one of the dominant plasma generated species in the gas phase [14]. They concluded that long living organic hydroperoxides mediate the DNA damaging effect of non-thermal plasma in mammalian cells. Haertel *et al* investigated the effect of DBD in argon and air on human skin cells (HaCaT keratinocytes) and observed that changes in integrin expression were related to intracellular reactive oxygen species (ROS) induction, while ozone has no influence [15]. Their study also discussed the dominant role of hydrogen peroxides (H_2O_2). Two years before, Sato *et al* already found that H_2O_2 is a key inactivation factor for HeLa cells treated by a pulsed corona discharge in air [16]. For a radio frequency driven atmospheric pressure argon plasma jet, Winter *et al* observed that increased feed gas humidity results in an elevated inhibition of indirectly treated HaCaT cells [17]. Interestingly, the gas phase ozone concentration generated under these experimental conditions showed an opposing trend and was thus not considered as the dominant species responsible for the observed cell effect. It was pointed out in this work that H_2O_2 in liquid phase increases with increasing feed gas humidity and a possible correlation with the cell response was discussed. Hydrogen peroxide was also identified as a central player in plasma-induced oxidative stress in human blood cells [18].

H_2O_2 is a quite important biologically relevant reactive species which can be detected throughout the human body. Peroxisomes and mitochondria show elevated levels as a by-product of mitochondrial respiration and β-oxidation of fatty acids, respectively [19–21]. Hydrogen peroxide is also an important mediator of wound healing processes, as it is secreted by epithelial cells after injuries have occurred, thereby initiating inflammatory processes [22]. In a similar setting, it is an effective antimicrobial means of innate immune cells (macrophages, neutrophils) upon the uptake of pathogens [23–25]. However, its omnipresence strongly requires control mechanisms to level the intra and extracellular H_2O_2 concentration. Many enzymes have evolved to that effect, the most efficient being catalase: one molecule of catalase readily transforms up to several million H_2O_2 molecules into water (H_2O) and oxygen (O_2) molecules every second [26]. Nevertheless, elevated levels or defective enzymes or detoxification pathways may cause serious damage to single cells or tissues, especially considering that it readily passes through cell membranes [19]. DNA damage has been described, from single base modifications to single and double strand breaks, as well as (per-) oxidation of (membrane) lipids (especially unsaturated lipids) and proteins leading to various cell changes, starting with mere modifications of cell shape and cytoskeleton to total loss of viability and disintegration of the cellular membrane [19, 20, 27–31]. Elevated levels of H_2O_2 are also considered to play an important role in the skin depigmentation disease Vitiligo [32].

Even though H_2O_2 is considered a mildly oxidizing species, it does not directly oxidize most biological molecules. It rather acts through its conversion to the highly reactive products hydroxyl radical ($^{\cdot}OH$) and hydroperoxyl radical ($HO_2^{\cdot}$), which can be formed by photodissociation of H_2O, by the decay of peroxynitrite/peroxynitrous acid ($O{=}NOO^-/O{=}N{-}OOH$) or by the Fenton reaction in the case of $^{\cdot}OH$ [33, 34].

The aim of the current study is to trace the H_2O_2 molecule from its plasma based generation in the gas phase to the liquid phase and show that H_2O_2 concentration correlates strongly with the inhibition of adherent human skin cells.

2. Materials and methods

2.1. Plasma jet

The plasma source, a cold atmospheric pressure plasma jet (kinpen, neoplas GmbH, Germany), used in this study is identical to the device used in the related study concerning the impact of feed gas humidity [17]. It consists of a centred rod electrode inside a ceramic capillary and a grounded ring electrode [35, 36]. The ceramic capillary has an inner and outer diameter of 1.5 mm and 2.5 mm, respectively. When a sinusoidal voltage signal of 2 to 6 kV_{pp} with a frequency of about 1 MHz is applied to the centred electrode, plasma is ignited within the core region of the jet and about a 10 mm long effluent becomes visible after ignition. The working gas was argon (Argon N50, Air Liquide) with a gas flow rate of 3 standard litres per minute (slm). In order to generate hydrogen peroxide by the plasma, the humidity concentration of the feed gas was changed by means of a bubbler setup exemplarily shown in figure 1. The feed gas humidification setting was similar to the setting used in [17]. The feed gas humidity was measured with a chilled mirror dew point hygrometer (DewMaster, EdgeTech, USA). For Fourier transformed infrared (FTIR) measurements the jet was equipped with a shielding gas device as reported in [37]. For details see section 2.3. All other plasma treatment results are performed without a shielding gas device.

2.2. Detection OH in the plasma jet effluent

The detection of gas phase hydroxyl radical density under atmospheric conditions by laser-induced fluorescence (LIF) is still under investigation and requires significant calibration efforts to yield absolute densities [38–41]. However, relative hydroxyl radical density is already interesting since basic information about chemistry dynamics can be concluded. In this work, the relative density of hydroxyl radicals is measured for different feed gas humidity settings by LIF using the P1(4) transition of the OH(A,X)(1,0) at 283.452 nm and chosen for its good absorption efficiency and its well isolated spectral position from neighbouring lines. The excitation is performed by a frequency doubled dye laser (Cobra Stretch, Sirah Laser und Plasmatechnik GmbH, Germany) pumped with a 10 Hz pulsed Nd : Yag laser (SpectraPhysics, Inc., USA). The LIF signal is transmitted through a 10 nm FWHM bandpass filter centred at 308 nm. The detection is performed by a photomultiplier tube (R5916U51, Hamamatsu, Japan) connected to a digital oscilloscope (DPO 4104, Tektronix Ltd., United Kingdom). The laser beam diameter is adjusted by a 500 μm aperture and not focused. The laser spot is pointed on-axis on the plasma effluent at 1.0 mm distance from the nozzle. In order to ensure a linear LIF response to the laser energy and to avoid saturation effects, a laser energy scan is performed. Consequently, the laser energy is set to 120 μJ per pulse. The LIF intensity I_{LIF} is known to be proportional to the laser energy I_L [39] and can be simplified in our case by:

$$I_{\mathrm{LIF}} \propto \frac{n_{\mathrm{OH}}}{\sum_i k_i \cdot n_i} \cdot I_{\mathrm{L}} \qquad (1)$$

where n_{OH} is the hydroxyl radical density, k_i the quenching and vibrational energy transfer (VET) coefficient and n_i is the density of a quencher species i which contributes to fluorescence losses. Argon from the feed gas, nitrogen and oxygen from the surrounding air and water from the admixture are the main quenchers of the fluorescence. However, it is a reasonable assumption to consider only water as a quencher since its density is a variable parameter, whereas argon, nitrogen and oxygen densities remain constant. The LIF signal is thus corrected from quenching and VET losses by using the following value reported in literature for water molecules, $k_{\mathrm{H_2O}} = 6.6 \times 10^{-10}\,\mathrm{cm^3\,s^{-1}}$ [42].

2.3. Detection of H_2O_2 in plasma afterglow

FTIR spectroscopy is a broadband absorption technique that enables the detection and quantification of molecules absorbing in the infrared spectral region. Since gas phase H_2O_2 has significant absorption bands in the spectral range from 1200 to 1330 cm^{-1} FTIR spectroscopy is the method of choice to analyse H_2O_2 [43]. In this study an FTIR spectrometer (Vertex 70v, Bruker Optics GmbH, Germany) was equipped with an additional white type multipass cell (A134G/QV, Bruker Optics GmbH, Germany), which provides a total absorption length of 19.2 m. The pressure in the multipass cell was reduced to 100 mbar by means of a vacuum pump in order to prolong the lifetime of the plasma generated species and to reduce the distracting influence of ambient water and carbon dioxide (CO_2). Due to this low-pressure setting the atmospheric pressure plasma jet could not be operated directly in the multipass cell. Thus, the jet was equipped with a pressurized air flushed shielding gas device with a nozzle diameter of 5 mm, similar to the one reported in [37], and attached to an additional glass chamber as displayed in figure 1. The gas from the shielding (5 slm compressed and dried air) and from the jet (3 slm argon) flows into the glass chamber and exhausts via an outlet. Hence, the pressure in the glass chamber is slightly higher than the ambient (1020–1030 mbar). Furthermore, the glass chamber was connected to the multipass cell by means of an adjustable needle valve so that a small fraction of the gas flow was sampled continuously by the FTIR system. The gas flow rate through the multipass cell is 1.5 slm. The gas mixing and particle residence time in the glass chamber was calculated by computational fluid dynamics simulations in a previous work for an identical geometry setting [37]. It was shown that the majority of particles remain within the mixing cell for a few seconds before they enter the FTIR multipass cell. This means that highly reactive species have enough time to react and form long living products, like H_2O_2 or O_3, which were detected with the FTIR setup.

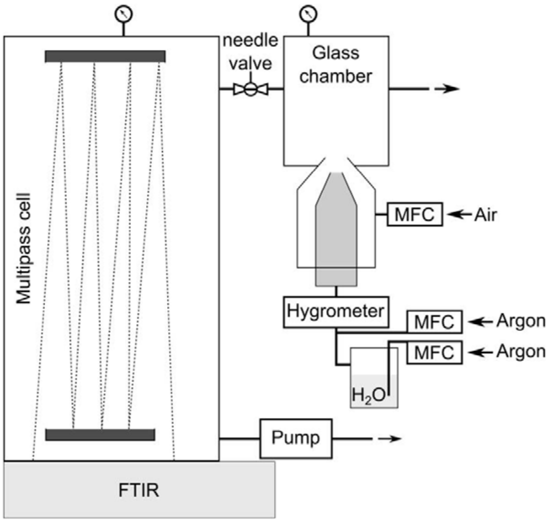

Figure 1. FTIR setup schematic for detecting H_2O_2 in the plasma jet downstream using FTIR spectroscopy combined with a multipass cell. MFC: mass flow controller.

In order to investigate the influence of feed gas humidity on the produced species the argon feed gas was humidified with the bubbler setup as displayed in figure 1. Before the FTIR measurement was performed the plasma jet was switched off while the particular gas mixture was flushed through the jet and the multipass cell. After 10 min the background signal was obtained. Subsequently, the jet was switched on. Several FTIR spectra were obtained for at least 10 min to validate the constant absorption band intensity. This proves a steady state measurement of species concentration in the multipass cell. The obtained spectra were fitted using fitting tool software (QMACSoft 1.1.3, neoplas control GmbH, Germany), that is based on the Hitran database and on the Levenberg–Marquardt algorithm [43, 44]. This allows for the identification of absorption bands as well as the calculation of species densities by applying Beer–Lambert's law to the measured optical depths. This measurement and evaluation procedure was performed for all humidity settings, so that an individual background signal was obtained for every humidity condition.

By replacing the humidifier bubbler by an identical vessel filled with 150 ml of 10% H_2O_2 solution, created by diluting a 30% H_2O_2 stock solution (9.7 M, Merck, Germany) and leaving everything else unaltered, gas phase H_2O_2 was generated without igniting the plasma. By varying the argon gas flow rate passing through the H_2O_2 bubbler the amount of gas phase H_2O_2 concentration was adjusted. The H_2O_2 concentration was determined analogue to the previously described procedure.

2.4. Plasma treatment of RPMI solution

As in the previous study [17], a volume of 5 mL complete cell growth medium (Roswell Park Memorial Institute RPMI

1640 + 8% fetal calf serum + 1% penicillin/streptomycin solution) filled in a polystyrene Petri dish (60 mm diameter TPP, Trasadingen, Switzerland) was plasma treated. The treatment time was varied between 0 and 100 s. During that treatment time the plasma jet was constantly moved in a meandering pattern over the Petri dish by means of a *xyz*-stepping motor. The distance between the nozzle and the liquid surface was 9 mm. During plasma treatment, the 3 slm argon gas flow rate leads to evaporation of the liquid. By measuring the remaining liquid volume after the longest treatment time (100 s), it was found that the initial 5 mL liquid volume misses 130 μl±10 μl. This evaporated liquid volume is only about 2.6% of the initial volume and is thus neglected in the H_2O_2 concentration evaluation.

By means of a thermometer the liquid temperature was measured before and after 100 s plasma treatment and no relevant temperature increase was observed.

2.5. Detection of reactive species concentrations in liquid cell growth medium

Hydrogen peroxide was measured with the test stripe method described in [17]. According to this method three times 30 μl of the plasma treated RPMI medium were sampled with a pipette directly after plasma treatment. These sample volumes were put onto three H_2O_2 test stripes (Merckoquant110011, Merck, Germany). After a waiting time of 60 s the test stripes were read out by a digital microscope camera (Conrad, Germany) in order to analyse their colour values. By comparing the obtained colour values with a calibration curve the H_2O_2 concentration was determined. This procedure was conducted three times so that finally nine test stripes were evaluated for every feed gas humidity setting investigated.

The same test stripe method was utilized for the H_2O_2 bubbler setup. For direct comparison the same H_2O_2 bubbler setup was used as for the FTIR measurements. In this experiment, the cell growth medium was exposed to the working gas flow for 40, 60 and 80 s without plasma ignition. The gas flow and treatment procedure is identical to the plasma treatment using humidified feed gas. By comparing the results of both experiments the effect of plasma for H_2O_2 production in liquid is investigated. The results are discussed in section 3.2.

Also the stability of plasma produced H_2O_2 in RPMI was investigated. Therefore, three H_2O_2 start concentrations of 0.8, 2.9 and 9.0 mg l^{-1} within a volume of 5 ml RPMI were produced via plasma treatment with three experimental settings, namely: dry argon gas and a treatment time of 20 or 180 s and with humidified argon (1660 ppm) and a treatment time of 80 s. Each setting was repeated three times. Subsequent to the plasma treatment the H_2O_2 concentrations in each Petri dish were measured at different times after plasma treatment applying the test stripe method described above. We intentionally did not use commercial H_2O_2 stock solution for the H_2O_2 life time experiments, since in contrast to plasma treated H_2O_2, it contains stabilizers. This would distort the results of the life time measurements in the RPMI solution.

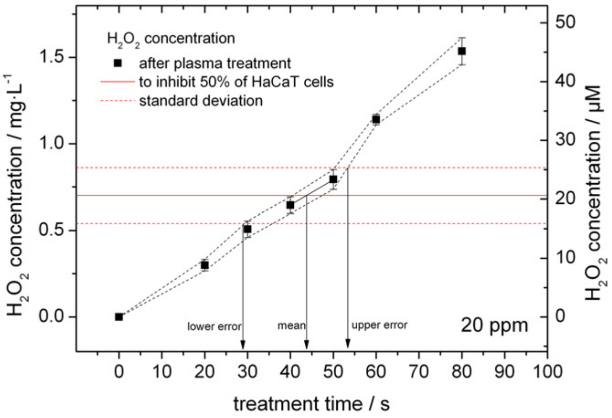

Figure 2. Method to obtain the H_2O_2 related inhibition time. The horizontal solid line depicts the H_2O_2 concentration that inhibits 50% of adherent HaCaT cells. This value was determined experimentally. Square dots are the measurement values for plasma generated H_2O_2 concentration in RPMI medium after different treatment times. The treatment time given by the interception point of both curves is the half inhibition treatment time, since the H_2O_2 concentration in the medium reaches the concentration to inhibit 50% of HaCaT cells. The dashed lines represent the error intervals of both measurements. From these lines the lower and upper error of the half inhibition treatment time were deduced.

The measurement of low H_2O_2 concentrations in the case of the dry feed gas for the purpose of cell viability comparison was performed by means of a homogeneous assay (Amplex Red Hydrogen Peroxide/Peroxidase Assay Kit, Invitrogen Ltd, USA). The assay was applied analogue to the method described in [17]. It is more sophisticated than the test stripe method but leads to a higher accuracy in H_2O_2 concentration determination. This is important for the correlation evaluation described in section 2.6 since errors made in H_2O_2 concentration measurement will directly affect the accuracy of the cell inhibition time determination (see figure 2).

The radical concentrations of hydroxyl ($^{\cdot}OH$) and superoxide anion ($O_2^{\cdot-}$) in cell growth medium for different feed gas humidity settings and a plasma treatment time of 40 s were measured by electron paramagnetic resonance (EPR) spectroscopy. The protocol applied in this work is described in [45]. Due to the short lifetime of these radicals in liquid spin traps, 5-tert-Butoxycarbonyl-5-methyl-1-pyrroline-N-oxide (BMPO, Dojindo Laboratoire, Japan) and 5,5-dimethy-1-pyrroline-N-oxide (DMPO, Dojindo Laboratoire, Japan) were used. DMPO was solved in the RPMI cell culture medium to a concentration of 100mM. This spin trap cannot distinguish between hydroxyl radicals ($^{\cdot}OH$) and superoxide anion radicals ($O_2^{\cdot-}$). BMPO on the other hand distinguishes between both species. However, until now we were not able to obtain an EPR signal from BMPO in RPMI. Thus, experiments with BMPO were conducted by solving 10mM of BMPO in Dulbecco's phosphate buffered saline (DPBS) solution instead of RPMI. Each EPR measurement was repeated three times.

Parallel to the above mentioned measurements the pH value of 40 s plasma treated RPMI solution was measured directly after plasma treatment using a pH meter (Sevenmulti M47, Mettler Toledo, Switzerland).

2.6. Relating H_2O_2 concentration to cell viability

To answer the question, whether plasma generated H_2O_2 correlates with the viability of indirectly treated adherent human keratinocytes (HaCaT cells), inhibition measurements are taken from figure 12 in [17]. This inhibition curve depicts how long a cell culture needs to be treated by the argon plasma jet at a certain feed gas humidity concentration in order to inhibit 50% of the cell metabolic activity. For instance, at completely dry conditions a plasma treatment duration of about 45 s is necessary to reach this inhibition level whereas at a significantly higher humidity concentration of 1250 ppm half the cells lose their viability already after a treatment time of 16 s. In order to relate H_2O_2 measurements with these data the inhibition concentration of H_2O_2 was determined. Therefore, the same HaCaT cell type was handled identically as in [17] with the difference that the cells were not covered with a plasma treated RPMI medium but with an RPMI medium containing different well defined H_2O_2 concentrations. These concentrations were produced by diluting 30% H_2O_2 stock solution (9.7 M, Merck, Germany) in RPMI. As a result, the H_2O_2 concentration to inhibit 50% of HaCaT cells was determined as $(21 \pm 4)\,\mu\text{M}$ (solid horizontal line in figure 2, corresponding to $(0.71 \pm 0.14)\,\text{mg l}^{-1}$). The uncertainty interval (horizontal dashed lines) is the standard deviation of 8 measurements.

Figure 2 also shows the increase of the H_2O_2 concentration in the RPMI cell growth medium for a plasma jet treatment with dry argon feed gas after different treatment times. From the intercept point of this curve with the solid horizontal line the half inhibition treatment time is deduced. At this time point of plasma treatment duration, the H_2O_2 concentration due to plasma treatment reaches $21\,\mu\text{M}$ and is as high as the H_2O_2 concentration to inhibit half of the HaCaT cells. Every plasma treatment that will produce this H_2O_2 level after a certain treatment time will inhibit at least half of the HaCaT cells. Moreover, if the treatment time to inhibit half of the HaCaT cells by plasma is similar to the time in which the H_2O_2 concentration due to the plasma treatment increased up to $21\,\mu\text{M}$, then H_2O_2 plays the major role in modulating cellular activities.

The method to estimate the uncertainty of the half inhibition treatment time is also indicated in figure 2. The lower and upper error is obtained by evaluating the intercept points of the H_2O_2 inhibition concentration uncertainty and the error interval of the plasma generated H_2O_2 measurement.

3. Results and discussion

3.1. Generation of H_2O_2 in the gas phase

A FTIR spectrum of the exhaust argon jet plasma gas is presented in figure 3 for a feed gas humidity concentration of 1220 ppm together with the resulting fit curve. The most dominant absorption in this spectrum is given by H_2O_2. Furthermore, distinct absorption bands of ozone (O_3) were obtained. Both band structures, H_2O_2 and O_3, were fitted and their concentration in the multipass cell was calculated. For this particular humidity setting the concentration of H_2O_2 and O_3 are 3.6 ppm and 2.0 ppm, respectively. Despite the long purging procedure and careful background acquisition CO_2 absorption bands originating from ambient impurities are detectable. The spectral range from 1350 to 1700 cm^{-1} is also influenced by ambient water absorption bands which influence the quantitative evaluation of other molecular absorption bands in that region. Even though nitrogen dioxide (NO_2) was also identified in the spectrum, it could not be evaluated quantitatively due to its small signal and the overlapping water bands.

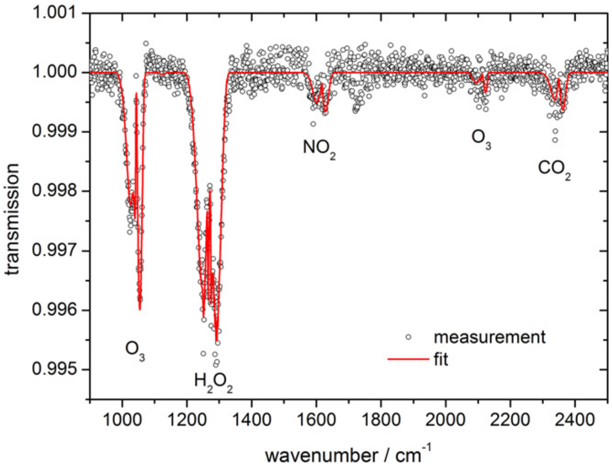

Figure 3. FTIR spectrum in the far field of an atmospheric pressure argon plasma jet for a feed gas humidity of 1220 ppm measured in a multipass cell with an absorption length of 19.2 m and a pressure of 100 mbar. Absorption bands of ozone, hydrogen peroxide, nitrogen dioxide and carbon dioxide were detected. The fit was performed by using the Hitran database. For clarity every fifth measurement point is shown.

Evaluating the H_2O_2 absorption band for every adjusted feed gas humidity value leads to the H_2O_2 concentration curve, which is displayed in figure 4(*a*). With increasing humidity in the argon feed gas the H_2O_2 concentration in the multipass cell rises from almost zero for dry feed gas condition to a concentration of 5.3 ppm for a humidity setting of 1800 ppm. Additional to the measurement results in figure 4(*a*) the result of a simulation, based on the far field chemical reaction simulation reported in [37], is plotted. From that simulation, relevant production and destruction reactions for H_2O_2 were obtained. However, since the model aims to simulate particle densities in the far field of the jet without considering electron processes, it is difficult to include H_2O_2 generation processes that occur in the plasma jets core, where electrons play a major role. With only H_2O and Ar present in the core zone H_2O_2 formation occurs by recombination of $^{\cdot}OH$ radicals that are previously created by particle impact dissociation of water molecules according to [46]

$$H_2O + P \rightarrow {}^{\cdot}OH + {}^{\cdot}H + P \tag{2}$$

and

$$^{\cdot}OH + {}^{\cdot}OH + M \rightarrow H_2O_2 + M, \tag{3}$$

where *P* is an energetic particle from the plasma (e.g. electron or excited argon atom) and *M* is a collision partner (e.g. argon).

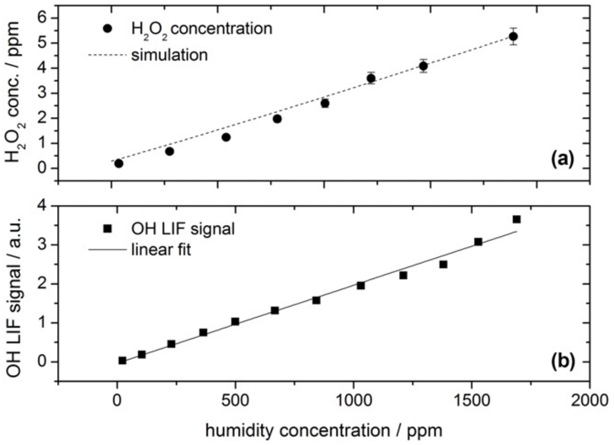

Figure 4. Results of absorption experiments in the gas phase. (*a*) H_2O_2 concentration in the multipass cell (far filed) and (*b*) relative LIF signal of the $^{\cdot}OH$ radical in dependence on the feed gas humidity (measured in plasma effluent). The $^{\cdot}OH$ LIF signal was fitted with a linear function whereas the dashed line in (*a*) is the simulation result.

The dissociation process of equation (2) cannot directly be included into the simulation. Even so, by considering the almost linear slope of the measured relative $^{\cdot}OH$ density (see figure 4(*b*)) and by varying the degree of dissociation of H_2O as long as, under consideration of all included reactions, the simulated H_2O_2 profile fits with the measured one, this shortcoming can be avoided. The experimental based simulation predicts a linear increase of the far field H_2O_2 concentration with rising humidity. This result, together with positive simulation benchmarks on other experimental data [37], indicates that the most relevant equations for describing the production and destruction of H_2O_2 are considered within the simulation. The fact that a slight H_2O_2 concentration is predicted for zero feed gas humidity, results from the model assumption of a 36% relative ambient humidity.

H_2O_2 cannot only be produced in the core region of the plasma. In the effluent plasma region ambient species like O_2 diffuse into the plasma zone and influence the plasma chemistry. Thus, atomic hydrogen ($H^{\cdot}$) reacts with molecular oxygen to form hydroperoxyl radicals ($HO_2^{\cdot}$)

$$^{\cdot}H + O_2 + M \rightarrow HO_2^{\cdot} + M. \tag{4}$$

The combination of two of these radicals

$$2HO_2^{\cdot} + M \rightarrow H_2O_2 + O_2 + M \tag{5}$$

leads to the production of H_2O_2. As discussed in Reuter *et al* the electron density and temperature in the effluent region is lower compared to the situation in the core plasma region [47]. Furthermore, the educts $^{\cdot}OH$ and $HO_2^{\cdot}$, important for the production of H_2O_2, strongly react with each other to form water and oxygen and are thus not available for H_2O_2 production. Both effects make the effluent region less efficient for H_2O_2 production as experimentally shown in [47]. It was shown by the help of the simulation that other reactions to form H_2O_2, for instance via the reaction of water and ozone, play only a minor role.

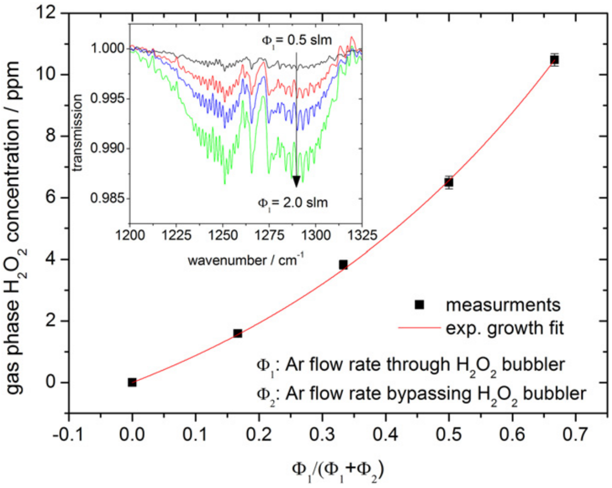

Figure 5. Gas phase H_2O_2 concentration increases as a consequence of higher argon flow rate through an H_2O_2 bubbler. No plasma is ignited in this experiment. As an inlay the FTIR transmission curves are given in the spectral range from 1200–1325 cm^{-1} for argon gas flow rates through the bubbler of 0.5, 1.0, 1.5 and 2.0 slm.

Besides H_2O_2 generation by the argon plasma jet, gas phase H_2O_2 was alternatively created by bubbling a fraction of the argon feed gas through a reservoir of hydrogen peroxide solution. The amount of gas phase H_2O_2 was adjusted by the ratio of the argon feed gas flow rate that passes the H_2O_2 bubbler and the total argon flow rate of 3 slm. The H_2O_2 concentration in the gas phase produced by this method is displayed in figure 5. The measured H_2O_2 spectrum, on which the concentration determination is based, is also given in figure 5 (inlay) for different flow rates through the H_2O_2 bubbler. When the gas flow rate through the bubbler is increased, more H_2O_2 molecules are present in the gas phase and consequently the transmission of radiation in the FTIR multipass cell decreases. Evaluating these transmission curves yields a rising H_2O_2 concentration curve, which is zero for no bubbling and 10.5 ppm when an argon flow rate of 2 slm passes through the H_2O_2 bubbler. The produced H_2O_2 concentrations are in the same range as the concentrations produced by the argon plasma jet for different feed gas humidity settings. An exponential growth function resembles the H_2O_2 concentration curve quite well. This non-linear behaviour is due to the increased bubble size and turbulence within the H_2O_2 bubbler with increasing gas flow rate, which leads to an increased interaction surface between the gas and liquid phases. This results in an increased amount of H_2O_2 molecules in the gas passing through the bubbler. Together with the rising mixing ratio of this H_2O_2 bubbled gas and the unbubbled gas, a disproportionate gas phase H_2O_2 concentration is obtained.

3.2. Transition of gas phase H_2O_2 into liquid phase

H_2O_2 can be generated in plasma treated liquids in different ways. Either it is created inside the liquid by plasma induced liquid chemistry processes or gas phase H_2O_2 is dissolved in the liquid. In the first case plasma generated agents like energetic radiation or particles transfer energy from the gas to

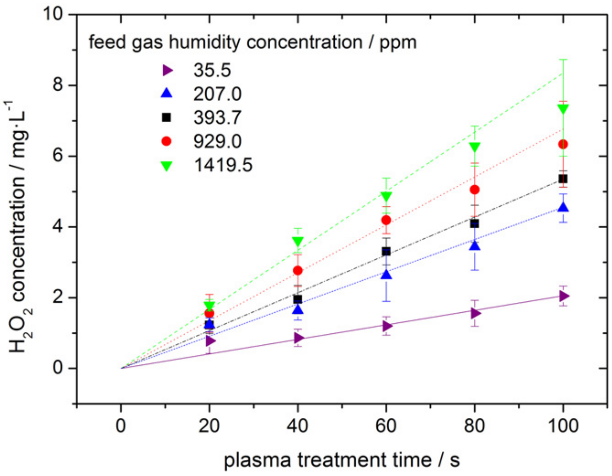

Figure 6. Increase of H_2O_2 concentration in 5 ml RPMI cell growth medium with plasma treatment time and for different feed gas humidity settings. The measurement was performed with colorimetric assays. The linear curves are results from linear regression.

the liquid phase and initiates the production of an $^{\cdot}$OH radical within the liquid. Two of these radicals can recombine to form H_2O_2.

If the solubility process dominates, a correlation between H_2O_2 production in the gas and liquid phase must exist. Therefore, the H_2O_2 net production rate P_g in s^{-1} in the gas phase is calculated from the measured concentrations c in ppm in the multipass cell according to

$$P_g = c \cdot 2.47 \times 10^{19}\,\text{cm}^{-3} \cdot (\Phi_1 + \Phi_2) \cdot 16.\bar{6}\,\text{cm}^3\,\text{s}^{-1}\,\text{slm}^{-1}, \tag{6}$$

where Φ_1 and Φ_2 are the feed gas flow rate (3 slm) and the curtain gas flow rate (5 slm), respectively. The factor 16.6 is due to the unit conversion of standard litre per minute into the SI unit $\text{cm}^{-3}\,\text{s}^{-1}$. The calculation of H_2O_2 net production rate P_L in the liquid cell growth medium is done by

$$P_L = \frac{A \cdot V_L \cdot N_A \cdot 10^{-3}}{M} \tag{7}$$

assuming a linear increase A (in $\text{mg}\,\text{l}^{-1}\,\text{s}^{-1}$) of H_2O_2 concentration with time. V_L in L is the volume of the treated medium, N_A is the Avogadro constant and M in g mol^{-1} is the molar mass of H_2O_2. According to figure 6, where the increase of H_2O_2 concentration in RPMI is displayed for different feed gas humidity settings, the assumption of a linear H_2O_2 increase with time is quite reasonable due to the good agreement of the measured values and the linear regression curves.

Figure 7 shows the result of the H_2O_2 net production rate determinations of the gas and liquid phases for different feed gas humidity settings. Interestingly, both curves are in a remarkable agreement.

This means that the H_2O_2 net production rate in the gas and liquid phases are identical for the investigated humidity conditions and implies that the presence of H_2O_2 molecules in the gas phase directly influences the liquid phase H_2O_2 concentration. Although this positive correlation is not proving that liquid phase H_2O_2 molecules originate from gas phase H_2O_2, at least it is strong evidence that in our experiment solubility processes play a major role in generating H_2O_2 in liquid.

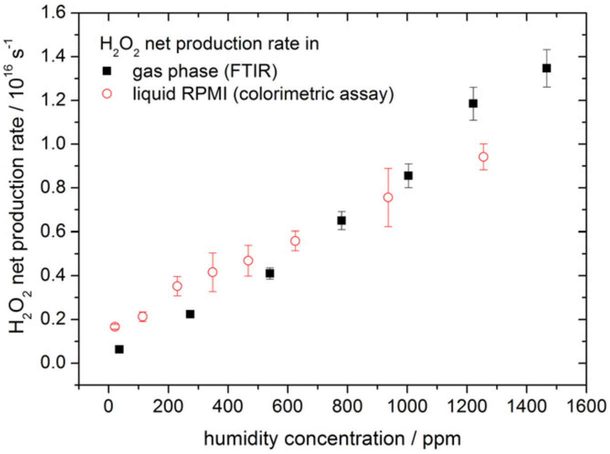

Figure 7. Net production rate of H_2O_2 molecules in the gas and liquid phase for different feed gas humidity settings.

In order to find further evidence for this indication an additional experiment was performed. If solubility processes determine the H_2O_2 concentration in plasma treated cell growth medium, then a simple non-plasma argon gas flow through the jet nozzle, containing the same H_2O_2 molecule density (in the multipass cell of the FTIR) as was generated by the humidified plasma jet, must result in the same liquid H_2O_2 concentration. In a first approximation, it is assumed that the H_2O_2 concentration above the liquid is identical for both the plasma generated and the bubbler produced H_2O_2. If plasma has a direct H_2O_2 production effect in addition to solubility processes on the cell growth medium, then the H_2O_2 concentration in the liquid will be higher for the plasma case than for the non-plasma case. As described in section 2, the non-plasma H_2O_2 generation was performed by using a H_2O_2 bubbler. The gas phase H_2O_2 concentrations for the plasma-on case (humidified argon gas) and for the H_2O_2 bubbler are taken from figures 4(*a*) and 5, respectively.

The results of this study are depicted in figure 8 for three different treatment times. With a rising H_2O_2 amount in the gas phase, the liquid phase H_2O_2 concentration increases. This general trend is independent whether the gas phase H_2O_2 is created by the plasma jet or by a H_2O_2 bubbler without any plasma. However, the resulting liquid phase H_2O_2 concentration is slightly higher for the plasma case. Especially for the longest investigated treatment time of 80 s, more liquid phase H_2O_2 is generated by the plasma jet than with the H_2O_2 bubbler at comparable gas phase H_2O_2 densities. Returning to the argumentation above, this discrepancy means that additional to the solubility of gas phase H_2O_2 in the liquid the plasma itself has a direct contribution to the liquid phase H_2O_2 amount. Thus, the hypothesis that entirely all hydrogen peroxide found in the liquid medium results from a solubility process of gas phase H_2O_2, is falsified. The amount of this direct plasma contribution, however, is smaller than the effect obtained by the H_2O_2 bubbler. On average, more than 60 % of

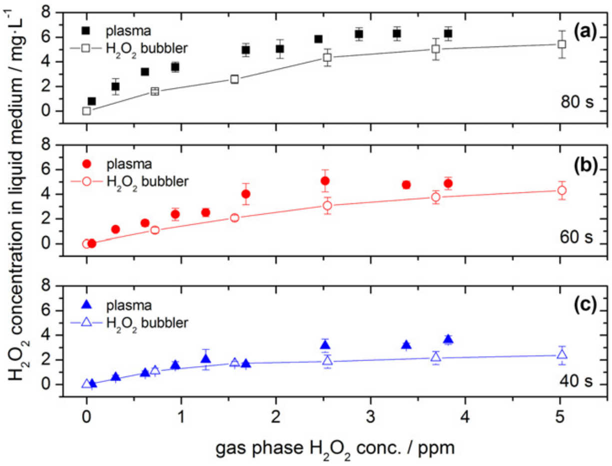

Figure 8. Influence of gas phase H_2O_2 on the H_2O_2 concentration in liquid medium. The RPMI cell growth medium was treated (*a*) 80 s, (*b*) 60 s or (*c*) 40 s by the argon plasma jet (full symbols) and by a non-plasma condition, where an argon gas flow was enriched with H_2O_2 molecules originating from a H_2O_2 bubbler (line connected open symbols). The corresponding gas phase H_2O_2 concentrations were obtained in the FTIR multipass cell (see figures 4(*a*) and 5) and do not represent the H_2O_2 concentration above the RPMI solution.

Table 1. Henry's constants at standard conditions for inorganic species present in gas or liquid phase in the current study.

Species	Henry's constant (mol l^{-1} Pa^{-1})	Reference
Oxygen (O_2)	1.2×10^{-8}	[49]
Argon (Ar)	1.4×10^{-8}	[50]
Nitrogen (N_2)	6.5×10^{-8}	[51]
Ozone (O_3)	1.1×10^{-7}	[52]
Nitrogen dioxide (NO_2)	4.0×10^{-7}	[53]
Hydroxyl radical ($^{\cdot}OH$)	2.9×10^{-4}	[54]
Hydroperoxyl radical ($HO_2^{\cdot}$)	4.0×10^{-2}	[55]
Hydrogen peroxide (H_2O_2)	8.3×10^{-1}	[56]

the liquid phase H_2O_2 was generated without direct plasma effect. Thus, the solubility of gas phase H_2O_2 plays an important role for the generation of liquid phase H_2O_2—at least in our experimental setup.

The question, why the H_2O_2 solubility process is so dominant, is answered when comparing Henry's constant for solubility of different species (see table 1). According to Henry's law the concentration of a species in aqueous solution is proportional to its partial pressure over the liquid [48]. The proportionality factor is Henry's constant. The higher the value of this constant, the better molecules dissolve into the liquid. Compared to argon or oxygen Henry's constant is more than 7 orders of magnitude higher for H_2O_2. In fact, H_2O_2 has one of the highest Henry's constants compared with other inorganic species. Hence, a gas phase H_2O_2 molecule in proximity to an aqueous solution will most likely enter it.

3.3. Stability of plasma generated H_2O_2 in RPMI

In principle, to have an effect on adherent cells the H_2O_2 molecule or its decomposition products must live long enough to reach the cells or be produced by post-plasma treatment reactions. Possible decomposition products like $^{\cdot}OH$ or $O_2^{\cdot-}$ have an extremely short lifetime. In biological systems the hydroxyl radical has a lifetime in the nanosecond and the superoxide anion radical in the microsecond range [57]. Thus, to be effective they must be produced in direct proximity to the cell molecule to be attacked. Compared to this, the lifetime of plasma generated H_2O_2 is quite long as the measured data in figure 9 depict. As described in section 2.5 three different H_2O_2 starting concentrations were produced by plasma treatment. Afterwards the degradation of the plasma generated H_2O_2 was determined. For the first half hour after plasma treatment the H_2O_2 concentration stayed almost unchanged, independent of the concentration reached directly after the plasma treatment. However, after a sufficient period of time the concentration decreases. For the highest starting value the H_2O_2 concentration in the RPMI medium decreases from 9 down to 1.5 mg l^{-1} after 2000 min. No H_2O_2 concentration was measurable for the lower starting concentrations after that time. A possible reason for this decay is the decomposition of H_2O_2 via the Fenton reaction, since the cell growth medium contains iron.

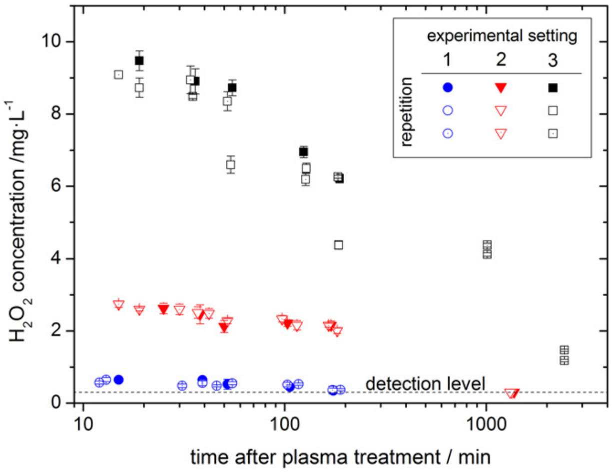

Figure 9. Stability of plasma produced H_2O_2 in RPMI medium in dependence of the time after the plasma treatment has finished. Experimental settings were: (1) feed gas humidity: <20 ppm, treatment time: 40 s, (2) feed gas humidity: <20 ppm, treatment time: 180 s, (3) feed gas humidity: 1660 ppm, treatment time: 80 s.

When performing this H_2O_2 life time experiment with H_2O_2 from stock solution that contains stabilizers, the concentration decrease is much lower. Within 120 h the H_2O_2 concentration decreases from an initial concentration of 10 to 6.7 mg l^{-1} (data not shown). For long time experiments this different behaviour of stock solution H_2O_2 and plasma generated H_2O_2 must be considered.

3.4. H_2O_2 correlates with inhibition of HaCaT cells

In figure 10, the half inhibition treatment time for different feed gas humidity settings is displayed for indirect plasma treatment (data taken from [17]) and for the case that the cell inhibition effect is based on H_2O_2 only. The data for

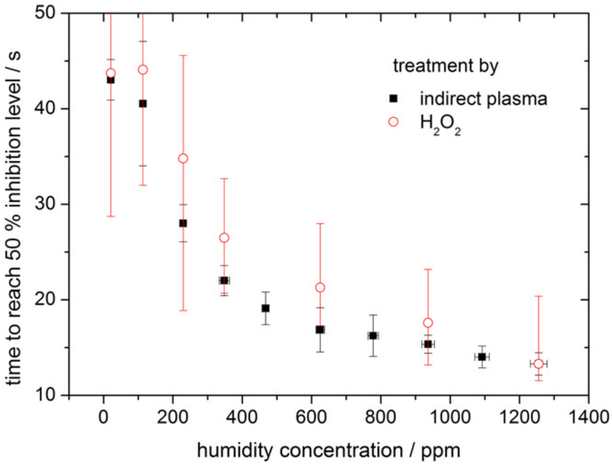

Figure 10. Time to reach 50% cell inhibition for different feed gas humidity concentrations. The results of indirect plasma treatment (data taken from [17], treatment time of the medium: 40 s) and for the case that H_2O_2 is the only agent agree remarkably well.

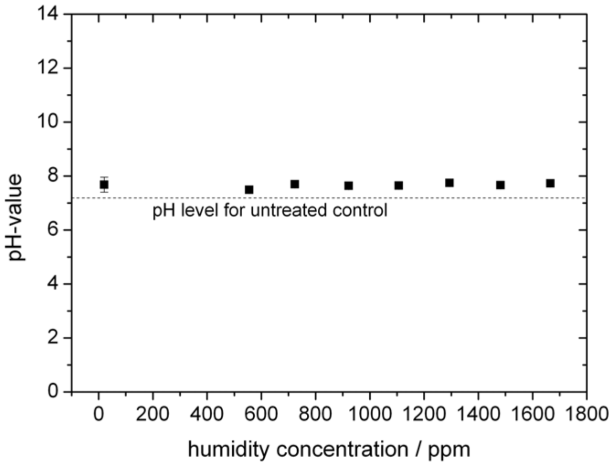

Figure 11. pH-value measured in RPMI after 40 s plasma treatment time for different feed gas humidity settings. The squares are the measurements after plasma treatment. The dashed line depicts the pH-value for the untreated control.

the latter is determined according to the procedure described in section 2.6. It is obvious that the effect of H_2O_2 not only follows the cell viability decrease but is almost identical to the effect that originates from plasma treatment. This means that for our treatment conditions H_2O_2 plays a dominant role for the inhibition of indirectly plasma treated HaCaT cells in RPMI cell growth medium. Whether this role has a direct H_2O_2 impact on the cells or is due to the impact of its decomposition products cannot be answered with this data. Either way, the amount of H_2O_2 produced within the liquid determines the viability of the cells. A similar effect of H_2O_2 on viability of human thyroid epithelial cells (HTori-3) was found by Marinov *et al* using a water discharge setup [58, 59].

Looking closer to the results in figure 10 the average time to reach the 50% inhibition level is slightly higher for the H_2O_2 case, which would mean that besides the H_2O_2 impact other agents must contribute to the cell inhibition. Owing to the large error bars the significance of this finding is debatable. However, to ensure the dominance of H_2O_2 measurements of pH-value and of $^{\cdot}OH$ and $O_2^{\cdot-}$ radical concentrations were also conducted.

Figure 11 shows the results for the pH-value. For different feed gas humidity settings no severe change in pH is observed and thus a contribution of pH to the cell inhibition is excluded. This was expected since the used cell growth medium is buffered. Only a general slightly elevated pH level is found when comparing the plasma treated values with the untreated control. This is due to a degassing effect [60]. During plasma treatment, the RPMI cell growth medium is strongly swirled by the feed gas flow and thus previously chemically bound CO_2 evaporates from the liquid. Since dissolved CO_2 can form carbonic acid within the liquid a lack of CO_2 leads to a more alkaline condition.

The radical concentrations for $^{\cdot}OH$ and $O_2^{\cdot-}$ in a plasma treated DPBS medium are shown in figure 12. With rising feed gas humidity little change in the radical concentration is observed. At most a slight decrease is detected. The $^{\cdot}OH$ and $O_2^{\cdot-}$ radical concentrations are between 0.2–0.3μM and 0.45–0.65μM, respectively. The observation that both concentrations do not increase with feed gas humidity implies two conclusions. Firstly, their production in the bulk medium is not directly or dominantly linked to the produced H_2O_2 concentration which itself increases with increasing feed gas humidity. If a direct link would exist the radicals are expected to resemble the H_2O_2 trend. Since this is not the case the radical production must be generated due to other plasma agents. Secondly, the bulk concentrations of $^{\cdot}OH$ and $O_2^{\cdot-}$ do not contribute directly to the inhibition of the investigated adherent HaCaT cells. However, since the measured concentrations are volume averaged values it might well be that directly at the cells the radical concentrations are quite inhomogeneous. Thus, their concentration might be much higher close to the cells than what is measured in the bulk medium.

It has to be mentioned that the presented EPR measurements were not performed in an RPMI medium, but in a DPBS medium while the other measurements were performed in RPMI. As discussed in section 2.5 this was due to the lack of signal obtained with the BMPO spin trap in RPMI. The spin trap BMPO is to be preferred since with it $^{\cdot}OH$ and $O_2^{\cdot-}$ radicals can be distinguished, whereas the spin trap DMPO only provides the sum of both radical densities. DMPO on the other hand was used in RPMI. In order to verify that the constant behaviour of both radicals with respect to the feed gas humidity is not only a DPBS specific observation the experiment was repeated in RPMI with a DMPO spin trap. The comparison of both measurements yielded that whether the sum of $^{\cdot}OH$ and $O_2^{\cdot-}$ density is obtained with BMPO in DPBS or with DMPO in RPMI the trends of both curves are identical (data not shown). Even the absolute concentrations are in good agreement. The combined radical concentration of $^{\cdot}OH$ and $O_2^{\cdot-}$ is only by a factor of less than two higher for the measurements of DMPO in RPMI. Thus, the results obtained in DPBS with the spin trap BMPO are transferable to the RPMI medium and are therefore relevant for the cell and H_2O_2 measurements performed in RPMI.

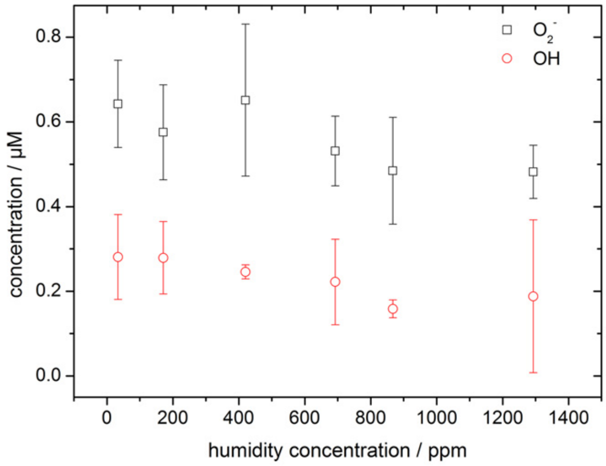

Figure 12. Radical concentrations of superoxide $O_2^{\cdot -}$ and hydroxyl $^{\cdot}$OH obtained by EPR spectroscopy in DPBS for different feed gas humidity concentrations. The plasma treatment time was 40 s.

Concluding this section, it was shown that plasma produced H_2O_2 correlates positively with the inhibition of adherent human skin cells. The concentrations of $^{\cdot}$OH and $O_2^{\cdot -}$ do not depend on the feed gas humidity and therefore do not correlate with the observed cell inhibition effect. As expected for the buffered cell growth medium no influence of pH value was detected. In the following it is discussed whether these findings can be generalized and what their impact for plasma medicine actually is.

Whenever H_2O_2 is generated by plasma treatment in a liquid medium it will affect human skin cells (as was shown in this work) and other cell types within this medium (as described in the introduction). However, the implication that H_2O_2 correlates in every case with an observed effect on cells and is therefore the only relevant agent in plasma medicine is not the correct conclusion. It was shown by Barton *et al* and Tresp *et al* with a similar plasma source that the viability of HaCaT cells, as well as of a monocyte cell line (THP-1), changes significantly when altering the nitrogen to oxygen surrounding gas ratio, while the H_2O_2 concentration in the medium stayed almost unchanged [61, 62]. Taking these results into account a more differentiated picture evolves. The strong role of H_2O_2 concerning cell viability is observable especially when the plasma parameter variation leads to a severe change of H_2O_2 concentration, as it is the case for feed gas humidity alteration. In other cases, where the resulting H_2O_2 level is zero or invariant against parameter variation, other effects on top of the H_2O_2 effect become visible. Hence, H_2O_2 is a quite an important molecule in plasma medicine concerning cell activity but not the only one.

4. Conclusion

In this work, the pathway of hydrogen peroxide was followed from its generation in the gas phase by a humidified argon atmospheric pressure plasma jet into liquid cell culture medium. For this, FTIR and LIF spectroscopy were applied to measure the gas phase H_2O_2 concentration and the relative $^{\cdot}$OH radical density in dependence of the feed gas humidity level. By means of an adapted far field simulation the most important production and destruction mechanisms of H_2O_2 were identified for the given experimental conditions. In the presented case, H_2O_2 is mainly produced inside the core plasma zone by the dissociation of water molecules. The resulting $^{\cdot}$OH radicals recombine to form H_2O_2.

By comparing the H_2O_2 net production rate in the gas and liquid phase a remarkable compliance was found. Moreover, by mimicking the H_2O_2 generation of the plasma jet with the help of an H_2O_2 bubbler it is concluded that the solubility of gas phase H_2O_2 plays a major role in generating hydrogen peroxide in the liquid. This finding is explained by the high Henry's constant of H_2O_2 compared to other present species.

The stability of this plasma generated and dissolved H_2O_2 was measured in the cell growth medium to exceed half an hour without changing. After 40 h however, almost no H_2O_2 was detected in the medium. Besides the physical and chemical focus on H_2O_2, its effect on the viability of adherent human skin cells was investigated. Pure plasma generated H_2O_2 has the similar effect on the cell viability than indirect plasma treatment. This finding was ensured by analysing the pH-value and liquid-borne radical densities of $^{\cdot}$OH and $O_2^{\cdot -}$ by EPR spectroscopy. Neither of those agents showed a significant dependence on the feed gas humidity variation. Hence, no correlation with cell viability is expected for bulk concentrations of these agents. This leaves H_2O_2 as the dominant species for our experimental conditions. Since experiments are known and discussed in this work where a variation of a biological marker does not correlate with H_2O_2 it is concluded that H_2O_2 is a quite important molecule in plasma medicine but not the only one.

Acknowledgments

This work is funded by German Federal Ministry of Education and Research (grant# 03Z2DN11 & 03Z2DN12). The authors thankfully acknowledge the valuable work of Liane Kantz, Sebastian Schlegel, Mattis Hänel, Sven Bordewick and Johannes von Saß.

References

[1] von Woedtke T, Reuter S, Masur K and Weltmann K D 2013 Plasmas for medicine *Phys. Rep.* **530** 291–320

[2] Laroussi M 2009 Low-temperature plasmas for medicine *IEEE Trans. Plasma Sci.* **37** 714–25

[3] Fridman G, Friedman G, Gutsol A, Shekhter A B, Vasilets V N and Fridman A 2008 Applied plasma medicine *Plasma Process. Polym.* **5** 503–33

[4] Kong M G, Kroesen G, Morfill G, Nosenko T, Shimizu T, van Dijk J and Zimmermann J L 2009 Plasma medicine: an introductory review *New J. Phys.* **11** 115012

[5] Babaeva N Y and Kushner M J 2013 Reactive fluxes delivered by dielectric barrier discharge filaments to slightly wounded skin *J. Phys. D: Appl. Phys.* **46** 025401

[6] Tian W, Norberg S, Babaeva N Y and Kushner M J 2013 The interaction of atmospheric pressure plasma DBDs and jets with liquid covered tissues: fluxes of reactants to underlying cells *Proc. 21st Int. Symp. Plasma Chemistry (Cairns)*

[7] Bruggeman P and Leys C 2009 Non-thermal plasmas in and in contact with liquids *J. Phys. D: Appl. Phys.* **42** 053001

[8] Yusupov M, Neyts E C, Simon P, Berdiyorov G, Snoeckx R, van Duin A C T and Bogaerts A 2014 Reactive molecular dynamics simulations of oxygen species in a liquid water layer of interest for plasma medicine *J. Phys. D: Appl. Phys.* **47** 025205

[9] Graves D B 2012 The emerging role of reactive oxygen and nitrogen species in redox biology and some implications for plasma applications to medicine and biology *J. Phys. D: Appl. Phys.* **45** 263001

[10] Pavlovich M J, Chang H-W, Sakiyama Y, Clark D S and Graves D B 2013 Ozone correlates with antibacterial effects from indirect air dielectric barrier discharge treatment of water *J. Phys. D: Appl. Phys.* **46** 145202

[11] Shimizu T, Sakiyama Y, Graves D B, Zimmermann J L and Morfill G 2012 The dynamics of ozone generation and mode transition in air surface micro-discharge plasma at atmospheric pressure *New J. Phys.* **14** 103028

[12] Kogelschatz U, Eliasson B and Egli W 1997 Dielectric-barrier discharges. Principle and applications *J. Phys. IV France* **7** 47–66

[13] Ehlbeck J, Schnabel U, Polak M, Winter J, von Woedtke T, Brandenburg R, von dem Hagen T and Weltmann K D 2011 Low temperature atmospheric pressure plasma sources for microbial decontamination *J. Phys. D: Appl. Phys.* **44** 013002

[14] Kalghatgi S, Fridman A, Azizkhan-Clifford J and Friedman G 2012 Damage in mammalian cells by non-thermal atmospheric pressure microsecond pulsed dielectric barrier discharge plasma is not mediated by ozone *Plasma Process. Polym.* **9** 726–32

[15] Haertel B, Straßenburg S, Oehmigen K, Wende K, von Woedtke T and Lindequist U 2013 Differential influence of components resulting from atmospheric-pressure plasma on integrin expression of human HaCaT keratinocytes *BioMed Res. Int.* **2013** 761451

[16] Sato T, Yokoyama M and Johkura K 2011 A key inactivation factor of HeLa cell viability by a plasma flow *J. Phys. D: Appl. Phys.* **44** 372001

[17] Winter J, Wende K, Masur K, Iseni S, Dünnbier M, Hammer M U, Tresp H, Weltmann K D and Reuter S 2013 Feed gas humidity: a vital parameter affecting a cold atmospheric-pressure plasma jet and plasma-treated human skin cells *J. Phys. D: Appl. Phys.* **46** 295401

[18] Bekeschus S, Kolata J, Winterbourn C, Kramer A, Turner R, Weltmann K D, Broker B and Masur K 2014 Hydrogen peroxide: a central player in physical plasma-induced oxidative stress in human blood cells *Free Radical Res.* **48** 542–9

[19] Halliwell B and Cutteridge J M C 1999 *Free Radicals in Biology and Medicine* (Oxford: Clarendon)

[20] Chance B, Sies H and Boveris A 1979 Hydroperoxide metabolism in mammalian organs *Physiol. Rev.* **59** 527–605

[21] de Groot H and Littauer A 1989 Hypoxia, reactive oxygen, and cell injury *Free Radical Biol. Med.* **6** 541–51

[22] Niethammer P, Grabher C, Look A T and Mitchison T J 2009 A tissue-scale gradient of hydrogen peroxide mediates rapid wound detection in zebrafish *Nature* **459** 996–9

[23] Aderem A and Underhill D M 1999 Mechanisms of phagocytosis in macrophages *Annu. Rev. Immunol.* **17** 593–623

[24] Bogdan C, Röllinghoff M and Diefenbach A 2000 Reactive oxygen and reactive nitrogen intermediates in innate and specific immunity *Curr. Opin. Immunol.* **12** 64–76

[25] Dahlgren C and Karlsson A 1999 Respiratory burst in human neutrophils *J. Immunol. Methods* **232** 3–14

[26] Lisanti M P, Martinez-Outschoorn U E, Lin Z, Pavlides S, Whitaker-Menezes D, Pestell R G, Howell A and Sotgia F 2011 Hydrogen peroxide fuels aging, inflammation, cancer metabolism and metastasis *Cell Cycle* **10** 2440–9

[27] Imlay J A and Linn S 1988 DNA damage and radical toxicity *Science* **240** 1302–9

[28] Jaruga P and Dizdaroglu M 1996 Repair of products of oxidative DNA base damage in human cells*Nucleic Acid Res.* **24** 1389–94

[29] Hinshaw D B, Sklar L A, Bohl B, Hyslop P A, Rossi M W and Spragg R G 1986 Cytoskeletal and morphologic impact of cellular oxidant injury *Am. J. Pathol.* **123**

[30] Simon R H, Scoggin C H and Patterson D 1981 Hydrogen peroxide causes the fatal injury to human fibroblasts exposed to oxygen radicals *J. Biol. Chem.* **256** 7181–6

[31] Weiss S J, Young J, LoBuglio A F, Slivka A and Nimeh N F 1981 Role of hydrogen peroxide in neutrophil-mediated destruction of cultured endothelial cells*J. Clin. Invest.* **68** 714–21

[32] Hasse S, Gibbons N C J, Rokos H, Marles L K and Schallreuter K U 2004 Perturbed 6-tetrahydrobiopterin recycling via decreased dihydropteridine reductase in vitiligo: more evidence for H_2O_2 stress *J. Invest. Dermatol.* **122** 307–13

[33] Ueda J, Saito N, Shimazu Y and Ozawa T 1996 A comparison of scavenging abilities of antioxidants against hydroxyl radicals *Arch. Biochem. Biophys.* **333** 377–84

[34] Hampton M B and Orrenius S 1997 Dual regulation of caspase activity by hydrogen peroxide: implications for apoptosis *FEBS Lett.* **414** 552–6

[35] Weltmann K D, von Woedtke T, Hähnel M, Stieber M and Brandenburg R 2010 Atmospheric-pressure plasma sources: prospective tools for plasma medicine *Pure Appl. Chem.* **82** 1223–37

[36] Reuter S, Winter J, Iseni S, Peters S, Schmidt-Bleker A, Dünnbier M, Schäfer J, Foest R and Weltmann K D 2012 Detection of ozone in a MHz argon plasma bullet jet *Plasma Sources Sci. Technol.* **21** 034015

[37] Schmidt-Bleker A, Winter J, Iseni S, Dünnbier M, Weltmann K D and Reuter S 2014 Reactive species output of a plasma jet with shielding gas device—combination of FTIR absorption spectroscopy and gas phase modelling *J. Phys. D: Appl. Phys.* **47** 145201

[38] Dilecce G and De Benedictis S 2011 Laser diagnostics of high-pressure discharges: laser induced fluorescence detection of OH in He/Ar–H_2O dielectric barrier discharges *Plasma Phys. Control. Fusion* **53** 124006

[39] Verreycken T, van der Horst R M, Sadeghi N and Bruggeman P J 2013 Absolute calibration of OH density in a nanosecond pulsed plasma filament in atmospheric pressure He–H_2O: comparison of independent calibration methods *J. Phys. D: Appl. Phys.* **46** 464004

[40] Voráč J, Dvořák P, Procházka V, Ehlbeck J and Reuter S 2013 Measurement of hydroxyl radical (OH) concentration in an argon RF plasma jet by laser-induced fluorescence *Plasma Sources Sci. Technol.* **22** 025016

[41] Verreycken T, Mensink R, Horst R v d, Sadeghi N and Bruggeman P J 2013 Absolute OH density measurements in the effluent of a cold atmospheric-pressure Ar–H_2O RF plasma jet in air *Plasma Sources Sci. Technol.* **22** 055014

[42] Williams L R and Crosley D R 1996 Collisional vibrational energy transfer of OH ($A\,^2\Sigma^+$, $v' = 1$) *J. Chem. Phys.* **104** 6507

[43] Rothman L S *et al* 2005 The HITRAN 2004 molecular spectroscopic database *J. Quant. Spectrosc. Radiat. Transfer* **96** 139–204

[44] Zimmermann H 2010 QMACSoft-HT (computer program)

[45] Tresp H, Hammer M U, Winter J, Weltmann K D and Reuter S 2013 Quantitative detection of plasma-generated radicals in

liquids by electron paramagnetic resonance spectroscopy *J. Phys. D: Appl. Phys.* **46** 435401

[46] Bruggeman P and Schram D C 2010 On OH production in water containing atmospheric pressure plasmas *Plasma Sources Sci. Technol.* **19** 045025

[47] Reuter S, Winter J, Iseni S, Schmidt-Bleker A, Dünnbier M, Masur K, Wende K and Weltmann K D 2014 The influence of feed gas humidity versus ambient humidity on atmospheric pressure plasma jet-effluent chemistry and skin cell viability *IEEE Trans. Plasma Sci.* in press

[48] Sander R 1999 *Compilation of Henry's Law Constants for Inorganic and Organic Species of Potential Importance in Environmental Chemistry* Version 3 www.henrys-law.org

[49] Carpenter J H 1966 New measurements of oxygen solubility in pure and natural water *Limnol. Oceanogr.* **11** 264–77

[50] Morrison T J and Johnstone N B 1954 Solubilities of the inert gases in water *J. Chem. Soc.* 3441–6

[51] Wilhelm E, Battino R and Wilcock R J 1977 Low-pressure solubility of gases in liquid water *Chem. Rev.* **77** 219–62

[52] Kosak-Channing L F and Helz G R 1983 Solubility of ozone in aqueous solutions of 0–0.6M ionic strength at 5–30 °C *Environ. Sci. Technol.* **17** 145–9

[53] Lee Y-N and Schwartz S E 1981 Reaction kinetics of nitrogen dioxide with liquid water at low partial pressure *J. Phys. Chem.* **85** 840–8

[54] Berdnikov V M and Bazhin N M 1970 Oxidation–reduction potentials of certain inorganic radicals in aqueous solutions *Russ. J. Phys. Chem.* **44** 395–8 English translation

[55] Hanson D R, Burkholder J B, Howard C J and Ravishankara A R 1992 Measurement of OH and HO_2 radical uptake coefficients on water and sulfuric acid surfaces *J. Phys. Chem.* **96** 4979–85

[56] O'Sullivan D W, Lee M, Noone B C and Heikes B G 1996 Henry's law constant determinations for hydrogen peroxide, methyl hy-droperoxide, hydroxymethyl hydroperoxide, ethyl hydroperoxide, and peroxyacetic acid *J. Phys. Chem.* **100** 3241–7

[57] Pryor W A 1986 Oxy-radicals and related species: their formation, lifetimes, and reactions *Ann. Rev. Physiol.* **48** 657–67

[58] Marinov I and Rousseau A 2013 personal communication

[59] Marinov I 2013 Plasmas in contact with liquids and at the interfaces. Application for living cell treatment *PhD Thesis* Paris, France: École Polytechnique, Laboratoire de Physique des Plasmas

[60] Buxton G V and Elliot A J 1986 Rate constant for reaction of hydroxyl radicals with bicarbonate ions *Int. J. Radiat. Appl. Instrum.* C **27** 241–3

[61] Barton A, Wende K, Bundscherer L, Weltmann K D, Lindequist U and Masur K 2013 Non-thermal atmospheric pressure plasma treatment of human cells: the effect of ambient conditions *Proc. 21st. Int. Symp. Plasma Chem. (Cairns)*

[62] Tresp H, Hammer M U, Weltmann K D, Winter J and Reuter S 2014 Effects of atmosphere composition and liquid type on plasma generated reactive species in biologically relevant solutions *Plasma Med.* in press

5.6 Article VI

Numerical analysis of the effect of nitrogen and oxygen admixtures on the chemistry of an argon plasma jet operating at atmospheric pressure

doi:10.1088/1367-2630/17/3/033003

New Journal of Physics
The open access journal at the forefront of physics

Deutsche Physikalische Gesellschaft DPG
IOP Institute of Physics
Published in partnership with: Deutsche Physikalische Gesellschaft and the Institute of Physics

CrossMark

OPEN ACCESS

RECEIVED
8 September 2014

REVISED
26 January 2015

ACCEPTED FOR PUBLICATION
27 January 2015

PUBLISHED
3 March 2015

PAPER

Numerical analysis of the effect of nitrogen and oxygen admixtures on the chemistry of an argon plasma jet operating at atmospheric pressure

W Van Gaens[1], S Iseni[2,3], A Schmidt-Bleker[2,3], K-D Weltmann[3], S Reuter[2,3] and A Bogaerts[1,4]

[1] Research group PLASMANT, Department of Chemistry, University of Antwerp, Universiteitsplein 1, B-2610 Antwerp, Belgium
[2] Centre for Innovation Competence Plasmatis, Felix-Hausdorff-Str. 2, D-17489 Greifswald, Germany
[3] Leibniz Institute for Plasma Science and Technology INP Greifswald e.V., Felix-Hausdorff-Str. 2, D-17489 Greifswald, Germany
[4] Author to whom any correspondence should be addressed.

E-mail: stephan.reuter@inp-greifswald.de **and** annemie.bogaerts@uantwerpen.be

Keywords: modelling, plasma jet, kinpen, infrared quantum cascade laser absorption spectroscopy, admixture, atmospheric pressure

Supplementary material for this article is available online

Abstract

In this paper we study the cold atmospheric pressure plasma jet, called kinpen, operating in Ar with different admixture fractions up to 1% pure N_2, O_2 and $N_2 + O_2$. Moreover, the device is operating with a gas curtain of dry air. The absolute net production rates of the biologically active ozone (O_3) and nitrogen dioxide (NO_2) species are measured in the far effluent by quantum cascade laser absorption spectroscopy in the mid-infrared. Additionally, a zero-dimensional semi-empirical reaction kinetics model is used to calculate the net production rates of these reactive molecules, which are compared to the experimental data. The latter model is applied throughout the entire plasma jet, starting already within the device itself. Very good qualitative and even quantitative agreement between the calculated and measured data is demonstrated. The numerical model thus yields very useful information about the chemical pathways of both the O_3 and the NO_2 generation. It is shown that the production of these species can be manipulated by up to one order of magnitude by varying the amount of admixture or the admixture type, since this affects the electron kinetics significantly at these low concentration levels.

1. Introduction

The cold atmospheric pressure radio frequency (RF) plasma jet is considered to be a promising technology in a wide range of biological and medical applications [1]. The underlying chemistry, however, is complex and requires characterization on multiple levels to ensure an efficient and a safe treatment.

First, it is necessary to understand how the geometry of the device and the operating conditions (e.g., gas flow velocity, duty cycle and air admixtures) affect the chemical composition of the gas effluent [2–13]. Second, it is important to know how the chemical composition of the gas phase changes when it comes into contact with a solid/liquid biological sample and passes through this interphase [14–17]. Third, it needs to be understood how the reactive species, i.e. reactive oxygen and nitrogen species (ROS and RNS), affect the biochemical processes and change the structure of biomolecules [19–21].

In this work we focus on the gas phase chemistry and the formation of biologically active species therein. More specifically, this study reports on the production of nitrogen dioxide (NO_2) and ozone (O_3) which are both identified as important RONS in plasma medicine applications.

When nitrogen oxides (NO_x) of the gas phase dissolve into the aqueous phase, they react further with water molecules to generate nitrite (NO_2^-), nitrate (NO_3^-), peroxynitrite ions ($ONOO^-$) and protons [17]. Although the exact ratio between the different NO_x and their reactivity depends on the pH of the biological sample, they generally cause oxidative reactions and are therefore highly bactericidal. The latter is also valid for O_3 generated

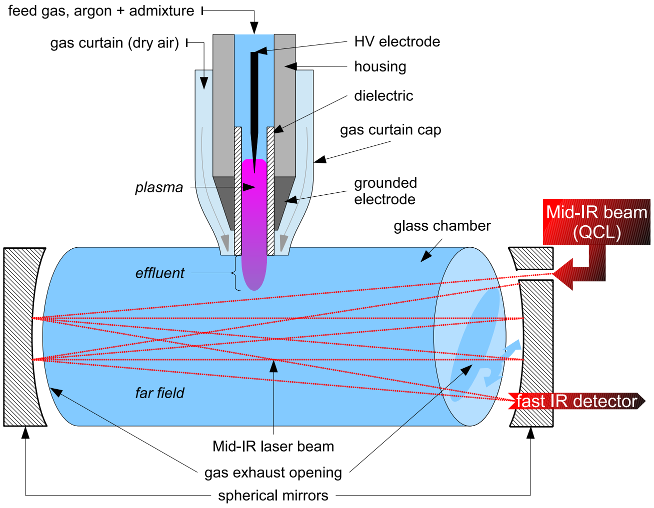

Figure 1. Sketch of the experimental setup illustrating the plasma source kinpen with the gas curtain cap connected with the diagnostic chamber of the QCL absorption setup located in a multipass cell.

in the gas phase, which causes oxidation of organic cell components in the aqueous phase. When O_3 enters the liquid phase it is converted into hydroxyl radicals (OH), especially at alkali conditions since O_3 is slightly more stable at acidic conditions. Furthermore, O_3 in the liquid is also rapidly decomposed by nitrite ions, forming nitrate ions [16]. However, it should be noted that O_3 in fact does not dissolve efficiently into liquid water. This might be compensated by the fact that it is a long-lived species in the gas phase and that, for most operating conditions [18], it is generated in high amounts in oxygen containing plasmas [15].

Besides the bactericidal properties of the RONS, these species are also important in other biological processes such as wound healing. Nitric oxide (NO) is an important signaling molecule for the wound healing process. Furthermore, nitrite ion formation can be important as it can act as storage form of NO [21]. At the right operating conditions, both NO and NO_2 can be generated in large quantities in the gas phase, as will be demonstrated in this paper. Moreover, in the liquid phase, NO_2 is rapidly converted into nitrite ions and thus indirectly contributes to the level of NO in the biological sample.

In this study we combine the results of laser infrared absorption measurements of NO_2 and O_3 in the plasma jet effluent with numerical simulations of the gas phase chemistry. Both methods are greatly complementary because the numerical simulations offer a very detailed insight in the discharge kinetics, although the complexity of the plasma processes is simplified in the model. For instance, some experimental input is used in the model to mimic the operating conditions correctly. Details about the experimental work and the model will be given in section 2.

The results of the measurements and the simulations for a range of operating conditions, i.e. different admixtures of O_2 and N_2 to the argon feed gas, are presented in section 3. Additionally, these results will be further discussed by means of a chemical analysis for O_3 and NO_2. The obtained information will result in a better control over the operating conditions and therefore a safer and more efficient methodology for plasma medicine.

2. Experimental setup and model description

2.1. Plasma source: kinpen

The room temperature, non-equilibrium atmospheric-pressure argon plasma jet considered in this work is a commercial device, the so-called kinpen (neoplas GmbH, Germany) [22, 23]. It is driven by 1 MHz RF electric excitation and can be described as a cold atmospheric pressure plasma jet [24].

Figure 1 depicts the basic geometrical and electrical configuration which consists of a high-voltage (HV) needle electrode centred within a dielectric capillary of radius 1.6 mm. The electrode potential is brought from 2 to 6 kV and dissipates an average power ranging from 0.9 to 2.2 W in the plasma (see also section 2.3).

A feed gas flow rate ranging from 0.5 to 3.0 slm of dry argon can be blown through the capillary and after excitation produces a visual plasma outside the nozzle between 0.3 and 15 mm length. The plasma length depends on the admixture type and fraction. Typically, O_2 and N_2 can be admixed to the feed gas up to 2.0%.

Also water vapour can be added to the feed gas in a smaller proportion (about 1400 ppm) to control the production of OH or hydrogen peroxide (H_2O_2) in the plasma and its effluent [11, 25].

In order to control the interaction of the plasma and its effluent with the surrounding atmosphere, an external gas flux is implemented by means of a gas curtain device. More information can be found in [4]. This gas curtain can be fed with different gases, however, for the purpose of this work dry air is used, only to keep the ambient humidity out of the active region, as reported in [26]. Additionally, the gas curtain enhances the reproducibility and the stability by excluding any variation of water vapour concentration which strongly depends on the location and time of operation. Furthermore, this gas curtain device is used to couple the plasma jet with the measurement chamber providing a similar atmosphere near the plasma effluent as in open conditions.

2.2. Quantum cascade laser absorption spectroscopy (QCLAS) diagnostic technique

Absolute density measurements of NO_2 and O_3 produced by the kinpen are performed by laser infrared absorption spectroscopy in the mid-infrared. The experimental setup is identical to the one we reported in previous work by Isni *et al* and which will be described briefly here [27].

The diagnostic apparatus is initially based on the Q-MACS system (neoplas control GmbH, Germany) although some optimizations were performed to allow investigations of plasma jets operating at atmospheric pressure [13, 27].

For the measurement of both species, NO_2 and O_3, a nanosecond single mode pulsed quantum cascade laser (QCL) is used as a mid-infrared source driven in inter-pulse mode [28, 29]. Unfortunately, pulsed QCLs have typically an emission range only within a few wavenumbers (about 5–15 cm^{-1}), whereas both NO_2 and O_3 have their absorption bands separated with a gap of about 600 cm^{-1}. Consequently, two different QCLs (Alpes Lasers SA, Switzerland) are used alternatively, emitting from 1607.72 to 1619.43 cm^{-1} and from 1024.5 to 1029.9 cm^{-1} to match the absorption band positions of NO_2 and O_3 respectively.

The intensity stability is enhanced by a Peltier element which permanently regulates the temperature. The tuning of the laser wavelength is performed by temperature variation induced by a fast current ramp. This method allows us to shift the laser wavelength over a range of 0.8 cm^{-1} in order to produce an absorption spectrum of many ro-vibrational transitions.

As the absorption properties of each molecule in the mid-infrared as well as the expected densities are rather low [30], a 60 cm multipass White cell is used in order to increase the absorption length. The laser beam is focused on the entrance of the multipass cell and is then reflected several times before reaching a very fast mercury cadmium telluride detector (Q-MACS IRDM-600A, neoplas control GmbH, Germany). The number of passes through the cell is tunable. In this work, a number of 32 passes and a total absorption length of 19.2 m is sufficient to observe a good absorption signal. The signal is acquired by a digitizer board controlled via a computer. The latter monitors the complete system by means of QMACSoft Monitor software [31].

Figure 1 illustrates the diagnostic bench and focuses on the coupling of the plasma source to the measurement chamber. In order to collect the reactive species produced by the plasma jet, a measurement chamber is mounted within the multipass cell. The chamber is a cylinder of 9.0 cm inner diameter and 57.5 cm length, yielding a volume of 3660 cm^3. It is made of glass in order to prevent reactions with the wall and thus reduces chemical losses.

The coupling of the plasma jet to the measurement chamber is achieved by an opening located at the half-height of the cylinder at the centre of the multipass cell to conserve symmetry between the two exhausts. The gas curtain cap mounted on the plasma device helps to keep the connection with the chamber tightened. It also provides air around the plasma effluent to reproduce the ambient conditions and prevent the chamber to be filled with argon.

As shown in figure 1, the mid-IR beam is reflecting on the multipass cell mirrors and passes through the chamber without interaction with the active visual plasma itself. The homogeneity of the gas mixture within the chamber has been checked in a previous work and confirmed by a numerical CFD model [27].

The absolute density measured within the chamber is determined as follows: the laser is tuned to scan a range of about 0.8 cm^{-1} yielding the absorption spectrum. The latter is fitted with a simulated spectrum based on the line strength reported in the HITRAN database [30, 32]. The procedure is automatically implemented through the QMACSoft Monitor software and allows a sample rate of 0.5 Hz in our experimental conditions. The absolute wavelength position and wavelength scale distortion during the laser tuning are corrected via a calibration procedure reported in [13]. Herein, a more detailed description of the fitting method is given.

In order to dry the pipes and the measurement chamber, the gas curtain was flushed with 5.0 slm dry air, at least 12 h before to start. Similarly, the argon pipes were flushed in advance with 0.5 slm for over 6 h. Indeed, water is known to have many broad absorption bands in the mid-IR which can lead to a significant disturbance and to an over-estimation of the production rates (or concentrations) of the species but also because even very low amounts of water will influence the plasma chemistry [9, 11, 26]. Moreover, this protocol enhances the repeatability and stability of the diagnostic.

From the measured densities n_i (cm^{-3}) of species i, the net production rates R_i:

$$R_i = n_i \times 8 \times 10^3/60 \text{ molec s}^{-1}$$

are calculated accounting for the total gas flux of 8 slm, i.e. combined curtain gas and argon feed gas flux.

2.3. Power

The power dissipated at the electrode is one of the key parameters to determine how much energy excites the electrons and it is a crucial input parameter for the simulations (see below).

In this work, the power measurement is performed in the same way as reported by Hofmann *et al* [33]. The current and voltage probes (Tektronix Tek CT-2 and Tek P6139A respectively) are installed before the matching coil directly on the kinpen electronics. Thus, current and voltage are recorded simultaneously with an oscilloscope (Tektronix DPO 4104) and allow the determination of the average power dissipated by the HV electrode. Losses induced by the coil and wires are taken into account following the protocol suggested in [33].

This results in a measured dissipated power ranging from 1.4 to 1.8 W in the case of impurity admixtures up to 1.0%. These values of dissipated power are in agreement with the power reported by other groups using similar argon RF atmospheric pressure plasma jets, i.e. with similar length and gas temperatures, geometry, gas flow rate, etc [24, 34].

2.4. Gas temperature

The gas temperature value is a crucial parameter for the application as it needs to be close to room temperature (a few millimeters from the nozzle) in order to avoid any thermal damage on the sample. Moreover, it is also important to know the evolution of the temperature throughout the plasma to be able to accurately model the reaction chemistry.

The gas temperature is measured with a non-metallic fiber-optics probe (diameter 1 mm) mounted on a three-axis linear table. The device determines the temperature by spectroscopically measuring the band gap of a GaAs crystal deposited at the tip of the optical fiber (FOTEMP1-OEM and TS3, Optocon AG, Germany). Unlike for metallic probes, there is no visible change in the emission of the plasma when the probe is brought in contact with the visible plasma. However, it is noted that with the probe merely average temperatures can be detected, while in a turbulent flow the local temperature can be expected to exhibit significant statistical fluctuations.

2.5. Admixture variation

The kinpen in this work is operated with 3.0 slm argon (99.999% purity) gas feed flow rate and an additional gas curtain of 5.0 slm dry air. The gas flow is regulated by mass-flow controllers (MFC, MKS Instruments, USA). To prevent any impurities and ambient humidity from penetrating the pipes and contaminating the argon, stainless-steel and PTFE gas tubes are used [11].

In this work, an admixture variation of O_2 and/or N_2 is applied from 0.0 to 1.0% of the total feed gas flow rate (0.0–30.0 sccm in absolute values, respectively). The purity is 99.995% for O_2 and 99.999% for N_2 according to the provider specifications (Air Liquide GmbH).

Additional water impurities may result from residual humidity in the tubing as well as diffusion through the tube walls. In the previous work [26] the resulting feed gas humidity was determined to be less than 20 ppm for this setup after flushing the tubes as specified in section 2.2. 1 ppm level water impurity in the feed gas was thus also included in the numerical model used in this work. Furthermore, the molecular admixtures N_2 and O_2 are expected to be much larger (0.1–1%) than the residual impurities from the gas bottles and the tubing and hence are expected to dominate the RONS chemistry.

The mixing of either of these molecular gases with argon is performed before the gas is blown through the plasma jet in order to obtain a better homogeneity. The admixture step is 0.1% (3.0 sccm) and controlled by calibrated mass-flow controllers.

Additionally, an artificial mixture of both N_2 and O_2 is also used in this work besides admixing both gases separately. Obviously, this should result again in a different gas composition of the plasma and the effluent. In this case, the argon/admixture ratio is fixed (Ar 99.0 + 1.0% admixture) but the content of the admixture fraction itself is varied from 0.0 to 100.0% O_2 with 100.0–0.0 % N_2. Hence, a 0.2% O_2/0.8% N_2 ratio is equivalent to a 1.0% dry air/99.0% argon admixture.

2.6. Model description

122 The numerical simulations are performed with a 0D chemical kinetics model which is based on the original GlobalKin source code, developed by Kushner and co-workers [35]. Previously we developed a large $Ar/N_2/O_2$

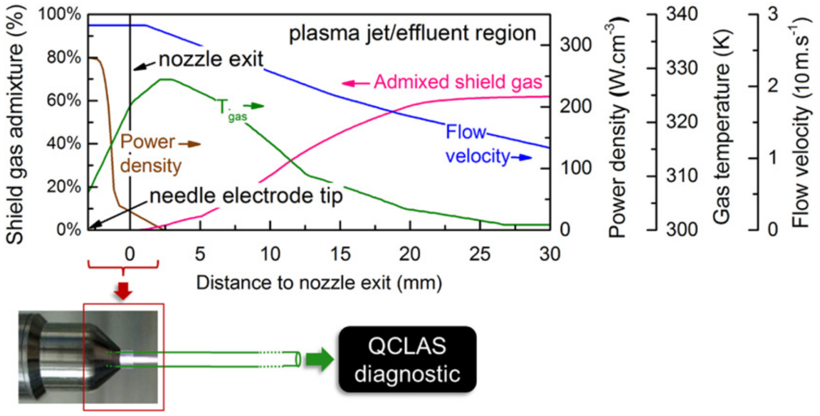

Figure 2. kinpen characteristics along the axial symmetry axis of the device. These profiles of the curtain gas diffusing into the argon feed gas stream, the power density, gas temperature and gas flow velocity are the input to our chemistry model and match either the experimental measurements or the fluid flow calculations (see text). The nozzle exit is located at the axial position of 0 mm. The powered needle electrode (and thus the highest power density) is located a few millimeters before this position. After the nozzle, the plasma jet can freely propagate and eventually enters the 'effluent' region when the power density has become zero and where the temperature drops to 300 K.

/H_2O reaction set of 85 species interacting by means of 302 electron impact reactions and 1626 heavy particle reactions. This extensive reaction set was presented previously [36] and for more details about this input data we refer to the supplementary information. This is necessary to calculate the densities of biomedically active species, which often have relatively low concentrations, within a broad parameter range. Some minor adjustments to the initial reaction set were reported by Van Gaens *et al* [9, 37].

Several modifications to the original code enable us to evaluate the species densities and chemical reaction pathways throughout the plasma jet propagating in an open humid air atmosphere. These modifications are thoroughly discussed in a previous paper [36], but the most important adjustments are briefly summarized below and in the appendix.

We assume that the active plasma species can be found within a cylindrical area along the plasma jet and its effluent, which has the same diameter as the inner diameter of the plasma jet tube. This area corresponds to the visual plasma jet and beyond (see figure 2). During the simulation, we track a cylinder segment that flows along the symmetry axis of the jet. The length of the segment is the distance that the gas travels within one time step of the calculations (order of μs). Since our model is 0D the plasma properties (such as the species densities) are volumetrically averaged over this cylinder segment.

The plasma properties for this cylinder segment will change when it moves further along the flow because it is subjected to a varying power deposition, flow velocity, gas temperature and impurities diffusing from the gas curtain, as a function of its position.

It is very important to mention that these plasma parameters are not calculated self-consistently within our model.

The gas flow velocity and the gas curtain entrainment rate follow from an external 2D computational fluid dynamics simulation of the neutral gas at room temperature using Reynolds-averaged Navier–Stokes equations with a standard k–ϵ model to account for the turbulence [38]. At a gas flow rate of 3 slm and a corresponding Reynolds number of Re $\approx$ 3000 the flow is expected to be fully turbulent. The computed ambient species densities agree well with mass spectrometric measurements [38–40].

In the far effluent region the gas will eventually become stationary and there we assume that the 3 slm argon feed gas is fully mixed with the 5 slm dry air of the gas curtain. However, it is obvious that there is also an admixture gradient of the gas curtain in the radial direction of the jet. As our model is 0D without a degree of freedom in the radial direction, we simply tested which of the admixture profiles (from different off-axis positions) resulted in the best agreement between the simulations and the measurements. Eventually, the gas curtain admixture profile at $r = 0.6$ mm (determined by the 2D fluid dynamics simulations) resulted in the best correspondence between the experimental and the calculated species densities. Due to this approximation some effects related to multiple dimensions might be neglected. In reality the situation is more complex as the propagation of the ionization wave is strongly linked to the turbulent flow pattern. It was recently found that the ionization wave preferentially propagates through the channel with the highest noble gas content and thus the lowest concentration of admixtures (in the order of 1% and lower) [39]. Moreover, as the ionization wave follows the vortices occurring in the turbulent flow, it is often positioned off-axis [41].

The power deposition profile within the device and the visual plasma obviously depends on the electric field generated by the electrodes and the plasma itself. It is greatly affected by the electrode setup, as was already demonstrated by this model in a previous work [9]. Because the electrode configuration of the kinpen has a very similar geometry, we use the same shape for the power deposition profile (see figure 2) but the magnitude of the power density is scaled down to match the operating conditions of the kinpen; we set the total power deposition equal to 1.5 W (see section 2.3). The power density determines in every timestep how much energy is transferred to the electrons in the electron energy equation.

Important is also that our power deposition profile shown in figure 2 does not explicitly take the RF excitation waveform into account. We apply this simplification since we are primarily interested in the dynamics of long-lived species and therefore neglect fluctuations on the sub-microsecond timescale. Thus, it should be sufficiently accurate that the total deposited power for the calculations is equivalent to the experimentally measured plasma power deposition, as long as the bulk chemistry does not change by neglecting the RF excitation. Our previous work showed that this assumption is valid for argon plasma jets operating at a higher frequency of 13.56 MHz [9, 42].

The experimentally measured gas temperature profile is plotted in figure 2 as well. We directly used the on-axis probe measurement, i.e., maximum temperature values, as described above and did not account for the effect of a radial gradient in the temperature. The gas temperature value can influence reaction rates since the coefficients are a function of this parameter. Also note that the experimental measurement (see section 2.4) indicates that the gas temperature already starts decreasing at a few millimeters from the nozzle exit. However, within the apparatus the temperature could not be measured accurately (with spatial resolution) and therefore needed to be estimated.

In some of our previous work a temperature profile that starts rising (from room temperature) at the needle tip position was used as an input, assuming that the temperature rise is mainly caused by exothermic reactions of highly reactive radicals or highly energetic species created by electron impact processes. Indeed, when the temperature is calculated by the 0D model itself, these processes cause a maximal temperature value at the same position, shortly after the nozzle exit. Nevertheless, we opted not to adopt the calculated temperature profile because it is not consistent with the experimentally measured values further into the effluent. The deviation is probably related to turbulent heat transfer.

The main advantage of our 0D semi-empirical approach is the possibility to implement the large chemistry set of an Ar/N_2/O_2/H_2O mixture necessary to simulate the kinetics of the biomedical species (which are often not the main plasma components) without excessive calculation times, and while staying close to the experimental conditions.

Evidently, this model needs a good validation by thorough comparison with experimental measurements, as previously demonstrated in Zhang *et al* [42] and Van Gaens *et al* [9]. In the latter paper, a good correspondence with the measured NO and O densities was presented for a kHz pulsed RF driven argon plasma jet with air admixtures. In Zhang *et al* [42] a good quantitative agreement was obtained for the O_3 density in an RF driven argon plasma jet with O_2 admixture. Note that in both studies this validation was done with spatial resolution along the symmetry axis of the jet.

3. Results and discussion

In this section the spectroscopically measured and numerically simulated O_3 and NO_2 net production rates in the far effluent of the plasma jet (measurement cell) are displayed and compared. In the following three subsections, this is done for N_2, O_2 or $N_2 + O_2$ admixtures, respectively. In each of these sections, we also present a detailed reaction kinetics analysis for both O_3 and NO_2 , as obtained from the model.

In the context of the comparison of these net production rates in the measurement cell (e.g. the values depicted in figure 3), it is important to mention that the model was previously only used for simulating the plasma jet and its effluent for a typical timescale of milliseconds. However, as the residence time of the plasma jet effluent within the measurement cell during sampling by the QCLAS is significantly longer (calculated to be around 25 s), we changed the end time for our simulations to 6 s, in order to allow for a correct comparison with the measured net production rates. At this point there are no drastic changes in the gas densities of O_3 and NO_2 anymore.

Additionally, it needs to be stressed that the values depicted in figure 3 (and similar figures below) are net production rates after 6 s residence time in the measurement chamber. This distinction has to be made in order to avoid any confusion with the values of figure 4 (and the consecutive similar figures) which represent the ongoing chemistry within a cylinder segment travelling within the plasma jet device, the active (visual) plasma jet and a first part of the effluent (i.e. a total of 10 ms). Also note that production and loss rates are presented separately in this type of graph unlike the net production rate shown in figure 3.

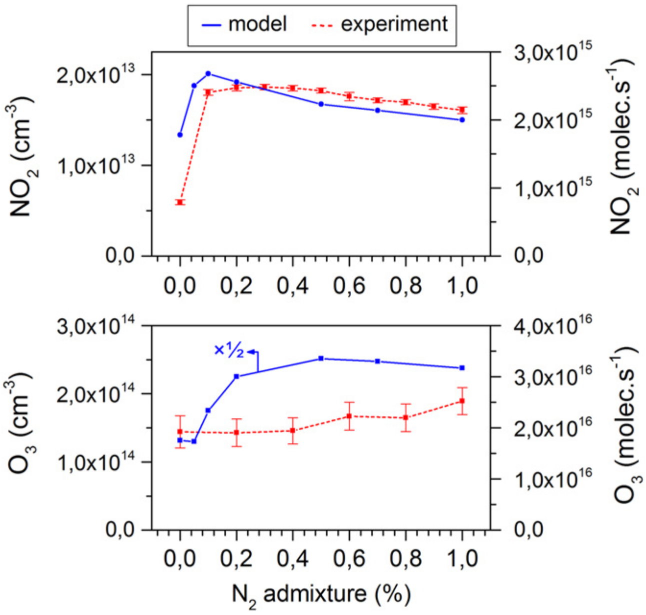

Figure 3. NO_2 and O_3 densities (left y-axis) or net production rates (right y-axis) after 25 s residence time in the measurement chamber as obtained by infrared absorption spectroscopy and the calculated data for a similar time scale (i.e. 6 s, after which the densities stay constant), for different N_2 fractions added to the argon feed gas.

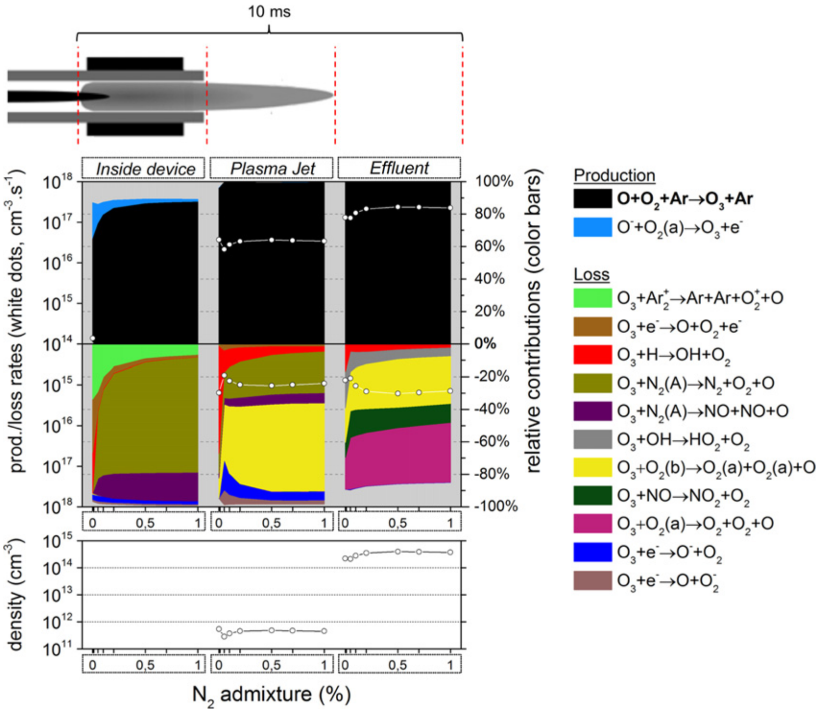

Figure 4. O_3 chemistry inside the device, the plasma jet and the initial effluent (10 ms in total), as a function of the N_2 admixture. Top graph: the white dots represent the total production/loss rates (cm^{-3} s^{-1}, left y-axis); the colour areas (linked to the right y-axis) represent for each region the spatially averaged relative contributions of the dominant reactions to the total production/loss. The production is plotted in the upper half and the loss in the lower half of the top graph. Note that the y-axis of the loss rates increases from top to bottom, hence opposite to the y-axis of the production rates, to clearly indicate their opposite effect. Bottom graph: spatially averaged O_3 densities in the three regions as a function of the N_2 admixture.

3.1. Nitrogen admixtures

Figure 3 (top) demonstrates a very good agreement between the experimentally measured and simulated NO_2 production rate, for the investigated range of N_2 admixtures between 0 and 1%: the trend as a function of the N_2 admixture and the absolute values are very similar, with at maximum a factor 2 difference for 0% N_2 .

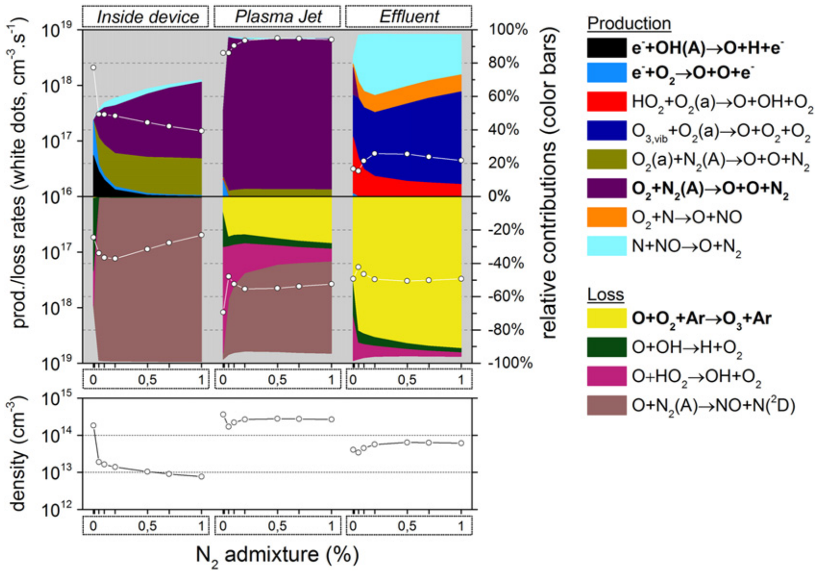

Figure 5. O chemistry inside the device, the plasma jet and the initial effluent (10 ms in total) as a function of the N_2 admixture (see figure 4 for an explanation about the top and bottom graph).

Unfortunately, this is not the case for the O_3 production rate where the difference is up to a factor 3 (see figure 3 (bottom)). Furthermore, the model predicts a steeply increasing O_3 production rate between 0 and 0.2% admixed N_2 , whereas the experiments indicate only a very slight increase over the entire operating range. Note that this might be explained by the fact that these O_3 concentrations are near the detection limit of the diagnostic setup under the present experimental conditions. Moreover, experimentally, very slight differences in the jet properties, such as turbulence or impurities in the tubes, can easily occur. This determines the concentration of molecular gases in the argon and therefore indirectly affects the O_3 concentrations. Indeed, we will show in this paper that the balance between production and loss rates is often very delicate and that a slight inaccuracy can have a large influence on the NO_2 and O_3 net production rate. In this context it needs to be mentioned that we chose to keep the gas curtain entrainment rate consistent for all the simulations, so for the different admixture amounts and for the different admixture gases.

We will now further clarify the production pathways of O_3 and NO_2 by means of a detailed chemical analysis, as obtained from the model, but now focussing mainly on the chemistry that occurs on the time scale of milliseconds. Indeed, this is the time frame where, chemically speaking, the most interesting changes happen. Obviously, this time frame corresponds to the distance that a gas element travels within the kinpen device, the active/visual plasma jet and finally the initial effluent region (thus not the entire measurement cell). The displayed values in figure 4–9 below (i.e. density, the total production and loss rates, the relative contributions of the reactions and electron temperature) are averages for one of these three regions, obtained by performing an integration along the symmetry axis of the jet. Accordingly, the most important chemical phenomena can be identified for each region.

For example, the density evolution of a species, from the vicinity of the needle electrode tip until the early effluent, is thus reduced to only three data points. Indeed, this turned out to be crucial for maintaining a relatively simple overview of the changing chemistry when varying the admixture ratios and at different distances from the nozzle and the needle tip. To make this concept easier to interpret, we added the schematic of the plasma jet above the reaction kinetics data in figure 4.

Also important is that in each figure the production rates are displayed in the upper part of the top graph and the loss rates in the bottom part of the top graph (both with white dots, left axis). Note that the y-axis of the loss rates increases from top to bottom, hence opposite to the y-axis of the production rates, to clearly indicate their opposite effect. The same top graph also displays the contribution of the different reactions to the total production and loss rates by colour areas (right axis). We only show the reactions which contribute more than 10% to the total loss or production of a species. Note that we show all these contributions, for the sake of completeness, but in the text we only discuss the most important production and loss processes. Therefore, the sum of the different contributions often does not reach the full 100%. The most important processes are indicated in bold in the legends at the right of the graphs. The bottom graph of these figures presents the species densities.

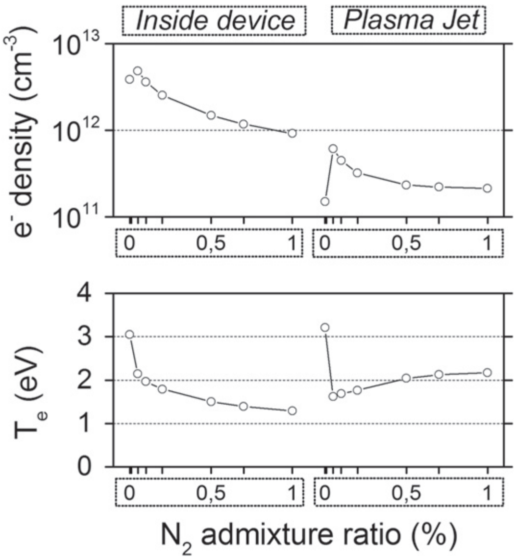

Figure 6. Spatially averaged electron densities (cm^{-3}) and average electron temperature (eV) inside the device and in the plasma jet, as a function of the N_2 admixture. The effluent region is not shown, as the electrons will be negligible in this region.

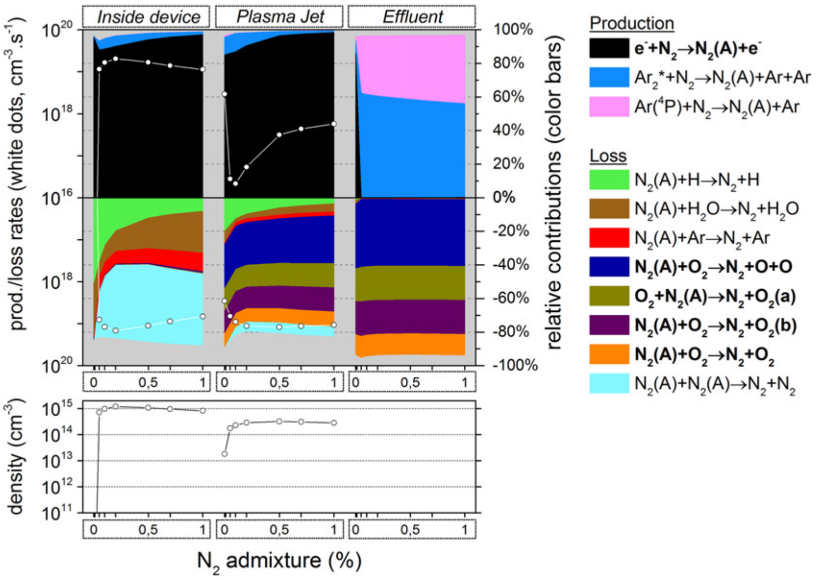

Figure 7. N_2 (A) chemistry inside the device, the plasma jet and the initial effluent (10 ms in total) as a function of the N_2 admixture (see figure 4 for an explanation about the top and bottom graph).

The short time-scale information in these plots (e.g. Figure 4) is, in general, sufficient to explain the trend observed on the longer time-scale (see figure 3).

3.1.1. O_3 formation

Figure 4 illustrates that O_3 is mainly formed in the effluent region (see white dots in the top graph) for all N_2 admixtures investigated. Indeed, the formation rate in the plasma jet is about one order of magnitude lower, and there is no O_3 formation at all inside the device. The figure shows the following dominant pathway:

$$O + O_2 + Ar \rightarrow O_3 + Ar. \tag{1}$$

It is clear from figure 4 that the production rate in the effluent region is more than two orders of magnitude higher than the loss rate (see upper and lower part of the top graph). Indeed, the main species responsible for the loss of O_3 are the electronically excited states $O_2(a)$ and $O_2(b)$ (see figure 4 as well), but they do not reach sufficiently high concentrations. The O_3 density as a function of the N_2 admixture in the early effluent therefore

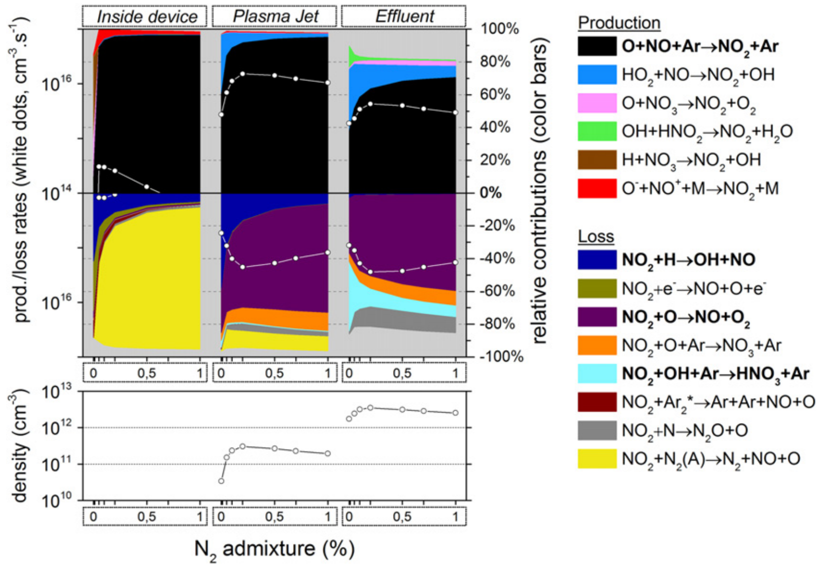

Figure 8. NO_2 chemistry inside the device, the plasma jet and the initial effluent (10 ms in total) as a function of the N_2 admixture (see figure 4 for an explanation about the top and bottom graph).

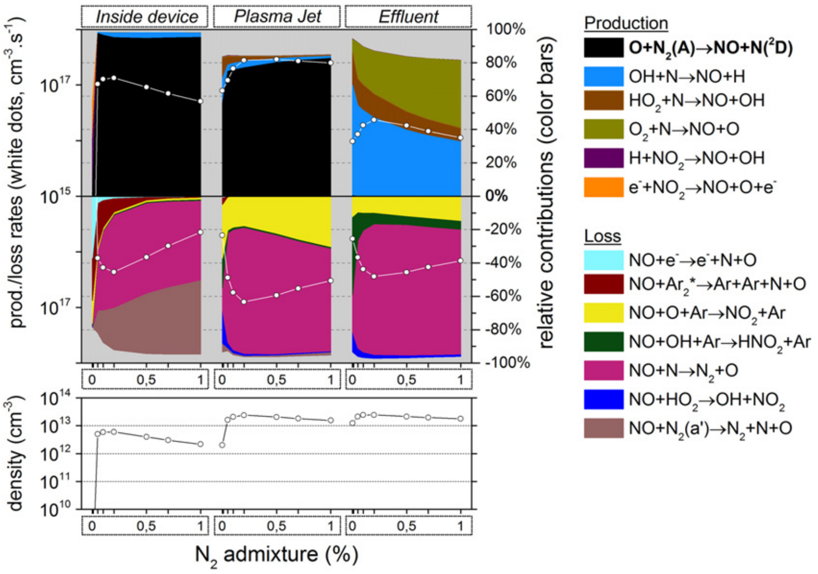

Figure 9. NO chemistry inside the device, the plasma jet and the initial effluent (10 ms in total) as a function of the N_2 admixture (see figure 4 for an explanation about the top and bottom graph).

corresponds to the production rate in the far effluent as predicted by the model and depicted in figure 3 (note the logarithmic scale in figure 4). Recall, however, that the agreement with the experimental result was not very good in this case.

As the O atoms are fully responsible for the O_3 production, we will now analyze the chemistry of this species.

Figure 5 illustrates that the variation of the O density as a function of the N_2 admixture is very similar to that of O_3. Furthermore, it can be seen that the O atom production occurs mainly in the plasma jet region. Indeed, in this region O_2 from the gas curtain starts to diffuse into the argon jet, as shown in [39, 40, 43].

Yet for 0% N_2 admixture, the O atom production inside the device is quite significant. Indeed, there is only some N_2 present in the form of impurities, because, as initial conditions of our simulations, we always impose a slight amount of N_2, O_2 and H_2O in the argon feed gas (1 ppm) to mimic the impurities in the gas bottles and desorbed molecules from the piping. This N_2 impurity level is insufficient to reduce the electron temperature as drastically as for cases with significant N_2 fractions (see figure 6), where a lot of energy is used for vibrational excitation of N_2. Fast electron impact dissociation of O_2 and electronically excited OH radicals, i.e. OH(A) created from H_2O, are therefore possible within the kinpen device at 0% N_2

$$e^- + O_2 \rightarrow e^- + O + O, \tag{2}$$

$$e^- + OH(A) \rightarrow e^- + O + H. \tag{3}$$

As a result, the O atom density is already significant within the kinpen device when no N_2 is admixed to the argon.

This also explains the maximum in the O atom density in the plasma jet region, at 0% N_2 , and the clear drop upon addition of small N_2 admixtures. However, at larger N_2 admixtures the O atom density increases again. Here, the O atoms are mainly created from collisions of O_2 species with the nitrogen metastable (N_2 (A)):

$$N_2(A) + O_2 \rightarrow 2\,O + N_2. \tag{4}$$

Moreover, in the plasma jet region the rates of the reactions (2) and (3) become insignificant for 0% N_2. This is because the electron density drastically drops as a result of electron attachment to oxygen species (see figure 6; note that the electron chemistry itself is, however, not explicitly shown in this paper) since the O_2 density quickly rises due to the mixing of curtain gas with the argon.

Note that figure 7 illustrates that $N_2(A)$ is also significantly quenched in this region but the quenching of this state is much slower than that of the electrons. Additionally, the rising O_2 density compensates for this $N_2(A)$ quenching and still causes the rate of reaction (4) to be high in the plasma jet region.

Besides, figure 7 also illustrates that N_2 (A) is mainly formed inside the kinpen device, i.e. by electron impact excitation of ground state N_2 :

$$e^- + N_2 \rightarrow e^- + N_2(A). \tag{5}$$

Thus one might expect a rising N_2 (A) density upon increasing N_2 admixture, simply because the density of one of the reactants becomes higher.

However, above 0.4% N_2 the electron density and electron temperature, plotted in figure 6, become quite low (due to the vibrational kinetics, as mentioned above) and this compensates for the rising N_2 density. This even causes a slight drop in the rate of reaction (5) above 0.4% N_2 and the same behavior is therefore seen for the N_2 (A) density in the bottom graph of figure 7. As a result the rate of reaction (4) (causing the dissociation of O_2 into O atoms in the plasma jet) will also first increase upon increasing N_2 fraction (after the initial drop, as explained above), but after 0.2% N_2 it will remain more or less constant (see figure 5). This explains the behaviour of the O atom density upon rising N_2 fraction, and because the O atoms are mainly responsible for the O_3 production, this also clarifies why the O_3 production and O_3 density first increase upon rising N_2 fraction, then remains more or less constant and eventually slightly decreases for N_2 fractions above 0.5% (see figure 4 and also figure 3 above).

The above explains the production rates predicted by the model. We believe that we at least identified all the dominant reactions correctly, although the agreement with the experiments is not perfect. Note that deviations can easily occur since the balance between the production and loss processes of all the species involved here is delicate. A more complete model approach might be better in this case.

3.1.2. NO_2 formation

Figure 8 illustrates the NO_2 production and loss rates, as well as the relative contributions of the different processes and the NO_2 density, as a function of N_2 admixture. It is clear that NO_2 is mainly produced from NO, especially by reaction (6), and to a lower extent also by reaction (7):

$$O + NO + Ar \rightarrow NO_2 + Ar, \tag{6}$$

$$HO_2 + NO \rightarrow OH + NO_2. \tag{7}$$

These processes are especially important in the plasma jet. Indeed, the total production rate of NO_2 is almost an order of magnitude larger than the total loss rate here. In the effluent region this production rate has already decreased by at least a factor 2, but additionally the loss rate (i.e. mainly the reaction $O + NO_2 \rightarrow NO + O_2$) is now of about the same magnitude. The net production rate is therefore much smaller in the effluent than in the plasma jet region.

Still, NO_2 is a rather long-lived species because there are no highly reactive species present in the effluent that are sufficiently abundant to cause considerable NO_2 loss within these time scales. Note that the O atoms are involved both in the main production and loss reactions of NO_2 and this species will eventually get depleted in the effluent region (see figure 5 above. The same is true for N, OH and HO_2, which are involved in several other loss processes).

Important to mention is that NO_2 reaches only its maximum concentration towards the end of the plasma jet region, whereas the density practically does not change any more in the effluent region and stays continuously

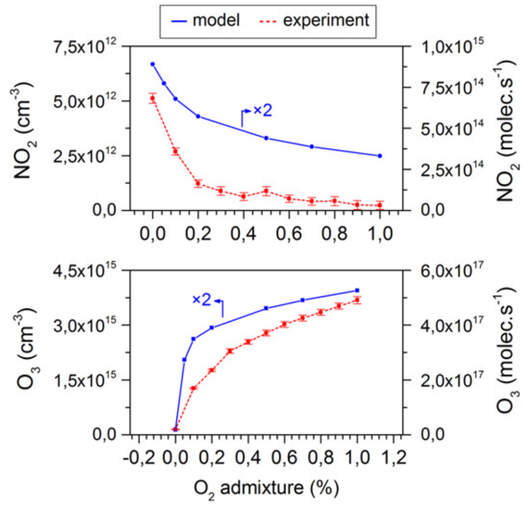

Figure 10. NO_2 and O_3 densities (left *y*-axis) or net production rates (right *y*-axis) after 25 s residence time in the measurement chamber as obtained by infrared absorption spectroscopy and the calculated data for a similar timescale (i.e. 6 s, after which the densities stay constant), for different O_2 fractions added to the argon feed gas.

high here. The averaging we performed thus results in a relatively low NO_2 density in the plasma jet region, although it is mainly produced here.

Because NO is the main NO_2 precursor, we show the NO chemistry in figure 9. NO is produced in large amounts early in the plasma jet region, by a reaction between N_2 (A) and O atoms:

$$N_2(A) + O \rightarrow NO + N(^2D). \tag{8}$$

The reason for this is twofold: first, the maximum N_2 (A) density is located close to the needle electrode where the power density is at maximum; further in the plasma jet it is rapidly quenched by O_2, thereby creating O atoms or excited O_2 molecules (see figure 7). Second, the O atoms only reach a maximum density in the plasma jet region, as illustrated in figure 5, because of the oxygen entrainment from the ambient into the argon, which obviously only starts after the nozzle exit. The combination of these two effects explains why the maximum rate of reaction (8) is located in the early plasma jet, close to the nozzle exit. Nevertheless, the production of NO by this reaction is also non-negligible inside the device, as is clear from figure 9.

As the excited N_2 (A) molecules mainly determine the NO formation, and NO is the dominant NO_2 precursor, the NO_2 production as a function of the N_2 admixture therefore largely follows the trend of the N_2 (A) state, which depends both on the N_2 fraction and on the electron temperature inside the kinpen device, as the latter determines the rate coefficient. Because the electron temperature (and hence the rate coefficient) drastically decreases upon increasing N_2 fraction, at least within the device (see figure 6 above), these two effects are opposite to each other.

Thus, the NO_2 production (and density) steeply rises immediately when small amounts of N_2 are added, but beyond 0.15% N_2 the NO_2 production (and density) drops again, because the effect of the electron temperature starts to play a more dominant role. Indeed, this explains the trend seen for the NO_2 production rate in figure 3 above.

3.2. Oxygen admixtures

This subsection is structured in exactly the same way as the previous one for nitrogen admixtures. We first look at the longer timescale, comparing experiments with simulations and consequently we explain the observed trends on the basis of a chemical reaction analysis of the short timescale.

The trends of both the NO_2 and the O_3 production rate as a function of the O_2 fraction in the argon feed gas (from 0 and 1%) are reproduced well by the model, as demonstrated in figure 10. The NO_2 production rate decays exponentially as a function of the O_2 fraction, while the O_3 trend is practically the inverse with a sharp increase between 0 and 0.2% O_2. The absolute values are, however, not fully comparable, although the difference is at most one order of magnitude within the investigated range of the O_2 fraction. As previously stated, this might be related to the inaccuracy on the amounts of curtain gas that diffuses into the jet (i.e. the absence of a radial gradient in the model or consequences of turbulence).

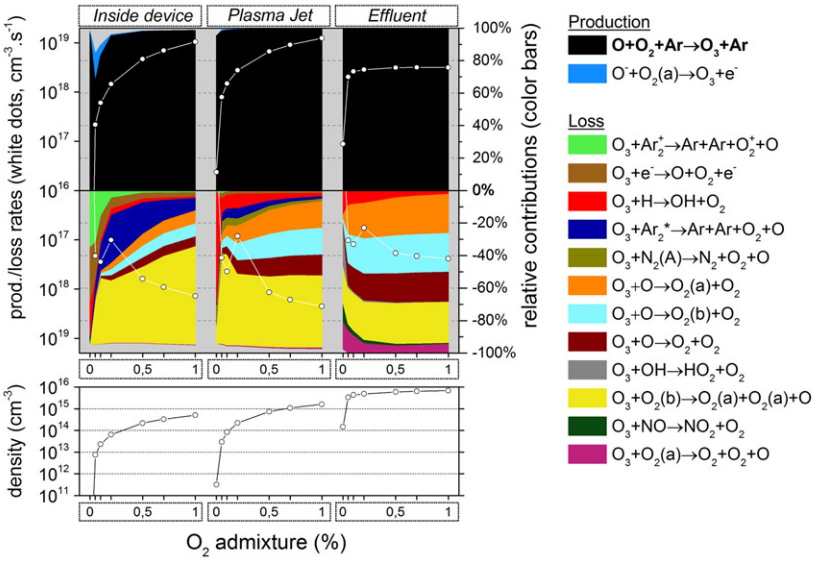

Figure 11. O_3 chemistry inside the device, the plasma jet and the initial effluent (10 ms in total) as a function of the O_2 admixture (see figure 4 for an explanation about the top and bottom graph).

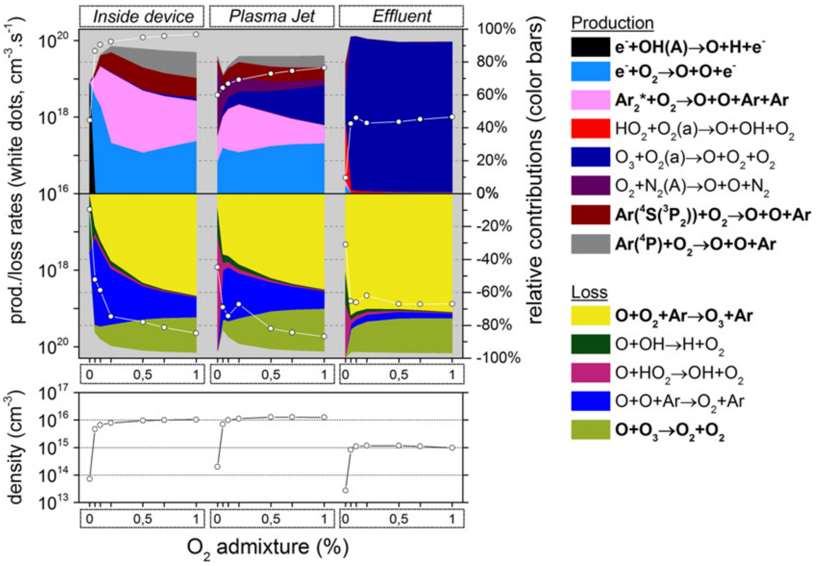

Figure 12. O chemistry inside the device, the plasma jet and the initial effluent (10 ms in total) as a function of the O_2 admixture (see figure 4 for an explanation about the top and bottom graph).

3.2.1. O_3 formation

As described in section 3.1.1, O_3 is almost exclusively produced by reaction 1. However, in the case of adding O_2, this occurs already in the plasma jet region and even inside the device, at least for O_2 fractions above 0.2%, as demonstrated in figure 11.

For lower O_2 levels there is clearly not yet enough O_2 present inside the device and in the (early) plasma jet to yield a large rate for reaction (1). Therefore, the production will occur in such a case mainly in the effluent region when there is enough diffusion of O_2 from the gas curtain.

At higher O_2 fractions, the production of O_3 is smaller in the effluent than in the plasma jet region or even inside the device. Nevertheless, since the O_3 loss is clearly negligible in the effluent region, the O_3 density is still at maximum here (see figure 11). This explains why O_3 is a relative long-lived species. As described in section 3.1.1, the O_3 production is mainly determined by the O atoms; therefore, the chemistry of the O atoms is displayed in figure 12. The O chemistry, however, is now considerably different from the case when adding N_2 (section 3.1.1).

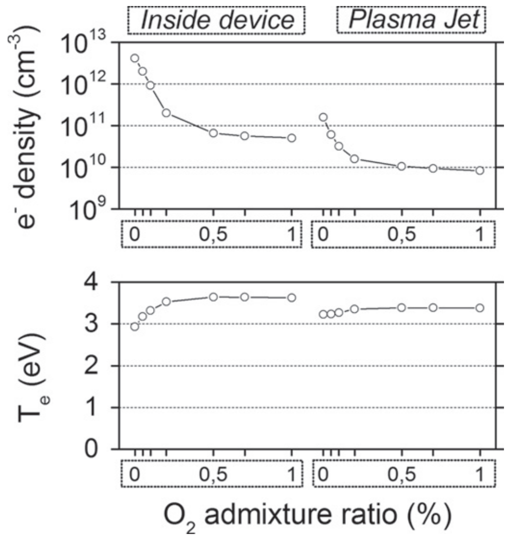

Figure 13. Spatially averaged electron densities (cm^{-3}) and average electron temperature (eV) inside the device and in the plasma jet, as a function of the O_2 admixture. The effluent region is not shown, as the electrons will be negligible in this region.

Indeed, the O atoms are now mainly produced within the kinpen device, so mainly from the oxygen admixture itself and not from the gas curtain.

Secondly, in the absence of significant N_2 admixtures, the O atom production is now mainly due to the dissociation of O_2 by direct electron impact and by collisions with energetic argon species (i.e. $Ar_2{}^*$excimers, $Ar(^4S(^3P_2))$ metastables, as well as higher excited states, grouped in the model as $Ar(^4P)$, but not by collisions with N_2 (A). Note that the heavy particle reactions with energetic argon species are in fact also an (indirect) result of electron impact reactions, because these species are created by electron impact excitation of Ar ground state atoms, possibly followed by an association with another Ar atom to form the $Ar_2{}^*$excimers (data not shown).

A third difference is that the contribution of O_2 dissociation upon collisions with the argon species increases with rising O_2 fraction, whereas the contribution of direct electron impact dissociation drops (at least between 0 and 0.2% O_2). Indeed, the contribution of the latter process is more than 60% at very small O_2 concentrations, compared to about 30% above 0.2% O_2. This can be explained by the electron temperature evolution as a function of the O_2 admixture (see figure 13). Clearly, the average electron temperature rises for higher O_2 admixtures and argon excitation therefore becomes relatively more important than O_2 dissociation because of the higher threshold energy and since the reaction coefficient thus drastically increases with the electron temperature.

Finally, note that after the initial rise in net O atom production (and thus O atom density) until 0.2% O_2, the O atom density stays relatively constant at higher O_2 admixtures (i.e. between 0.2 and 1.0% O_2). This is not only because the average electron temperature is rather constant in this range but also because the O atoms seem to be 'self-quenching' as the main loss pathway of the O atoms creates O_3 (see reaction (1)) and the latter is also quite important for the loss of O atoms (see figure 12 again):

$$O_3 + O \rightarrow 2\,O_2. \tag{9}$$

The O_3 production is therefore almost linearly dependent on the O_2 fraction between 0.2 and 1.0% (or between 0.3 and 1.0% for the experimental values), as was depicted in figure 10. Indeed, the rate of reaction (1) is practically first order because the O atom concentration does not change much in this range.

3.2.2. NO_2 formation

The admixture of O_2 does not change the dominant production pathway for NO_2 compared to the admixture of N_2 (see section 3.1.2). NO_2 is still mainly formed by the reaction between O and N_2 (A) producing NO (by reaction (8) above, data not shown again here), which then oxidises further by the three-body reaction with O atom and Ar as the third collision partner (see reaction (6) above), as depicted in figure 14.

The net production rate is the highest towards the end of the plasma jet region (the loss is significantly lower than the production although this is difficult to see due to the log scale). Note that some NO_2 production also occurs in the effluent region but the loss rate is now more comparable to the production rate here. However, the

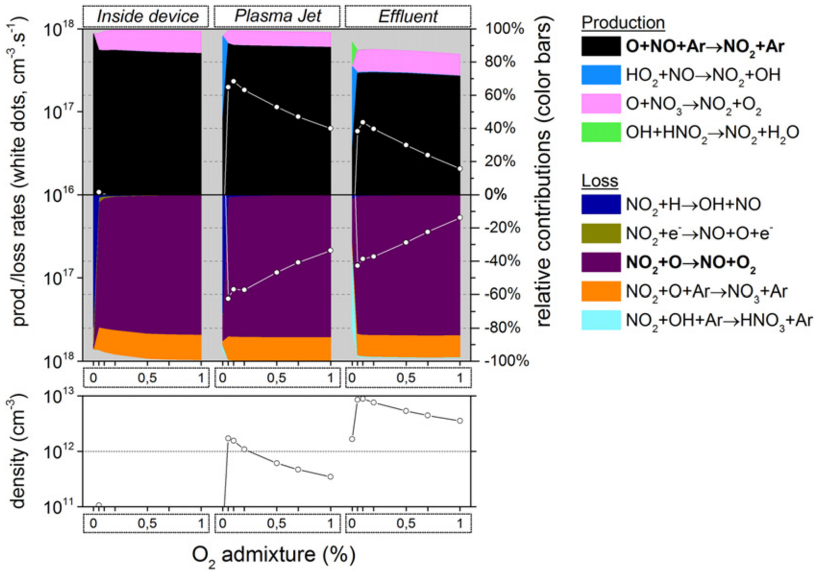

Figure 14. NO_2 chemistry inside the device, the plasma jet and the initial effluent (10 ms in total) as a function of the O_2 admixture (see figure 4 for an explanation about the top and bottom graph).

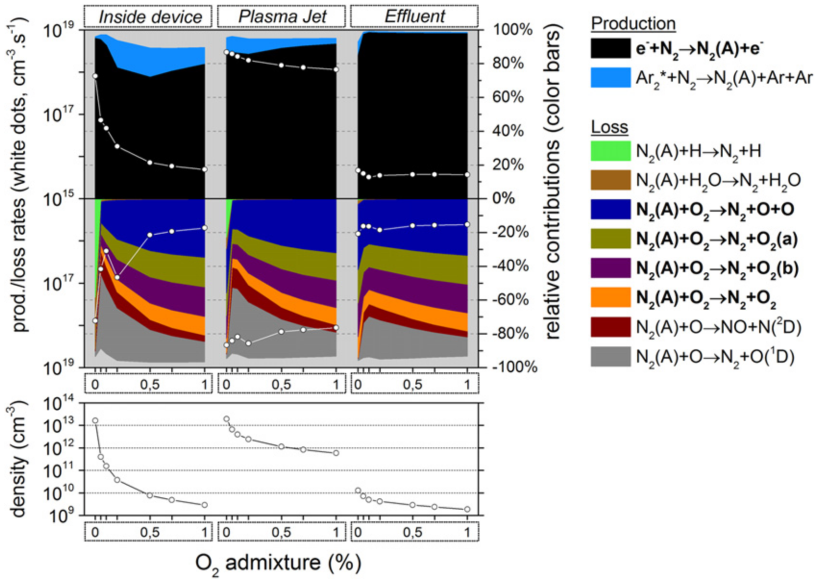

Figure 15. N_2 (A) chemistry inside the device, the plasma jet and the initial effluent (10 ms in total) as a function of the O_2 admixture (see figure 4 for an explanation about the top and bottom graph).

NO_2 density shown in figure 14 is not as high in the plasma jet region as in effluent region, again simply due to the averaging (as explained above).

The NO_2 formation once more depends indirectly on the N_2 (A) formation and this species is produced less upon increasing O_2 admixture (see figure 15). This is because N_2 (A) is mainly formed from electron impact excitation, as can be seen from this figure, and the density of the electrons, which are involved in this reaction, rapidly drops when increasing the O_2 content (see figure 13). The latter is caused by efficient electron attachment processes for O_2 species. Obviously, the reaction rate of electron impact excitation (reaction (5)) also depends on the electron temperature which determines the rate coefficient, but this is less important in this range of electron temperatures (3–3.5 eV). Therefore, the production of N_2 (A), as well as the N_2 (A) density, clearly drop upon increasing O_2 fraction, as shown in figure 15.

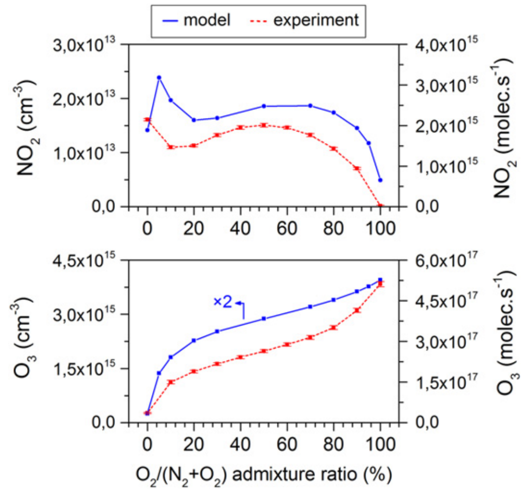

Figure 16. NO_2 and O_3 densities (left *y*-axis) or net production rates (right *y*-axis) after 25 s residence time in the measurement chamber as obtained by infrared absorption spectroscopy and the calculated data for a similar time scale (i.e. 6 s, after which the densities stay constant), in different $O_2/(O_2 + N_2)$ ratios.

Secondly, the NO_2 formation also depends on the concentration of the other reactant, i.e. the O atoms. The density of this species drastically rises when very small amounts of O_2 are added to the feed gas, but afterwards (beyond 0.1%) the density remains more or less constant, as discussed above (see figure 12).

Combining the N_2 (A) and the O density trends upon increasing O_2 admixture indeed leads to the observed behaviour of the NO_2 density as a function of the O_2 fraction, depicted in figure 14: a steep rise between 0 and 0.1% O_2 to a maximum of about 10^{13}cm^{-3} followed by a clear drop for higher O_2 fractions.

Note, however, that the calculated and measured net NO_2 production rates as a function of the O_2 admixture, illustrated in figure 10 above, do not exhibit this initial rise between 0 and 0.1% O_2, that is observed in figure 14 (not only for the NO_2 density, but also for the NO_2 production rate). The reason is that the calculated and measured NO_2 net production rates, shown in figure 10 above, apply to a much longer time scale (i.e. in the order of seconds; see the total residence time in the measurement cell, as described at the beginning of section 3), whereas the calculation results of the effluent region depicted in figure 14, apply to a time scale in the order of milliseconds.

Within this shorter time frame, the loss of NO_2 occurs predominantly by collision with O atoms, and these species will eventually disappear from the discharge (for example by forming O_3 as described above). Therefore, in a later stage of the effluent, O_3 will be the only available molecule able to react with NO_2 as it is the only reactive species that is at least as abundant as NO_2. Note that the reaction $NO_2 + O_3$ is not displayed in figure 14 because only the dominant reactions contributing more than 10% are presented, but at longer residence times, this reaction eventually becomes important. As the O_3 density is rather small for O_2 admixtures between 0 and 0.1%, the NO_2 loss at these longer time scales will also be negligible at these low O_2 admixtures. Therefore the net production of NO_2 will be higher between 0 and 0.1% at these longer time scales, and indeed the NO_2 net production rate will continuously drop from 0 to 1% O_2 as illustrated in figure 10 above.

3.3. Oxygen+nitrogen admixtures

An interesting combination of the two chemistries clarified in the previous sections is obtained when O_2 and N_2 are simultaneously added to the argon feed gas. Recall that in this case, a fixed 1% $O_2 + N_2$ admixture is used, but with the $O_2/(O_2 + N_2)$ ratio varied between 0 and 100%. Therefore, 0% $O_2/(O_2 + N_2)$ in figures 17–21 correspond to the conditions of 1% N_2 admixture in figures 4–9, whereas 100% $O_2/(O_2 + N_2)$ corresponds to the case of 1% O_2 in figures 11–15.

Figure 16 illustrates that the simulated evolution of the NO_2 and O_3 net production rates is also well in accordance with the measurements. For both species, the shape of the curve is quite complex. The NO_2 production rate initially drops (except for a first rise between 0 and 5% O_2 for the model results), but increases again at about 20% $O_2/(N_2 + O_2)$. A second maximum is formed at about 50% $O_2/(N_2 + O_2)$ before the production rate steeply drops close to 100% O_2 (thus for low N_2 levels).

The shape of the O_3 production rate as a function of the admixture composition is clearly x^3-shaped, although more pronounced in the experimental measurements. Indeed, the difference between the simulated

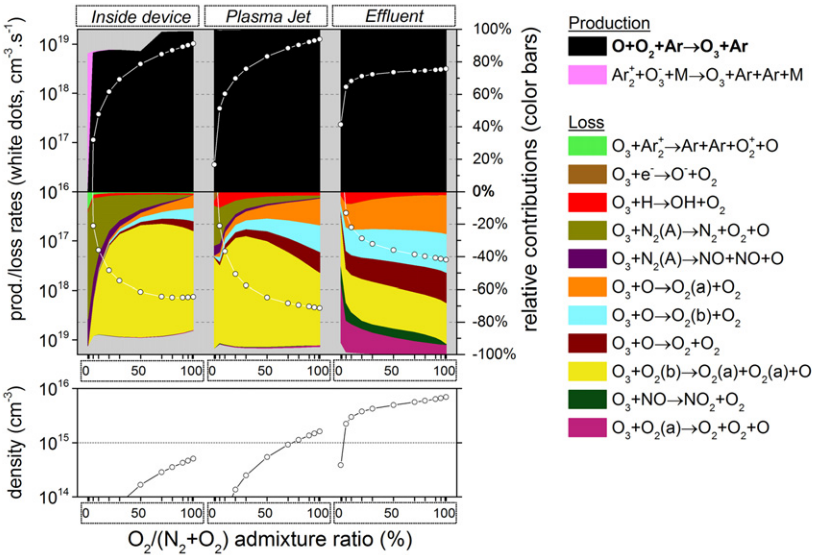

Figure 17. O_3 chemistry inside the device, the plasma jet and the initial effluent (10 ms in total) as a function of the $O_2 + N_2$ admixture (see figure 4 for an explanation about the top and bottom graph).

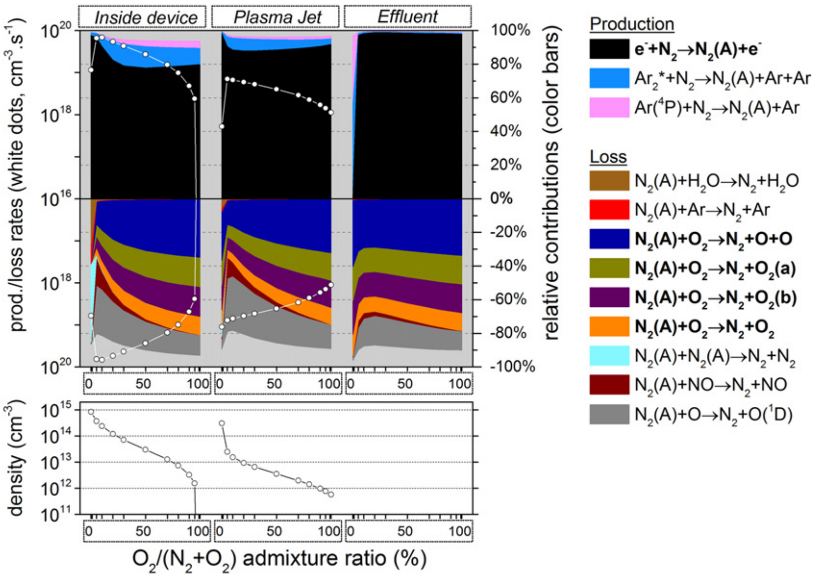

Figure 18. N_2 (A) chemistry inside the device, the plasma jet and the initial effluent (10 ms in total) as a function of the $O_2 + N_2$ admixture (see figure 4 for an explanation about the top and bottom graph).

and measured O_3 production rate is in general about a factor 2, but in the middle of the investigated range, at an O_2/N_2 ratio close to 1, this difference has increased to a factor 3.

3.3.1. O_3 formation

The O_3 formation pathway was found to be similar for O_2 or N_2 admixtures, as demonstrated above. Therefore, figure 17 indicates that the same mechanisms are applicable here when admixing both gases at the same time, i.e. the formation is mainly due to the three-body reaction between O atoms and O_2 molecules, with Ar as third body (see reaction (1)).

Again, like in the case of O_2 addition, the production is highest in either the plasma jet (and inside the device) or very early in the effluent region, depending on the O_2 content, as explained in section 3.2.1 above.

A dissimilarity between figures 10 and 16 concerning the net O_3 production rate as a function of the O_2 fraction is that for pure O_2 admixtures the net production rate first rapidly rises (between 0 and 0.2% O_2 in argon) but it tends to saturate at higher O_2 concentrations (see figure 10), whereas for $O_2 + N_2$ admixtures (see

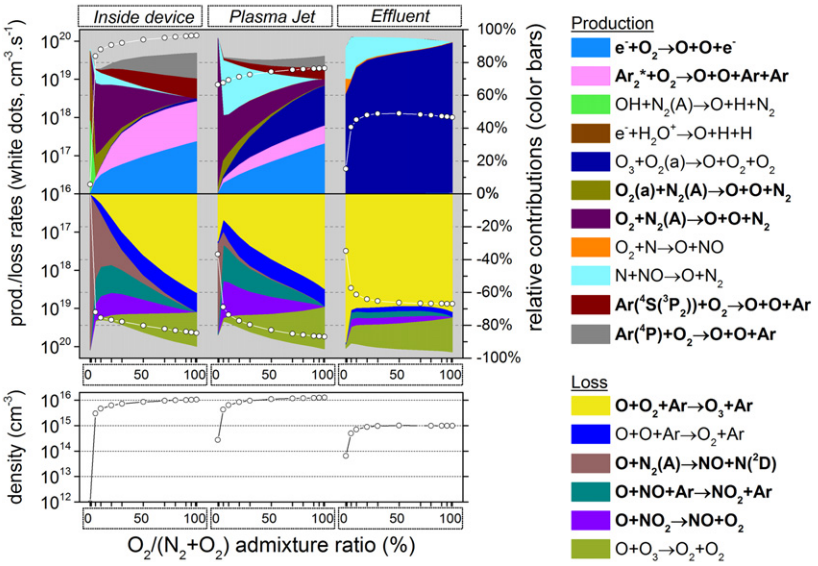

Figure 19. O chemistry inside the device, the plasma jet and the initial effluent (10 ms in total) as a function of the O_2+N_2 admixture (see figure 4 for an explanation about the top and bottom graph).

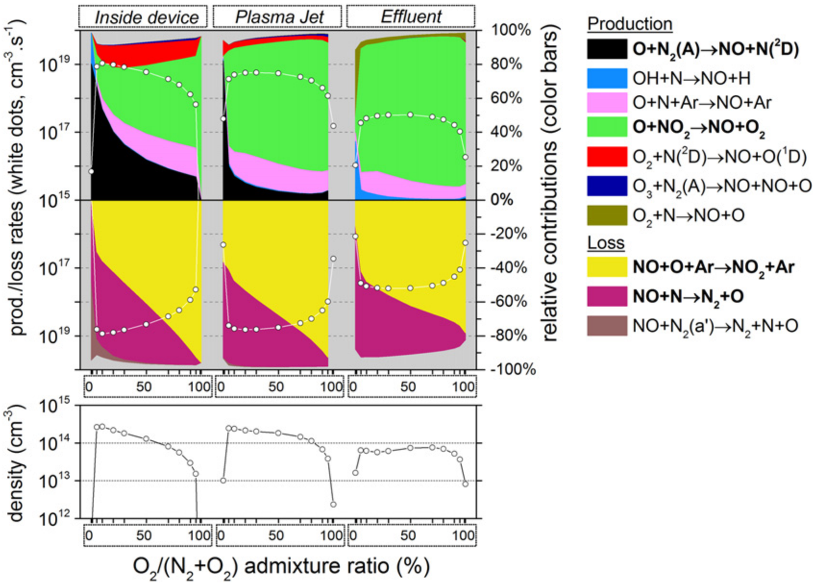

Figure 20. NO chemistry inside the device, the plasma jet and the initial effluent (10 ms in total) as a function of the O_2 + N_2 admixture (see figure 4 for an explanation about the top and bottom graph).

figure 16) the first rise (between 0 and 0.2% in argon) is less steep and is followed by a gradual rise (between 0.2 and 0.8% O_2 in argon) and, finally, a more drastic increase between 0.8 and 1% O_2 in argon (which is more pronounced in the experimental data). The O_3 production without N_2 (for pure O_2 admixtures) is thus higher between 0 and 0.8% O_2 than with N_2 (in the case of O_2 + N_2 admixtures).

Indeed, the observed effect must be explained by the role of N_2 (A) (which is created from the N_2 admixture molecules in reaction (5), see figure 18) in the generation of O atoms, which eventually leads to O_3 production by reaction 1. This O chemistry is illustrated in figure 19.

As demonstrated in section 3.1.1 above, the O atoms can easily be formed by reaction (4) (i.e. between N_2 (A) and O_2 molecules) when significant amounts of N_2 are present. Indeed, figure 19 illustrates that this reaction gains importance when the $O_2/(O_2 + N_2)$ ratio drops and it takes over the role of O_2 dissociation by collision with argon species and by electron impact as the most important O atom production process.

Consequently, the N_2 (A) chemistry in figure 18 provides the final answer. The increase in N_2 (A) density upon decreasing O_2 fraction in the plasma jet region is not linear between 100 and 0% $O_2/(O_2 + N_2)$ (looking

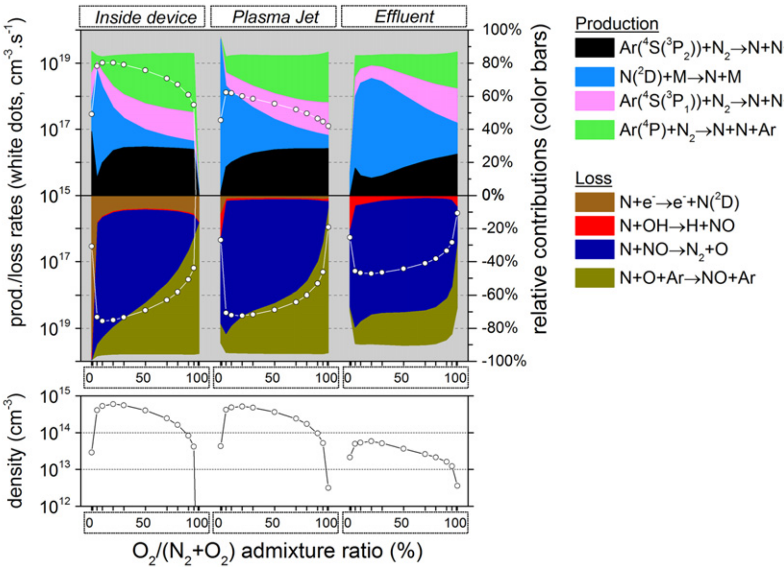

Figure 21. N chemistry inside the device, the plasma jet and the initial effluent (10 ms in total) as a function of the $O_2 + N_2$ admixture (see figure 4 for an explanation about the top and bottom graph).

from right to left on the x-axis). Indeed, the N_2 (A) density seems to be somewhat suppressed until 10% $O_2/(O_2 + N_2)$, yet for even lower $O_2/(O_2 + N_2)$ fractions than 10% the N_2 (A) density will finally increase drastically.

It is clear from the loss reactions in figure 18 that even small amounts of O_2 (above 0.1% $O_2/(O_2 + N_2)$) efficiently quench the N_2 (A) molecules, not only by chemical quenching leading to O atoms and thus O_3 formation, but also by physical quenching. Thus, it can be concluded that the O_3 production is partially inhibited when significant amounts of O_2 and N_2 are added simultaneously, explaining why the rise in the net O_3 production is higher between 80 and 100% $O_2/(O_2 + N_2)$ than between 20 and 80% $O_2/(O_2 + N_2)$, as depicted in figure 16 above.

3.3.2. NO_2 formation

For the NO_2 production rate as a function of the $O_2/(O_2 + N_2)$ admixture ratio one might expect the highest value for equivalent O_2 and N_2 fractions, but this does not seem to be the case (see figure 16 above). From the above sections, we know that NO_2 is formed from NO and this is also valid here (therefore, the NO_2 chemistry is not explicitly shown, as it does not give new information). Thus, by studying the chemistry of NO in figure 20 it is possible to explain the observed trend for the net NO_2 production rate displayed in figure 16.

In the plasma jet region the NO density is, as expected, the highest between 10 and 70% $O_2/(O_2 + N_2)$ ratio. However, in the effluent region a small dip at 20% starts to develop. This is due to significant NO destruction upon collision with N atoms:

$$N + NO \rightarrow N_2 + O. \tag{10}$$

Indeed, the concentration of the N atoms is at maximum at this $O_2/(O_2 + N_2)$ ratio, as demonstrated by figure 21.

As a result, the measured and modelled net NO_2 production rate further in the measurement cell (shown in figure 16 above) exhibits a similar profile as the NO density in the effluent region of figure 20, because NO_2 is created from NO.

4. Conclusions

In this work we presented the results of both a semi-empirical numerical model, which describes the chemical kinetics within the kinpen plasma jet device (with a surrounding dry air gas curtain), and experimental measurements of the jet (far) effluent by high resolution QCL infrared absorption spectroscopy. The net production rates of the biomedical species, O_3 and NO_2, were determined with both techniques for multiple different operating conditions.

In the first two cases either O_2 or N_2 is admixed from 0 to 1.0% of the total argon feed gas flow rate. Additionally, an artificial mixture of $N_2 + O_2$ is used and in this case, the admixture fraction is fixed at 1% but its content is varied from 0 to 100% O_2 with 100–0 % N_2.

We obtained a good qualitative agreement in all cases for the net production rates of NO_2 as a function of the different admixtures. Concerning O_3, the similarity of the results computed in the model and the experimental data is qualitatively correct for most of the investigated conditions. Nevertheless, in case of N_2 admixtures, a mismatch between the calculation and the measurement is observed. It is not clear whether this is caused by a possible inaccuracy in the reaction set or due to the gas curtain diffusion profile assumed in our 0D model, which is much more complex in reality [39]. In the latter case, a more sophisticated model approach might offer a solution.

Quantitatively, the results of both techniques do not vary by more than a factor three at maximum within the investigated range (i.e. a consistent overestimation compared to the experimental measurements). The highest O_3 production rate was achieved at the highest investigated O_2 admixture of 1%, see figures 10 and 16 (i.e. 4.9×10^{17} molec s^{-1} measured and 1.0×10^{18} molec s^{-1} simulated). These figures also illustrate that the O_3 production initially drops steeply when O_2 is being replaced by N_2 (between 100 and 80% $O_2/N_2 + O_2$) while the decrease is much more gradual between 1 and 0.3% pure O_2 admixtures.

For the net production rate of NO_2 in the case of N_2 and $N_2 + O_2$ the agreement is almost perfect. It is remarkable that the calculated NO_2 production rate is quite comparable to the measured results within the investigated ranges of pure N_2 admixtures and $N_2 + O_2$ admixtures, i.e. between 1×10^{15} and 3×10^{15} molec s^{-1}. Moreover, in both cases the NO_2 production rate becomes significantly lower when the N_2 fraction is lower than 0.1% in the argon gas, see figures 3 and 16.

Due to the complementarity of the two distinct techniques that have been used, we have acquired important insight in the reaction kinetics in all regions of the kinpen device, even in areas that are not accessible by optical diagnostics. The pathways for the formation of O_3 and NO_2 are quite complex. From the analysis of the model output, it is demonstrated that the production of NO_2 and O_3 is mostly triggered by two common species: atomic oxygen (O) as well as metastables of nitrogen ($N_2(A)$), which are both energy carriers and lead to the formation and/or destruction of NO_2 and O_3. O and $N_2(A)$, among other species like Ar metastables, can be considered as transient particles that are direct results of the electron chemistry and eventually lead to the formation of longer living molecules outside the kinpen device.

Even more important is that admixture differences, even at these relatively low levels, can significantly alter the electron density and temperature and therefore have a large impact on the chemistry. In general, it can be concluded that the production of these important biomedically active species can be manipulated by up to one order of magnitude by varying the amount of admixture or the admixture type. Based on these results, the feed gas and also the gas curtain composition can be selected even more carefully to optimize the applications.

Acknowledgments

The simulations were carried out using the Turing HPC infrastructure of the CalcUA core facility of the University of Antwerp, a division of the Flemish Supercomputer Center VSC, partially funded by the Hercules Foundation of the Flemish Government (department EWI). Furthermore, we are very grateful to Professor Mark Kushner for providing the original numerical code that is used as a basis for our simulations. Sincere gratitude is expressed towards Dr Andrei V Pipa for the discussions and knowledge about IR absorption spectroscopy, and to Dipl. Ing. Henrik Zimmermann and Dipl. Ing. Sven Glitsch for their expertise about QCLAS. François Riberi is acknowledged for assistance during the measurement campaign. Dr Jörn Winter is gratefully acknowledged for the fruitful discussions. The Institute for the Promotion of Innovation by Science and Technology in Flanders (IWT Flanders) is acknowledged for providing financial support to WVG. ASB, SI and SR gratefully acknowledge the funding by the Federal German Ministry of Education and Research (BMBF, grant #03Z2DN12).

Appendix

In this appendix we describe the features of the numerical model, as already described in our previous work [9, 36, 37].

Pseudo-one-dimensional plug flow

By using a 'pseudo-one-dimensional plug flow' approximation in this 0D model, it is possible to represent the time dependent evolution of species densities (as is typically the case in a 0D model) as a spatial dependence, hence, as a function of the position in the plasma jet device and effluent. This approach was previously successfully applied in [44] for a He/O_2 discharge. We assume that the tube of the plasma jet device, the plasma jet itself and the initial effluent can be represented by a long cylinder, where constant atmospheric pressure conditions rule. The magnitude of the flow velocity determines the change of position of a volume averaged (0D)

Table A1. Plasma species included in the model.

Ground state neutrals	Excited state neutrals	Charged species
Ar	$Ar(^4S[^3P_2])$, $Ar(^4S[^3P_1])$, $Ar(^4S[^3P_0])$, $Ar(^4S[^1P_1])$, $Ar(^4P)$[a], $Ar_2^*(a^3\Sigma_u^+)$	e^-, Ar^+, Ar_2^+, ArH^+
N, N_2	$N(^2D)$, $N_{2,rot}$, $N_{2,vib(1-8)}$, $N_2(A^3\Sigma_u^+)$, $N_2(a'^1\Sigma_u^-)$	N^+, N_2^+, N_3^+, N_4^+
O, O_2, O_3	$O(^1D)$, $O_{2,rot}$, $O_{2,vib(1-4)}$, $O_2(a^1\Delta_g)$, $O_2(b^1\Sigma_g^+)$, $O_{3,vib}$	O^+, O_2^+, O_4^+, O^-, O_2^-, O_3^-
NO, NO_2, N_2O, NO_3, N_2O_3, N_2O_4, N_2O_5	$N_2O_{vib(1-3)}$	NO^+, NO_2^+, NO_2^-, NO_3^-
H, H_2, OH, H_2O, HO_2, H_2O_2	H^*[b], $H_{2,rot}$, $H_{2,vib(1-2)}$, H_2^*[c], OH(A), $H_2O_{vib(100,010,001)}$	H^+, H_2^+, H_3^+, OH^+, H_2O^+, H_3O^+, H^-, OH^-
NH, HNO, HNO_2, HNO_3, HNO_4		

[a] This species groups the electronically excited states ^4P, ^5D, ^5S and ^5P

[b] This species groups the electronically excited states with $n = 2–4$

[c] This species groups the electronically excited states $(b^3\Sigma_u^+)$ and $(c^3\Pi_u)$

Table A2. Water clusters included in the model.

$H_4O_2^+$, $H_2O_3^+$, $H_5O_2^+$, $H_7O_3^+$, $H_9O_4^+$, $H_{11}O_5^+$, $H_{13}O_6^+$, $H_{15}O_7^+$
$H_2NO_2^+$, $H_4NO_3^+$, $H_6NO_4^+$

plug flow element, i.e. a cylindrical segment, along the jet stream. In our approach, we assume that axial transport of mass and energy due to drift and concentration gradients is negligible in comparison to axial transport by convection. Furthermore, no species transport in the radial direction is considered in this approach. Due to the very high axial flow speed (typically in the order of 10^3 cm s^{-1}) compared to the radial flow speed, this seems acceptable for the first few cm's after the nozzle exit. We want to stress once more that the original dependency in our 0D model is density versus time and that the distance dependency is not an extra dimension solved by the equations.

Evidently, the flow velocity should decrease along the jet symmetry axis. This is due to gas expansion and obstruction by the relatively stationary surrounding atmosphere. Therefore, the gas flow velocity was fitted to the fluid dynamics simulation results, only considering neutral gas species, thus electric field forces of the plasma have no influence on the flow field calculation.

The relation between the time scale and the length scale is thus not simply the initial velocity at the nozzle exit as a constant factor but the time correlates with position through the variable flow speed, i.e. a nonlinear decreasing value along the jet effluent obtained from the 2D fluid model. An average of several velocity profiles over the radial direction (which are known from our 2D computational fluid dynamics simulation, as mentioned in the paper) is used for this purpose, which thus includes both the high and low flow speeds in the jet. The velocity is a nonlinear decreasing value along the jet axis.

Species continuity equation

The following continuity equation is solved for all plasma species included in the model (see tables A1 and A2):

$$\frac{dn_i}{dt} = \sum_j \left[\left(a_{ij}^R - a_{ij}^L \right) k_j \prod_l n_l^L \right] + S_{\text{diff}}(i)$$
$$(\text{with } S_{\text{diff}}(i) = 0 \text{ if } i \neq \text{Ar, N}_2\text{, O}_2 \text{ or H}_2\text{O}), \tag{11}$$

where n_i is the density of species i, a_{ij}^R and a_{ij}^L are the right-hand side and left-hand side stoichiometric coefficients of species i in reaction j, k_j is the reaction rate coefficient and n_l^L is the density of the lth species in the left-hand side of reaction j. All these coefficients are input values, obtained from literature, according to a predefined reaction scheme (see supplemenatry information, available at stacks.iop.org/njp/17/033003/mmedia). Note that each new time step dt describes the length of the next volume averaged segment of the plug flow cylinder. In addition, since fluid dynamics are not included in this 0D model, the humid air diffusion (from the surroundings into the argon flow) is handled by adding a production/loss term, S_{diff}, for Ar, N_2, O_2 and H_2O. This makes that argon is gradually being replaced by a humid air mixture starting from the nozzle exit. Of course, these artificial source terms will vary along the jet effluent. We considered several diffusion profiles for different off-axis positions (as determined by the 2D computational fluid dynamics simulations) and we adopted the $r = 0.6$ cm off-axis values as they resulted in the best agreement with the experimental results. Effects related to multiple dimensions are therefore neglected by our model approach.

Electron energy density equation

In the model electrons are assumed to be mainly heated by Joule heating, under the influence of an electric field. The time evolution of the electron energy is calculated from

$$\frac{\mathrm{d}}{\mathrm{d}t}\left(\frac{3}{2}n_e k_b T_e\right) = \vec{j}\cdot\vec{E} + \sum_l n_e k_l N_l \Delta\varepsilon_i - \sum_i \frac{3}{2} n_e \nu_{mi}\left(\frac{2m_e}{M_i} k_b\left(T_e - T_i\right)\right), \qquad (12)$$

where n_e is the electron density, k_b is Boltzmann's constant, T_e is the electron temperature, $\vec{j}$ and $\vec{E}$ are the current density and the electric field in the discharge, k_l is the reaction rate coefficient for the lth electron impact process, N_l is the density of the gas phase collision partner and $\Delta\varepsilon_i$ is the corresponding change in the electron energy. ν_{mi} is the electron momentum transfer collision frequency with species i, m_e is the electron mass and T_i and M_i are the temperature and mass of species i. In an experimental setup, the value of the electric field throughout the plasma jet is greatly dependent on the applied electrode voltage, the electrode configuration, etc. Moreover, it fluctuates in time. Unfortunately, this complexity cannot be captured by a 0D kinetics model. Therefore, the Joule heating term is determined by an estimated power deposition density (W cm^{-3}) which is also an input parameter in our model. The electron energy value, calculated from equation (12), is used to determine the reaction rate coefficients for most electron impact reactions. For this purpose a look-up table of these coefficients as a function of a wide range of electron temperatures is constructed by an internal Boltzmann equation solver using electron collision cross sections obtained from literature (see below). It is important to mention that these look-up tables need to be regularly updated by running the Boltzmann code again, because of the drastic change in background gas composition due to humid air diffusion. In practice, in our model the Boltzmann solver was updated every 10 μs, for a typical time step of the calculations of 0.1 ns.

References

[1] Laroussi M, Kong M G, Morfill G E and Stolz W 2012 *Plasma Medicine: Applications of Low-Temperature Gas Plasmas in Medicine and Biology* (Cambridge: Cambridge University Press)
[2] Yonemori S, Nakagawa Y, Ono R and Oda T 2012 *J. Phys. D: Appl. Phys.* **45** 225202
[3] McKay K, Liu D X, Rong M Z, Iza F and Kong M G 2012 *J. Phys. D: Appl. Phys.* **45** 172001
[4] Reuter S, Winter J, Schmidt-Bleker A, Tresp H, Hammer M U and Weltmann K D 2012 *IEEE Trans. Plasma Sci.* **40** 2788
[5] Wagenaars E, Gans T, O'Connell D and Niemi K 2012 *Plasma Sources Sci. Technol.* **21** 042002
[6] Maletić D, Puač N, Lazović S, Malović G, Gans T, Schulz-von der Gathen V and Petrović Z L 2012 *Plasma Phys. Control. Fusion* **54** 124046
[7] Ellerweg D, Benedikt J, von Keudell A, Knake N and Schulz-von der Gathen V 2010 *New J. Phys.* **12** 013021
[8] Pipa A V, Reuter S, Foest R and Weltmann K D 2012 *J. Phys. D: Appl. Phys.* **45** 085201
[9] van Gaens W, Bruggeman P J and Bogaerts A 2014 *New J. Phys.* **16** 063054
[10] Kelly S and Turner M M 2014 *Plasma Sources Sci. Technol.* **23** 065012
[11] Winter J, Wende K, Masur K, Iseni S, Dünnbier M, Hammer M U, Tresp H, Weltmann K D and Reuter S 2013 *J. Phys. D: Appl. Phys.* **46** 295401
[12] Sousa J S, Niemi K, Cox L J, Algwari Q T, Gans T and O'Connell D 2011 *J. Appl. Phys.* **109** 123302
[13] Reuter S, Winter J, Iseni S, Peters S, Schmidt-Bleker a, Dünnbier M, Schäfer J, Foest R and Weltmann K D 2012 *Plasma Sources Sci. Technol.* **21** 034015
[14] Yusupov M, Neyts E C, Simon P, Berdiyorov G, Snoeckx R, van Duin A C T and Bogaerts a 2014 *J. Phys. D: Appl. Phys.* **47** 025205
[15] Tian W and Kushner M J 2014 *J. Phys. D: Appl. Phys.* **47** 165201
[16] van Gils C A J, Hofmann S, Boekema B K H L, Brandenburg R and Bruggeman P J 2013 *J. Phys. D: Appl. Phys.* **46** 175203
[17] Lukes P, Dolezalova E, Sisrova I and Clupek M 2014 *Plasma Sources Sci. Technol.* **23** 015019
[18] Shimizu T, Sakiyama Y, Graves D B, Zimmermann J L and Morfill G E 2012 *New J. Phys.* **14** 103028
[19] Yusupov M, Bogaerts A, Huygh S, Snoeckx R, van Duin A C T and Neyts E C 2013 *J. Phys. Chem.* C **117** 5993
[20] van der Paal J, Aernouts S, van Duin A C T, Neyts E C and Bogaerts A 2013 *J. Phys. D: Appl. Phys.* **46** 395201
[21] Graves D B 2012 *J. Phys. D: Appl. Phys.* **45** 263001
[22] von Woedtke T, Reuter S, Masur K and Weltmann K-D 2013 *Phys. Rep.* **530** 291
[23] Weltmann K, Kindel E, Brandenburg R, Meyer C, Bussiahn R and Wilke C 2009 *Contrib. Plasma Phys.* **49** 631
[24] Lu X, Laroussi M and Puech V 2012 *Plasma Sources Sci. Technol.* **21** 034005
[25] Verreycken T, Mensink R, Horst R V D, Sadeghi N and Bruggeman P J 2013 *Plasma Sources Sci. Technol.* **22** 055014
[26] Reuter S, Winter J, Iseni S, Schmidt-Bleker A, Dünnbier M, Masur K, Wende K and Weltmann K 2014 *IEEE Trans. Plasma Sci.* doi:10.1109/TPS.2014.2361921
[27] Iséni S, Reuter S and Weltmann K D 2014 *J. Phys. D: Appl. Phys.* **47** 075203

[28] Welzel S, Hempel F, Hubner M, Lang N, Davies P B and Ropcke J 2010 *Sensors* **10** 6861

[29] Röpcke J, Davies P B, Lang N, Rousseau A and Welzel S 2012 *J. Phys. D: Appl. Phys.* **45** 423001

[30] Rothman L *et al* 2009 *J. Quant. Spectrosc. Radiat. Transfer* **110** 533

[31] neoplas control GmbH, Q-MACSoft Monitor software, version 1.2.8.929, 2011, http://neoplas-control.de/

[32] neoplas control GmbH, Q-MACSoft HT software, version 1.2.8.929, 2011, http://neoplas-control.de/

[33] Hofmann S, van Gessel A F H, Verreycken T and Bruggeman P 2011 *Plasma Sources Sci. Technol.* **20** 065010

[34] Hofmann S, van Gils K, van der Linden S, Iseni S and Bruggeman P 2014 *Eur. Phys. J.* D **68** 56

[35] Dorai R and Kushner M J 2003 *J. Phys. D: Appl. Phys.* **36** 666

[36] van Gaens W and Bogaerts A 2013 *J. Phys. D: Appl. Phys.* **46** 275201

[37] van Gaens W and Bogaerts A 2013 *Plasma Sources Sci. Technol.* **23** 035015

[38] Dünnbier M, Schmidt-Bleker A, Winter J, Wolfram M, Hippler R, Weltmann K-D and Reuter S 2013 *J. Phys. D: Appl. Phys.* **43** 435203

[39] Iseni S, Schmidt-Bleker A, Winter J, Weltmann K D and Reuter S 2014 *J. Phys. D: Appl. Phys.* **47** 152001

[40] Iséni S, Zhang S, van Gessel A F H, Hofmann S, van Ham B T J, Reuter S, Weltmann K D and Bruggeman P J 2014 *New J. Phys.* **16** 123011

[41] Iseni S, Reuter S, Schmidt-Bleker A and Weltmann K D 2014 *IEEE Trans. Plasma Sci.* **42** 2458

[42] Zhang S, van Gaens W, van Gessel B, Hofmann S, van Veldhuizen E, Bogaerts A and Bruggeman P 2013 *J. Phys. D: Appl. Phys.* **46** 205202

[43] Reuter S, Winter J, Schmidt-Bleker A, Schroeder D, Lange H, Knake N, Schulz-von der Gathen V and Weltmann K-D 2012 *Plasma Sources Sci. Technol.* **21** 024005

[44] Stafford D S and Kushner M J 2004 *J. Appl. Phys.* **96** 2451

5.7 Article VII

The Influence of Feed Gas Humidity versus Ambient Humidity on Atmospheric Pressure Plasma Jet-Effluent Chemistry and Skin Cell Viability[a]
doi:10.1109/TPS.2014.2361921

---

[a]

The Influence of Feed Gas Humidity Versus Ambient Humidity on Atmospheric Pressure Plasma Jet-Effluent Chemistry and Skin Cell Viability

Stephan Reuter, *Member, IEEE*, Jörn Winter, Sylvain Iséni, Ansgar Schmidt-Bleker, Mario Dünnbier,
Kai Masur, Kristian Wende, and Klaus-Dieter Weltmann, *Member, IEEE*

Abstract—**The influence of ambient air species especially humidity is an ever-present challenge for atmospheric pressure plasma jet applications. Especially, where the plasma-induced effects are extremely sensitive to humidity, such as in the field of plasma medicine, an understanding of the influence of ambient species diffusion on plasma chemistry and on reactive component composition is crucial. In this paper, we investigate the influence of ambient humidity versus feed gas humidity on the production of reactive components by atmospheric pressure plasma jets. By the use of a shielding gas curtain, we control the surrounding atmosphere around the active effluent region of the investigated argon RF-plasma jet (kinpen) and control the gas humidity of the ambient gas. By quantum cascade laser absorption spectroscopy and by Fourier transformed infrared (IR) absorption spectroscopy, the effect of diffusing surrounding molecular species on the chemistry of the long-living reactive oxygen species is investigated. Mechanisms of H_2O_2 and O_3 production are studied. In this paper, we have quantified the influence that ambient species, namely, water molecules, have on the reactive species' generation in the gas phase. It is shown that the effect of ambient humidity is important for the long-living species production, feed gas humidity, however, has the much stronger effect. Finally, with the focus of applications in plasma medicine, the cell viability of human skin cells (HaCaT keratinocytes) as a function of feed gas and ambient gas humidity is compared.**

Index Terms—**Ambient humidity, ambient species, atmospheric pressure plasma jet, cell viability, feed gas humidity, plasma chemistry, plasma medicine.**

I. INTRODUCTION

ESPECIALLY in plasma medicine, the use of cold atmospheric pressure plasma jets [1] has become promising within the past decade [2]–[5]. In this field of application, it is vital that plasma and operating conditions are held stable to ensure constant and controllable therapeutic effects. Due to the necessity of plasma operation in ambient air for *in vivo* treatment, potentially uncontrollable conditions arise. It is therefore vital to investigate the influence of these uncontrollable conditions of the ambient surrounding on the reactive species generation mechanisms. Humidity and diffusing air species threaten to be responsible for a distortion of the reactive species composition generated by atmospheric pressure plasma jets.

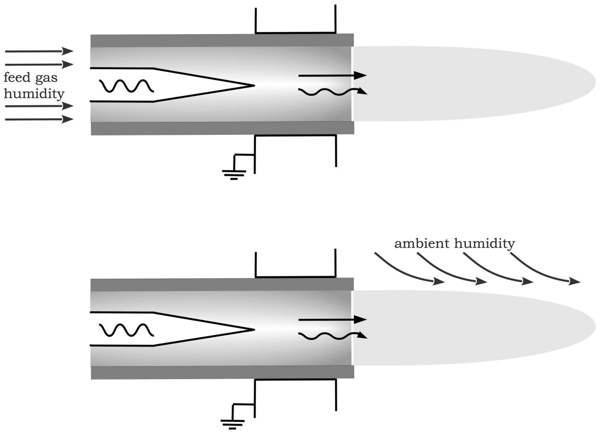

Fig. 1. Schematics of the plasma jet investigated for humidity admixture to the feed gas (top) and humidity admixture to the active effluent region (bottom).

This paper investigates the influence of humidity on long-living reactive species (lifetime > millisecond) generated by an atmospheric pressure argon plasma jet (kinpen [6], [7]) shielded by a gas curtain with a defined gas composition [8], [9]. These reactive species are detected by infrared absorption spectroscopy in the far field of the plasma jet, where no charged or metastable species are expected.

II. PLASMA JET AND GAS CURTAIN

For our study, an atmospheric pressure plasma jet—the kinpen was used, Fig. 1. The plasma jet consists of a centered rod electrode inside a ceramic capillary and a grounded outer ring electrode [6], [10]. To the powered central electrode, a voltage of about 2 kV_{pp} is applied with a frequency in the

---

Manuscript received December 20, 2013; revised June 12, 2014; accepted September 26, 2014. This work was supported by the German Federal Ministry of Education and Research under Grant 03Z2DN11 and Grant 03Z2DN12.

S. Reuter, J. Winter, S. Iséni, A. Schmidt-Bleker, M. Dünnbier, K. Masur, and K. Wende are with the Center for Innovation Competence plasmatis, Leibniz Institute for Plasma Science and Technology, Greifswald 17489, Germany (e-mail: stephan.reuter@inp-greifswald.de; winter@inp-greifswald.de; ansgar.schmidt-bleker@inp-greifswald.de; kai.masur@inp-greifswald.de; kristian.wende@inp-greifswald.de).

K.-D. Weltmann is with the Leibniz Institute for Plasma Science and Technology, Greifswald 17489, Germany (e-mail: weltmann@inp-greifswald.de).

Color versions of one or more of the figures in this paper are available online at http://ieeexplore.ieee.org.

Digital Object Identifier 10.1109/TPS.2014.2361921

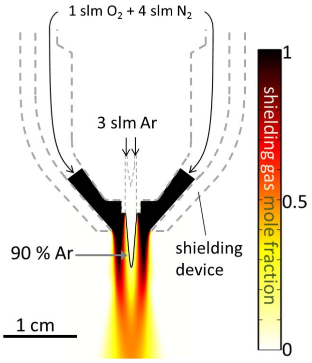

Fig. 2. Effect of gas curtain at 3-slm jet flux and 5-slm curtain gas flux.

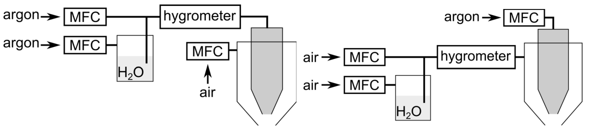

Fig. 3. Feed gas humidification setup (left) and shielding gas humidification (right).

order of 1 MHz. The working gas argon (purity 99.999%) with a gas flow rate of 3 slm is guided directly into the head of the kinpen.

To shield the effusing argon gas from ambient air species, an additional surrounding hull made of glass is constructed around the plasma jet. The operating principle and the efficiency have been shown in [8]. The shielding gas surrounds the active effluent zone. As shielding gas artificial air consisting of 80% nitrogen (N_2 purity 99.999%) and 20% oxygen (O_2 purity 99.995%) with a gas flow rate of 5 slm is used. Fluid simulations (Fig. 2) show the shielding effect of the gas curtain. The simulations are described in detail in [8]. Fig. 2 shows the mole fractions of the shielding gas obtained by the computational fluid dynamics simulations. The contour line, indicating a mole fraction of 90% argon, roughly marks the boundary of the visible effluent. It can be observed that a shielding gas curtain forms around the visible effluent. While the desired interaction of the argon plasma with the shielding gas is enabled, the ambient air is almost completely shielded and reaches only values well below 0.1% in the region of the visible effluent. The varying mass densities for different shielding gases (dry/humid) do not significantly alter the shielding gas distribution. The observed variations of the experimental results are thus associated with the shielding gas composition only.

For the studies, the humidity is varied and determined by a hygrometer (DewMaster, EdgeTech, USA). On the one hand, the humidity is varied from 0 to 2000 ppm in the feed gas at dry artificial air shielding gas conditions. On the other hand, the humidity of artificial air shielding gas is varied in the range between 0 and 20 000 ppm at dry argon feed gas conditions. For the feed gas humidity variation, a bypass argon flux of up to 0.5 slm is fed through a water bubbler (left side of Fig. 3). All gas flows are controlled by mass flow controllers (MKS). For the shielding gas humidification, the total gas flux (20% oxygen and 80% nitrogen controlled by mass flow controllers) bypassing through the bubbler is regulated by a needle valve (right side of Fig. 3).

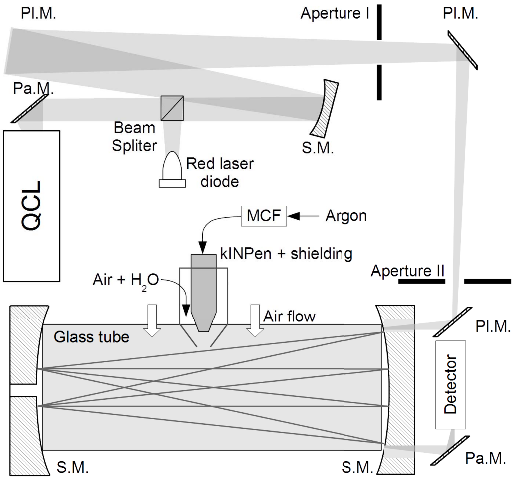

Fig. 4. Schematics of QMACS setup.

III. Diagnostic Setups

In this paper, the long-living species produced by the plasma jets effluent and its interaction with the ambient atmosphere is diagnosed by multipass cell infrared absorption spectroscopy. Using a multipass cell increases the total absorption length and thus the sensitivity of the setup.

A. Optical Emission Spectroscopy

Space-resolved optical emission spectroscopy in the effluent region of the plasma jet is performed using an Andor Shamrock 500 spectrograph with a grating of 2400 lines. The effluent of the plasma jet is imaged onto the entrance slit. The spectra are recorded with an Andor Istar Electron multiplying charge-coupled device. Three maps of the OH(A-X) emission intensity integrated from 305 to 313 nm are recorded, one for dry feed gas and humid shielding gas, one for dry shielding gas and humid feed gas, and one for dry feed gas and dry shielding gas.

B. IR Quantum Cascade Laser Absorption Spectroscopy

The ozone density has been investigated by quantum cascade laser (QCL) spectroscopy in the infrared region [10], [11]. Fig. 4 shows the complete diagnostic setup with the kinpen and the gas shielding device. The measurement system is based on the Q-MACS system developed by neoplas control GmbH, which has been optimized for operation at atmospheric conditions [12]. The midinfrared light source is a pulsed QCL emitting in the spectral range from 1024 to 1030 cm^{-1}. The radiation is controlled by temperature adjustment. The QCL operates in single mode. The system can be tuned within a small range of 0.4 cm^{-1} by an increasing of the operating current. The laser beam divergence is corrected by a parabolic gold-coated off-axis mirror. It is

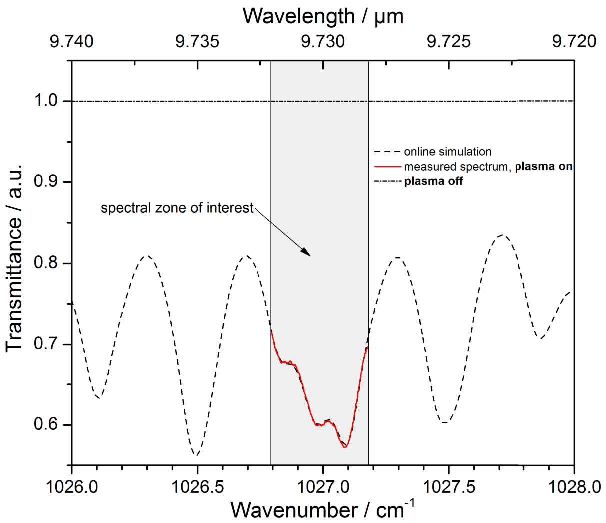

Fig. 5. Absorption spectrum of the Q-MACS IR-measurements.

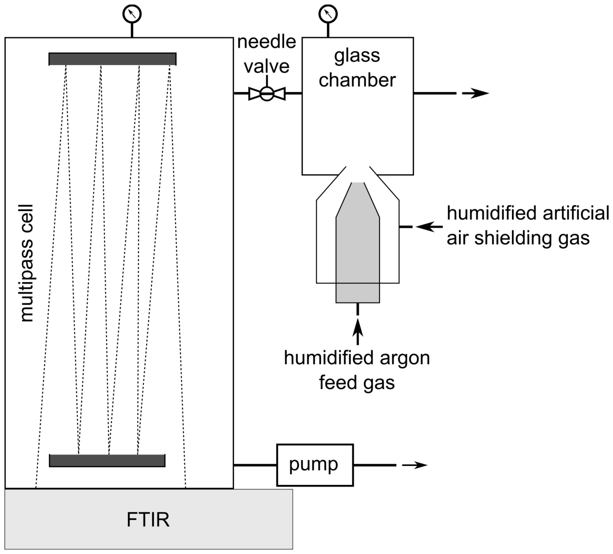

Fig. 6. Schematics of FTIR setup for the case of shielding gas humidification.

then focused onto a spherical mirror with a focal length of 1 m and guided through a 60-cm length multipass white cell. After 28 reflections within the cell, resulting in a total absorption length inside the multipass cell of 16.80 m, the intensity is measured by a fast mercury cadmium telluride detector.

A detailed description of the measurement procedure can be found in [10] and [12]. Briefly, the measurements were performed at atmospheric pressure in a glass tube with openings at each end for the mirrors, where the midinfrared reflection of the beam passes without disturbance. As shown in Fig. 4, the plasma jet is positioned in the middle of the multipass cell, without the laser passing through the plasma itself. The plasma source feed gas is blown directly into the glass chamber. The species distribution is assumed to be homogeneous.

Fig. 5 shows a simulated and a recorded spectrum of the ozone absorption at standard pressure and temperature conditions. The spectral region of interest, corresponding to the maximum tuning range of the QCL source, ranges from 1026.8 to 1027.2 cm^{-1} (shaded area in Fig. 5). The concentration of ozone is calculated from a fit algorithm implemented in the Q-MACSoft Monitor Software, which links the measured spectrum with the simulation [10]. The fit data are taken from the HITRAN database [13]. Fig. 5 shows the perfect agreement of measurement and fit result. For an accurate determination of ozone concentration, a spectrum is recorded every 2 s for approximately 5 min and then averaged. The errors are assumed as twice the standard deviation.

C. Fourier Transformed Infrared Absorption Spectroscopy

For the hydrogen peroxide (H_2O_2) measurement, in this paper, Fourier transformed infrared (FTIR) absorption spectroscopy in a multipass cell using a Bruker Vertex 70 v (Bruker GmbH) was applied. Fig. 6 shows a schematic diagram of the setup. To guide the plasma activated gas into the multipass cell of the FTIR spectrometer, a glass chamber around the effluent of the kinpen was constructed. The gas flow into the multipass cell was regulated with a needle valve. The pressure inside the multipass cell was reduced from the atmosphere and measured with a pressure gauge (Baratron, MKS).

The advantage of the lower pressure is the reduction of the particle collision rate and, as a consequence, a longer lifetime of the investigated species. Nevertheless, only long-living species (>millisecond lifetime) can be detected with this setup. In addition, the pressure broadening of the absorption signal is decreased, thus, a discrimination of the measured signal from the background is easier and thus an attribution of the absorption features to the respective molecules is more specific.

The measurement procedure is as follows. First, the gas supply of the kinpen and the shielding device are switched on. Second, the initially evacuated multipass cell is filled with the working gas up to the desired pressure (100 and 600 mbar in our study). Then, the background is measured with the FTIR. Immediately afterward, the plasma jet is switched on and the signal is measured for 15 min until it reaches a constant value. Finally, the plasma jet is switched off and the subsequent set of parameter is adjusted. After flushing the multipass cell for at least 15 min with the new gas mixture, the next measurement is started. Fig. 7 shows an exemplary FTIR spectrum of a gas shielded atmospheric pressure argon plasma jet operated with humid feed gas (3-slm argon and humidity concentration: 1890 ppm) and dry shielding gas (compressed air). The multipass cell pressure and absorption length were 100 mbar and 19.2 m, respectively. For clarity, only every fifth measurement data point is displayed. The spectrum is fitted by Q-MACSoft HT using spectroscopic data of O_3 and H_2O_2 from the HITRAN database [13]. For the quantification of the H_2O_2 production, metallic surfaces in the experimental setup were reduced as much as possible, but could not be completely avoided. However, due to the large volume of the multipass cell and the resulting high volume to surface ratio, as well as the reduced pressure, the interaction of the molecules with

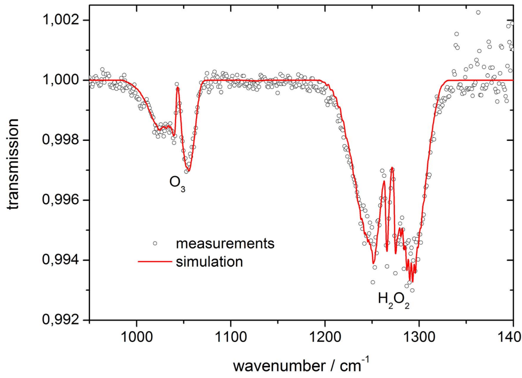

Fig. 7. Fitted FTIR spectrum at humid feed gas and dry air shielding gas conditions.

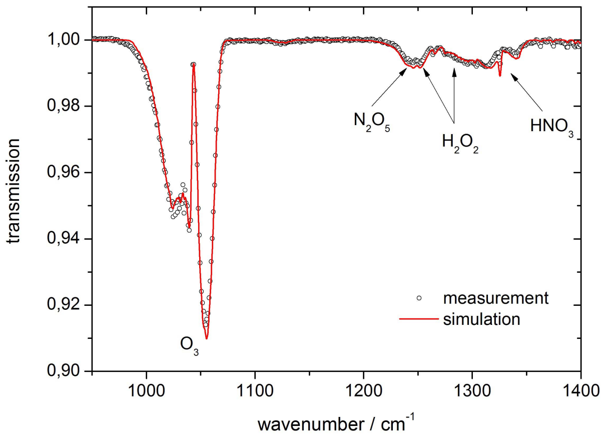

Fig. 8. Fitted FTIR spectrum of at dry feed gas and humid shielding gas conditions.

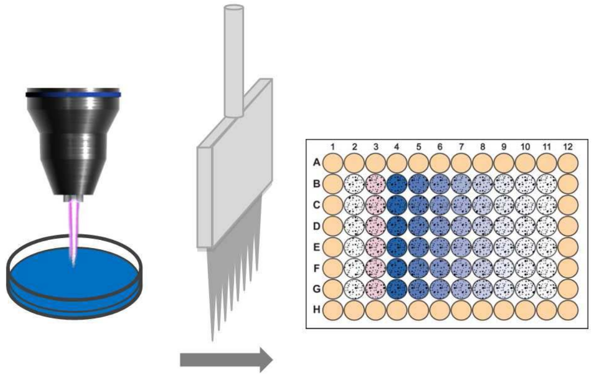

Fig. 9. Treatment procedure for separate treatment of HaCaT cells with variation of feed gas humidity where cell culture medium is treated and then pipetted into a cell containing 96 well plate (based on [14]).

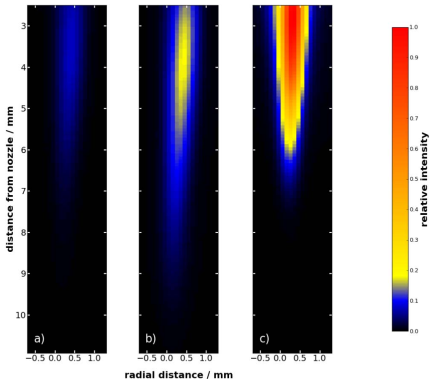

Fig. 10. 2-D emission profile of the OH(A-X) emission band for (a) almost dry conditions (<20 ppm), (b) ambient humidity (10 000 ppm), and (c) feed gas humidity (490 ppm).

the surface, including the metallic one is considered not to dominate the chemical processes.

Fig. 8 shows an exemplary FTIR spectrum of a gas shielded atmospheric pressure argon plasma jet operated with dry feed gas (3-slm argon) and humid shielding gas (humid air, humidity concentration: 3655 ppm). The multipass cell pressure and absorption length were 600 mbar and 32 m, respectively. For clarity, only every fifth measurement data point is displayed. The spectrum is fitted using spectroscopic data of O_3, N_2O_5, H_2O_2, and HNO_3 from HITRAN database via Q-MACSoft HT [13]. From the measurements, an HNO_3 concentration of roughly $3 \cdot 10^{12}$ cm^{-3} can be estimated.

D. HaCaT Skin Cell Treatment and Cell Viability Assay

For the investigation of biological effects, Human Keratinocyte cells (HaCaT) are treated indirectly with the plasma jet. For this procedure, the plasma jet is moved with an xyz stage in a meandering circular shape across a 60-mm petri dish with 5-ml Roswell Park Memorial Institute cell culture medium (Fig. 9). After the given treatment time, the plasma treated medium was pipetted into a 96 well plate (qualitative sketch in Fig. 9). Afterward, a dilution series is started according to [14]. Cell viability was assessed after 72 h by resazurin conversion assay (50 μm and 1 h), indicating the impact of the plasma treatment on cell proliferation rate.

IV. RESULTS AND DISCUSSION

A. Influence of H_2O Admixture on the Spatial OH Emission Profile

As a first insight into the influence of water admixture on the reactive species generation, space-resolved optical emission spectroscopy was performed for various dry and humid parameter sets. The wavelength-integrated space-resolved OH(A-X) emission band is shown in Fig. 10. The various parameters shown are wet feed gas and dry shielding gas, wet shielding gas and dry feed gas, as well as dry feed gas and shielding gas.

A very intense emission can be observed for the case of humid feed gas. It decreases monotonously from the nozzle.

For the case of humid shielding gas, a maximum OH emission can be observed outside the jet nozzle. Due to limited excitation outside the jet, this maximum can be attributed to the precursor inflow from ambient water molecules.

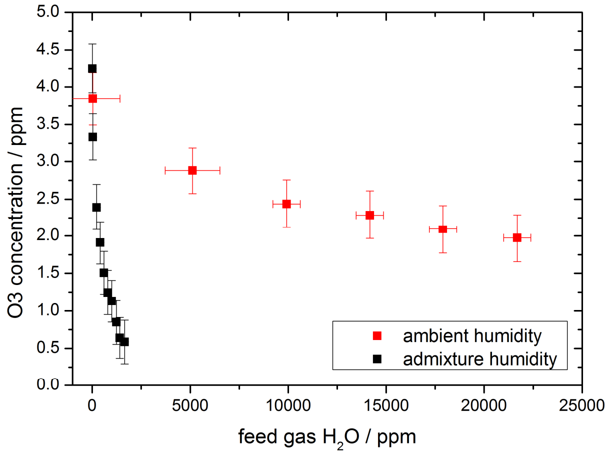

Fig. 11. Effect of feed gas humidity versus ambient humidity on ozone concentration in the multipass cell.

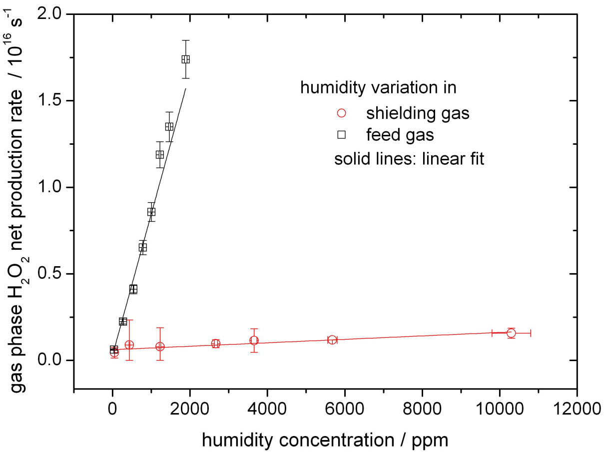

Fig. 12. Gas phase H_2O_2 concentration derived from FTIR measurements in the multipass cell for different humidity concentrations either in the feed gas (data taken from [2]) or in the shielding gas.

Near dry conditions exhibit a very low OH emission with only a slight maximum outside the nozzle. This seems to be an overlay of both effects.

The interesting fact is that a high OH emission signal achieved for feed gas humidity is reached at water admixture of 10 times lower than that of outside humidity. This agrees with the investigations performed in [2].

These results lead to the assumption that humidity related processes in the feed gas have greater impact than ambient humidity.

B. Influence of H_2O Admixture on Ozone and H_2O_2 Concentration

A vital role in plasma chemistry is played by H_2O [2]. However, the mechanism and consequence of humidity diffusing into the active effluent have not been deeply investigated so far. Since atmospheric pressure plasma jets are usually operated in ambient air at different humidity levels, a thorough humidity influence investigation is necessary, especially for these kinds of plasma sources.

Fig. 11 shows the influence of different shielding gas humidity concentrations on ozone. Since only H_2O is admixed to the feed gas (humid feed gas conditions), the observed O_3 concentrations for the case of humid feed gas mostly, and for the case of dry feed gas only, originate from reactions of indiffusing oxygen and H_2O molecules from the shielding gas.

For the ozone concentration, a strong decrease is observed with increasing humidity concentration. It can be observed that water reduces the concentration of ozone in the multipass cell by a factor of two for the case of shielding gas admixture and by a factor of three for the case of feed gas admixture.

The ozone reduction is either due to a reduced production or an increased destruction of ozone.

The major ozone production process is the reaction of molecular oxygen with atomic oxygen according to

$$O_2 + O + M \rightarrow O_3 + M \tag{1}$$

with a reaction coefficient $5.92 \cdot 10^{-34}$ $cm^6/mol^2 \cdot s$ at 298 K. In the present case, it is considered that the production of O or O_3 by UV radiation is minor and less than 5% compared with the chemical reactions [15]. Therefore, ozone results only from the reactions of molecular oxygen and atomic oxygen. Obviously, the production of ozone can be highly influenced by an admixture of molecular oxygen within the feed gas [10].

Since the concentration of the collision partner M and the molecular oxygen in (1) are independent of the humidity concentration, only a humidity-induced decrease of atomic oxygen would explain a decrease in the production of ozone. This can be attributed to the loss of electrons due to the molecular admixture. This loss of electrons will reduce excited or ionized argon species and reduce the dissociation of oxygen from air and water.

On the other hand, the destruction of ozone can generally occur for our conditions via the following channels:

$$O_3 + AB \rightarrow AO_2 + BO \tag{2}$$

$$O_3 + A \rightarrow AO + O_2 \tag{3}$$

$$O_3 + A \rightarrow O + O_2 + A \tag{4}$$

where A and B are nitrogen, oxygen and/or hydrogen reaction partners. Since the concentration of the most reactants A and AB depend on H_2O concentration the destruction of O_3 itself is humidity dependent. Presumably, the observed O_3 decline is not only a reduced production or increased destruction processes but also a superposition of both.

From Fig. 11, it can be observed that both for the admixture of water to the feed gas and to the shielding gas, the ozone density decreases monotonously. The shape of ozone concentration reduction is almost the same for both cases, and the quantity is different by a factor of 20.

Fig. 12 shows the development of H_2O_2 concentration as a function of humidity admixture both for the case of H_2O admixture to the feed gas and to the shielding gas.

Clearly, a linear increase can be observed as a function of humidity both for the feed gas and shielding gas humidity admixture. To analyze the measurements, three different plasma regions need to be considered for the production and destruction of H_2O_2, namely, the core plasma region with electron and excited species dominating the processes, the effluent plasma region, where additionally ambient species chemistry is present, and the far field region, where plasma species play no dominant role and only chemical reactions occur. Since only argon and water molecules are feed into the core plasma zone H_2O_2 is produced by dissociation of water via the production of OH according to

$$P + H_2O \rightarrow OH + H + P \tag{5}$$

where P is a plasma species, namely, electrons or excited argon species. OH recombines in a three-body collision with a collision partner M to H_2O_2

$$OH + OH + M \rightarrow H_2O_2 + M.$$

If ambient humidity is present, this process also occurs in the second region—the effluent region. Since the electron density and temperature are much lower in this region, the amount of H_2O_2 produced is lower compared with the core plasma region. In addition to the H_2O_2 production via OH, the abundance of ambient O_2 in that region opens a second way of generating H_2O_2

$$H + O_2 + M \rightarrow HO_2 + M \tag{6}$$

where atomic hydrogen reacts with molecular oxygen to form the perhydroxyl radical. Subsequently, two perhydroxyl radicals can finally react to H_2O_2

$$2HO_2 + M \rightarrow H_2O_2 + O_2 + M. \tag{7}$$

However, perhydroxyl also reacts with remaining OH radicals according to

$$HO_2 + OH \rightarrow H_2O + O_2 \tag{8}$$

yielding in a self-destruction of educts necessary for H_2O_2 generation.

From the results, the relevance of the respective production processes can be deduced. Since adding water to the feed gas yields the most efficient way to generate H_2O_2, the dissociation of H_2O by plasma species to generate OH is the dominant reaction pathway, and (6) and (7) provide only minor contribution to the hydrogen peroxide generation.

It can be observed that as for the ozone generation, the H_2O_2 concentration requires a more than tenfold higher humidity admixture in the shielding gas compared with the admixture to the feed gas to have the same effect.

C. Influence on Cell Viability

Fig. 13 shows the cellular viability of HaCaT skin cells treated by the procedure described above after 72 h of incubation. The viability is shown as a function of feed gas humidity (black squares) and of shielding gas humidity (open circles). It can be clearly observed that the cell viability decreases with higher humidity (for the case of feed gas admixture) or remains unchanged for the case of shielding gas humidity.

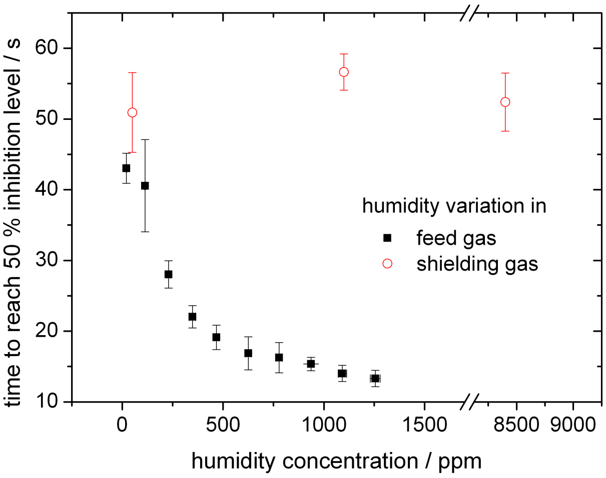

Fig. 13. Cell viability of HaCaT skin cells for the treatment with humidity added to the feed gas (black squares) and to the shielding gas (open circles).

From the species measurements, we can observe that for increasing feed gas humidity admixture, viability decreases, and ozone production also decreases. For the shielding gas humidity variation, the viability remains constant while the ozone concentration drops by a third.

More interestingly, the H_2O_2 concentration increases with humidity admixture, which correlates with a reduced cell viability. In earlier work, the effect of humidity was investigated on the cell viability [2]. Already, the assumption was made that the viability correlates with the H_2O_2 dynamics. This is confirmed by this paper, but more studies are needed to verify the assumption.

Finally, the shielding gas humidity variation shows little effect on the H_2O_2 concentration, which is reflected in the cell viability response.

V. CONCLUSION

In this paper, the influence of ambient and feed gas humidity on reactive species generation by plasma and their effect on cell viability was investigated. It could be shown that for feed gas humidity variation, the ozone concentration rapidly decreased by a factor of three. For humidity variation in the shielding gas, also a decrease of ozone was detected, but the effect was 20 times lower than for the feed gas humidity variation.

The H_2O_2 concentration increased linearly by almost an order of magnitude, while again, for an ambient humidity variation, the effects were more subtle and the H_2O_2 concentration increases only slightly.

From this paper, it could be shown that electron or energetic plasma species-based dissociation of water to the OH molecule is the relevant production pathway for the generation of H_2O_2.

The cell viability reaction to the plasma treatment rather followed the development of the H_2O_2 species than the ozone species. Further investigations will ensure the effect of H_2O_2 in indirect plasma treatment of skin cells.

ACKNOWLEDGMENT

The authors would like to thank L. Kantz for the cell viability measurements and H. Zimmermann for the support with the Q-MACS measurements, as well as Dr. R. Foest and Dr. J. Schäfer for the support with the QCL equipment.

REFERENCES

[1] X. Lu, M. Laroussi, and V. Puech, "On atmospheric-pressure non-equilibrium plasma jets and plasma bullets," *Plasma Sour. Sci. Technol.*, vol. 21, no. 3, p. 034005, 2012.

[2] J. Winter *et al.*, "Feed gas humidity: A vital parameter affecting a cold atmospheric-pressure plasma jet and plasma-treated human skin cells," *J. Phys. D, Appl. Phys.*, vol. 46, no. 29, p. 295401, 2013.

[3] K.-D. Weltmann, M. Polak, K. Masur, T. von Woedtke, J. Winter, and S. Reuter, "Plasma processes and plasma sources in medicine," *Contrib. Plasma Phys.*, vol. 52, no. 7, pp. 644–654, Aug. 2012.

[4] A. Kramer *et al.*, "Suitability of tissue tolerable plasmas (TTP) for the management of chronic wounds," *Clin. Plasma Med.*, vol. 1, no. 1, pp. 11–18, Jun. 2013.

[5] T. von Woedtke, S. Reuter, K. Masur, and K.-D. Weltmann, "Plasmas for medicine," *Phys. Rep.*, vol. 530, no. 4, pp. 291–320, Sep. 2013.

[6] K.-D. Weltmann *et al.*, "Atmospheric pressure plasma jet for medical therapy: Plasma parameters and risk estimation," *Contrib. Plasma Phys.*, vol. 49, no. 9, pp. 631–640, Nov. 2009.

[7] K. D. Weltmann, E. Kindel, T. von Woedtke, M. Hähnel, M. Stieber, and R. Brandenburg, "Atmospheric-pressure plasma sources: Prospective tools for plasma medicine," *Pure Appl. Chem.*, vol. 82, no. 6, pp. 1223–1237, 2010.

[8] S. Reuter, J. Winter, A. Schmidt-Bleker, H. Tresp, M. U. Hammer, and K.-D. Weltmann, "Controlling the ambient air affected reactive species composition in the effluent of an argon plasma jet," *IEEE Trans. Plasma Sci.*, vol. 40, no. 11, pp. 2788–2794, Nov. 2012.

[9] S. Reuter *et al.*, "From RONS to ROS: Tailoring plasma jet treatment of skin cells," *IEEE Trans. Plasma Sci.*, vol. 40, no. 11, pp. 2986–2993, Nov. 2012.

[10] S. Reuter *et al.*, "Detection of ozone in a MHz argon plasma bullet jet," *Plasma Sour. Sci. Technol.*, vol. 21, no. 3, p. 034015, Jun. 2012.

[11] J. Röpcke, P. B. Davies, N. Lang, A. Rousseau, and S. Welzel, "Applications of quantum cascade lasers in plasma diagnostics: A review," *J. Phys. D, Appl. Phys.*, vol. 45, no. 42, p. 423001, Oct. 2012.

[12] S. Iséni, S. Reuter, and K.-D. Weltmann, "NO_2 dynamics of an Ar/Air plasma jet investigated by *in situ* quantum cascade laser spectroscopy at atmospheric pressure," *J. Phys. D, Appl. Phys.*, vol. 47, no. 7, p. 075203, 2014.

[13] *Q-MACSoft HT*, Neoplas Control GmbH, Greifswald, Germany: 2012.

[14] K. Wende, S. Reuter, T. von Woedtke, K.-D. Weltmann, and K. Masur, "Redox based assay for assessment of biological impact of plasma treatment," *Plasma Processes Polym.*, vol. 11, no. 7, pp. 655–663, 2014.

[15] S. Reuter, *Formation Mechanisms of Atomic Oxygen in an Atmospheric Pressure Plasma Jet Characterised by Spectroscopic Methods*. Göttingen, Germany: Cuvillier Verlag, 2008.

Stephan Reuter (M'12) received the M.E. (Dipl.-Phys.Ing.) and M.Sc.(Dipl.-Phys.) degrees in plasma physics from the University of Duisburg-Essen, Essen, Germany, and the Ph.D. (Dr.rer.nat.) degree in 2007 at the University of Duisburg-Essen for the investigation of oxygen formation mechanisms in atmospheric pressure plasma jets.

He became a Research Fellow at the Centre for Plasma Physics, Queen's University Belfast, Belfast, U.K., in 2008. He is currently the Head of the Extracellular Effects Junior Research Group with the German Federal Ministry of Education and Research-Funded Centre for Innovation Competence Plasmatis, Leibniz Institute for Plasma Science and Technology, Greifswald, Germany, where he performs research on controlling the interaction of atmospheric pressure plasmas with biological liquids in the field of plasma medicine. The focus of his research group lies on optical diagnostics and modeling of atmospheric pressure plasma jets interacting with liquids.

Dr. Reuter is a member of the German Physical Society, the International Society for Plasma Medicine, the Nationales Zentrum für Plasmamedizin, and the International Society for Plasma Chemistry.

Jörn Winter received the Diploma degree in physics and the Ph.D. (Dr.rer.nat.) degree in experimental physics from the University of Greifswald, Greifswald, Germany, in 2005 and 2009, respectively.

He became a Scientific Staff Member at the Leibniz Institute for Plasma Science and Technology, Greifswald, in 2006, where he was involved in mercury-free low-pressure gas discharges for lighting, and plasma diagnostics. In 2008, he joined the Department of Research and Development, Webeco GmbH and Company KG., Selmsdorf, Germany, where he was involved in plasma generation for the sterilization of endoscopes. Since 2010, he has held a post-doctoral position with the German Federal Ministry of Education and Research-Funded Centre for Innovation Competence Plasmatis, Leibniz Institute for Plasma Science and Technology, where he is investigating plasma-cell interactions with a focus on plasma diagnostic.

Sylvain Iséni was born in France in 1988. He received the M.Sc. degree in physics from the University of Orléans, Orléans, France, in 2011, the M.Eng. degree in optics, laser, and plasma physics and processes and the Dipl.Eng.M.Sc. degree from the École Polytechnique de l'Université d'Orléans, Orléans in 2011. In 2011, he performed his master's thesis at the Eindhoven University of Technology, Eindhoven, The Netherlands, and the Leibniz Institute for Plasma Science and Technology, Greifswald, Germany, with the topic of diagnostics of atmospheric pressure plasma jets applied for biomedical applications. He is currently pursuing the Ph.D. degree with the German Federal Ministry of Education and Research-Funded Center for Innovation Competence Plasmatis, Leibniz Institute for Plasma Science and Technology, with a focus on electrical characterization and laser diagnostics of atmospheric plasma microdischarges.

Mr. Iséni has been a member of the International Society for Plasma Medicine since 2012.

Ansgar Schmidt-Bleker received the Diploma degree in physics from RWTH Aachen University, Aachen, Germany, in 2010. He is currently pursuing the German Federal Ministry of Education and Research-Funded Centre for Innovation Competence Plasmatis, Leibniz Institute for Plasma Science and Technology, Greifswald, Germany, with a focus on simulations for biomedical applications of plasmas.

He investigated nonlinear effects in quantum plasmas with the Institute for Theory of Statistical Physics until 2011 as a scientific employee with RWTH Aachen University.

Mario Dünnbier received the B.Sc. and M.Sc. degrees in plasma physics from the University of Greifswald, Greifswald, Germany, in 2009 and 2011, respectively. He is currently pursuing the Ph.D. degree with the German Federal Ministry of Education and Research-Funded Centre for Innovation Competence Plasmatis, Leibniz Institute for Plasma Science and Technology, Greifswald, with a focus on investigating atmospheric pressure plasmas in the field of medical applications.

Mr. Dünnbier has been a member of the International Society for Plasma Medicine since 2012.

Kai Masur was born in Germany in 1974. He received the Diploma degree in biochemistry in 1998, and the Ph.D. (Dr.rer.nat.) degree from the University of Witten/Herdecke, Witten, Germany, in 2001, with a focus on the signal transduction of metastasizing tumor cells.

He was involved in signal transduction of pancreatic beta cells with the New England Medical Centre, Tufts University, Boston, MA, USA, from 2001 to 2003. From 2003 to 2009, he was a Principal Investigator with the University of Witten/Herdecke, where he established his own work group by combining diabetes research and oncology. Since 2009, he has been the Head of the Cellular Effects Junior Research Group with the German Federal Ministry of Education and Research-Funded Centre for Innovation Competence Plasmatis, Leibniz Institute for Plasma Science and Technology, Greifswald, Germany, where his group is investigating the interplay of nonthermal plasma with living cells and tissues—focusing on the alterations of the genome and proteome—to stimulate cellular activities. His current research interests include cellular signal transduction cascades and how to manipulate those signals.

Dr. Masur is a member of the German Society for Biochemistry and Molecular Biology, the International Society for Plasma Medicine, and the Society for Signal Transduction.

Kristian Wende received the Diploma and Ph.D. (Dr.rer.nat.) degrees from the University of Greifswald, Greifswald, Germany, in 1998 and 2003, respectively.

He was involved in the phytochemical composition of plants and different analytical techniques from 1998 and 2003. From 2004 to 2009, he investigated the interaction of marine/terrestrial natural products, UV light, and nonthermal plasmas with different cellular models with the Institute for Pharmacy, Greifswald, as a Group Leader of Cell Biology. Since 2010, he has been a member of the German Federal Ministry of Education and Research-Funded Centre for Innovation Competence Plasmatis with the Leibniz Institute for Plasma Science and Technology, Greifswald, Germany. His current research interests include eukaryotic cell responses after exogenic stimuli.

Dr. Wende is a member of the International Society of Plasma Medicine and the German Pharmaceutical Society.

Klaus-Dieter Weltmann (M'95) received the Diploma degree in electronics and the Ph.D. (Dr.rer.nat) degree in applied physics from the University of Greifswald, Greifswald, Germany, in 1989 and 1993, respectively.

He was involved in nonlinear dynamics in low-temperature plasmas and plasma diagnostics. In 1994, he was a Visiting Scientist with the Plasma Physics Laboratory, West Virginia University, Morgantown, WV, USA. In 1995, he joined ABB Corporate Research Ltd., Baden-Dättwil, Switzerland, where he was involved in the research and development of HV and MV switchgear. In 1998, he became the Head of the High Voltage Systems Group, ABB Corporate Research Ltd. In 2000, he was appointed to lead Research and Development of Gas Insulated Switchgear (GIS) at ABB High Voltage Technologies Ltd., Zurich, Switzerland, where he became the Business Unit Research and Development Manager GIS in 2002. Since 2003, he has been the Director and Chairman of the Board of the Leibniz Institute for Plasma Science and Technology, Greifswald, and a Professor of Experimental Physics with the University of Greifswald. His current research interests include switchgears, arc physics, atmospheric plasmas, modeling and simulation, plasma-medicine and plasma decontamination.

Prof. Weltmann is the President of the International Society for Plasma Medicine, and a member of the German Physical Society and several consulting committees in industry and research. He is an initiator of three spinoff companies.

5.8 Article VIII

Nitrogen Shielding of an Argon Plasma Jet and its Effects on Human Immune Cells[a]

doi:10.1109/TPS.2015.2393379

---

[a] © 2015 IEEE. Reprinted, with permission, from [Bekeschus, Iseni, Reuter, Masur, and Weltmann, Nitrogen Shielding of an Argon Plasma Jet and its Effects on Human Immune Cells, IEEE TRANSACTIONS ON PLASMA SCIENCE, March 2015]

Nitrogen Shielding of an Argon Plasma Jet and Its Effects on Human Immune Cells

Sander Bekeschus, Sylvain Iséni, Stephan Reuter, *Member, IEEE*, Kai Masur,
and Klaus-Dieter Weltmann, *Member, IEEE*

***Abstract*— Atmospheric pressure plasmas are widely used in research for biomedical or clinical applications. Reactive oxygen species and reactive nitrogen species (RNS) produced by plasmas are thought to be of major significance in plasma-cell interactions. Different applications, however, may demand for different plasma properties. Tailoring plasma devices by modulating the supply gas or the surrounding is a suitable way to alter reactive species composition, vacuum ultra violet emission, or temperature. Treatment regimens involving availability of oxygen or humidity may lead to increased hydrogen peroxide deposition in liquids and thus will be toxic to cells. Using an atmospheric pressure argon plasma jet, we applied a nitrogen gas curtain to its visible effluent during treatment of human immune cells. The curtain deprived the plasma of molecular oxygen. This excluded gas-phase oxygen plasma chemistry and led to generation of highly energetic metastables. Planar laser-induced fluorescence spectroscopy verified laminar gas flow and complete elimination of surrounding air by the gas curtain. We used human immune cells to monitor cytotoxic effects as they are highly relevant in potential clinical plasma applications, e.g., treatment of chronic wounds. Air curtain plasma treatment led to significantly higher cytotoxicity compared with nitrogen curtain plasma treatment. Scavenging of hydrogen peroxide abrogated cell death in both gas curtain conditions. This indicated a negligible contribution of highly energetic metastables or increased gas temperature to cytotoxicity. Finally, the results suggested an oxygen-independent generation of hydrogen peroxide pointing to an indirect role of UV or RNS in plasma-mediated cytotoxicity.**

***Index Terms*— Atmospheric pressure plasma jet, gas curtain, hydrogen peroxide, immune cells, plasma medicine.**

I. INTRODUCTION

IN PLASMA medicine, cold atmospheric pressure plasmas are applied to cells and tissues [1]. Details on plasma-cell interactions, however, still remain to be elucidated. A vital parameter influencing reactive species composition and cellular responses is the feed gas and gas curtain being used [2]. The gas curtain provides a controlled gas area around the plasma effluent, enhancing the reproducibility of the plasma properties [3]. In addition, external parameters, e.g., humidity can be monitored to tailor the reactive species produced in the effluent and its vicinity [2], [4]. However, various input parameters can be modified, which affects the plasma and its chemistry of reactive oxygen species (ROS) and reactive nitrogen species (RNS) [5]. We recently reported on the laminar or turbulent flow pattern resulting from the feed gas flow rate [6]. Following these observation, this paper focuses on using the same plasma source in a laminar regime. Moreover, we applied a gas curtain cap to fully control the surrounding of the plasma effluent from the jet nozzle to the cell suspension. Here, a laminar argon flow propagated into an ionization front, whereas a pure and dry nitrogen shroud prevented any molecular oxygen or water molecules to interact with the plasma. Consequently, the plasma chemistry in the gas phase was reduced to RNS only. Optical emission spectroscopy revealed the presence and spatial distribution of highly energetic metastables. Liquid chemistry was not investigated in this paper.

To differentiate between air and nitrogen curtain plasma effects, we evaluated their cytotoxicity on human immune cells. Specifically, we referred to three specific populations within those cells. Two of them are lymphocytic origin and their important role in pathological wounds has been implied previously [7]. In addition, they display the highest sensitivity toward plasma compared with various other cell types [8], [9]. This also allows one to distinguish subtle differences in oxidation by plasma [10]. As a third cell type, monocytes were investigated. When differentiated to macrophages, these phagocytes are highly relevant in tissue regeneration [11]. Our previous work had identified significant amounts of plasma-generated hydrogen peroxide (H_2O_2) being deposited in treated liquids [12], [13]. H_2O_2 is thought to be derived from hydroxyl radical ($^{\cdot}HO$) and has a dominant role in cell toxicity [10]. The nitrogen gas curtain shielded the plasma from any oxygen and we hypothesized to find toxic agents other than H_2O_2 in this regime. While cell survival differed between gas curtain conditions, cytotoxicity remained to be dependent on H_2O_2 as results using catalase suggested.

II. PLASMA JET AND GAS CURTAIN

The plasma source used was the *kinpen* (Neoplas, Germany). This jet was operated at atmospheric pressure and argon (99.999% purity, Air Liquide, France) was used as feed gas [14]. It consists of a concentric needle electrode located in a 1.6-mm diameter dielectric capillary and a ground ring

Manuscript received July 31, 2014; revised September 15, 2014; accepted December 8, 2014. This work was supported by the Federal German Ministry of Education and Research under Grant 03Z2DN11 and Grant 03Z2DN12.

The authors are with the Centre for Innovation Competence Plasmatis, Leibniz-Institut für Plasmaforschung und Technologie e.V., Greifswald 17489, Germany (e-mail: sander.bekeschus@inp-greifswald.de; sylvain.iseni@inp-greifswald.de; stephan.reuter@inp-greifswald.de; kai.masur@inp-greifswald.de; weltmann@inp-greifswald.de).

Color versions of one or more of the figures in this paper are available online at http://ieeexplore.ieee.org.

Digital Object Identifier 10.1109/TPS.2015.2393379

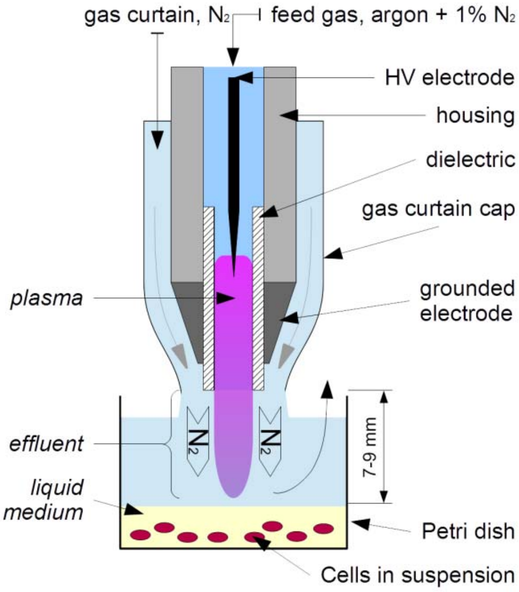

Fig. 1. Schematic of the plasma source and the gas curtain used to treat the human immune cells in suspension.

electrode on the outer diameter. The electrode was powered with an electric excitation of 1 MHz and dissipates between 0.9 and 2.2 W. The device can be operated at various feed gas flow rates ranging from 0.5 to 3 slm and yields a visible effluent length between 8 and 15 mm. At the tip of the effluent (~10 mm, 3 slm feed gas flow rate), the average gas temperature does not exceed 350 K.

Fig. 1 shows the geometrical and electrical configuration of the plasma source including the gas curtain cap. The feed gas flow rate was fixed at 1 slm argon to operate the plasma jet in a laminar regime. The plasma was shielded from the capillary nozzle to the liquid surface by 2 slm of nitrogen or dry synthetic air (99.999% purity, Air Liquide, France). By this way, any room air molecules were excluded. Feed gas and gas curtain were run for at least 1 h prior to experiments to eliminate residual humidity (<20 ppm) in tubing. All gases were low on molecular oxygen (<2 ppm) as stated by the supplier. Independent of the gas curtain condition, 1% of N_2 was admixed to the feed gas to increase the production of RNS.

III. MATERIALS AND METHODS

A. Planar Laser-Induced Fluorescence (PLIF)

The optimum shielding conditions were determined experimentally. By injecting an organic compound into the gas curtain, it was possible to visualize the flow pattern using planar laser-induced fluorescence (PLIF). Here, a planar laser sheath excited a fluorescent probe within the feed or curtain gas. Its fluorescent emission can be used as a flow profile visualization tool. Details on this method can be read elsewhere [6].

B. Optical Emission Spectroscopy of $N_2(C)$

To the human eye, the plasma effluent is visible due to radiation in the visible spectra. Radiation is emitted by molecules and atoms being excited by the plasma. This is a result of either electron impacts or nonelastic collisions between particles. Spatially resolved observations of the spontaneous emission of the second positive system of nitrogen $N_2(C)$ was important to identify the area of potentially high energy within the effluent. The experimental apparatus consisted of an intensified charge-coupled device camera (LaVision GmbH, Germany) with a 100-mm focal length optics mounted on the front. An optical bandpass (bp) filter centered at 335 nm (7-nm bandwidth, Semrock, USA) was inserted to exclusively visualize $N_2(C)$ emission.

C. Cell Isolation

Human peripheral blood mononuclear cells (PBMCs) were isolated by density gradient centrifugation using lymphocyte separation medium (PanBiotech, Germany), as described before [15]. Subsequent counting was done using a hemocytometer. Cell viability after isolation was always greater than 97%, as determined by trypan blue exclusion assay. Cells were suspended at 1×10^6 ml^{-1} in RPMI1640 without phenol red and supplemented with 1% penicillin/streptomycin, 2% glutamine (all PanBiotech), and 10% fetal bovine serum (Sigma, USA). Upon blood donation at the blood bank (University Medicine of Greifswald, Germany), healthy blood donors gave written and informed consent about anonymous usage of blood for research purposes in the case of the donation is not suitable for clinical application.

D. Plasma Treatment of Cells

The plasma device was oriented vertically at a distance of 8–10 mm from the tip of the capillary to the liquid surface (1 ml of cell suspension). The effluent was close to the surface, but did not connect to it. In this setup, the electrical properties of the plasma, e.g., the current, were identical compared with the jet running in free atmosphere [16]. Cells were plasma-treated in 24 well plates (Sarstedt, Germany) for 1 or 5 min and in duplicates for each condition and experiment. Where indicated, catalase (50 μg/ml in phosphate-buffered saline (PBS); Sigma, USA) was added to each well prior to treatment. The jet was not moved during treatment of one well and immediately and manually transferred to the next well of the plate after treatment was finished. In addition to untreated controls, cytotoxicity of gas but not plasma-treated cells was also evaluated and always resembled untreated controls (data not shown). After exposure, cells were incubated at 37 °C in a cell culture incubator (Binder, Germany) with humidified air and 5% CO_2. Twenty-four hours after treatment, the cells were harvested in 12 mm × 75 mm tubes (Sarstedt, Germany) and washed once with PBS prior to antibody-staining.

E. Flow Cytometry

Cells were investigated using a *Gallios* flow cytometer (Beckman Coulter, USA) equipped with three solid-state diode lasers (405 nm at 40 mW, 488 nm at 22 mW, and 638 nm at 25 mW). Determination of viability was done as described before [8], [10], [17]. Briefly, 24 h after

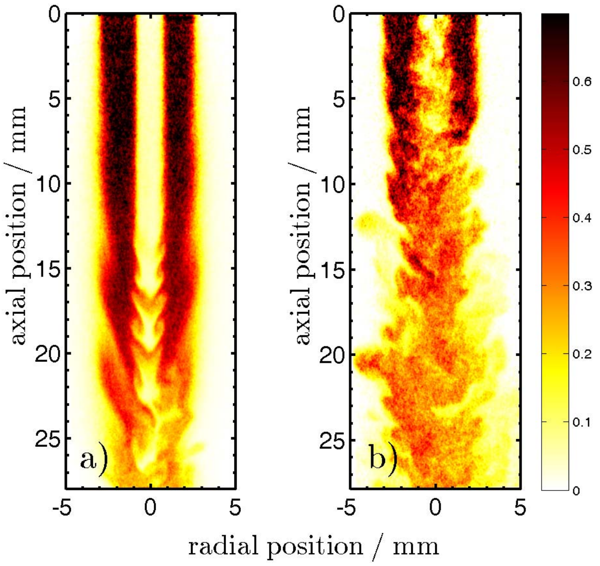

Fig. 2. PLIF image (200-ns exposure time) from an organic compound admixed within the gas curtain (here nitrogen). The plasma is off, but argon feed gas is flowing. Depicted are the flow patterns of the gas curtain at 1.7 slm with 1 slm argon feed gas flow rate (a, laminar), and gas curtain at 5 slm with 3 slm argon flow rate (b, turbulent).

treatment, the cells were stained with annexin V fluorescein isothiocyanate, allophycocyanin-conjugated anti-CD4 (T helper cell marker), phycoerythrin-conjugated anti-CD8 (cytotoxic T cell marker), and phycoerythrin-cyanine-7-conjugated anti-CD14 (monocyte marker) monoclonal antibodies in annexin V binding buffer for 15 min in the dark (all Biolegend, USA). After washing, cells were suspended in binding buffer containing 4’, 6-diamidino-2-phenylindole (DAPI; Thermo, USA) to stain deoxyribonucleic acid of cells with compromised membranes. Light was collected using the following filters (center/bandwidth in nanometer; all Semrock, USA): 450/40 (bp, DAPI), 525/40 (bp, Annexin V), 660/20 (bp, CD4), and 755 nm longpass (CD14). Only Annexin V-negative/DAPI-negative cells were counted as viable cells. At least 5×10^4 cells were acquired per sample using *Kaluza Acquisition* 1.0 software (Beckman Coulter). Flow-cytometry-standard 3.0 files (>200 single measurements) were batch-analyzed applying the same gating strategy with *Kaluza* 1.3 software (Beckman Coulter).

IV. RESULTS AND DISCUSSION

A. Gas Curtain Effectively Minimized Ambient Air Influx

The efficiency of the gas curtain has been reported before [2] using pure argon as feed gas and molecular nitrogen or oxygen as curtain gas. This allows to control plasma properties, e.g., the reactive species output [4]. However, the gas flow rate used in these studies resulted in a turbulent effluent [6]. Comparison of gas curtain flow patterns in laminar [Fig. 2(a)] or turbulent conditions [Fig. 2(b)] revealed differences in gas flow structures. The figures can be compared with in [6, Fig. 1(b)]. In case of plasma on, the visible plasma effluent is located along the first 10–15 mm (axial position). Using higher flow rates, turbulences resulted in mixing of plasma and shielding gas [Fig. 2(b)]. Thus, the plasma was fully shielded only in laminar but not in turbulent conditions. Due to this full shielding, effects of the gas curtain on the plasma chemistry composition reported previously [2]–[4] are very likely to be enhanced in the present conditions. Effective nitrogen shielding also suggested ROS depletion in the plasma gas phase due to exclusion of molecular oxygen. Any remaining ROS may exclusively rely on the impurities remaining from the gas bottles. Concurrently, an enhancement of the RNS in the gas phase was expected, e.g., N_2^+, $N_2(A)$, and N.

Having a laminar gas flow results in an increase of the gas temperature [18]. The rotational temperature of NO is assimilated to the gas temperature, and thus reflects the temperature on the ionization propagation time scale. The temperature at a 7.5-mm distance from the nozzle was measured to be around 400 K in the same experimental conditions.

B. $N_2(C)$ Emission and Metastables

Preventing influx of oxygen to the plasma and its effluent inhibits the formation of ozone and atomic oxygen. The dissociation energy of molecular oxygen is 6 eV which is close to the $N_2(A)$ energy level requiring 6.2 eV. Thus, molecular oxygen is a serious quencher for the highly energetic metastable state of nitrogen, which has a natural lifetime of ~2 s and acts as a significant energy carrier [19]. Nonetheless, its direct detection remains a challenge at atmospheric pressure. Only recently, chemical plasma modeling was compared with experimental data on the production of nitric oxide and atomic oxygen [20], and the plasma jet used in this previous study is similar to the device used in the present work. Interestingly, it was reported that $N_2(A)$ is a very important precursor for the generation of NO and O. Using nitrogen as gas curtain, molecular oxygen was not present. As the ground state of molecular nitrogen cannot quench $N_2(A)$ [21], the latter is a credible energy carrier to be transported from the plasma to the liquid surface, possibly reaching cells. Argon metastables are also important to consider and their effects on plasma chemistry were reported in similar conditions [4].

Fig. 3 shows the spontaneous emission of $N_2(C)$ from plasma. Significant energy is needed to excite the second positive system of nitrogen which can be provided by either electron impacts or can originate from near resonant energy transfer between argon metastables of the ($^3P_{0,2}$) states to excite $N_2(X)$ to $N_2(C)$ [22]. In a similar plasma jet configuration operated with argon, the same mechanism was proposed to explain the excitation of $N_2(C)$ [16]. As discussed in [6], diffusion of nitrogen from the vicinity into the argon channel takes place a few millimeter from the nozzle (on-axis position). In addition, the ionization front propagates along an argon channel bounded by the surrounding atmosphere and follows the higher argon density. If the flow is laminar, the highest argon density remains along the axis of the argon channel. In contrast, the discharge and the highest argon density had identical trajectories in turbulent conditions and the memory effect of the argon metastable was motivated [6]. Subsequently, nitrogen and argon metastables were seriously considered

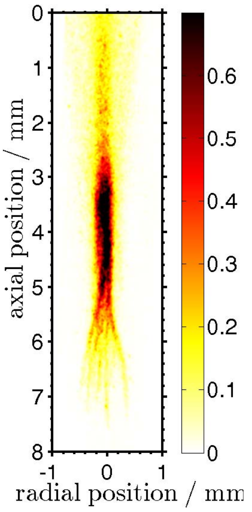

Fig. 3. Optical emission spectroscopy of spontaneous emission of the second positive system of nitrogen, $N_2(C)$, collected via a 7-nm bp filter centered at 335 nm. The plasma was operated using 1 slm argon and 2 slm N_2 gas flow rate for the gas curtain. The image was averaged over 300 single image acquisitions using an exposure time of 200 ns each.

to be transported from the gas phase to the liquid surface. Due to their high energy, a change of the liquid chemistry is anticipated but is out of the scope of this paper.

C. Lymphocyte Viability After Gas Curtain Plasma Exposure

We measured cell viability in primary human immune cells to investigate differences in shielding gas effects. Previously, we have shown that plasma treatment induced apoptosis in human blood cells (PBMC) [17]. Two distinct susceptibility types were: fragile lymphocytes and robust monocyte [8]. In this paper, we found similar differences [Fig. 4(a) and (c) versus (e)]. Compared with the previous setup (3 slm of argon, no gas curtain), cytotoxicity was much lower. A treatment of 1 min resulted in ∼75% [10], compared with ∼20% [Fig. 4(a) and (c)], nonviable cells 24 h after treatment. This may be due to differences in gas fluxes.

Comparing the effects between air and nitrogen shielding, the latter was significantly less toxic in lymphocytes but not in monocytes. This was in line with our hypothesis in which nitrogen shielded plasma yields lower concentrations of H_2O_2 due to the lack of $^{\cdot}HO$ as discussed above. On the other hand, highly energetic argon and nitrogen metastables may have also led to cytotoxic effects.

To investigate the origin of plasma cytotoxicity in either setup, we added catalase prior to exposure of cells. Independent of the gas curtain used or treatment time applied, the cells remained fully viable as determined by flow cytometry. Generation of H_2O_2 was previously thought to originate from gaseous $^{\cdot}HO$ [12], [13]. Here, results using catalase suggested that in the case of nitrogen shielding, H_2O_2 must be a product of RNS and liquid molecules [18]. The contribution of vacuum ultra violet (V–UV) to H_2O_2 production may also be of significance. It was estimated that one-thirds of $^{\cdot}HO$ radical deposition in cell culture medium may originate from V–UV [23]. Finally, temperatures of up to 400 K in the core of the plasma seem to be only local and did not adversely affect viability as our results suggested [Fig. 4(b), (d), and (f)].

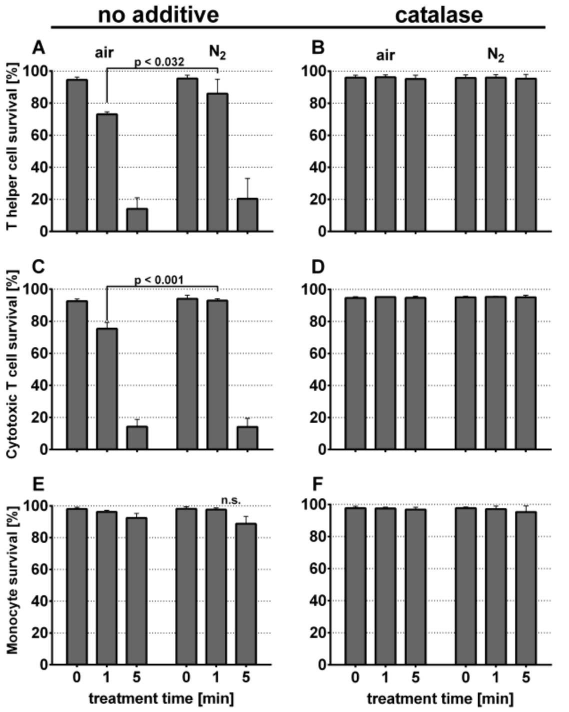

Fig. 4. (a) and (c) Comparison of nitrogen and air gas curtain showed significant differences in viability of T lymphocytes. (e) Monocytes were not strongly affected in either shielding configuration. (b), (d), and (f) Addition of H_2O_2 scavenging enzyme catalase prior to plasma treatment protected each cell type from cytotoxic plasma effects. Data are presented mean + SD of three-independent experiments.

V. CONCLUSION

Although no oxygen was present in nitrogen shielded plasma treatment of immune cells, cytotoxicity was still directly or indirectly dependent on the presence of H_2O_2. We speculate that H_2O_2 originated from the reaction of RNS or V–UV with components of the liquid cell suspension. Effective protection via catalase also suggested that highly energetic plasma argon or nitrogen metastables or increased temperatures in this particular setup were negligible in plasma-mediated cytotoxicity.

ACKNOWLEDGMENT

The authors would like to thank E. Fruneau for laboratory assistance as well as A. Schmidt-Bleker and Dr. J. Winter for their pioneering work related to these findings.

REFERENCES

[1] T. von Woedtke, S. Reuter, K. Masur, and K.-D. Weltmann, “Plasmas for medicine,” *Phys. Rep.*, vol. 530, no. 4, pp. 291–320, 2013.

[2] S. Reuter *et al.*, “From RONS to ROS: Tailoring plasma jet treatment of skin cells,” *IEEE Trans. Plasma Sci.*, vol. 40, no. 11, pp. 2986–2993, Nov. 2012.

[3] S. Reuter, J. Winter, A. Schmidt-Bleker, H. Tresp, M. U. Hammer, and K.-D. Weltmann, "Controlling the ambient air affected reactive species composition in the effluent of an argon plasma jet," *IEEE Trans. Plasma Sci.*, vol. 40, no. 11, pp. 2788–2794, Nov. 2012.

[4] A. Schmidt-Bleker, J. Winter, S. Iseni, M. Dünnbier, K.-D. Weltmann, and S. Reuter, "Reactive species output of a plasma jet with a shielding gas device—Combination of FTIR absorption spectroscopy and gas phase modelling," *J. Phys. D, Appl. Phys.*, vol. 47, no. 14, p. 145201, 2014.

[5] D. B. Graves, "The emerging role of reactive oxygen and nitrogen species in redox biology and some implications for plasma applications to medicine and biology," *J. Phys. D, Appl. Phys.*, vol. 45, no. 26, pp. 263001–263042, 2012.

[6] S. Iséni, A. Schmidt-Bleker, J. Winter, K.-D. Weltmann, and S. Reuter, "Atmospheric pressure streamer follows the turbulent argon air boundary in a MHz argon plasma jet investigated by OH-tracer PLIF spectroscopy," *J. Phys. D, Appl. Phys.*, vol. 47, no. 15, p. 152001, 2014.

[7] M. A. M. Loots, E. N. Lamme, J. Zeegelaar, J. R. Mekkes, J. D. Bos, and E. Middelkoop, "Differences in cellular infiltrate and extracellular matrix of chronic diabetic and venous ulcers *versus* acute wounds," *J. Invest. Dermatol.*, vol. 111, pp. 850–857, Jul. 1998.

[8] S. Bekeschus *et al.*, "Differential viability of eight human blood mononuclear cell subpopulations after plasma treatment," *Plasma Med.*, vol. 3, nos. 1–2, pp. 1–13, 2013.

[9] L. Bundscherer *et al.*, "Viability of human blood leukocytes compared with their respective cell lines after plasma treatment," *Plasma Med.*, vol. 3, nos. 1–2, pp. 71–80, 2013.

[10] S. Bekeschus *et al.*, "Hydrogen peroxide: A central player in physical plasma-induced oxidative stress in human blood cells," *Free Radical Res.*, vol. 48, no. 5, pp. 542–549, 2014.

[11] E. Engelhardt, A. Toksoy, M. Goebeler, S. Debus, E.-B. Bröcker, and R. Gillitzer, "Chemokines IL-8, GROα, MCP-1, IP-10, and Mig are sequentially and differentially expressed during phase-specific infiltration of leukocyte subsets in human wound healing," *Amer. J. Pathol.*, vol. 153, no. 6, pp. 1849–1860, 1998.

[12] J. Winter *et al.*, "Tracking plasma generated H_2O_2 from gas into liquid phase and revealing its dominant impact on human skin cells," *J. Phys. D, Appl. Phys.*, vol. 47, no. 28, p. 285401, 2014.

[13] J. Winter *et al.*, "Feed gas humidity: A vital parameter affecting a cold atmospheric-pressure plasma jet and plasma-treated human skin cells," *J. Phys. D, Appl. Phys.*, vol. 46, no. 29, p. 295401, 2013.

[14] K.-D. Weltmann *et al.*, "Atmospheric pressure plasma jet for medical therapy: Plasma parameters and risk estimation," *Contrib. Plasma Phys.*, vol. 49, no. 9, pp. 631–640, 2009.

[15] A. Boyom, "Separation of leucocytes from blood and bone marrow," *Scandin. J. Clin. Lab. Invest.*, vol. 97, no. 7, pp. 77–81, 1968.

[16] S. Hofmann, K. van Gils, S. van der Linden, S. Iseni, and P. Bruggeman, "Time and spatial resolved optical and electrical characteristics of continuous and time modulated RF plasmas in contact with conductive and dielectric substrates," *Eur. Phys. J. D*, vol. 68, no. 3, pp. 1–14, 2014

[17] S. Bekeschus *et al.*, "Human mononuclear cell survival and proliferation is modulated by cold atmospheric plasma jet," *Plasma Process. Polym.*, vol. 10, no. 8, pp. 706–713, 2013.

[18] H. Tresp, M. U. Hammer, K.-D. Weltmann, and S. Reuter, "Effects of atmosphere composition and liquid type on plasma-generated reactive species in biologically relevant solutions," *Plasma Med.*, vol. 3, nos. 1–2, pp. 45–55, 2014.

[19] Y. Teramoto, R. Ono, and T. Oda, "Measurement of $N_2(A^3\Sigma_u^+)$ metastable in N_2 pulsed positive corona discharge with trace amounts of additives," *J. Phys. D, Appl. Phys.*, vol. 42, no. 2, p. 235205, 2009.

[20] W. Van Gaens, P. J. Bruggeman, and A. Bogaerts, "Numerical analysis of the NO and O generation mechanism in a needle-type plasma jet," *New J. Phys.*, vol. 16, p. 063054, Jun. 2014.

[21] S. Hofmann, A. Sobota, and P. Bruggeman, "Transitions between and control of guided and branching streamers in DC nanosecond pulsed excited plasma jets," *IEEE Trans. Plasma Sci.*, vol. 40, no. 11, pp. 2888–2899, Nov. 2012.

[22] T. D. Nguyen and N. Sadeghi, "Rotational and vibrational distributions of $N_2(C^3\Pi_u)$ excited by state-selected $Ar(^3P_2)$ and $Ar(^3P_0)$ metastable atom," *Chem. Phys.*, vol. 79, no. 1, pp. 41–55, 1983.

[23] H. Tresp *et al.*, "Plasma jet (V)UV-radiation impact on biologically relevant liquids and cell suspension," in presented at the 67th Annu. Gaeous Electron. Conf., Nara, Japan, 2014, vol. 59, no. 16.

Sander Bekeschus was born in Berlin, Germany, in 1985. He received the Diploma degree in human biology with a major in immunology from the University of Greifswald, Greifswald, Germany, in 2011. He is currently pursuing the Ph.D. degree with the Centre for Innovation Competence (ZIK) Plasmatis, Greifswald.

He was a Visiting Scholar with the Centre for Free Radical Research, Christchurch, New Zealand, and the Flow Cytometry Core Facility, Harvard Stem Cell Institute, Boston, MA, USA, in 2013. He has extensive knowledge in the field of flow cytometry, and is the Chief Operator of numerous devices at ZIK Plasmatis. His current research interests include the reaction of human immune cells to cold atmospheric pressure plasmas to elucidate how plasma may have positives effects in wound healing.

Mr. Bekeschus is a member of the Society for Leukocyte Biology, the German Society for Immunology, the European Society for Free Radical Research, and the International Society for Plasma Medicine.

Sylvain Iséni was born in France in 1988. He received the M.Sc. degree in physics from the University of Orléans, Orléans, France, in 2011, and the M.Eng. degree from the École Polytechnique de l'Université d'Orléans, Orléans, with a focus on optics, laser, and plasma physics and processes. He is currently pursuing the Ph.D. degree with the Center for Innovation Competence Plasmatis, Leibniz-Institut für Plasmaforschung und Technologie e.V. (INP Greifswald e.V.), Greifswald, Germany, funded by BMBF, with a focus on electrical characterization and laser diagnostics of atmospheric plasma micro discharges. In 2011, he performed his master's thesis with the Eindhoven University of Technology, Eindhoven, The Netherlands, and INP Greifswald e.V., with the topic of diagnostics of atmospheric pressure plasma jets applied for biomedical applications.

Mr. Iséni has been a member of the International Society for Plasma Medicine since 2012.

Stephan Reuter (M'12) received the M.Eng. (Dipl.-Phys.-Ing.) and M.Sc. (Dipl.-Phys.) degrees in plasma physics from the University of Duisburg-Essen, Essen, Germany, and the Ph.D. (Dr.rer.nat.) degree with a focus on the investigation of oxygen formation mechanisms in atmospheric pressure plasma jets, in 2007.

He became a Research Fellow with the Centre for Plasma Physics, Queen's University Belfast, Belfast, U.K., in 2008. He is currently the Head of the Junior Research Group Extracellular Effects with the Centre for Innovation Competence Plasmatis, Leibniz-Institut für Plasmaforschung und Technologie e.V., Greifswald, Germany, funded by BMBF, where he performs research on controlling the interaction of atmospheric pressure plasmas with biological liquids in the field of plasma medicine. The focus of his research group lies on optical diagnostics and modeling of atmospheric pressure plasma jets interacting with liquids.

Dr. Reuter is a member of the German Physical Society, the International Society for Plasma Medicine, the Nationales Zentrum für Plasmamedizin, and the International Society for Plasma Chemistry.

Kai Masur was born in Germany in 1974. He received the Diploma degree in biochemistry from the University of Duisburg-Essen, Essen, Germany, in 1998, and the Ph.D. (Dr.rer.nat.) degree from the University of Witten/Herdecke, Witten, Germany, in 2001, with a focus on the signal transduction of metastasizing tumor cells.

He was involved in the signal transduction of pancreatic beta cells with the New England Medical Centre/Tufts University, Boston, MA, USA, from 2001 to 2003. From 2003 to 2009, he was a Principal Investigator with the University of Witten/Herdecke, where he established his own work group by combining diabetes research and oncology. Since 2009, he has been the Head of the Junior Research Group Cellular Effects with the Centre for Innovation Competence (ZIK) Plasmatis, Leibniz-Institut für Plasmaforschung und Technologie e.V., Greifswald, Germany, funded by BMBF. His group is investigating the interplay of nonthermal plasma with living cells and tissues with ZIK Plasmatis, where he focuses on the alterations of the genome and proteome to stimulate cellular activities. His focus lies on cellular signal transduction cascades and how to manipulate those signals.

Dr. Masur is a member of the German Society for Biochemistry and Molecularbiology, the International Society for Plasma Medicine, and the Society for Signal Transduction.

Klaus-Dieter Weltmann (M'95) received the Diploma degree in electronics and the Ph.D. (Dr.rer.nat.) degree in applied physics from the University of Greifswald, Greifswald, Germany, in 1989 and 1993, respectively.

He was involved in nonlinear dynamics in low-temperature plasmas and plasma diagnostics. In 1994, he was a Visiting Scientist with the Plasma Physics Laboratory, West Virginia University, Morgantown, WV, USA. In 1995, he joined ABB Corporate Research Ltd., Zurich, Switzerland, where he is involved in the research and development of HV and MV switchgear. In 1998, he became the Head of the High Voltage Systems Group with ABB Corporate Research Ltd. In 2000, he was appointed as a Research and Development Leader of Gas Insulated Switchgear (GIS) and Performance and Save Space with ABB High Voltage Technologies Ltd., Zurich, and became the Business Unit Research and Development Manager of GIS in 2002. Since 2003, he has been the Director and Chairman of the Board with the Leibniz-Institut für Plasmaforschung und Technologie e.V., Greifswald, and a Professor of Experimental Physics with the University of Greifswald. He is an Initiator of three spin-off companies. His current research interests include switchgears, arc physics, atmospheric plasmas, modeling and simulation, plasma-medicine, and plasma decontamination.

Prof. Weltmann is the President of the International Society for Plasma Medicine, and a member of the German Physical Society and several consulting committees in the industry and research.

Bibliography

[1] W. Crookes. The bakerian lecture: On the illumination of lines of molecular pressure, and the trajectory of molecules. *Philosophical Transactions of the Royal Society of London*, 170(0):135–164, 1879.

[2] I. Langmuir. Oscillations in ionized gases. *Proceedings of the National Academy of Sciences of the United States of America*, 14(8):627–37, 1928.

[3] L. Tonks. The birth of "Plasma". *American Journal of Physics*, 35(9):857, 1967.

[4] Yuri P Raizer, Vitaly I Kisin, and John E Allen. *Gas discharge physics*, volume 1. Springer-Verlag Berlin, 1991.

[5] J.L. Delcroix and A. Bers. *Physique des plasmas*, volume I. EDP Sciences, Les Ulis, France, 1994.

[6] J.L. Delcroix and A. Bers. *Physique des plasmas*, volume II. EDP Sciences, Les Ulis, France, 1994.

[7] J. E. Harry. *Introduction to Plasma Technology: Science, Engineering and Applications.* Wiley-VCH Verlag, Berlin, 2010.

[8] R. Hippler, H. Kersten, M. Schmidt, and K. H. Schoenbach. *Low temperature plasma physics: fundamental aspects and applications, 2^{nd} edition*, volume II. Wiley-VCH, Berlin, 2008.

[9] C. Tendero, C. Tixier, P. Tristant, J. Desmaison, and P. Leprince. Atmospheric pressure plasmas: A review. *Spectrochimica Acta Part B-Atomic Spectroscopy*, 61(1):2–30, 2006.

[10] Alexander Fridman. *Plasma chemistry.* Cambridge University Press, 2008. ISBN 9781107684935.

[11] E. Stoffels, A. J. Flikweert, W. W. Stoffels, and G. M. W. Kroesen. Plasma needle: a non-destructive atmospheric plasma source for fine surface treatment of (bio)materials. *Plasma Sources Science and Technology*, 11(4):383–388, 2002.

[12] R. Foest, E. Kindel, A. Ohl, M. Stieber, and K. D. Weltmann. Non-thermal atmospheric pressure discharges for surface modification. *Plasma Physics and Controlled Fusion*, 47 (12B):B525–B536, 2005.

[13] R. Morent, N. De Geyter, J. Verschuren, K. De Clerck, P. Kiekens, and C. Leys. Non-thermal plasma treatment of textiles. *Surface and Coatings Technology*, 202(14):3427–3449, 2008.

[14] D. Pappas. Status and potential of atmospheric plasma processing of materials. *Journal of Vacuum Science and Technology A*, 29(2), 2011.

[15] K. Fricke, H. Steffen, T. von Woedtke, K. Schroder, and K. D. Weltmann. High rate etching of polymers by means of an atmospheric pressure plasma jet. *Plasma Processes and Polymers*, 8(1):51–58, 2011.

[16] M. Noeske, J. Degenhardt, S. Strudthoff, and U. Lommatzsch. Plasma jet treatment of five polymers at atmospheric pressure: surface modifications and the relevance for adhesion. *International Journal of Adhesion and Adhesives*, 24(2):171–177, 2004.

[17] S. Yonson, S. Coulombe, V. Leveille, and R. L. Leask. Cell treatment and surface functionalization using a miniature atmospheric pressure glow discharge plasma torch. *Journal of Physics D: Applied Physics*, 39(16):3508–3513, 2006.

[18] F. Hempel, H. Steffen, B. Busse, B. Finke, J. B. Nebe, A. Quade, H. Rebl, C. Bergemann, K.-D. Weltmann, and K. Schröder. *On the Application of Gas Discharge Plasmas for the Immobilization of Bioactive Molecules for Biomedical and Bioengineering Applications*, chapter 15. R. Fazel-Rezai, ed., 2011.

[19] K. D. Weltmann, M. Polak, K. Masur, T. von Woedtke, J. Winter, and S. Reuter. Plasma processes and plasma sources in medicine. *Contributions to Plasma Physics*, 52(7):644–654, 2012.

[20] P. Romeo. Violet ray in the treatment of variola. *Boston Medical and Surgical Journal*, 187:215–216, 1922.

[21] M. S. Goulette. The ultra violet ray in the treatment of tubercular bone lesions in children. *American Journal of Nursing*, 24(11):883–884, 1924.

[22] F. F. Tisdall. An adress on the value of ultra-violet ray therapy in childhood. *Canadian Medical Association Journal*, 17:667–670, 1927.

[23] J. Raiser and M. Zenker. Argon plasma coagulation for open surgical and endoscopic applications: state of the art. *Journal of Physics D: Applied Physics*, 39(16):3520–3523, 2006.

[24] G. Fridman, M. Peddinghaus, H. Ayan, A. Fridman, M. Balasubramanian, A. Gutsol, A. Brooks, and G. Friedman. Blood coagulation and living tissue sterilization by floating-electrode dielectric barrier discharge in air. *Plasma Chemistry and Plasma Processing*, 26(4):425–442, 2006.

[25] Th von Woedtke, S. Reuter, K. Masur, and K. D. Weltmann. Plasmas for medicine. *Physics Reports*, 530(4):291–320, 2013.

[26] M. Laroussi. Low temperature plasma-based sterilization: Overview and state-of-the-art. *Plasma Processes and Polymers*, 2(5):391–400, 2005.

[27] R. A. Venezia, M. Orrico, E. Houston, S. M. Yin, and Y. Y. Naumova. Lethal activity of nonthermal plasma sterilization against microorganisms. *Infection control and hospital epidemiology: the official journal of the Society of Hospital Epidemiologists of America*, 29(5):430–436, 2008.

[28] K.D. Weltmann, J. Winter, M. Polak, J. Ehlbeck, and Th. von Woedtke. *Atmospheric Pressure Plasmas for Decontamination of Complex Medical Devices*, chapter 1, pages 3–15. NATO Science for Peace and Security Series A: Chemistry and Biology. Springer Netherlands, 2012.

[29] J. H. Choi, I. Han, H. K. Baik, M. H. Lee, D. W. Han, J. C. Park, I. S. Lee, K. M. Song, and Y. S. Lim. Analysis of sterilization effect by pulsed dielectric barrier discharge. *Journal of Electrostatics*, 64(1):17–22, 2006.

[30] G. Fridman, A. Shereshevsky, M. M. Jost, A. D. Brooks, A. Fridman, A. Gutsol, V. Vasilets, and G. Friedman. Floating electrode dielectric barrier discharge plasma in air promoting apoptotic behavior in melanoma skin cancer cell lines. *Plasma Chemistry and Plasma Processing*, 27(2):163–176, 2007.

[31] K. Oehmigen, J. Winter, M. Hahnel, C. Wilke, R. Brandenburg, K. D. Weltmann, and T. von Woedtke. Estimation of possible mechanisms of escherichia coli inactivation by plasma treated sodium chloride solution. *Plasma Processes and Polymers*, 8(10):904–913, 2011.

[32] R. E. J. Sladek and E. Stoffels. Deactivation of escherichia coli by the plasma needle. *Journal of Physics D: Applied Physics*, 38(11):1716–1721, 2005.

[33] M. Laroussi, C. Tendero, X. Lu, S. Alla, and W. L. Hynes. Inactivation of bacteria by the plasma pencil. *Plasma Processes and Polymers*, 3(6-7):470–473, 2006.

[34] G. Fridman, G. Friedman, A. Gutsol, A. B. Shekhter, V. N. Vasilets, and A. Fridman. Applied plasma medicine. *Plasma Processes and Polymers*, 5(6):503–533, 2008.

[35] M. Laroussi and A. Fridman. Plasma medicine. *Plasma Processes and Polymers*, 5(6): 501–501, 2008.

[36] M. G. Kong, G. Kroesen, G. Morfill, T. Nosenko, T. Shimizu, J. van Dijk, and J. L. Zimmermann. Plasma medicine: an introductory review. *New Journal of Physics*, 11 (11):115012, 2009.

[37] M. Laroussi. Low-temperature plasmas for medicine? *IEEE Transactions on Plasma Science*, 37(6):714–725, 2009. Times Cited: 155.

[38] G. E. Morfill, M. G. Kong, and J. L. Zimmermann. Focus on plasma medicine. *New Journal of Physics*, 11, 2009.

[39] K. D. Weltmann, E. Kindel, T. von Woedtke, M. Hahnel, M. Stieber, and R. Brandenburg. Atmospheric-pressure plasma sources: Prospective tools for plasma medicine. *Pure and Applied Chemistry*, 82(6):1223–1237, 2010.

[40] K. D. Weltmann and T. von Woedtke. Basic requirements for plasma sources in medicine. *European Physical Journal: Applied Physics*, 55(1), 2011.

[41] S. Samukawa, M. Hori, S. Rauf, K. Tachibana, P. Bruggeman, G. Kroesen, J. C. Whitehead, A. B. Murphy, A. F. Gutsol, S. Starikovskaia, U. Kortshagen, J. P. Boeuf, T. J. Sommerer, M. J. Kushner, U. Czarnetzki, and N. Mason. The 2012 plasma roadmap. *Journal of Physics D: Applied Physics*, 45(25), 2012.

[42] K. D. Weltmann, E. Kindel, R. Brandenburg, C. Meyer, R. Bussiahn, C. Wilke, and T. von Woedtke. Atmospheric pressure plasma jet for medical therapy: Plasma parameters and risk estimation. *Contributions to Plasma Physics*, 49(9):631–640, 2009.

[43] A. B. Shekhter, R. K. Kabisov, A. V. Pekshev, N. P. Kozlov, and Y. L. Perov. Experimental and clinical validation of plasmadynamic therapy of wounds with nitric oxide. *Bulletin of Experimental Biology and Medicine*, 126(8):829–834, 1998.

[44] E. Stoffels, I. E. Kieft, and R. E. J. Sladek. Superficial treatment of mammalian cells using plasma needle. *Journal of Physics D: Applied Physics*, 36(23):2908–2913, 2003.

[45] R. E. J. Sladek, E. Stoffels, R. Walraven, P. J. A. Tielbeek, and R. A. Koolhoven. Plasma treatment of dental cavities: A feasibility study. *IEEE Transactions on Plasma Science*, 32(4):1540–1543, 2004.

[46] J. Heinlin, G. Isbary, W. Stolz, G. Morfill, M. Landthaler, T. Shimizu, B. Steffes, T. Nosenko, J. Zimmermann, and S. Karrer. Plasma applications in medicine with a special focus on dermatology. *Journal of the European Academy of Dermatology and Venereology*, 25(1):1–11, 2011.

[47] H. Kajiyama, K. Nakamura, F. Utsumi, H. Tanaka, M. Hori, and F. Kikkawa. Perspective of strategic plasma therapy in patients with epithelial ovarian cancer: A short review of plasma in cancer treatment. *Japanese Journal of Applied Physics*, 53(5), 2014.

[48] E. Robert, M. Vandamme, L. Brullé, S. Lerondel, A. Le Pape, V. Sarron, D. Riès, T. Darny, S. Dozias, G. Collet, C. Kieda, and J. M. Pouvesle. Perspectives of endoscopic plasma applications. *Clinical Plasma Medicine*, 1(2):8–16, 2013.

[49] V. I Pârvulescu, M. Magureanu, and P. Lukes. *Plasma chemistry and catalysis in gases and liquids*. John Wiley and Sons, 2012.

[50] J. Winter, K. Wende, K. Masur, S. Iseni, M. Dünnbier, M. U. Hammer, H. Tresp, K. D. Weltmann, and S. Reuter. Feed gas humidity: a vital parameter affecting a cold atmospheric-pressure plasma jet and plasma-treated human skin cells. *Journal of Physics D: Applied Physics*, 46(29):295401, 2013.

[51] H. Tresp, M. U. Hammer, J. Winter, K. D. Weltmann, and S. Reuter. Quantitative detection of plasma-generated radicals in liquids by electron paramagnetic resonance spectroscopy. *Journal of Physics D: Applied Physics*, 46(43), 2013.

[52] A. B. Shekhter, V. A. Serezhenkov, T. G. Rudenko, A. V. Pekshev, and A. F. Vanin. Beneficial effect of gaseous nitric oxide on the healing of skin wounds. *Nitric Oxide*, 12 (4):210–9, 2005.

[53] A. Barton, S. Holtz, L. Bundscherer, K. Masur, and K. D. Weltmann. Influence of atmospheric pressure plasma on keratinocytes. *Experimental Dermatology*, 21(3), 2012.

[54] L. Bundscherer, A. Barton, K. Masur, and K. D. Weltmann. Impact of physical plasma on T lymphocytes. *Experimental Dermatology*, 21(3), 2012.

[55] S. Bekeschus, K. Masur, J. Kolata, K. Wende, A. Schmidt, L. Bundscherer, A. Barton, A. Kramer, B. Broker, and K. D. Weltmann. Human mononuclear cell survival and proliferation is modulated by cold atmospheric plasma jet. *Plasma Processes and Polymers*, 10(8):706–713, 2013.

[56] A. Barton, S. Hasse, L. Bundscherer, K. Wende, K. Weltmann, U. Lindequist, and K. Masur. Growth factors and cytokines are regulated by non-thermal atmospheric pressure plasma. *Experimental Dermatology*, 23(3), 2014.

[57] K. Wende, S. Strassenburg, B. Haertel, M. Harms, S. Holtz, A. Barton, K. Masur, T. von Woedtke, and U. Lindequist. Atmospheric pressure plasma jet treatment evokes transient oxidative stress in HaCaT keratinocytes and influences cell physiology. *Cell biology international*, 38(4):412–25, 2014.

[58] L. Bundscherer, K. Wende, K. Ottmuller, A. Barton, A. Schmidt, S. Bekeschus, S. Hasse, K. D. Weltmann, K. Masur, and U. Lindequist. Impact of non-thermal plasma treatment on MAPK signaling pathways of human immune cell lines. *Immunobiology*, 218(10): 1248–55, 2013.

[59] X. Yan, F. Zou, X. P. Lu, G. Y. He, M. J. Shi, Q. Xiong, X. Gao, Z. L. Xiong, Y. Li, F. Y. Ma, M. Yu, C. D. Wang, Y. S. Wang, and G. X. Yang. Effect of the atmospheric pressure nonequilibrium plasmas on the conformational changes of plasmid DNA. *Applied Physics Letters*, 95(8), 2009.

[60] J. Y. Kim, D. H. Lee, J. Ballato, W. G. Cao, and S. O. Kim. Reactive oxygen species controllable non-thermal helium plasmas for evaluation of plasmid DNA strand breaks. *Applied Physics Letters*, 101(22), 2012.

[61] A. Schmidt, K. Wende, S. Bekeschus, L. Bundscherer, A. Barton, K. Ottmuller, K. D. Weltmann, and K. Masur. Non-thermal plasma treatment is associated with changes in transcriptome of human epithelial skin cells. *Free Radic Res*, 47(8):577–92, 2013.

[62] L. Brulle, M. Vandamme, D. Ries, E. Martel, E. Robert, S. Lerondel, V. Trichet, S. Richard, J. M. Pouvesle, and A. Le Pape. Effects of a non thermal plasma treatment alone or in combination with gemcitabine in a MIA PaCa2-luc orthotopic pancreatic carcinoma model. *Plos One*, 7(12):e52653, 2012.

[63] M. Vandamme, E. Robert, S. Pesnel, E. Barbosa, S. Dozias, J. Sobilo, S. Lerondel, A. Le Pape, and J. M. Pouvesle. Antitumor effect of plasma treatment on U87 Glioma Xenografts: Preliminary results. *Plasma Processes and Polymers*, 7(3-4):264–273, 2010.

[64] F. Utsumi, H. Kajiyama, K. Nakamura, H. Tanaka, M. Mizuno, K. Ishikawa, H. Kondo, H. Kano, M. Hori, and F. Kikkawa. Effect of indirect nonequilibrium atmospheric pressure plasma on anti-proliferative activity against chronic chemo-resistant ovarian cancer cells in vitro and in vivo. *Plos One*, 8(12):e81576, 2013.

[65] J. Schlegel, J. Köritzer, and V. Boxhammer. Plasma in cancer treatment. *Clinical Plasma Medicine*, 1(2):2–7, 2013.

[66] G. Collet, E. Robert, A. Lenoir, M. Vandamme, T. Darny, S. Dozias, C. Kieda, and J. M. Pouvesle. Plasma jet-induced tissue oxygenation: potentialities for new therapeutic strategies. *Plasma Sources Science and Technology*, 23(1), 2014.

[67] G. Isbary, G. Morfill, H. U. Schmidt, M. Georgi, K. Ramrath, J. Heinlin, S. Karrer, M. Landthaler, T. Shimizu, B. Steffes, W. Bunk, R. Monetti, J. L. Zimmermann, R. Pompl, and W. Stolz. A first prospective randomized controlled trial to decrease bacterial load using cold atmospheric argon plasma on chronic wounds in patients. *The British journal of dermatology*, 163(1):78–82, 2010.

[68] J. W. Fluhr, S. Sassning, O. Lademann, M. E. Darvin, S. Schanzer, A. Kramer, H. Richter, W. Sterry, and J. Lademann. In vivo skin treatment with tissue-tolerable plasma influences skin physiology and antioxidant profile in human stratum corneum. *Exp Dermatol*, 21(2):130–4, 2012.

[69] G. Isbary, J. L. Zimmermann, T. Shimizu, Y. F. Li, G. E. Morfill, H. M. Thomas, B. Steffes, J. Heinlin, S. Karrer, and W. Stolz. Non-thermal plasma-more than five years of clinical experience. *Clinical Plasma Medicine*, 1(1):19–23, 2013.

[70] Hans-Robert Metelmann, Thi Thom Vu, Hoang Tung Do, Thi Nguyen Binh Le, Thi Ha Anh Hoang, Thi Thu Trang Phi, Tran My Linh Luong, Van Tien Doan, Thi Trang Huyen Nguyen, Thi Hong Minh Nguyen, Thuy Linh Nguyen, Dinh Quyen Le, Thi Kim Xuan Le, Thomas von Woedtke, René Bussiahn, Klaus-Dieter Weltmann, Roya Khalili, and Fred Podmelle. Scar formation of laser skin lesions after cold atmospheric pressure plasma (CAP) treatment: A clinical long term observation. *Clinical Plasma Medicine*, 1(1):30–35, 2013.

[71] P. Al Ghazal, A. Korber, J. Klode, E. N. Schmid, J. Buer, and J. Dissemond. Evaluation of the essen rotary as a new technique for bacterial swabs: results of a prospective controlled clinical investigation in 50 patients with chronic leg ulcers. *International wound journal*, 11(1):44–9, 2014.

[72] F. Brehmer, H. A. Haenssle, G. Daeschlein, R. Ahmed, S. Pfeiffer, A. Gorlitz, D. Simon, M. P. Schon, D. Wandke, and S. Emmert. Alleviation of chronic venous leg ulcers with a hand-held dielectric barrier discharge plasma generator (PlasmaDerm VU-2010): results of a monocentric, two-armed, open, prospective, randomized and controlled trial (NCT01415622). *Journal of the European Academy of Dermatology and Venereology*, pages 1–8, 2014.

[73] Mounir Laroussi and Tamer Akan. Arc-free atmospheric pressure cold plasma jets: A review. *Plasma Processes and Polymers*, 4(9):777–788, 2007.

[74] F. Iza, G. J. Kim, S. M. Lee, J. K. Lee, J. L. Walsh, Y. T. Zhang, and M. G. Kong. Microplasmas: Sources, particle kinetics, and biomedical applications. *Plasma Processes and Polymers*, 5(4):322–344, 2008.

[75] X. Lu, M. Laroussi, and V. Puech. On atmospheric-pressure non-equilibrium plasma jets and plasma bullets. *Plasma Sources Science and Technology*, 21(3):034005, 2012.

[76] W. van Gaens and A. Bogaerts. Reaction pathways of biomedically active species in an Ar plasma jet. *Plasma Sources Science and Technology*, 23(3):035015, 2014.

[77] David B. Graves. The emerging role of reactive oxygen and nitrogen species in redox biology and some implications for plasma applications to medicine and biology. *Journal of Physics D: Applied Physics*, 45(26):263001, 2012.

[78] D. B. Graves. Low temperature plasma biomedicine: A tutorial reviewa). *Physics of Plasmas*, 21(8):080901, 2014.

[79] E. Stoffels, Y. Aranda Gonzalvo, T. D. Whitmore, D. L. Seymour, and J. A. Rees. A plasma needle generates nitric oxide. *Plasma Sources Scienceand Technology*, 15(3):501–506, 2006.

[80] H.-R. Metelmann, Th. von Woedtke, R. Bussiahn, K.-D. Weltmann, M. Rieck, R. Khalili, F. Podmelle, and P. D. Waite. Experimental recovery of CO2-Laser skin lesions by plasma stimulation. *American Journal of Cosmetic Surgery*, 29(1):52–56, 2012.

[81] J. Lademann, C. Ulrich, A. Patzelt, H. Richter, F. Kluschke, M. Klebes, O. Lademann, A. Kramer, K. D. Weltmann, and B. Lange-Asschenfeldt. Risk assessment of the application of tissue-tolerable plasma on human skin. *Clinical Plasma Medicine*, 1(1):5–10, 2013.

[82] R. Bussiahn, N. Lembke, R. Gesche, T. Von Woedtke, and K. D. Weltmann. Plasma sources for biomedical applications. *HygMed*, 38(5):212–216, 2013.

[83] W. Lochte-Holtgreven. *Plasma diagnostics.* North-Holland / Wiley, 1968.

[84] H. R. Griem. *Principles of Plasma Spectroscopy.* Cambridge University Press, 1997.

[85] T. Fujimoto. *Plasma Spectroscopy.* Oxford University Press, 2004.

[86] I.H. Hutchinson. *Principles of Plasma Diagnostics.* Cambridge University Press, 1987.

[87] V. N. Ochkin. *Spectroscopy of Low Temperature Plasma.* Wiley-VCH, 2009.

[88] P. J. Bruggeman, N. Sadeghi, D. C. Schram, and V. Linss. Gas temperature determination from rotational lines in non-equilibrium plasmas: a review. *Plasma Sources Science and Technology*, 23(2):023001, 2014.

[89] W. van Gaens and A. Bogaerts. Kinetic modelling for an atmospheric pressure argon plasma jet in humid air. *Journal of Physics D: Applied Physics*, 46(27):275201, 2013.

[90] M. Laroussi and X. Lu. Room-temperature atmospheric pressure plasma plume for biomedical applications. *Applied Physics Letters*, 87(11), 2005.

[91] E. Panousis, A. Ricard, J. F. Loiseau, F. Clement, and B. Held. Estimation of densities of active species in an atmospheric pressure N_2 DBD flowing afterglow using optical emission spectroscopy and analytical calculations. *Journal of Physics D: Applied Physics*, 42(20), 2009.

[92] A. Sarani, A. Y. Nikiforov, and C. Leys. Atmospheric pressure plasma jet in Ar and Ar/H_2O mixtures: Optical emission spectroscopy and temperature measurements. *Physics of Plasmas*, 17(6), 2010.

[93] C. A. J. van Gils, S. Hofmann, Bkhl Boekema, R. Brandenburg, and P. J. Bruggeman. Mechanisms of bacterial inactivation in the liquid phase induced by a remote RF cold atmospheric pressure plasma jet. *Journal of Physics D: Applied Physics*, 46(17), 2013.

[94] P. Lukes, E. Dolezalova, I. Sisrova, and M. Clupek. Aqueous-phase chemistry and bactericidal effects from an air discharge plasma in contact with water: evidence for the formation of peroxynitrite through a pseudo-second-order post-discharge reaction of H_2O_2 and HNO_2. *Plasma Sources Science and Technology*, 23(1), 2014.

[95] S. Iseni, S. Reuter, A. Schmidt-Bleker, and K. D. Weltmann. Flow and discharge development in an argon atmospheric pressure plasma jet observed by ICCD and PLIF imaging. *IEEE Transactions on Plasma Science*, 42(10):2458–2459, 2014.

[96] P. Bruggeman and R. Brandenburg. Atmospheric pressure discharge filaments and microplasmas: physics, chemistry and diagnostics. *Journal of Physics D: Applied Physics*, 46(46), 2013.

[97] L. B. Loeb and J. M. Meek. The mechanism of spark discharge in air at atmospheric pressure. I. *Journal of Applied Physics*, 11(6):438–447, 1940.

[98] L. B. Loeb and J. M. Meek. The mechanism of spark discharge in air at atmospheric pressure. II. *Journal of Applied Physics*, 11(7):459–474, 1940.

[99] M. Teschke, J. Kedzierski, E. G. Finantu-Dinu, D. Korzec, and J. Engemann. High-speed photographs of a dielectric barrier atmospheric pressure plasma jet. *IEEE Transactions on Plasma Science*, 33(2):310–311, 2005.

[100] X. Lu and M. Laroussi. Dynamics of an atmospheric pressure plasma plume generated by submicrosecond voltage pulses. *Journal of Applied Physics*, 100(6), 2006.

[101] S. Reuter, J. Winter, S. Iseni, S. Peters, A. Schmidt-Bleker, M. Dünnbier, J. Schafer, R. Föest, and K. D. Weltmann. Detection of ozone in a MHz argon plasma bullet jet. *Plasma Sources Science and Technology*, 21(3):034015, 2012.

[102] J. M. Meek. A theory of spark discharge. *Physical Review*, 57(8):722–728, 1940.

[103] J. P. Boeuf, L. L. Yang, and L. C. Pitchford. Dynamics of a guided streamer ("plasma bullet") in a helium jet in air at atmospheric pressure. *Journal of Physics D: Applied Physics*, 46(1), 2013.

[104] K. D. Weltmann, R. Brandenburg, T. von Woedtke, J. Ehlbeck, R. Foest, M. Stieber, and E. Kindel. Antimicrobial treatment of heat sensitive products by miniaturized atmospheric pressure plasma jets (APPJs). *Journal of Physics D: Applied Physics*, 41(19), 2008.

[105] R. Foest, E. Kindel, H. Lange, A. Ohl, M. Stieber, and K. D. Weltmann. RF capillary jet - a tool for localized surface treatment. *Contributions to Plasma Physics*, 47(1-2): 119–128, 2007.

[106] R. Brandenburg, J. Ehlbeck, M. Stieber, T. v. Woedtke, J. Zeymer, O. Schlüter, and K. D. Weltmann. Antimicrobial treatment of heat sensitive materials by means of atmospheric pressure Rf-driven plasma jet. *Contributions to Plasma Physics*, 47(1-2):72–79, 2007.

[107] R. Brandenburg, H. Lange, T. von Woedtke, M. Stieber, E. Kindel, J. Ehlbeck, and K. D. Weltmann. Antimicrobial effects of UV and VUV radiation of nonthermal plasma jets. *IEEE Transactions on Plasma Science*, 37(6):877–883, 2009.

[108] A. Schutze, J. Y. Jeong, S. E. Babayan, J. Park, G. S. Selwyn, and R. F. Hicks. The atmospheric-pressure plasma jet: A review and comparison to other plasma sources. *IEEE Transactions on Plasma Science*, 26(6):1685–1694, 1998.

[109] S. Reuter, J. Winter, A. Schmidt-Bleker, H. Tresp, M. U. Hammer, and K. D. Weltmann. Controlling the ambient air affected reactive species composition in the effluent of an argon plasma jet. *IEEE Transactions on Plasma Science*, 40(11):2788–2794, 2012.

[110] L. S. Rothman, I. E. Gordon, A. Barbe, D. C. Benner, P. E. Bernath, M. Birk, V. Boudon, L. R. Brown, A. Campargue, J. P. Champion, K. Chance, L. H. Coudert, V. Dana, V. M. Devi, S. Fally, J. M. Flaud, R. R. Gamache, A. Goldman, D. Jacquemart, I. Kleiner, N. Lacome, W. J. Lafferty, J. Y. Mandin, S. T. Massie, S. N. Mikhailenko, C. E. Miller, N. Moazzen-Ahmadi, O. V. Naumenko, A. V. Nikitin, J. Orphal, V. I. Perevalov, A. Perrin, A. Predoi-Cross, C. P. Rinsland, M. Rotger, M. Simeckova, M. A. H. Smith, K. Sung, S. A. Tashkun, J. Tennyson, R. A. Toth, A. C. Vandaele, and J. Vander Auwera. The hitran 2008 molecular spectroscopic database. *Journal of Quantitative Spectroscopy and Radiative Transfer*, 110(9-10):533–572, 2009.

[111] J. B. McManus, D. Nelson, M. Zahniser, L. Mechold, M. Osiac, J. Ropcke, and A. Rousseau. TOBI: A two-laser beam infrared system for time-resolved plasma diagnostics of infrared active compounds. *Review of Scientific Instruments*, 74(5):2709–2713, 2003.

[112] J. Röpcke, G. Lombardi, A. Rousseau, and P. B. Davies. Application of mid-infrared tuneable diode laser absorption spectroscopy to plasma diagnostics: a review. *Plasma Sources Science and Technology*, 15(4):148–168, 2006.

[113] A. V. Pipa, T. Bindemann, R. Foest, E. Kindel, J. Ropcke, and K. D. Weltmann. Absolute production rate measurements of nitric oxide by an atmospheric pressure plasma jet (APPJ). *Journal of Physics D: Applied Physics*, 41(19):194011, 2008.

[114] J. Röpcke, P. B. Davies, N. Lang, A. Rousseau, and S. Welzel. Applications of quantum cascade lasers in plasma diagnostics: a review. *Journal of Physics D: Applied Physics*, 45 (42):423001, 2012.

[115] J. Faist, F. Capasso, D. L. Sivco, C. Sirtori, A. L. Hutchinson, and A. Y. Cho. Quantum cascade laser. *Science*, 264(5158):553–559, 1994.

[116] R. Bartlome, A. Feltrin, and C. Ballif. Infrared laser-based monitoring of the silane dissociation during deposition of silicon thin films. *Applied Physics Letters*, 94(20), 2009.

[117] S. Iseni, S. Reuter, and K. D. Weltmann. NO_2 dynamics of an Ar/Air plasma jet investigated by in situ quantum cascade laser spectroscopy at atmospheric pressure. *Journal of Physics D: Applied Physics*, 47(7):075203, 2014.

[118] J. U. White. Long optical paths of large aperture. *Journal of the Optical Society of America*, 32(5):285–288, 1942.

[119] W. Van Gaens, S. Iseni, A. Schmidt-Bleker, K. D. Weltmann, S. Reuter, and A. Bogaerts. Numerical analysis of the effect of nitrogen and oxygen admixtures on the chemistry of an argon plasma jet operating at atmospheric pressure. *New Journal of Physics*, 17(3): 033003, 2015.

[120] R. M. Measures. Selective excitation spectroscopy and some possible applications. *Journal of Applied Physics*, 39(11):5232, 1968.

[121] D.R. Crosley. *Laser probes for combustion chemistry.* American Chemical Society, 1980.

[122] D. R. Crosley. Laser-induced fluorescence in combustion chemical-kinetics. *Abstracts of Papers of the American Chemical Society*, 183(Mar):77, 1982.

[123] D. R. Crosley and G. P. Smith. Laser-induced fluorescence spectroscopy for combustion diagnostics. *Optical Engineering*, 22(5):545–553, 1983.

[124] D. D. Burgess and C. H. Skinner. Dye laser-induced fluorescence of plasmas and its application to measurement of lower state decay-rates. *Journal of Physics B: Atomic Molecular and Optical Physics*, 7(9):L297–L301, 1974.

[125] A. Ershov and J. Borysow. Dynamics of OH ($X^2\Pi$, v=0) in high-energy atmospheric pressure electrical pulsed discharge. *Journal of Physics D: Applied Physics*, 28(1):68–74, 1995.

[126] S. Nemschokmichal. *Temporal and spatial characterisation of nitrogen metastables in atmospheric pressure barrier discharges.* Ph.D. thesis, Ernst-Moritz-Arndt-Universität Greifswald, 2013.

[127] J. W. Daily. Laser induced fluorescence spectroscopy in flames. *Progress in Energy and Combustion Science*, 23(2):133–199, 1997.

[128] Jr. Partridge, W. P. and N. M. Laurendeau. Formulation of a dimensionless overlap fraction to account for spectrally distributed interactions in fluorescence studies. *Applied Optics*, 34(15):2645–7, 1995.

[129] T. Verreycken, R. Mensink, R. van der Horst, N. Sadeghi, and P. J. Bruggeman. Absolute OH density measurements in the effluent of a cold atmospheric-pressure Ar-H_2O RF plasma jet in air. *Plasma Sources Science and Technology*, 22(5), 2013.

[130] G. Herzberg. *Molecular Spectra and Molecular Structure: Diatomic molecules.* New York: van Nostrand Company, 1939.

[131] S. Iseni, S. Zhang, A. F. H. van Gessel, S. Hofmann, B van Ham, S. Reuter, K. D. Weltmann, and P. Bruggeman. Nitric Oxide density distributions in the effluent of an RF argon APPJ: effect of gas flow rate and substrate. *New Journal of Physics*, 16(12): 123011, 2015.

[132] A. F. van Gessel and P. J. Bruggeman. Thermalization of rotational states of NO $A^2\Sigma^+(v{=}0)$ in an atmospheric pressure plasma. *Journal of Chemical Physics*, 138(20): 204306, 2013.

[133] A. F. H. van Gessel, K. M. J. Alards, and P. J. Bruggeman. NO production in an RF plasma jet at atmospheric pressure. *Journal of Physics D: Applied Physics*, 46(26):265202, 2013.

[134] S. Reuter, J. Winter, A. Schmidt-Bleker, D. Schroeder, H. Lange, N. Knake, V. Schulz-von der Gathen, and K. D. Weltmann. Atomic oxygen in a cold argon plasma jet: TALIF spectroscopy in ambient air with modelling and measurements of ambient species diffusion. *Plasma Sources Science and Technology*, 21(2), 2012.

[135] M. Dünnbier, A. Schmidt-Bleker, J. Winter, M. Wolfram, R. Hippler, K. D. Weltmann, and S. Reuter. Ambient air particle transport into the effluent of a cold atmospheric-pressure argon plasma jet investigated by molecular beam mass spectrometry. *Journal of Physics D: Applied Physics*, 46(43), 2013.

[136] E. Stoffels, Y. Aranda Gonzalvo, T. D. Whitmore, D. L. Seymour, and J. A. Rees. Mass spectrometric detection of short-living radicals produced by a plasma needle. *Plasma Sources Science and Technology*, 16(3):549–556, 2007.

[137] A. F. H. van Gessel, B. Hrycak, M. Jasinski, J. Mizeraczyk, J. J. A. M. van der Mullen, and P. J. Bruggeman. Temperature fitting of partially resolved rotational spectra. *Journal of Instrumentation*, 7, 2012.

[138] A. F. H. van Gessel, B. Hrycak, M. Jasinski, J. Mizeraczyk, J. J. A. M. van der Mullen, and P. J. Bruggeman. Temperature and NO density measurements by LIF and OES on an atmospheric pressure plasma jet. *Journal of Physics D: Applied Physics*, 46(9):095201, 2013.

[139] J. Winter, H. Tresp, M. U. Hammer, S. Iseni, S. Kupsch, A. Schmidt-Bleker, K. Wende, M. Dünnbier, K. Masur, K. D. Weltmann, and S. Reuter. Tracking plasma generated H_2O_2 from gas into liquid phase and revealing its dominant impact on human skin cells. *Journal of Physics D: Applied Physics*, 47(28):285401, 2014.

[140] Seiji Kanazawa, Hiroto Tanaka, Atsushi Kajiwara, Toshikazu Ohkubo, Yukiharu Nomoto, Marek Kocik, Jerzy Mizeraczyk, and Jen-Shih Chang. LIF imaging of OH radicals in DC positive streamer coronas. *Thin Solid Films*, 515(9):4266–4271, 2007.

[141] X. Pei, Y. Lu, S. Wu, Q. Xiong, and X. Lu. A study on the temporally and spatially resolved OH radical distribution of a room-temperature atmospheric-pressure plasma jet by laser-induced fluorescence imaging. *Plasma Sources Science and Technology*, 22(2): 025023, 2013.

[142] R. Ono and T. Oda. Measurement of hydroxyl radicals in an atmospheric pressure discharge plasma by using laser-induced fluorescence. *IEEE Transactions on Industry Applications*, 36(1):82–86, 2000.

[143] T. Verreycken, R. M. van der Horst, A. H. F. M. Baede, E. M. van Veldhuizen, and P. J. Bruggeman. Time and spatially resolved LIF of OH in a plasma filament in atmospheric pressure He-H_2O. *Journal of Physics D: Applied Physics*, 45(4), 2012.

[144] R. B. Miles, W. R. Lempert, and J. N. Forkey. Laser rayleigh scattering. *Measurement Science and Technology*, 12(5):R33–R51, 2001.

[145] G. Schweiger. Raman-scattering on single aerosol-particles and on flowing aerosols - a review. *Journal of Aerosol Science*, 21(4):483–509, 1990.

[146] J. Vorac, P. Dvorak, V. Prochazka, J. Ehlbeck, and S. Reuter. Measurement of hydroxyl radical (OH) concentration in an argon RF plasma jet by laser-induced fluorescence. *Plasma Sources Science and Technology*, 22(2), 2013.

[147] T. Verreycken, R. M. van der Horst, N. Sadeghi, and P. J. Bruggeman. Absolute calibration of OH density in a nanosecond pulsed plasma filament in atmospheric pressure He-H_2O: comparison of independent calibration methods. *Journal of Physics D: Applied Physics*, 46(46), 2013.

[148] P. Bruggeman, F. Iza, P. Guns, D. Lauwers, M. G. Kong, Y. A. Gonzalvo, C. Leys, and D. C. Schram. Electronic quenching of OH(A) by water in atmospheric pressure plasmas and its influence on the gas temperature determination by OH(A-X) emission. *Plasma Sources Science and Technology*, 19(1), 2010.

[149] G. Dilecce and S. De Benedictis. Laser diagnostics of high-pressure discharges: laser induced fluorescence detection of OH in He/Ar-H_2O dielectric barrier discharges. *Plasma Physics and Controlled Fusion*, 53(12), 2011.

[150] T. Verreycken. *Spectroscopic investigation of OH dynamics in transient atmospheric pressure plasmas.* Ph.D. thesis, Technische Universiteit Eindhoven, Eindhoven, The Netherlands, 2013.

[151] Q. Xiong. *Spectroscopic diagnostics of low temperature atmospheric pressure plasma jets.* Ph.D. thesis, Universiteit Gent, Gent, Belgium, 2012.

[152] J. Vorac. *Plasma diagnostics based on laser induced fluorescence.* Ph.D. thesis, Masarykova Univerzita, Brno, Czech Republic, 2014.

[153] J. W. Jacobs. Shock-induced mixing of a light-gas cylinder. *Journal of Fluid Mechanics*, 234:629–649, 1992.

[154] R. A. Bryant, J. M. Donbar, and J. F. Driscoll. Acetone laser induced fluorescence for low pressure/low temperature flow visualization. *Experiments in Fluids*, 28(5):471–476, 2000.

[155] K. Muraoka and M. Maeda. *Laser-Aided Diagnostics of Plasmas and Gases.* Taylor & Francis, 2000.

[156] S. Yonemori, Y. Nakagawa, R. Ono, and T. Oda. Measurement of OH density and air-helium mixture ratio in an atmospheric-pressure helium plasma jet. *Journal of Physics D: Applied Physics*, 45(22), 2012.

[157] S. Iseni, A. Schmidt-Bleker, J. Winter, K. D. Weltmann, and S. Reuter. Atmospheric pressure streamer follows the turbulent argon air boundary in a MHz argon plasma jet investigated by OH-tracer PLIF spectroscopy. *Journal of Physics D: Applied Physics*, 47 (15):152001, 2014.

[158] GS Settles. *Schlieren and Shadowgraph Techniques.* Springer, 2001.

[159] S. Bekeschus, S. Iseni, S. Reuter, K. Masur, and K.-D. Weltmann. Nitrogen shielding of an argon plasma jet and its effects on human immune cells. *IEEE Transactions on Plasma Science*, 43(3):776–781, 2015.

[160] S. Hofmann, A. F. H. van Gessel, T. Verreycken, and P. Bruggeman. Power dissipation, gas temperatures and electron densities of cold atmospheric pressure helium and argon RF plasma jets. *Plasma Sources Science and Technology*, 20(6), 2011.

[161] S. Reuter, J. Winter, S. Iseni, A. Schmidt-Bleker, M. Dünnbier, K. Masur, K. Wende, and K. D. Weltmann. The influence of feed gas humidity versus ambient humidity on atmospheric pressure plasma jet-effluent chemistry and skin cell viability. *IEEE Transactions on Plasma Science*, 99, 2015.

[162] A. V. Pipa and J. Ropcke. Analysis of the Mid-Infrared spectrum of the exhaust gas from an atmospheric pressure plasma jet (APPJ) working with an argon-air mixture. *IEEE Transactions on Plasma Science*, 37(6):1000–1003, 2009.

[163] R. Dorai and M. J. Kushner. A model for plasma modification of polypropylene using atmospheric pressure discharges. *Journal of Physics D: Applied Physics*, 36(6):666–685, 2003.

[164] YA Zeldovich, D Frank-Kamenetskii, and P Sadovnikov. *Oxidation of nitrogen in combustion*. Publishing House of the Acad of Sciences of USSR, 1947.

[165] B. van Gessel, R. Brandenburg, and P. Bruggeman. Electron properties and air mixing in radio frequency driven argon plasma jets at atmospheric pressure. *Applied Physics Letters*, 103(6), 2013.

[166] P. Bruggeman and D. C. Schram. On OH production in water containing atmospheric pressure plasmas. *Plasma Sources Science and Technology*, 19(4):045025, 2010.

[167] A. Schmidt-Bleker, J. Winter, S. Iseni, M. Dünnbier, K. D. Weltmann, and S. Reuter. Reactive species output of a plasma jet with a shielding gas device-combination of FTIR absorption spectroscopy and gas phase modelling. *Journal of Physics D: Applied Physics*, 47(14):145201, 2014.

[168] W. van Gaens, P. J. Bruggeman, and A. Bogaerts. Numerical analysis of the NO and O generation mechanism in a needle-type plasma jet. *New Journal of Physics*, 16(6):063054, 2014.

[169] A. V. Pipa, S. Reuter, R. Foest, and K. D. Weltmann. Controlling the NO production of an atmospheric pressure plasma jet. *Journal of Physics D: Applied Physics*, 45(8):085201, 2012.

[170] N. Jiang, J. L. Yang, F. He, and Z. X. Cao. Interplay of discharge and gas flow in atmospheric pressure plasma jets. *Journal of Applied Physics*, 109(9), 2011.

[171] J. S. Oh, O. T. Olabanji, C. Hale, R. Mariani, K. Kontis, and J. W. Bradley. Imaging gas and plasma interactions in the surface-chemical modification of polymers using microplasma jets. *Journal of Physics D: Applied Physics*, 44(15), 2011.

[172] E. Moreau. Airflow control by non-thermal plasma actuators. *Journal of Physics D: Applied Physics*, 40(3):605–636, 2007.

[173] E. Robert, V. Sarron, T. Darny, D. Ries, S. Dozias, J. Fontane, L. Joly, and J. M. Pouvesle. Rare gas flow structuration in plasma jet experiments. *Plasma Sources Science and Technology*, 23(1), 2014.

[174] M. Boselli, V. Colombo, E. Ghedini, M. Gherardi, R. Laurita, A. Liguori, P. Sanibondi, and A. Stancampiano. Schlieren high-speed imaging of a nanosecond pulsed atmospheric pressure non-equilibrium plasma jet. *Plasma Chemistry and Plasma Processing*, 34(4): 853–869, 2014.

[175] P. K. Papadopoulos, P. Vafeas, P. Svarnas, K. Gazeli, P. M. Hatzikonstantinou, A. Gkelios, and F. Clément. Interpretation of the gas flow field modification induced by guided streamer ("plasma bullet") propagation. *Journal of Physics D: Applied Physics*, 47(42): 425203, 2014.

[176] X. J. Shao, Z. S. Chang, H. B. Mu, W. L. Liao, and G. J. Zhang. Experimental and numerical investigation on the interaction between Ar flow channel and Ar plasma jet at atmospheric pressure. *IEEE Transactions on Plasma Science*, 41(4):899–906, 2013.

[177] J. P. Boeuf and L. C. Pitchford. Electrohydrodynamic force and aerodynamic flow acceleration in surface dielectric barrier discharge. *Journal of Applied Physics*, 97(10):103307, 2005.

[178] L. R. Williams and D. R. Crosley. Collisional vibrational energy transfer of OH($A^2\Sigma^+$, $v\prime = 1$). *The Journal of chemical physics*, 104(17):6507, 1996.

[179] A. Schmidt-Bleker, S. Reuter, and K. D. Weltmann. Non-dispersive path mapping approximation for the analysis of ambient species diffusion in laminar jets. *Physics of Fluids*, 26(8):083603, 2014.

[180] S. Hofmann, A. Sobota, and P. Bruggeman. Transitions between and control of guided and branching streamers in DC nanosecond pulsed excited plasma jets. *IEEE Transactions on Plasma Science*, 40(11):2888–2899, 2012.

[181] M. J. Kushner. Comparison of plasma activation of thin water layers by direct and remote plasma sources. In *67th Gaseous Electronics Conference (67th GEC)*, Raleigh, North Carolina, USA, 2014.

[182] Wei Tian and Mark J. Kushner. Atmospheric pressure dielectric barrier discharges interacting with liquid covered tissue. *Journal of Physics D: Applied Physics*, 47(16):165201, 2014.

[183] B. K. H. L. Boekema, S. Hofmann, B. J. T. van Ham, P. J. Bruggeman, and E. Middelkoop. Antibacterial plasma at safe levels for skin cells. *Journal of Physics D: Applied Physics*, 46(42):422001, 2013.

[184] J. Foster, B. S. Sommers, S. N. Gucker, I. M. Blankson, and G. Adamovsky. Perspectives on the interaction of plasmas with liquid water for water purification. *IEEE Transactions on Plasma Science*, 40(5):1311–1323, 2012.

[185] K. Wende, S. Reuter, T. von Woedtke, K. D. Weltmann, and K. Masur. Redox-based assay for assessment of biological impact of plasma treatment. *Plasma Processes and Polymers*, 11(7):655–663, 2014.

[186] H. Tresp, M. U. Hammer, K. D. Weltmann, and S. Reuter. Effects of atmosphere composition and liquid type on plasma-generated reactive species in biologically relevant solutions. *Plasma Medicine*, 3(1-2):45–55, 2013.

[187] B. R. Locke and K. Y. Shih. Review of the methods to form hydrogen peroxide in electrical discharge plasma with liquid water. *Plasma Sources Science and Technology*, 20(3), 2011.

[188] J. F. Noxon. Active nitrogen at high pressure. *Journal of Chemical Physics*, 36(4):926, 1962.

[189] J. Olsen, B. Minaev, O. Vahtras, H. Agren, P. Jorgensen, H. J. A. Jensen, and T. Helgaker. The vegard-kaplan band and the phosphorescent decay of N_2. *Chemical Physics Letters*, 231(4-6):387–394, 1994.

[190] S. Nemschokmichal, F. Bernhardt, B. Krames, and J. Meichsner. Laser-induced fluorescence spectroscopy of $N_2(A\,^3\Sigma_u^+)$ and absolute density calibration by rayleigh scattering in capacitively coupled rf discharges. *Journal of Physics D: Applied Physics*, 44(20):205201, 2011.

[191] S. Nemschokmichal and J. Meichsner. $N_2(A\,^3\Sigma_u^+)$ metastable density in nitrogen barrier discharges: I. LIF diagnostics and absolute calibration by rayleigh scattering. *Plasma Sources Science and Technology*, 22(1):015005, 2013.

[192] Ryo Ono, Chihiro Tobaru, Yoshiyuki Teramoto, and Tetsuji Oda. Laser-induced fluorescence of $N_2(A\,^3\Sigma_u^+)$ metastable in N_2 pulsed positive corona discharge. *Plasma Sources Science and Technology*, 18(2):025006, 2009.

[193] G. D. Stancu, M. Janda, F. Kaddouri, D. A. Lacoste, and C. O. Laux. Time-resolved CRDS measurements of the $N_2(A\,^3\Sigma_u^+)$ density produced by nanosecond discharges in atmospheric pressure nitrogen and air. *The Journal of Physical Chemistry A*, 114(1): 201–8, 2010.

[194] M. Simek, P. F. Ambrico, S. De Benedictis, G. Dilecce, V. Prukner, and J. Schmidt. $N_2(A\,^3\Sigma_u^+)$ behaviour in a N_2–NO surface dielectric barrier discharge in the modulated ac regime at atmospheric pressure. *Journal of Physics D: Applied Physics*, 43(12):124003, 2010.

[195] G. Dilecce, P. F. Ambrico, and S. De Benedictis. Density measurement in a dielectric barrier discharge in N_2 and N_2 with small O_2 admixtures. *Plasma Sources Science and Technology*, 16(3):511–522, 2007.

[196] A. M. Pointu and G. D. Stancu. N_2(A) as the source of excited species of N_2, N and O in a flowing afterglow of N_2/NO mixture at atmospheric pressure. *Plasma Sources Science and Technology*, 20(2), 2011.

[197] S. Hofmann, K. van Gils, S. van der Linden, S. Iseni, and P. Bruggeman. Time and spatial resolved optical and electrical characteristics of continuous and time modulated RF plasmas in contact with conductive and dielectric substrates. *European Physical Journal D*, 68(3), 2014.

[198] M. Lisnyak, A. V. Pipa, S Gorchakov, S. Iseni, S. Franke, A. Khakpour, R. P. Methling, and K. D. Weltmann. Overview spectra and axial distribution of spectral line intensities in a high-current vacuum arc with CuCr electrodes. *Journal of Applied Physics*, 2015, *submitted.*

[199] M. Dünnbier, M. M. Becker, S. Iseni, R. Bansemer, D. Loffhagen, S Reuter, and K.-D. Weltmann. Stability and excitation dynamics of an argon micro-scaled atmospheric pressure plasma jet. *Plasma Source Science and Technology*, 2015, *submitted.*

[200] S. Reuter, A. Schmidt-Bleker, S. Iseni, J. Winter, and K.-D. Weltmann. On the bullet-streamer dualism. *IEEE Transactions on Plasma Science*, 42(10):2428–2429, 2014.

[201] S. Reuter, A. Schmidt-Bleker, H. Tresp, J. Winter, S. Iseni, M. Hammer, Dünnbier, and K. D. Weltmann. Interaction of atmospheric pressure plasma jets with liquids. *Plasma Physics and Technology*, 1(2):55–57, 2014.

[202] S. Iseni, A Schmidt-Bleker, J. Winter, K. D. Weltmann, and S. Reuter. Laminar versus turbulent flow of an argon RF APPJ investigated by OH PLIF and its influence on the discharge propagation. *Gas discharge proceeding book*, 2014.

List of publications and conference contributions

Publication in Scientific Journals

- **2015**

  [1] M. Lisnyak, A. V. Pipa, S Gorchakov, S. Iseni, S. Franke, A. Khakpour, R. P. Methling, and K. D. Weltmann. Overview spectra and axial distribution of spectral line intensities in a high-current vacuum arc with CuCr electrodes. *Journal of Applied Physics*, 2015, *submitted*

  [2] M. Dünnbier, M. M. Becker, S. Iseni, R. Bansemer, D. Loffhagen, S Reuter, and K.-D. Weltmann. Stability and excitation dynamics of an argon micro-scaled atmospheric pressure plasma jet. *Plasma Source Science and Technology*, 2015, *submitted*

  [3] S. Bekeschus, S. Iseni, S. Reuter, K. Masur, and K.-D. Weltmann. Nitrogen shielding of an argon plasma jet and its effects on human immune cells. *IEEE Transactions on Plasma Science*, 43(3):776–781, 2015

  [4] W. Van Gaens, S. Iseni, A. Schmidt-Bleker, K. D. Weltmann, S. Reuter, and A. Bogaerts. Numerical analysis of the effect of nitrogen and oxygen admixtures on the chemistry of an argon plasma jet operating at atmospheric pressure. *New Journal of Physics*, 17(3):033003, 2015

  [5] S. Reuter, J. Winter, S. Iseni, A. Schmidt-Bleker, M. Dünnbier, K. Masur, K. Wende, and K. D. Weltmann. The influence of feed gas humidity versus ambient humidity on atmospheric pressure plasma jet-effluent chemistry and skin cell viability. *IEEE Transactions on Plasma Science*, 99, 2015

- **2014**

  [1] S. Iseni, S. Zhang, A. F. H. van Gessel, S. Hofmann, B van Ham, S. Reuter, K. D. Weltmann, and P. Bruggeman. Nitric Oxide density distributions in the effluent of an RF argon APPJ: effect of gas flow rate and substrate. *New Journal of Physics*, 16(12):123011, 2015

  [2] S. Iseni, S. Reuter, A. Schmidt-Bleker, and K. D. Weltmann. Flow and discharge development in an argon atmospheric pressure plasma jet observed by ICCD and PLIF imaging. *IEEE Transactions on Plasma Science*, 42(10):2458–2459, 2014

  [3] S. Iseni, A. Schmidt-Bleker, J. Winter, K. D. Weltmann, and S. Reuter. Atmospheric pressure streamer follows the turbulent argon air boundary in a MHz argon plasma jet investigated by OH-tracer PLIF spectroscopy. *Journal of Physics D: Applied Physics*, 47(15):152001, 2014

  [4] S. Iseni, S. Reuter, and K. D. Weltmann. NO_2 dynamics of an Ar/Air plasma jet investigated by in situ quantum cascade laser spectroscopy at atmospheric pressure. *Journal of Physics D: Applied Physics*, 47(7):075203, 2014

  [5] J. Winter, H. Tresp, M. U. Hammer, S. Iseni, S. Kupsch, A. Schmidt-Bleker, K. Wende, M. Dünnbier, K. Masur, K. D. Weltmann, and S. Reuter. Tracking plasma generated H_2O_2 from gas into liquid phase and revealing its dominant impact on human skin cells. *Journal of Physics D: Applied Physics*, 47(28):285401, 2014

  [6] A. Schmidt-Bleker, J. Winter, S. Iseni, M. Dünnbier, K. D. Weltmann, and S. Reuter. Reactive species output of a plasma jet with a shielding gas device-combination of FTIR absorption spectroscopy and gas phase modelling. *Journal of Physics D: Applied Physics*, 47(14):145201, 2014

  [7] S. Reuter, A. Schmidt-Bleker, S. Iseni, J. Winter, and K.-D. Weltmann. On the bullet-streamer dualism. *IEEE Transactions on Plasma Science*, 42(10):2428–2429, 2014

  [8] S. Hofmann, K. van Gils, S. van der Linden, S. Iseni, and P. Bruggeman. Time and spatial resolved optical and electrical characteristics of continuous and time modulated RF plasmas in contact with conductive and dielectric substrates. *European Physical Journal D*, 68(3), 2014

- **2013**

  [1] J. Winter, K. Wende, K. Masur, S. Iseni, M. Dünnbier, M. U. Hammer, H. Tresp, K. D. Weltmann, and S. Reuter. Feed gas humidity: a vital parameter affecting a cold atmospheric-pressure plasma jet and plasma-treated human skin cells. *Journal of Physics D: Applied Physics*, 46(29):295401, 2013

- **2012**

  [1] S. Reuter, J. Winter, S. Iseni, S. Peters, A. Schmidt-Bleker, M. Dünnbier, J. Schafer, R. Föest, and K. D. Weltmann. Detection of ozone in a MHz argon plasma bullet jet. *Plasma Sources Science and Technology*, 21(3):034015, 2012

Paper proceeding

[1] S. Reuter, A. Schmidt-Bleker, H. Tresp, J. Winter, S. Iseni, M. Hammer, Dünnbier, and K. D. Weltmann. Interaction of atmospheric pressure plasma jets with liquids. *Plasma Physics and Technology*, 1(2):55–57, 2014

[2] S. Iseni, A Schmidt-Bleker, J. Winter, K. D. Weltmann, and S. Reuter. Laminar versus turbulent flow of an argon RF APPJ investigated by OH PLIF and its influence on the discharge propagation. *Gas discharge proceeding book*, 2014

Invited talk

[1] S. Iseni, S. Reuter and K. D. Weltmann, "Laser based spectroscopy, PLIF — Atm. Pres. Plasma jets: turbulent vs laminar"
Workshop 4: Major challenges in the diagnostics of non thermal plasma sources relevant

for biomedical applications.
20th International Conference on Gas Discharges and their Applications , 6.-12.07, 2014, Orléans, France

[2] S. Iseni, S. Zhang, A.F.H van Gessel, S. Hofmann, BTJ van Ham, S. Reuter, K. D. Weltmann and P. Bruggeman, "Nitric Oxide absolute density distribution of an Ar APPJ: effect of gas flow and substrate"
Workshop MP1101 European COST Action – Bioplasma, 13.-14.10, 2014, Paris, France

Conference talks

[1] S.Reuter, A. Schmidt-Bleker, S. Iseni, H. Jablonowski, J. Winter and K. D. Weltmann, "Diagnostics of Atmospheric Pressure Plasma Jets"
68th Gaseous Electronics Conference, 12.-16.10, 2015, Honolulu - Hawaii, United-States

[2] S.Reuter, A. Schmidt-Bleker, S. Iseni, J. Winter, H. Jablonowski, and K. D. Weltmann, "LIF spectroscopy on cold Plasma Jets for Plasma Medicine"
17th International Symposium on Laser-Aided Plasma Diagnostics, 27.09-01.10, 2015, Hokkaido, Japan

[3] S.Reuter, A. Schmidt-Bleker, H. Jablonowski, J. Winter, S. Iseni, Th. v. Woedtke and K. D. Weltmann, "Interaction of pasma jets with liquids for biomedical applications"
6th Central European Symposium on Plasma Chemistry, 06.-10.09, 2015, Bressanone, Italy

[4] S.Reuter, S. Bekeschus, M. Dünnbier, M. Hammer, S. Hasse, S. Iseni, H. Jablownowski, K. Masur, A. Schmidt, A. Schmidt-Bleker, Th. v. Woedtke, K. Wende, J. Winter and K. D. Weltmann, "Reactive Species in Plasma Medicine"
22nd International Symposium on Plasma Chemistry, 05.-10.07, 2015, Antwerp, Belgium

[5] S.Reuter, A. Schmidt-Bleker, H. Jablonowski, J. Winter, A. Bösel, M. Hammer, S. Iseni and K. D. Weltmann, "Fundamental Aspects of Filamentary Jet Discharges Interacting with Biologically Relevant Liquids and with Cells"
32nd International Conference on Phenomena in Ionized Gases, 26.-31.07, 2015, Iasi, Romania

[6] S.Reuter, A. Schmidt-Bleker, H. Jablonowski, S. Iseni, J. Winter, S. Norberg, J. S. Sousa, Th. v. Woedtke, V. Puech, M. J. Kushner and K. D. Weltmann, "Diagnostics of Atmospheric and Liquid Plasmas"
XIth Frontiers in Low Temperature Plasma Diagnostics, 24.-28.05, 2015, Hyéres, France

[7] S. Iseni, A. Schmidt-Bleker, J. Winter, K. D. Weltmann and S. Reuter, "Laminar versus turbulent flow of an argon RF APPJ investigated by OH PLIF and its influence on the discharge propagation"
20th International Conference on Gas Discharges and their Applications, 6.-12.07, 2014, Orléans, France

[8] S. Reuter, J. Winter, A. Schmidt-Bleker, S. Iseni, H. Tresp, A. Barton, M. Hammer, M. Dünnbier, K. Masur, K. Wende and K. D. Weltmann, "Reactive Species Processes in Plasma-, Gas-, and Liquid- Phase "

66th Annual Gaseous Electronics Conference (GEC 66th), 29.9.-4.10, 2013, Princeton, USA

[9] S. Iseni, K. D. Weltmann and S. Reuter, "From low to atmospheric pressure plasma diagnostics based on quantum cascade laser absorption spectroscopy"
19th International Vacuum Congress (IVC 19th), 09.-13.09, 2013, Paris, France

[10] S. Reuter, M. Hammer, J. Winter, H. Tresp, S. Iseni, A. Schmidt-Bleker, J. Sousa, M. Dünnbier, K. Masur, V. Puech and K. D. Weltmann, "Controlled Application of Atmospheric Pressure Plasma Jets interacting with Liquids"
19th International Vacuum Congress (IVC 19th), 09.-13.09, 2013, Paris, France

[11] J. Winter, K. Wende, M. Hammer, H. Tresp, S. Iseni, M. Dünnbier, K. Masur, K. D. Weltmann and S. Reuter, "Feed gas humidity: small concentrations – large effects"
21st International Symposium on Plasma Chemistry (ISPC 21st), 04.-09.08, 2013, Cairns, Australia

[12] S. Iseni, K. D. Weltmann and S. Reuter, "Absolute reactive molecule densities from an argon RF atmospheric pressure plasma jet measured by quantum cascade laser absorption spectroscopy"
40th IEEE International Conference on Plasma Science (ICOPS 40th), 16.-21.07, 2013, San Francisco, USA

[13] J. Winter, M. Hammer, M. Dünnbier, H. Tresp, K. Wende, S. Iseni, K. Masur, K. D. Weltmann and S. Reuter, "Feed gas humidity versus ambient humidity – What matters more in plasma medicine and what makes cells care?"
40th IEEE International Conference on Plasma Science (ICOPS 40th), 16.-21.07, 2013, San Francisco, USA

[14] J. Sousa, H. Tresp, M. Dünnbier, S. Iseni, M. Hammer, J. Winter, V. Martin, V. Puech, K. D. Weltmann and S. Reuter, "Plasma-generated reactive oxygen species for biomedical applications"
International Conference on Plasma Medicine 4 (ICPM 4), 17.-21.06, 2012, Orléans, France

[15] S. Hofmann, S. J. A. Linden, C. A. J. van Gil, S. Iseni and P. J. Bruggeman, "A comparison of different cold atmospheric pressure plasma jets for biomedical applications: gas temperatures, morphology, power dissipation and biological activity"
39th IEEE International Conference on Plasma (ICOPS 39th), 08.-13.06, 2012, Edinburgh, Scotland

Workshop talks

[1] S. Iseni, A. Schmidt-Bleker, K. D. Weltmann and S. Reuter, "Gas flow and discharge propagation interaction of a non-thermal atmospheric pressure plasma"
3rd Young Professionals Workshop on Plasma Medicine, 18.-20.09, 2014, Zinnowitz, Germany

[2] S. Iseni, K. D. Weltmann and S. Reuter, "Laser diagnostics for atmospheric pressure plasma jets investigation from UV to mid-IR"
2nd Young Professionals Workshop on Plasma Medicine, 15.-18.09, 2013, Kölpinsee, Germany

[3] S. Reuter, J. Winter, M. Hammer, H. Tresp, S. Iseni, A. Schmidt-Bleker, M. Dünnbier, K. Masur, K. Wende and K. D. Weltmann, "Tailoring Reactive Oxygen and Nitrogen Species in Micro Plasma Jets Interacting with Biological Liquids"
7th International Workshop on Microplasmas, 20.-25.05, 2013, Peking, China

[4] S. Reuter, J. Winter, M. Hammer, H. Tresp, S. Iseni, A. Schmidt-Bleker, M. Dünnbier, K. Masur, K. Wende and K. D. Weltmann, "Tailoring Reactive Oxygen and Nitrogen Species in Micro Plasma Jets Interacting with Biological Liquids"
3rd Workshop Plasmamedicine des AK-ADP, 03.-04.06., 2013, Berlin, Germany

[5] S. Iseni, J. Winter, K. D. Weltmann and S. Reuter, "A mid-infrared eye to look into reactive species from plasma jets: let's focus on ozone"
1st Young Professionals Workshop on Plasma Medicine, 16.-19.12, 2012, Boltenhagen, Germany

[6] J. Winter, M. Dünnbier, S. Iseni, A. Schmidt-Bleker, K. D. Weltmann and S. Reuter, "Measurement of Ozone in Atmospheric Pressure Plasmas"
14th Workshop des AK-ADP "Plasma im Visier", 16.-17.10, 2012, Bochum, Germany

[7] M. Dünnbier, J. Winter, S. Iseni, A. Schmidt-Bleker, K. D. Weltmann and S. Reuter, "Detektion von Ozon in einem MHz-Argon-Plasmajet"
DPG Frühjahrstagung, 25.-30.05, 2012, Stuttgart, Germany

[8] J. Winter, M. Dünnbier, S. Iseni, A. Schmidt-Bleker, K. D. Weltmann and S. Reuter, "Detection of Ozone in an Atmospheric Pressure Plasma Jet"
5th International Workshop on Plasma Spectroscopy, 13.-16.05, 2012, Presqu'Île de Giens, France

[9] S. Hofmann, C. A. J. van Gil, S. Iseni and P. J. Bruggeman, "Electrical and optical diagnostics of an RF and a nanosecond pulsed DC cold atmospheric pressure plasma jet for biomedical applications"
24th NNV-symposium on Plasma Physics and Radiation Technology, 6.-7.03, 2012, Lunteren, The netherlands

Conference and workshop posters

[1] S. Iseni, A. Schmidt-Bleker, J. Winter, K. D. Weltmann and S. Reuter, "Gas flow and discharge propagation interaction of a non-thermal, non-equilibrium RF argon atmospheric pressure plasma jet investigated by planar laser induced fluorescence"
XXII Europhysics Conference on Atomic and Molecular Physics of Ionized Gases (ESCAMPIG XXII), 15.-19.07, 2014, Greifswald, Germany

[2] A. Schmidt-Bleker, J. Winter, S. Iseni, M. Dünnbier, K. D. Weltmann and S. Reuter, "The Influence of Shieling Gas Composition on the Dynamics, Temperature and Reactive

Species Generated by a Cold Atmospheric Pressure Plasma Jet with Gas Shielding Device"
XXII Europhysics Conference on Atomic and Molecular Physics of Ionized Gases (ESCAMPIG XXII), 15.-19.07, 2014, Greifswald

[3] J. Winter, K. Wende, M. Hammer, H. Tresp, S. Iseni, M. Dünnbier, K. Masur, K. D. Weltmann and S. Reuter, "Feed gas humidity: small concentrations – large effects"
21st International Symposium on Plasma Chemistry (ISPC 21st), 04.-09.08, 2013, Cairns, Australia

[4] S. Reuter, S. Iseni, H. Tresp, A. Schmidt-Bleker, J. Winter, M. Hammer, M. Dünnbier and K. D. Weltmann, "Diagnostics of Plasma Jets interacting with Liquids for Life Science"
31st International Conference on Plasmas and Ionized Gases (ICPIG 31st), 14.-19.07, 2013, Granada, Spain

[5] S. Iseni, T. Darny, D. Ries, E. Robert, J. M. Pouvesle, K. D. Weltmann and S. Reuter, "Analysis of NO_x production in an RF Kinpen and a µs driven Plasma Gun"
IEEE Pulsed Power & Plasma Science Conference (PPPS 2014), 16.-24.06, 2013, San Francisco, USA

[6] S. Reuter, J. Winter, M. Hammer, S. Iseni, H. Tresp, A. Schmidt-Bleker, M. Dünnbier and K. D. Weltmann, "Absorption Spectroscopy on Plasma Jets Interacting with Liquids"
10th Frontiers in Low Temperature Plasma Diagnostics (FLTPD 10th), 28.04-02.05, 2013, Kerkrade, The Netherlands

[7] S. Iseni, J. Winter, M. Dünnbier, K. D. Weltmann and S. Reuter, "Diagnostic of plasma jet by mid-IR absorption spectroscopy with quantum cascade laser"
65th Gaseous Electronics Conference (GEC), 22.-26.10, 2012, Austin, USA

[8] S. Iseni, J. Winter, M. Dünnbier, K. D. Weltmann and S. Reuter, "Ozone detection and production rate measurement by Mid-Infrared absorption spectroscopy in a plasma jet operating at atmospheric pressure"
International Conference on Plasma Medicine 4 (ICPM 4), 17.-21.06, 2012, Orléans, France

[9] M. Dünnbier, J. Winter, S. Iseni, A. Schmidt-Bleker, K. D. Weltmann and S. Reuter, "Space resolved ozone detection in the effluent of a cold atmospheric pressure plasma jet"
XXI Europhysics Conference on Atomic and Molecular Physics of Ionized Gases (ESCAMPIG XXI), 10.-14.06, 2012, Viana do Castelo, Portugal

[10] M. Dünnbier, J. Winter, S. Iseni, A. Schmidt-Bleker, K. D. Weltmann and S. Reuter, "Absorption spectroscopy of ozone produced by an atmospheric pressure plasma jet"
Plasmamedizin AK-ADP, 2.-3.12, 2011, Erfurt, Germany

Eigenständigkeitserklärung

Hiermit erkläre ich, dass diese Arbeit bisher von mir weder an der Mathematisch-Naturwissenschaftlichen Fakultät der Ernst-Moritz-Arndt-Universität Greifswald noch einer anderen wissenschaftlichen Einrichtung zum Zwecke der Promotion eingereicht wurde.
Ferner erkläre ich, dass ich diese Arbeit selbständig verfasst und keine anderen als die darin angegebenen Hilfsmittel und Hilfen benutzt und keine Textabschnitte eines Dritten ohne Kennzeichnung übernommen habe.

Read and approved,

Sylvain R. R. Iséni

Date

Sylvain Iséni

M.Sc., Dipl.Eng.

Bahnhofstraße 2/3, whg.N22,
17489 Greifswald, Deutschland
☎ *00 33 6 78 62 13 16*
✉ *iseni.sylvain@gmail.com*

Personal Information

date of birth	October 17th, 1988
place of birth	Gien (Loiret), France
nationality	French

Education

University

since 2012	**PhD candidate**, *Ernst-Moritz-Arndt-Universität Greifswald*, Greifswald, Germany. Faculty of Mathematics and Natural Science. Supervisor: Prof. Dr. K.-D. Weltmann.
2011	**Master of Physics**, *Université d'Orléans*, Orléans, France, upper honors. specialty: plasma physics, energy, environment and space.
Jan.-Jul. 2011	**ERASMUS program**, *University of Technology Eindhoven*, the Netherlands. Master project; subject: diagnostics of atmospheric pressure plasma jet for biomedical application. Supervisor: Prof. Dr. P. Bruggeman.
2011	**French Engineering Title**, *École Polytechnique de l'Université d'Orléans*, Orléans, France. specialty: optics, laser and plasma processes.

Schools

2006	**Scientific Baccalauréat**, *Lycée Bernard Palissy*, Gien (Loiret), France, upper second class honors.

Job Training

Jun.-Aug.2010	**Research Optics Engineer assistant**, *Maquet Critical Care SA*, Ardon, France. subject: Characterization and colorimetry simulation of LED surgical lightning spot.

Professional Experience Abroad

Jul. 2013 **Guest Researcher**, *University of Technology Eindhoven*, THE NETHERLANDS.
visiting Prof. Dr. P. Bruggeman.

Dec. 2012 **Guest Researcher**, *Masaryk University*, Brno, CZECH REPUBLIC.
visiting Dr. J. Voráč and Dr. P. Dvořák.

2012-2015 **Researcher**, *INP Greifswald e.V. / ZIK plasmatis*, Greifswald, GERMANY.
topic: PhD work. Supervisor: Prof. Dr. K.-D. Weltmann.

Jul.-Dec. 2011 **Final studies internship**, *INP Greifswald e.V. / ZIK plasmatis*, Greifswald, GERMANY.
subject: Mid-IR absorption spectroscopy to diagnose atmospheric pressure plasma jets for biomedical application. Supervisor: Dr. S. Reuter.

International Collaboration

2014 PLASMANT, University of Antwerp, BELGIUM

2012 GREMI, University of Orléans, FRANCE

2013 EPG–TU/e, University of Technology Eindhoven, THE NETHERLANDS

2012 Department of Physical Electronics, Masaryk University, CZECH REPUBLIC

Distinction

2013 **European COST-Action Bioplasma fellowship**, *COST-STSM-MP1101.*
visiting Prof. Bruggeman at the University of Technology Eindhoven, THE NETHERLANDS

March 2013 **Certification Pulsed Laser Advanced skills**, *Sirah, Laser- und Plasmatechnik GmbH*, Grevenbroich, GERMANY.

2013 **Best interdisciplinary talk**, *2nd Young Professional Workshop on Plasma-Medicine*, Kölpinsee, GERMANY.
September 15th-18th.

2012 **Best interdisciplinary talk**, *1st Young Professional Workshop on Plasma-Medicine*, Boltenhagen, GERMANY.
September 16th-19th.

Languages

French	-	*native*
English	**TOEIC B2+**	*fluent, full professional competences*
German	**A2**	*read, basic daily conversation*

CV Sylvain Iséni

Remerciements

Dans cette dernière section, je souhaite m'exprimer sur un fond plus personnel et ainsi faire part de ma sincère gratitude envers les personnes avec qui j'ai interagi au cours de ces trois dernières années.

Mes premiers remerciements sont adressés à mon directeur de thèse, Prof. Dr. Weltmann pour sa confiance ainsi que pour son aide tout au long de mon doctorat qui m'a ainsi permis de mener à bien ce travail de recherche. Ses encouragements et précieux conseils dans l'orientation de mes travaux ont été nécessaires du commencement à la fin de ce travail et m'ont permis d'élargir mon champ de vision pour mieux recentrer ma recherche au sein de la communauté plasma médecine. Je le remercie également pour son implication avec le Prof. Dr. von Woedtke et leurs collaborateurs pour leurs engagements et travaux d'initiations au concept du projet *plasmatis*.

C'est en effet dans le cadre du Zentrum für Innovationskompetenz (ZIK) *plasmatis* que j'ai pu réaliser ce travail. À ce propos, je remercie très sincèrement le Bundesministerium für Bildung und Forschung (BMBF) d'Allemagne d'avoir généreusement financé ce projet.

Mes remerciements sont également adressés aux membres du groupe *plasmatis* et à ses deux dirigeants, Dr. Reuter et Dr. Masur. Ce projet interdisciplinaire mettant en interaction quotidienne biologistes et physiciens des plasmas a été une immense richesse pour moi. À ce titre, je tiens à remercier très sincèrement l'équipe de biologistes, à savoir, Sybille, Annemarie, Lena, Anke, Kristian et Sander pour leur patience ainsi que leur coopération. Merci également à Liane ainsi qu'à Christin pour leur sympathie et précieuse aide dans les divers démarches avec l'administration. Je souhaite également remercier mes collègues de bureau, Helena, Ansgar et Mario pour leur sympathie, assistance, traduction et bonne humeur. Je n'oublie pas d'ajouter à ces derniers les deux post-docs de l'équipe ; Malte toujours prêt à jouer la carte de l'humour ainsi que Jörn et son approche de la physique moderne (la bouteille d'ozone ou encore la cavité résonante à onde de choque...).

Plus généralement, je souhaiterai remercier l'INP et ses employés avec une attention particulière au personnel administratif, à l'atelier mécanique et l'électronique ainsi que le service Marketing qui ont un rôle essentiel d'accompagnement des scientifiques et sans qui peu de choses ne seraient possible. Je saisi ici l'opportunité de remercier le Prof. Dr. Kolb pour ses conseils et fructueux échanges que nous avons partagé. À ce dernier, je souhaiterai remercier Dipl. Ing. Henrik Zimmermann et Dipl. Ing. Sven Glitsch pour leur assistance absolument indispensable à la préparation des mesures effectuées par lasers à cascade quantique. À ce sujet, je suis également très reconnaissant envers Dr. Jean-Pierre van Helden et Prof. Dr. Röpcke pour leur coopération. Le dernier, mais non le moindre, je souhaite à présent remercier très sincèrement mon collègue et ami Dr. Andrei Pipa pour sa patience à m'enseigner les bases de la spectroscopie moléculaire ainsi que les Sciences en général. Philosophe à ses heures, il est vraisemblablement un des rares scientifiques du doute tel a pu l'être René Descartes...

J'exprime à présent toute ma gratitude et sincère reconnaissance envers Prof. Dr. Bruggeman et ses étudiants avec qui j'ai eu la chance de collaborer. Je le remercie tout particulièrement pour son invitation ainsi que pour tous les conseils et connaissances qu'il a pu me transmettre

et qui m'ont permis d'acquérir le niveau de confiance nécessaire pour m'engager dans ce long projet de doctorat.

Je voudrais également dire merci à tous les scientifiques impliqués au sein des collaborations internationales auxquelles j'ai participées. Merci donc à Wouter van Gaens et son directeur de thèse Prof. Dr. Bogaerts pour leur collaboration et leur modèle cinétique chimique. Je remercie également Dr. Éric Robert et Prof. Jean-Michel Pouvesle pour leur invitation à participer au séminaire traitant du diagnostic plasma ainsi que pour toutes les conversations que nous avons pu avoir ces dernières années. Merci à eux également pour leur sympathie et générosité. Je ne voudrais pas oublier de remercier Dr. Jan Vorac de l'Université Masaryk de Brno ainsi que Dr. Sebastian Nemschokmichal de l'Université de Greifswald pour répondre à toutes mes questions au sujet du diagnostic LIF.

Merci également à tous les étudiants qui m'ont assisté dans les travaux de laboratoire, à savoir, Paul, François, Renko et Émile.

Je voudrais également remercier mes amis, Kamil, Vesna & Goran, Michal (for being my best english teacher)...

Je termine en remerciant du fond du cœur mes parents et plus généralement ma famille pour m'avoir toujours soutenu dans mes choix et ma volonté de m'absenter quelque temps pour partir vivre à l'étranger. Je les remercie pour leur soutien et encouragement constant. Merci également à Marina de m'avoir accompagné et si bien compris dans mes choix. Enfin je souhaiterai remercier très sincèrement ma grand-mère d'avoir constamment été à mon écoute et de m'avoir soutenu depuis toujours ainsi que pour avoir accepté mon départ mais aussi, et surtout, pour avoir attendu mon retour... Merci.